



PhD-FSTM-2024-008

Faculty of Science, Technology and Medicine

DISSERTATION

Presented on 08/02/2024 in Luxembourg

to obtain the degree of

DOCTEUR DE L'UNIVERSITE DU LUXEMBOURG

EN SCIENCES DE L'INGENIEUR

by

Thierry DECKER

APPLICATION OF FUNCTIONALLY GRADED LATTICE STRUCTURES SUITABLE FOR ADDITIVE MANUFACTURING IN MECHANICAL PARTS

Dissertation defence committee

Prof. Dr. Slawomir KEDZIORA, dissertation supervisor

University of Luxembourg - Faculty of Science, Technology and Medicine

Prof. Dr. Stefan MAAS

University of Luxembourg - Faculty of Science, Technology and Medicine

Prof. Dr. Michael WAHL

UAS Trier – Department of Environmental Planning and Technology

Prof. Dr. Olaf BRUCH

UAS Bonn-Rhein-Sieg – Department of Engineering and Communication

Prof Dr. hab. Eng. Wiktoria WOJNICZ

Polytechnika Gdanska, Institute of Mechanics and Machine Design

Abstract

Additive manufacturing (AM), also known as 3D printing, has transformed scientific and manufacturing fields with its rapid design iterations and ability to produce intricate geometries, making it accessible through its low entry prices and versatile applications. Within this domain, Functionally Graded Lattice Structures (FGLS) have emerged as a significant development: these low-density cellular structures, spanning large volumes, can be customized and optimized for specific needs. Numerous recent publications delve into their application fields, potential improvements over conventional designs, and appropriate optimization methods, emphasizing advantages in both performance and production efficiency. However, the transfer from theoretical exploration to practical engineering implementation of FGLS remains a challenge, demanding the integration of various critical elements, including detailed material modelling, production requirements, and optimization routines.

In this dissertation, a comprehensive investigation is conducted to address these challenges. The study explores suitable design software, lattice types, manufacturing techniques, and materials, aiming to develop a general-purpose optimization technique. The research evaluates the results based on their performance, providing valuable insights into the potential applications of FGLS. To illustrate the practical aspects of this research, two real-world examples are presented: a steel bicycle crank arm manufactured using metal Fused Deposition Modelling (FDM) printing and a bicycle helmet made of Polyamide produced with Multi Jet Fusion (MJF). These applications showcase the versatility of FGLS, as the optimization goals differ: the crank arm lattice is optimized for maximum stiffness under a mass constraint, while the helmet lattice is optimized for the wearer's maximum protection. Furthermore, the research includes a synthetic test featuring a cuboid lattice geometry subjected to compressive loads, exploring its optimal thickness distribution following mathematical functions. The study demonstrates different lattice splitting and optimization techniques, varying in complexity levels.

Physical testing plays a crucial role in this research, allowing the correlation of simulative findings with actual behaviours. The dissertation includes detailed physical tests of several material and manufacturing options, evaluating their suitability for the presented applications. However, challenges arise during physical testing due to geometrical and material deviations resulting from manufacturing procedures, complicating reliable simulative predictions. Despite these challenges, the optimization routine proves its capability to enhance the performance of lattice structures in numerical simulations, suggesting the potential of FGLS to outperform conventionally produced appliances. These findings highlight the promising future of Functionally Graded Lattice Structures in engineering applications, showcasing their potential to change various industries.

Acknowledgements

The presented work would not have been feasible without the help of many supportive people.

First and foremost, I thank my supervisor Prof. Dr. Slawomir Kedziora whose support, resourcefulness, expertise, and stoic determination proved invaluable during the many challenges that occurred in the projects.

I thank the other defence committee members Prof. Dr. Michael Wahl, Prof, Dr. Stefan Maas, Prof. Dr. Wiktoria Wojnicz, and Prof. Dr. Olaf Bruch for taking the time to review and guide my research progress. I especially thank Prof. Dr. Olaf Bruch for his advice and support provided during my Bachelor's and Master's theses, which encouraged me to pursue a doctoral degree and a career in research.

I thank my friends and family for their support, no matter in which shape or form, throughout the course of all my studies. I especially thank my friend Daniel Grotenburg for his insights and sense of direction. Most importantly, I thank my partner Mayssa Ghiloufi for her love, and for keeping me grounded during this time.

Declaration of Authorship

I, Thierry Decker, declare that this thesis titled

Application of Functionally Graded Lattice Structures Suitable for Additive Manufacturing in Mechanical Parts

and the work presented in it are my own. I confirm that:

- This work was done wholly or mainly while in candidature for a research degree at this University.
- Where any part of this theses has previously been submitted for a degree or any other qualification at this University or any other institution, this has been clearly stated.
- Where I have consulted the work of others, this is always clearly attributed.
- Where I have quoted from the work of others, the source is always given. With the exception of such quotations, this thesis is entirely my own work.
- I have acknowledged all main sources of help.

Luxembourg, 28th of December 2023

Place and Date



Signature

List of Publications

1. Practical Implementation of Functionally Graded Lattice Structures in a Bicycle Crank Arm

Authors: Thierry Decker, Slawomir Kedziora, Claude Wolf

Presented at 885th International Conference on Science, Technology, Engineering and Management (ICSTEM)

25-26.11.2020, Vienna (AT)

ISBN 978-93-90150-16-8

Author contributions based on to CRediT system: Conceptualization, Data Curation, Formal Analysis, Investigation, Methodology, Software, Validation, Visualization, Writing – original draft, Writing – review and editing.

2. Strength Properties of 316L and 17-4 PH Stainless Steel Produced with Additive Manufacturing

Authors: Slawomir Kedziora, Thierry Decker, Elvin Museyibov, Julian Morbach, Steven Hohmann, Adrian Huwer, Michael Wahl

Published in MDPI Materials on 09.09.2022

<https://doi.org/10.3390/ma15186278>

Author contributions based on to CRediT system: Data Curation, Formal Analysis, Investigation, Writing – review & editing.

3. Comparison of strength properties of common Powder Bed Fusion and Stereolithography materials

Authors: Thierry Decker, Slawomir Kedziora, Elvin Museyibov

Presented at 11th International Conference on Nano and Materials Science (ICNMS)

13-15.1.2023, Singapore (SG)

<https://doi.org/10.4028/p-Sgu1sR>

Author contributions based on CRediT system: Conceptualization, Data Curation, Formal Analysis, Investigation, Methodology, Software, Validation, Visualization, Writing – original draft, Writing – review and editing.

4. Application of Functionally Graded Shell Lattice as Infill in Additive Manufacturing

*Authors: Slawomir Kedziora, **Thierry Decker**, Elvin Museyibov*

Published in MDPI Materials on 15.06.2023

<https://doi.org/10.3390/ma16124401>

Author contributions based on CRediT system: Conceptualization, Investigation, Methodology, Validation, Writing – review & editing.

5. Local Thickness Optimization of Functionally Graded Lattice Structures in Compression

*Authors: **Thierry Decker**, Slawomir Kedziora*

Published in MDPI Applied Sciences on 23.10.2023

<https://doi.org/10.3390/app132312969>

Author contributions based on CRediT system: Conceptualization, Data Curation, Formal Analysis, Investigation, Methodology, Software, Validation, Visualization, Writing – original draft, Writing – review and editing.

6. Optimizing the Thickness of Functionally Graded Lattice Structures for High-Performance Energy Absorption: A Case Study based on a Bicycle Helmet

*Authors: **Thierry Decker**, Slawomir Kedziora*

Submitted for review in MDPI Applied Sciences on 18.01.2024

Author contributions based on CRediT system: Conceptualization, Data Curation, Formal Analysis, Investigation, Methodology, Software, Validation, Visualization, Writing – original draft, Writing – review and editing.

Table of Contents

Table of Figures	II
Table of Abbreviations	VII
1 Introduction	1
1.1 Motivation & Problem Statement.....	1
1.2 Objective & Approach	3
1.3 Thesis Structure	3
2 Fundamentals & State of the Art	4
2.1 Cellular Structures	4
2.1.1 Foams and their Structural Properties	6
2.1.2 Surface-Based Lattices	15
2.1.3 Graph-Based Lattices	18
2.1.4 Functionally Graded Lattice Structures.....	21
2.1.5 Industry Applications of Functionally Graded Lattice Structures.....	26
2.1.6 Summary	28
2.2 Additive Manufacturing Techniques	29
2.2.1 Preprocessing	30
2.2.2 Fused Deposition Modelling	31
2.2.3 Light Polymerisation	33
2.2.4 Powder Bed Fusion	34
2.2.5 Suitable Additive Manufacturing Methods for Lattice Geometries	36
2.2.6 Summary	37
2.3 Lattice Design and Simulation Software	38
3 Research Methodology & Objectives	44
3.1 Research Objectives	44
3.2 Research Methodology	45
3.3 Scope	47
3.4 Lattice Optimization Method & Application.....	48
4 Publications	55
4.1 Graded Graph Lattice in a Bicycle Crank Arm	55
4.2 Material Properties of Steel Produced with Metal FDM.....	56
4.3 Graded Shell Lattice in a Bicycle Crank Arm	57
4.4 Strength Properties of PBF and SLA Materials.....	58

4.5	Optimization of a Graded Lattice Structure in Compression	59
4.6	Optimizing the Thickness of a Graded Lattice in a Bicycle Helmet	60
5	Discussion	62
5.1	Responses to Research Questions.....	62
5.2	Limitations.....	67
6	Summary & Outlook	70
6.1	Summary.....	70
6.2	Outlook	72
7	Addendum	73
7.1	MATLAB Conversion Code from LTCX to OptiStruct Input File.....	73
7.2	MATLAB Conversion Code from RADIOSS Input File to LTCX.....	76
7.3	Beam Lattice Splitting Script in TCL/TK	78
7.4	Shell Lattice Splitting Script in TCL/TK	81
7.5	Supplemental Content of Investigation on Graph Lattice in Crank Geometry	84
7.6	Markforged Metal X System	87
7.7	Printing Tests of Crank with Lattice Geometry	91
7.8	Omitted Results of Thickness Optimization in Cuboid Lattice Structure	94
7.9	Test Stand for Helmet Drop Tests.....	97
7.10	Helmet Geometry with Lattice Structure	99
	Bibliography	101

Table of Figures

Figure 1.1: Example of Topology Optimization procedure demonstrated on General Electric jet bracket. (Tony Abbey, 2018).....	1
Figure 1.2: Bracket with Topology Optimization and subsequent lattice optimization performed with Altair OptiStruct. (Altair University Fall Webinar Series 2020, n.d.)	1
Figure 2.1: Example of honeycomb (top), open-cell foam (middle), and closed-cell foam (bottom), adapted from (Gibson & Ashby, 1997).	5
Figure 2.2: Cellular structure of cork depending on its direction, adapted from (Le Barbenchon et al., 2019).	6
Figure 2.3: Scanning Electron Microscope pictures of cuttlefish bone structure (Birchall & Thomas, 1983).	6
Figure 2.4: Bubble foam (right) (Frido Verweij, 2023) and 2D Voronoi representation of foam cells (left) (Gibson & Ashby, 1997).	7
Figure 2.5: Compressive stress-strain response of elastomeric foam (top), an elastic-plastic foam (middle) and a brittle foam (bottom). (Gibson & Ashby, 1997)	8
Figure 2.6: Schematic composition of an open cell with equal edge lengths. Its cell extents are denoted by l and the edge thickness by t . (Gibson & Ashby, 1997).....	10
Figure 2.7: Deformation of open cell during the linear elastic phase. (Gibson & Ashby, 1997).....	10
Figure 2.8: Schematic composition of closed cell. (Gibson & Ashby, 1997).....	10
Figure 2.9: Deformation mode of a hexagonal closed cell in tension and compression with folds appearing on the cell wall. (Gibson & Ashby, 1997).....	10
Figure 2.10: Elastic buckling of an open cell. (Gibson & Ashby, 1997)	10
Figure 2.11: Plastic hinge formation of an open cell. (Gibson & Ashby, 1997).....	10
Figure 2.12: Plastic deformation of a closed cell. (Gibson & Ashby, 1997)	10
Figure 2.13: Compressive stress-strain response of expanded polyurethane (left) and polyethylene (right) foams at different densities (Gibson & Ashby, 1997).....	13
Figure 2.14: Example of edge alignment in hexagonal unit cell at increasing tensile strains, adapted from (Gibson & Ashby, 1997).	14
Figure 2.15: Crack propagation through open-cell foam structure caused by tensile load (Gibson & Ashby, 1997).	14
Figure 2.16: Tensile and compressive stress response of PVC foam at different densities. (Walter et al., 2009)	14
Figure 2.17: Examples of surface-based unit cells: (a) triangular honeycomb, (b) hexagonal honeycomb, (c) Face-Centred Cubic.	15
Figure 2.18: Examples of TPMS unit cells: (a) Gyroid, (b) Schwarz, (c) Diamond, (d) Lidinoid, (e) SplitP, (f) Neovius.	15
Figure 2.19: Von Mises stress distribution of a Gyroid TPMS lattice in compression, adapted from (Al-Ketan et al., 2020).	16
Figure 2.20: TPMS lattice with smooth transition from Gyroid to Schwarz Primitive lattice type. (Maskery et al., 2018)	16
Figure 2.21: Gyroid lattice structure in butterfly wing scales, adapted from (Gan et al., 2016).	17
Figure 2.22: Diamond lattice structure found in weevil scales. (L. Han & Che, 2018)	17

Figure 2.23: Compressive stress-strain response of cubic Gyroid structure made of PA2200 with 4x4x4 unit cells at different relative density ratios from 7% to 46%, adapted from (Abueidda et al., 2019)).	18
Figure 2.24: Graph-based lattice structure in Radiolaria skeleton. (Radiolaria - Geology Is the Way, n.d.)	18
Figure 2.25: Selection of graph unit cells. First row: Simple Cubic, Body Centred Cubic, Face Centred Cubic, Diamond. Second row: Fluorite, Octet, Truncated Cube, Truncated Octahedron. Third row: Kelvin cell, Isotruss, Re-entrant, Weaire-Phelan.	19
Figure 2.26: Maxwell's rule for 3D unit cells: bending-dominated cell (left), stretching-dominated cell (middle) and overconstrained cell (right). (Tamburrino et al., 2018)	20
Figure 2.27: Non-rigid (left) and rigid (right) infinite 2D lattices. (Deshpande et al., 2001)	20
Figure 2.28 Compressive stress-strain behaviour of stretch-dominated and bending-dominated lattices. (Tamburrino et al., 2018)	21
Figure 2.29: Shear band formation in BCC lattice composed of Al-12Si. (Liu et al., 2021)	21
Figure 2.30: Cross-section of a human femur showing solid cortical shell and trabecular, lattice-like bone structure with orientations and densities varying as function of local conditions. (Voo et al., 2004)	22
Figure 2.31: Stepwise density grading of graph lattice via unit cell height alteration. (Xiao & Song, 2018)	23
Figure 2.32: Continuous grading of TPMS Gyroid lattice via thickness alteration (left) or cell size alteration (right). (Al-Ketan et al., 2020)	23
Figure 2.33: Damage-resistant lattice containing varying unit cell types (Face-Centred Cubic (FCC) and Body-Centred Cubic (BCC)) separated into regions mimicking metallic crystals, adapted from (Pham et al., 2019b).	23
Figure 2.34: Drop test setup of simplified helmet geometry with size graded lattice liner. (Khosroshahi et al., 2018)	24
Figure 2.35: Pressure, velocity, and temperature in lattice heat exchanger after optimization, adapted from (Takezawa et al., 2019).	25
Figure 2.36: Relative density, voxel representation and mesh representation of TPMS lattice after optimization, adapted from (Simsek et al., 2021).	25
Figure 2.37: Optimisation of strut-based lattice in a three-point bending case with beams following principal stress directions, adapted from (Daynes et al., 2017).	25
Figure 2.38: Anisotropic lattice graded in unsupported bending load case, adapted from (Li et al., 2020).	25
Figure 2.39: Compliance-based optimization result of L-shaped bracket (Fernandes & Tamijani, 2021).	25
Figure 2.40: Graded lattice in shoe sole by Adidas and Carbon 3D. (Carbon 3D Print Lattice Innovation — The Adidas Story, n.d.)	27
Figure 2.41: Specialized Mirror saddle with size-graded lattice. (S-Works Romin EVO with Mirror, n.d.)	27
Figure 2.42: Heat exchanger with TPMS structure by HRL Laboratories. (How NTopology Was Used to Design, Analyze and Print a Fuel-Cooled Oil Cooler, n.d.)	28

Figure 2.43: Cobra Aero drone engine block with lattice heat exchanger. (NTop Cross Section of a Drone Engine Cylinder Designed in NTop Platform by Cobra Aero - MANUFACTUR3D, n.d.)	28
Figure 2.44: Titanium orthopaedic implant with controllable porosity and surface roughness to aid osseointegration. (Medical Additive Complex Structures - Titanium Complex Medical Structure Manufacturer, n.d.).....	28
Figure 2.45: Manufacturing processes (top to bottom): formative, subtractive and additive, adapted from (Redwood Ben, Schöffner Filemon, 2018)	29
Figure 2.46: Ishikawa diagram of manufacturing parameters influencing a part’s quality. (Diegel et al., 2019)	30
Figure 2.47: Stair-stepping resulting from discretized build process of Additive Manufacturing. (Diegel et al., 2019)	31
Figure 2.48: Working principle of Fused Deposition Modelling printing process. (Redwood Ben, Schöffner Filemon, 2018)	32
Figure 2.49: Layer-wise part building process, adapted from (Redwood Ben, Schöffner Filemon, 2018).	32
Figure 2.50: Examples of increasing infill densities with prismatic pattern. (Diegel et al., 2019)	33
Figure 2.51: Working principle of light polymerisation technique, adapted from (Redwood Ben, Schöffner Filemon, 2018).	34
Figure 2.52: Working principle of laser-based powder bed fusion process, adapted from (Redwood Ben, Schöffner Filemon, 2018).....	35
Figure 2.53: Schematic depiction of the Multi Jet Fusion manufacturing process. (O’Connor et al., 2018)	35
Figure 2.54: Implicit representation of a body with local values F as function of the pints P ’s position on the inside, outside and on the body’s border. (Allen, 2019)	40
Figure 2.55: Implicit scaling operation achieved by adding a constant value to the implicit function. (Allen, 2019).....	40
Figure 2.56: Boundary representation of a 2D rectangle (left) and its implicit representation (right), adapted from (Allen, 2019).....	40
Figure 2.57: Examples of applying a functionally graded lattice to a cantilever beam.....	41
Figure 2.58: Examples of unit cells and their equivalent, homogenized directional stiffness properties, adapted from (Johnathan, 2020).	42
Figure 3.1: Primary and secondary research methodology steps.....	45
Figure 3.2: Bicycle crank arm geometry used for first investigation.	47
Figure 3.3: Bicycle helmet geometry used for second investigation.	47
Figure 3.4: Cuboid lattice structures in compression used for auxiliary investigation.....	47
Figure 3.5: Beam element without (left) and with thickness property representation (right).....	48
Figure 3.6: Shell element representation without thickness representation (left) and with discrete thickness steps (right). The colours of the elements in the right image correspond to their respective property collector, underlining that they have different thickness properties.....	49
Figure 3.7: Thick body of a bicycle crank arm modelled with solid tetrahedral elements.....	49
Figure 3.8: Surface lattice represented by shell elements (green), with the thicker surrounding body being modelled with solid elements.....	49
Figure 3.9: Graph lattice represented by beam elements.....	49

Figure 3.10: Beam element property section of input file, with the numerical value of thickness property marked in red (left) and its replacement variable definition (right).....	50
Figure 3.11: Manual (top) and scripting-aided splitting (bottom) of lattice geometry.	51
Figure 3.12: Regions of lattice structure being linked via mathematical function to reduce computational efforts during optimization.....	52
Figure 3.13: Helmet with segregated lattice whose thickness is governed by a quadratic function....	53
Figure 3.14: Flowchart outlining the optimization method and its components.	54
Figure 5.1: Influences of application constraints on choice of unit cell type (Chatzigeorgiou et al., 2022)	66
Figure 7.1: Overview of all tested unit cell types used in the preliminary crank tests	84
Figure 7.2: Influence of lattice rotation on crank displacement for both chosen types	84
Figure 7.3: Cross-section of von Mises stresses in validation model of crank with optimized FCC lattice.....	85
Figure 7.4: Details of von Mises stress concentrations in validation model of crank with optimized FCC lattice	85
Figure 7.5: Cross-section of von Mises stresses in validation model of crank with optimized Re-entrant lattice.....	86
Figure 7.6: Details of von Mises stress concentrations in validation model of crank with optimized Re-entrant lattice.....	86
Figure 7.7: Markforged Metal X system installed at the University of Luxembourg with its sintering oven (left), washing station for chemical binder removal (middle) and the printer (right). Picture kindly provided by Rabie Hayder.	87
Figure 7.8: Example of custom inserted ceramic release layer (orange), replacing the support structure in the crank model with gyroid lattice (white).....	88
Figure 7.9: Test piece for support bypassing with Face-Centred Cubic lattice (left quadrant, 1mm thickness), Tetrahedral lattice (lower quadrant, 1mm thickness), Diamond TPMS (right quadrant, 1mm thickness) and Gyroid TPMS (upper quadrant, 2mm thickness).....	89
Figure 7.10: Aborted print of test piece due to significant stringing and under-extrusion in the beam lattice structures	89
Figure 7.11: First few layers of Markforged 17-4 PH SS metal filament on a Prusa i3 Mk3s printer	90
Figure 7.12: Prototype manufactured with the Markforged Metal X system, 17-4 PH SS and regular, triangular infill.	91
Figure 7.13: Drooping extrusion lines on the underside of the crank manufactured on the Metal X system	91
Figure 7.14: Section of crank model with functionally graded TPMS lattice printed with BASF Ultrafuse 316L (Part and image courtesy of Hochschule Trier)	91
Figure 7.15: Test print of BASF Ultrafuse 17-4 PH SS with cracks occurring during printing.....	92
Figure 7.16: Crack happening during printing (left), fracture during removal of support structure (right)	92
Figure 7.17: Degraded outer wall, probably due to retraction or Z-seam settings	92
Figure 7.18: Sintered BASF Ultrafuse 17-4 print with cracks caused by layer delamination during sintering.....	93
Figure 7.19: Successful print with Markforged 17-4 PH SS	93

Figure 7.20: Simple Cubic lattice made of PA12 with mesh morphing optimization, tests versus simulation.....	94
Figure 7.21: Isotruss lattice made of PA12 with mesh morphing optimization, tests versus simulation	94
Figure 7.22: Simulations of Simple Cubic and Isotruss lattices made with Tough 2000 resin, FEA model optimization results.....	94
Figure 7.23: Simple Cubic lattice made with Tough 2000 resin, base model, tests versus simulations	95
Figure 7.24: Simple Cubic lattice made with Tough 2000 resin, model with linear law thickness optimization, tests versus simulations.....	95
Figure 7.25: Simple Cubic lattice made with Tough 2000 resin, model with mesh morphing optimization, tests versus simulations.....	95
Figure 7.26: Simple Cubic lattice made with Tough 2000 resin, base model, tests versus simulations	95
Figure 7.27: Isotruss lattice made with Tough 2000 resin, model with linear law thickness optimization, tests versus simulations.....	96
Figure 7.28: Isotruss lattice made with Tough 2000 resin, model with mesh morphing optimization, tests versus simulations.....	96
Figure 7.29: Helmet drop test stand.....	97
Figure 7.30: Cast AZ91 magnesium dummy head following EN 960.....	98
Figure 7.31: TE Connectivity 633 acceleration and gyro sensor with six degrees of freedom with upper limits of $\pm 2000G$ translational acceleration and $\pm 12.000^\circ/s$ rotational velocity capacity	98
Figure 7.32: Mikrotron Cube 7 high speed camera used for visual correlation with simulations.....	98
Figure 7.33: HBM U10 12.5kN load cell placed below the anvil's impact surface to log its reaction force	98
Figure 7.34: First prototype of lattice liner helmet printed with SLS in PA12 by GCL Technologies to check its manufacturability	99
Figure 7.35: Helmet with Truncated Cube lattice at 1.5mm thickness used for material optimization study.....	99
Figure 7.36: Helmet with tetrahedral lattice with insufficient strut thickness.....	100
Figure 7.37: Powder accumulation at impact site of optimized Reentrant lattice helmet	100
Figure 7.38: Re-entrant lattice helmet cut open after test to check the excess powder distribution..	100
Figure 7.39: Re-entrant lattice helmet model with additional powder drainage holes	100

Table of Abbreviations

AM	Additive Manufacturing
CAD	Computer-Aided Design
CFD	Computational Fluid Dynamics
DE	Design Exploration
DIC	Digital Image Correlation
DOE	Design Of Experiment
EBM	Electron Beam Melting
EPP	Expanded Polystyrene
EPS	Expanded Polystyrene
EPU	Expanded Polyurethane
FCC	Face Centred Cubic
FDM	Fused Deposition Modelling
FEM	Finite Element Method
FEP	Fluorinated Ethylene Propylene
FGLS	Functionally Graded Lattice Structures
GRSM	Global Response Search Method
HP	Hewlett-Packard
MELS	Modified Extensible Lattice Sequence
MJF	Multi Jet Fusion
PA	Polyamide
PBF	Powder Bed Fusion
PC	Polycarbonate
PEEK	Polyether Ether Ketone
PEKK	Polyether Ketone Ketone
PH	Precipitation Hardened
PLA	Polylactic Acid
SC	Simple Cubic
SEA	Specific Energy Absorption
SLA	Stereolithography
SLM	Selective Laser Melting
SLS	Selective Laser Sintering
SS	Stainless Steel
TO	Topology Optimisation
TPMS	Triply Periodic Minimal Surface
TPU	Thermoplastic Polyurethane

1 Introduction

1.1 Motivation & Problem Statement

With the progress of additive manufacturing (AM) technologies, manufacturers are taking advantage of previously unattainable levels of design flexibility and prototyping possibilities. Design cycles can be drastically shortened, multiple parts consolidated into one and shapes formerly impossible to manufacture can be realised, all while using less energy and material (Diegel et al., 2019). AM simplifies manufacturing designs mimicking nature-inspired organic shapes, for example stemming from topology optimisations (TO). It permits the removal of material from a pre-defined design space where it is not essential for the considered load case. An example of a topology optimized appliance is the jet engine bracket shown in Figure 1.1, where material was removed to reduce the total weight. Producing these organic shapes can be a substantial challenge for subtractive manufacturing methods, and they commonly require manual rebuilding in Computer-Aided Design software (CAD). However, the limits of subtractive methods are quickly reached when trying to produce more complex or hollow structures. Additive Manufacturing allows their production with relative ease and has opened up new areas of research. The next step after TO in the process of reaching for better, bioinspired engineering designs is considered to be cellular structures (Plocher & Panesar, 2019).

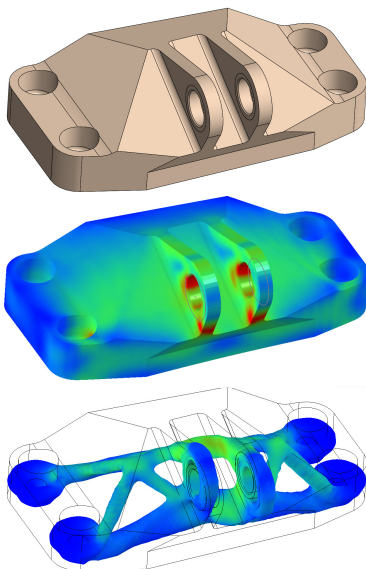


Figure 1.1: Example of Topology Optimization procedure demonstrated on General Electric jet bracket. (Tony Abbey, 2018)



Figure 1.2: Bracket with Topology Optimization and subsequent lattice optimization performed with Altair OptiStruct. (Altair University Fall Webinar Series 2020, n.d.)

Researchers strive to mimic the hierarchical, often nonuniform cellular composition found in sponges, wood, fungi, leaves, bones, and many other biological structures (Gibson & Ashby, 1997). The aim of this growing research domain is to benefit from their high strength-to-weight ratio, energy absorption capacity, vibrational damping capability, heat transfer property, and other beneficial traits (Seharing et al., 2020). Most importantly, AM readily allows for the production of locally varying lattice structures (a subcategory of cellular structures) enabling application-specific, tailored designs. Their cell size, type, orientation, material thickness and even material types can be altered according

to local requirements depending on the use case or user (Uribe-Lam et al., 2021). Such a design is referred to as a Functionally Graded Lattice Structure (FGLS). They can be designed with manually defined property gradients to achieve a certain desired behaviour or be based on external loads (Kang et al., 2019). The latter strives to make optimal use of the material in a specific application such that no performance potential is wasted. A demonstration of an application using a locally optimized lattice structure is shown in Figure 1.2. To achieve this, the bracket has first undergone a TO step. Material was removed from the solid design domain where not required for that specific load case, reducing the part's mass. In a second optimization step, the part's shape was not altered any further, however a lattice structure is introduced to locally decrease its mass even further where possible. The structure's cell size and strut diameter were altered based on the local stress field visible behind the latticed part. High stress regions (coloured in red) remain solid to carry the load adequately, whereas lattices are introduced in low stresses areas (coloured in blue) since less material is required here.

An increasing number of publications revolving around the design, optimization, manufacturing, and performance of FGLS is available. The studied designs are commonly kept simplistic to adhere to facilitate the analysis and comparability. Most only consider manually applied property gradients, commonly by linearly changing the thickness across one axis the structure (Ajdari et al., 2011; Choy et al., 2017; Maskery et al., 2018; Maskery, Hussey, et al., 2017; Niknam & Akbarzadeh, 2020; Tao et al., 2018). If optimization strategies are applied, they are often tackled by heavy use of programming scripts interfacing with commercial or custom physical solvers (Nazir et al., 2019; Pan et al., 2020). In an industrial setting, these customized procedures do not permit an adequate usage of FGLS since complex geometries and load cases are the norm, and simple workflow handling along with versatility is required to iterate on the designs effectively. Despite their clear advantages in numerous tasks, industrial applications are slow to adopt lattice structures and do not yet make use of FGLS on a broad scale. Observation shows that the presented appliances making use of FGLS are mainly used for demonstrative purposes. They tend not to make use of optimization routines, instead relying purely on manual adaptations. The main limitations preventing the wide-spread use of FGLS in industry are the lack of adequate lattice design tools, usable lattice optimization routines compatible with or included in established physical solver suites, simple geometry extraction options, and sufficient knowledge concerning the additive manufacturing of lattices (Aghajani et al., 2023; Nazir et al., 2019; Plocher & Panesar, 2019; Sajjad et al., 2022).

Fuelled by the increasing accessibility of AM, industries strive to benefit from graded and ungraded lattice structures to improve upon existing designs despite the current limitations. The potential use cases include a wide array of domains such as implants in biomedical settings (Mahmoud & Elbestawi, 2017), wearable protective gear like helmets (Khosroshahi et al., 2018; Nasim et al., 2022), impact absorption devices in automotive settings (Hou et al., 2018), lightweight structures in aerospace applications (Zhu et al., 2018), heat exchangers (Cheng et al., 2018) and others (Aghajani et al., 2023).

It is essential to enable efficient and fast design pipelines to implement FGLS in mechanical parts such that designers and consumers alike can reap their benefits. Therefore, the assembled work presented in this thesis provides a holistic method enabling the efficient design, optimization, and manufacturing of FGLS in mechanical parts. It is applicable to complex geometries, supports the numerical simulation of diverse physical phenomena, the structure's optimization for arbitrary goals,

provides an approach to reducing the computational efforts of lattice optimization studies, and ensures the part's manufacturability.

1.2 Objective & Approach

This thesis focuses on developing a comprehensive strategy to include FGLS in mechanical parts, to devise a generalised optimisation strategy compatible with engineering requirements, and to ensure manufacturability of the achieved design via additive methods. Industrial settings demand workflows to be versatile, fast, and to make use of existing tools as much as possible. Hence, the method avoids the use of customized scripts as much as possible and utilizes existing design and analysis software to meet these requirements. Only where they fall short are such scripts used.

Consequently, software suites capable of adequately handling the design, analysis and optimization of lattice structure is determined and employed. A compatible numerical modelling and optimisation method is established, and adequate AM methods are chosen. The findings culminate in applications showcasing the efficacy and flexibility of the devised design pipeline while also demonstrating the applications' performance.

Two devices with realistic geometries are fitted with optimized lattice structures. Common and approachable appliances are chosen: a bicycle crank arm as well as a helmet. They are compared to their conventional counterparts via numerical simulation and physical testing. An auxiliary study investigating the optimal thickness distribution of lattice structures in compression is executed to assess the suitability of different grading methods. The employed production techniques and materials are selected based on manufacturability and the required properties. In addition, physical investigations of the chosen materials are performed to obtain the required material data for numerical modelling.

1.3 Thesis Structure

This introductory section is followed by Chapter 2 covering the fundamentals of cellular structures and lattices, detailing their composition and behaviour under loads. In addition, the current state of relevant research topics, industrial applications and lattice design software is given along with an overview of contemporary Additive Manufacturing techniques. Chapter 3 describes the research objectives and methodology employed in this thesis, as well as the proposed lattice design and optimization routine. Chapter 4 presents the publications containing the practical aspects of the thesis in chronological order, demonstrating the required simulative and experimental steps. Chapter 5 discusses the findings and research questions, listing the encountered complexities and limitations of the chosen approaches. Chapter 6 summarizes the results and provides an outlook for potential future research.

2 Fundamentals & State of the Art

This section gives an overview of the principles applied in these projects. First, a short explanation of cellular structures in general with their occurrences in nature and technical applications, their different subtypes, and behaviour modes under loads is given. Foams are well-researched and share numerous properties with lattice structures, therefore this section explains them in more detail. Following this, Additive Manufacturing techniques and their respective suitability for the models to be manufactured in this project are discussed. Additionally, a short review of simulation techniques is given at the end of this section.

2.1 Cellular Structures

Cellular structures are composed of cells, i.e. small, enclosed spaces repeated throughout a part of or the entirety of larger volume. Their composition entails that they can span large volumes at low weight since they are mostly composed of voids, therefore requiring little material. Biological materials in both flora and fauna are composed of cells serving various functions, such as lightweight structures as found in wood (Ulm, 2001) and bone (Gibson, 1985), water filtration for nutriment extraction in sea sponges (Hadas et al., 2009), fluid transport in plants (Molz & Ikenberry, 1974) and many more. Due to their advantages, artificial cellular appliances mimicking these structures for similar purposes are ubiquitous in engineering tasks. Filters found in various mechanical devices have the purpose of removing unwanted solid particles to keep the transported fluid clean (Mullen & Fischer, 1999). Foams have excellent thermal insulation properties (Demharter, 1998), capillary fluid transport properties (Langlois et al., 2018), sound absorption (Cao et al., 2018), as well as lightweight structural (Suh et al., 2000) and impact energy absorption capabilities (Sherwood & Frost, 1992).

Both naturally occurring and artificial cellular structures are found on various length scales, ranging from micrometres in biological cells to centimetres in sponges. In addition, they can be composed of a wide array of material types. In engineering-related tasks, cellular structures are produced in large quantities out of polymers such as expanded polystyrene (EPS) or expanded polypropylene (EPP) for packaging, flotation devices, or insulation solutions (Raps et al., 2015). Other materials can equally be foamed, such as aluminium for high energy impact absorption (Gibson & Ashby, 1997), or ceramics or glass for thermal and sound insulation in buildings (Arulrajah et al., 2015; Gibson & Ashby, 1997). Further forms of engineered cellular structures can be found in the food industry, where foaming via yeast is used to regulate the consistency of bread where the gas can take up to 70% of the total volume (Wilde, 2012). Likewise, the softness of ice cream and chocolate is controlled by introducing gas bubbles through stirring or whipping (Ellis & Lazidis, 2018; Pugh et al., 2023).

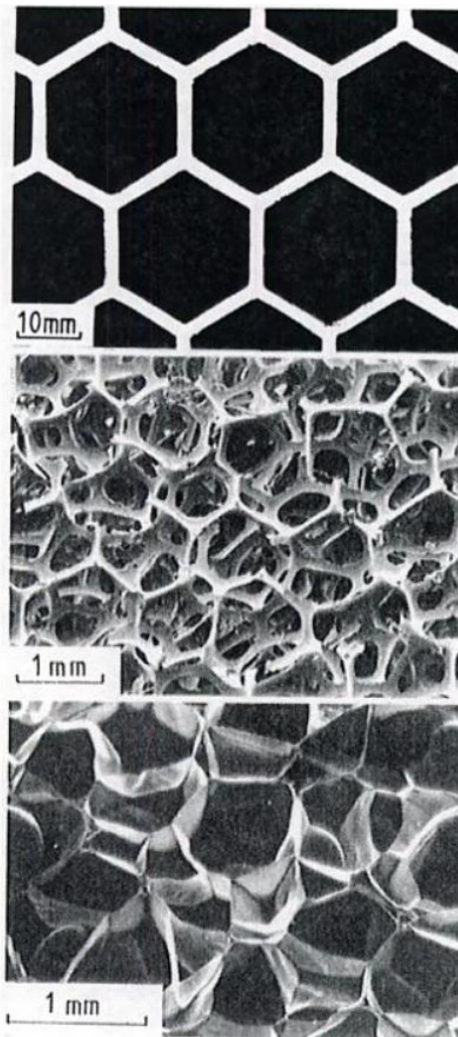


Figure 2.1: Example of honeycomb (top), open-cell foam (middle), and closed-cell foam (bottom), adapted from (Gibson & Ashby, 1997).

Beyond their material configuration, cellular structures are subcategorized depending on their geometrical composition. Two-dimensional arrangements of regular cells are known as honeycombs, even if the cells do not possess the hexagonal cell structure found in beehives. Cells in the form of irregularly shaped, three-dimensional polyhedra distributed throughout a three-dimensional volume are considered to be a foam. Examples of a honeycomb and foams are given in Figure 2.1. However, if a volume is composed of cells with consistent shape and distribution, it is thought of as a lattice. The smallest entity repeated throughout a lattice is known as the unit cell.

Three-dimensional cellular structures can be categorized in open-cell and closed-cell subtypes. The former is characterized by open faces connected to the neighbouring cells, i.e. the material is solely concentrated on the cell edges, while the latter has closed cell faces commonly trapping a fluid inside. While the cell size and its edge or face connectivity can vary throughout a cellular structure, most foams exhibit a common cell shape (Gibson & Ashby, 1997). A certain degree of anisotropy is often present and generally introduced by unequal cell extents in one dimension. One such example is found in cork cells as depicted in Figure 2.2. Their length scale in tangential direction is noticeably smaller than in axial or radial direction. Other forms of anisotropy can be found in differing cell cross-sections depending on the considered axis. Cork cells exhibit prismatic sections in both axial and tangential directions, but

a hexagonal shape in radial direction. Another example is cuttlefish bone which consists of layers interconnected with separate columns as shown in Figure 2.3. The bone not only serves as skeletal structure, but also as a buoyancy device regulating the animal's swimming depth. Its lamellar structure permits the exchange of gas and liquid while being very lightweight and able to withstand pressure differences of up to 2.4MPa (Birchall & Thomas, 1983). Due to its regularity, the bone structure can be considered a naturally occurring lattice structure.

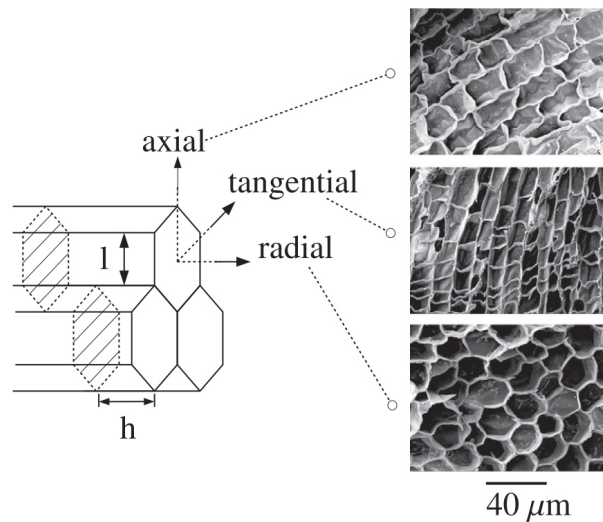


Figure 2.2: Cellular structure of cork depending on its direction, adapted from (Le Barbenchon et al., 2019).

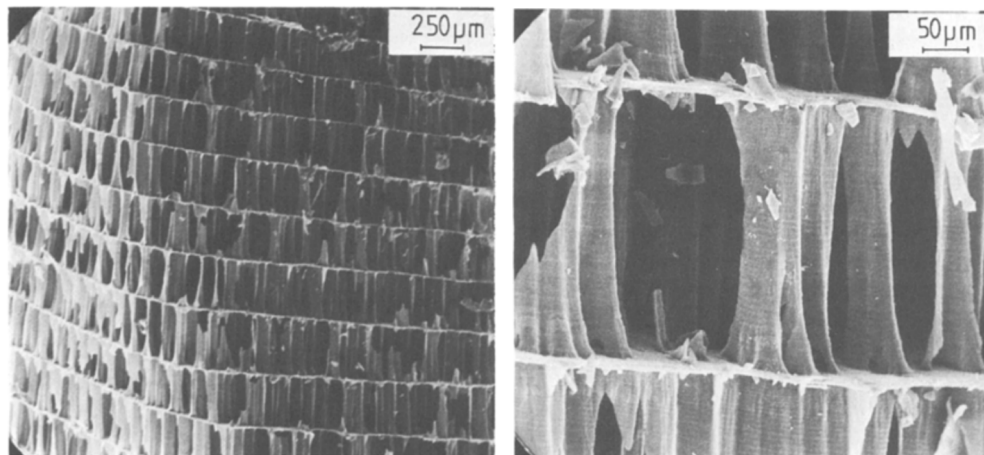


Figure 2.3: Scanning Electron Microscope pictures of cuttlefish bone structure (Birchall & Thomas, 1983).

2.1.1 Foams and their Structural Properties

The structural properties of foams are outlined here within the context of and in relation with lattice structures. Numerous publications investigating lattice structures found that the formulae assembled and refined in (Gibson & Ashby, 1997) also effectively describe lattices. It is therefore referred to as the *Gibson & Ashby Model*, such as by (Maconachie et al., 2019; Song et al., 2023; Yan et al., 2021). While the authors did not lay the entire foundations of this domain, their work is considered the de-facto standard regarding the description of foams and lattices.

As previously described, a foam consists of three-dimensional polyhedral cells of differing sizes and connectivity. In engineered foams, this composition stems from the production processes themselves (Hilyard & Cunningham, 1994). Depending on the material, foams can be manufactured by simple stirring of the liquid monomer or melted base material which introduces bubbles into the mix. Another method is to add physical blowing agents at high ambient pressure, i.e. inert gases such

as carbon dioxide or nitrogen, which then expand when the surrounding pressure is reduced. Other physical blowing agents are heat-activated and change into their gaseous phase at high temperatures, creating bubbles. Other methods make use of chemical blowing agents which decompose or react, releasing gases in the process. Specific production processes or postprocessing operations offer control over the cell type (closed or open cell) as well as the cell size, and to a lesser extent anisotropy by precisely controlling the solidification step through temperature or timing the addition of foaming agents. (Gibson & Ashby, 1997)

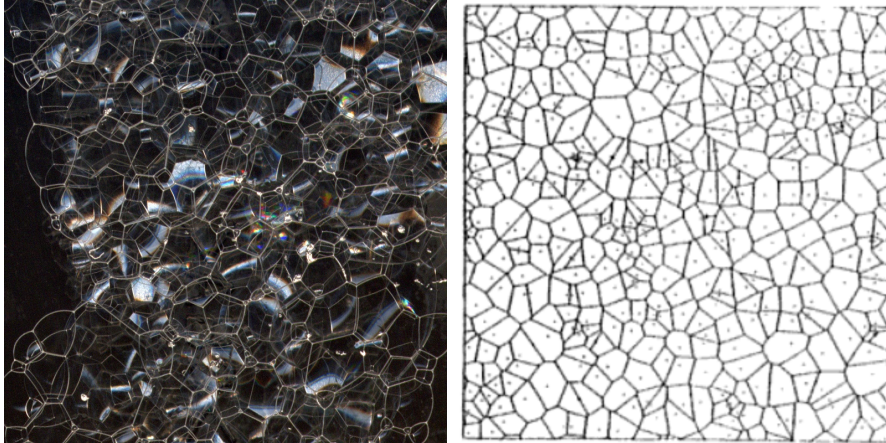


Figure 2.4: Bubble foam (right) (Frido Verweij, 2023) and 2D Voronoi representation of foam cells (left) (Gibson & Ashby, 1997).

The process results in structures seen in Figure 2.4, where a soap bubble foam is shown to easily visualize the three-dimensional composition, as well as a two-dimensional Voronoi diagram representing the formation of bubbles in a liquid medium. The depicted structure is formed when bubbles nucleate simultaneously at random points in a domain and grow with an identical rate (Gibson & Ashby, 1997). Voronoi structures not only occur in foams, but also have major importance in a very wide range of domains such as geography, meteorology, crystallography, chemistry, physics, biology, and computer science (Aurenhammer et al., 2013). Evidently, bubbles do not necessarily nucleate simultaneously in reality, and time delays can result in vastly different cell sizes and connectivity states in a single foam structure.

Foams are readily and primarily used in compressive load cases as they exhibit high energy absorption capabilities with low peak accelerations and very low densities (Gibson & Ashby, 1997; Hilyard & Cunningham, 1994; Suh, 2000). Their behaviour is depicted in Figure 2.5, where three schematic compressive stress-strain responses for elastomeric, elastic-plastic and brittle foams are shown. As described by Gibson & Ashby, the properties extracted from the stress-strain curves refer to the moduli and stresses based on the cross-sectional area of the total structure's extents, and not on the actual area of the material. Therefore, the distinction is made between the material's actual properties, i.e. its Young's modulus E_s and yield strength σ_y , and the structure's apparent properties such as its apparent modulus E^* and apparent yield strength σ_y^* . One of the most important characteristics of cellular structures is their relative density ρ^*/ρ_s . It is defined as the structure's density ρ^* (denoted by the volume of its total extents, not the volume actually occupied by

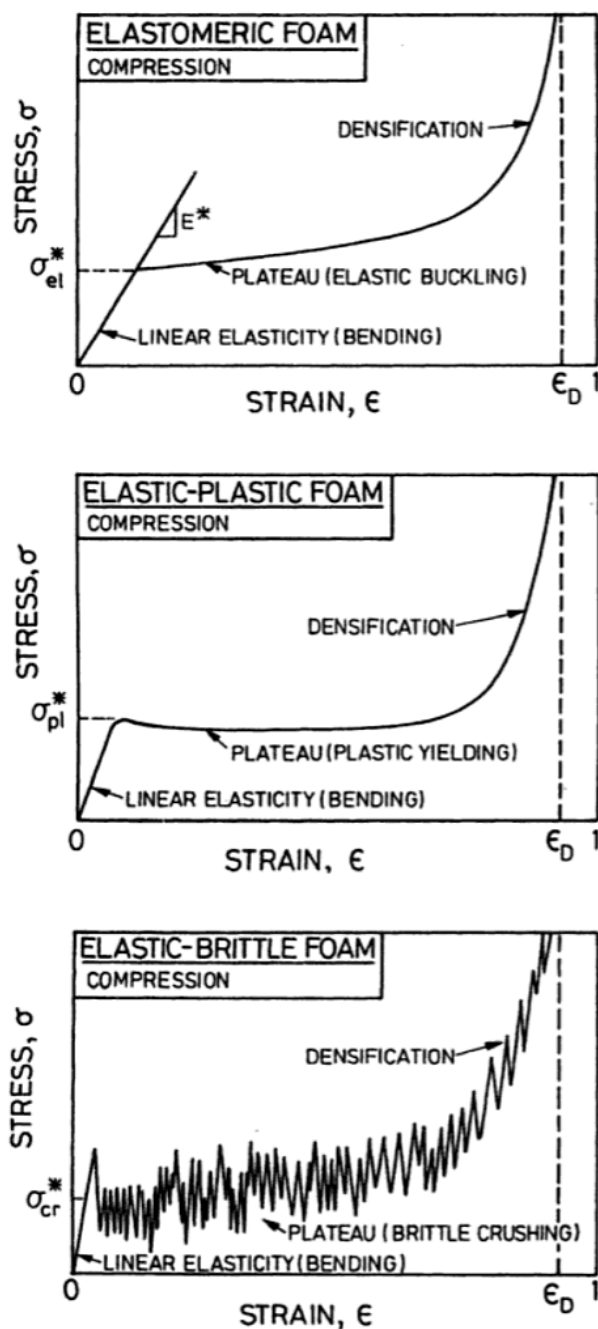


Figure 2.5: Compressive stress-strain response of elastomeric foam (top), an elastic-plastic foam (middle) and a brittle foam (bottom). (Gibson & Ashby, 1997)

the skeleton cubic cell model which provides a decent approximation of both open-cell and closed-cell foams. Other models for different cell geometries are provided in (Hössinger-Kalteis et al., 2021).

In this section, the equations developed by several research groups, then assembled and refined by Gibson & Ashby into a congruent model based on the relative density is given. Poisson's ratios of different foamed materials ranges from 0.1-0.55 with an average value of 1/3 and is largely independent of the relative density (Gibson & Ashby, 1997). As described by (Kraynik & Warren, 1994), a foam's bulk modulus K^* linearly relates to the relative density with:

material) divided by the density of its constitutive material ρ_s . A related characteristic is the porosity defined as $1 - \rho^*/\rho_s$. While the cell size has a small effect on the overall mechanical properties, the structure's relative density has a much larger influence. At constant cell size, cell walls thicken with increasing relative density and above a ratio of 0.3, the cellular structure is better described by considering it to be a porous solid (Gibson & Ashby, 1997). Below this ratio, it is strongly influenced by its cellular composition and is then considered to be a metamaterial (Surjadi et al., 2019). Its cell shape, orientation, and its cell edge and face connectivity contribute to the overall mechanical behaviour (Hössinger-Kalteis et al., 2021).

In compression, a foam's response exhibits three distinct phases which begin with a linear elastic phase, followed by a long plateau phase with little or no stress increase, and a densification phase as soon as the foam cells are nearly fully compacted (Altenbach & Öchsner, 2010; Gibson & Ashby, 1997; Hilyard & Cunningham, 1994). Distinctions occur depending on the base material's properties, i.e. whether it is elastomeric, elastic-plastic or brittle, but the primary behaviour is similar. The linear elastic phase is described with identical laws for elastomeric, elastic-plastic and brittle materials. Its derivative is the foam's apparent elastic modulus E^* , similarly to bulk materials in tension or compression. For both tensile and compressive loads, the main deformation mode is cell edge and wall bending as shown in Figure 2.6 to Figure 2.9. The descriptions provided here are based on the

$$\frac{K^*}{E_s} = \frac{\rho^*}{9 \cdot \rho_s} \quad (1)$$

In the case of open-cell foams with equal cell side lengths, the apparent Young's modulus E^* relates to the relative density with:

$$\frac{E^*}{E_s} = C_1 \cdot \left(\frac{\rho^*}{\rho_s}\right)^2 \quad (2)$$

The cell shape differences result in varying C_1 parameters, but the factor remains close to a value of 1. Similarly, for open-cell foams, the apparent shear modulus G^* relates to the relative density with:

$$\frac{G^*}{E_s} = C_2 \cdot \left(\frac{\rho^*}{\rho_s}\right)^2 \quad (3)$$

Eq. (2) and (3) given by (Gibson & Ashby, 1997) are based on work by (Ko, 1965; Menges & Knipschild, 1975; Warren & Kraynik, 1988). Here, the constant C_2 includes the influence of different cell shape parameters and is generally close to a value of 3/8. The detailed description of closed-cell foams is more complex since membrane stresses and internal gas pressure must be considered. Here, the foam's properties are defined as:

$$\frac{E^*}{E_s} = C_1 \cdot \left(\frac{\rho^*}{\rho_s}\right)^2 + C_1' \cdot (1 - \phi) \cdot \frac{\rho^*}{\rho_s} \quad (4)$$

The factor C_1' again relates to the exact cell composition. The constant ϕ is the fraction of material contained within the cell's edges, $1 - \phi$ is therefore the material fraction of the cell's walls. Similarly, the structure's shear modulus is defined as:

$$\frac{G^*}{E_s} = C_2 \cdot \left(\frac{\rho^*}{\rho_s}\right)^2 + C_2' \cdot (1 - \phi) \cdot \frac{\rho^*}{\rho_s} \quad (5)$$

Eq. (4) and (5) are based on work by (Christensen, 1986; Gent & Thomas, 1959, 1963; Green & Hoagland, 1985; Lederman, 1971; Maiti et al., 1984) and again refined by Gibson & Ashby. In practice, closed-cell foams produced from liquid material tend to have material accumulations at their cell edges and comparatively thin faces which do not significantly contribute to the total stiffness (Gibson &

Ashby, 1997). Therefore, the equations given for open-cell foams can be applied here as well within certain limits.

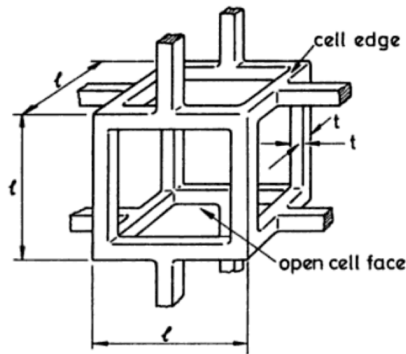


Figure 2.6: Schematic composition of an open cell with equal edge lengths. Its cell extents are denoted by l and the edge thickness by t . (Gibson & Ashby, 1997)

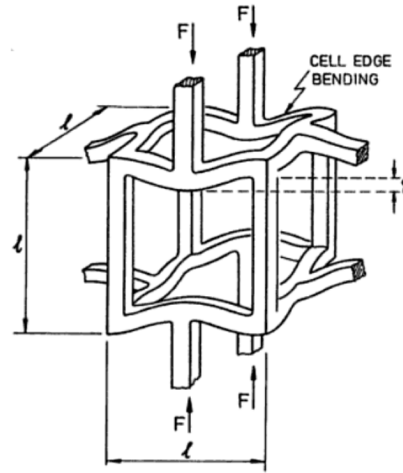


Figure 2.7: Deformation of open cell during the linear elastic phase. (Gibson & Ashby, 1997)

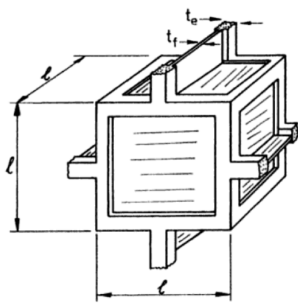


Figure 2.8: Schematic composition of closed cell. (Gibson & Ashby, 1997)

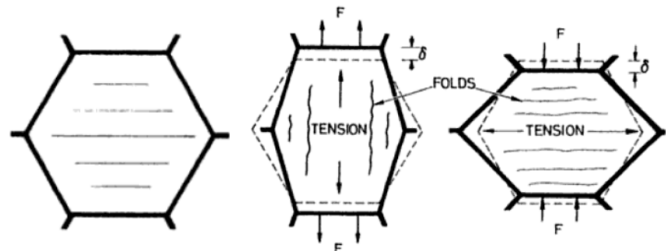


Figure 2.9: Deformation mode of a hexagonal closed cell in tension and compression with folds appearing on the cell wall. (Gibson & Ashby, 1997)

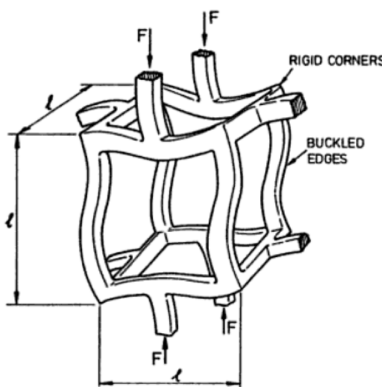


Figure 2.10: Elastic buckling of an open cell. (Gibson & Ashby, 1997)

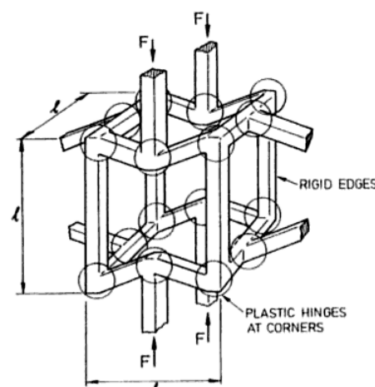


Figure 2.11: Plastic hinge formation of an open cell. (Gibson & Ashby, 1997)

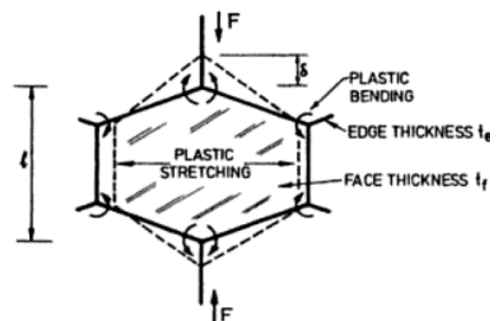


Figure 2.12: Plastic deformation of a closed cell. (Gibson & Ashby, 1997)

After the linear elastic portion, the stress response flattens and enters the plateau phase. Differences between the constitutive materials now begin to show in the response. Elastomeric foam cells buckle after the linear elastic portion (c.f. Figure 2.10) as the elastic plateau region begins. Below a relative density of 0.3, the stress σ_{el}^* at which the intersection of both phases begins relates to the other foam properties with:

$$\frac{\sigma_{el}^*}{E_s} \approx C_3 \cdot \left(\frac{\rho^*}{\rho_s}\right)^2 \quad (6)$$

For elastomeric, closed-cell foams, the internal cell pressure p_0 and the ambient pressure p_{atm} influence σ_{el}^* as well. In artificial foams, both internal and ambient pressures are often identical, and this influence is more relevant in biological cellular structures where larger pressure differences can occur. This results in a rising stress response during the plateau phase due to increasing internal pressure as shown in Figure 2.5. Open-cell foams do not inherently show this stress rise. For closed-cell foams, σ_{el}^* is defined with:

$$\frac{\sigma_{el}^*}{E_s} \approx C_3 \cdot \left(\frac{\rho^*}{\rho_s}\right)^2 + \frac{p_0 - p_{atm}}{E_s} \quad (7)$$

Eq. (6) and (7) stem from work by (Barma et al., 1978; Chan & Nakamura, 1969; Christensen, 1986; Gent & Thomas, 1959; Menges & Knipschild, 1975) and were brought to a simpler form by Gibson & Ashby.

Elastic-plastic base materials cause plastic yielding, i.e. the structure does not entirely recover its shape upon unloading as would be the case with elastomeric materials. Open-cell foams deform via plastic hinges at the cell corners (Gibson et al., 1982) as shown in Figure 2.11. The structure's yield strength σ_{pl}^* is defined with:

$$\frac{\sigma_{pl}^*}{\sigma_y} = C_4 \cdot \left(\frac{\rho^*}{\rho_s}\right)^{3/2} \quad (8)$$

In closed-cell elastic-plastic foams, the influence of wall stretching is added to that of plastic hinges as shown in Figure 2.12. The formula is extended like before with the constants C_4 and C_4' changing depending on the cell's exact properties:

$$\frac{\sigma_{pl}^*}{\sigma_y} = C_4 \cdot \left(\frac{\rho^*}{\rho_s}\right)^{\frac{3}{2}} + C_4' \cdot (1 - \phi) \cdot \frac{\rho^*}{\rho_s} \quad (9)$$

Eq. (8) and (9) are based on (Gibson et al., 1982) and refined in (Gibson & Ashby, 1997).

For brittle materials, the formulae are nearly identical to those describing the elastic-plastic behaviour. The crushing strength σ_{cr}^* of a brittle open-cell foam is defined as:

$$\frac{\sigma_{cr}^*}{\sigma_{fs}} = C_5 \cdot \left(\frac{\rho^*}{\rho_s}\right)^{3/2} \quad (10)$$

Here, σ_{fs} denotes the material's flexural strength. For closed-cell foams, the crushing strength σ_{cr}^* is:

$$\frac{\sigma_{cr}^*}{\sigma_{fs}} = C_5 \cdot \left(\frac{\rho^*}{\rho_s}\right)^{\frac{3}{2}} + C_5' \cdot (1 - \phi) \cdot \frac{\rho^*}{\rho_s} \quad (11)$$

Eq. (10) and (11) given in (Gibson & Ashby, 1997) are based on work by (Ashby, 1983; Kurauchi et al., 1984; Maiti et al., 1984; Morgan et al., 1981; Rusch, 1970). It is worth underlining that the relative density has a quadratic influence on elastomeric structure properties, while its influence is reduced to an exponent of 3/2 for elastic-plastic and brittle materials.

At the end of the plateau phase, the densification regime is reached as the foam's cells are nearly completely collapsed. The stress increases rapidly and is dominated by the elastic modulus of the solid material rather than the cellular structure, and to a lesser degree by the compressive behaviour of fluids trapped inside closed cells. Trapped gases naturally add a lower stress increase than liquids due to their compressibility. In case of open cell walls, the escaping fluid adds an additional time-dependent component to the response, however this becomes relevant only at high fluid viscosities or high strain rates. (Gibson & Ashby, 1997) The influence of the relative density can be seen in Figure 2.13, where examples of a compressive response of Expanded Polyurethane (EPU) and expanded polyethylene (EPE) are depicted. The increase of the relative density is clearly accompanied by increasing stress levels all throughout the three compression stages, along with an earlier densification onset. As worked out in (Gibson & Ashby, 1997), the densification strain ε_D can be calculated by the same relation for both elastomeric and elastic-plastic materials:

$$\varepsilon_D = 1 - 1.4 \cdot \frac{\rho^*}{\rho_s} \quad (12)$$

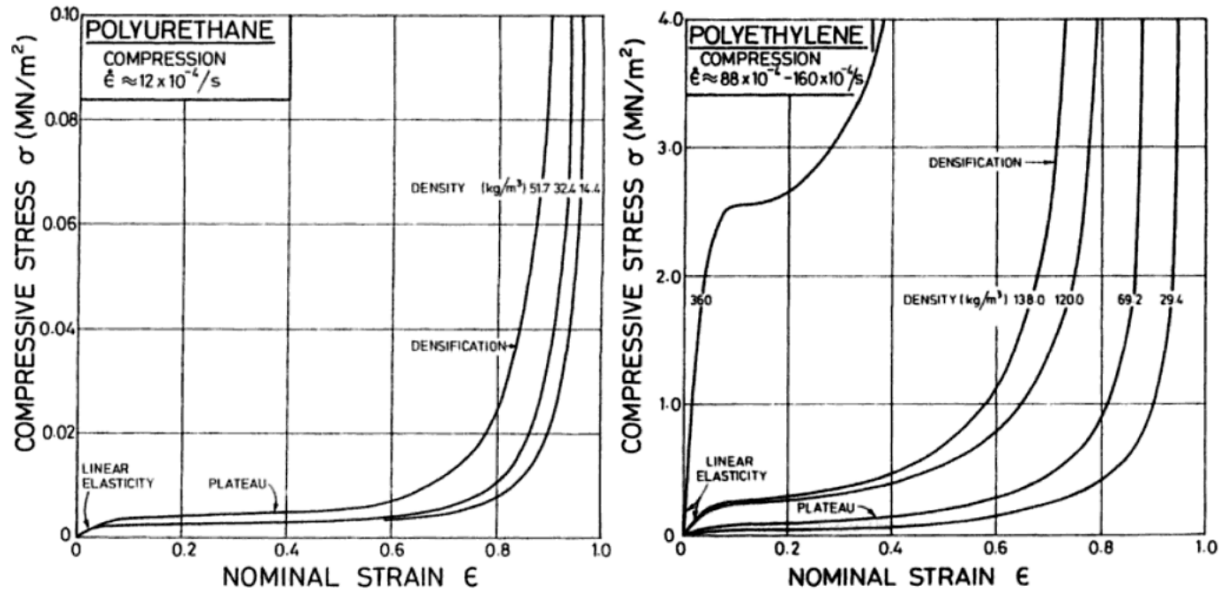


Figure 2.13: Compressive stress-strain response of expanded polyurethane (left) and polyethylene (right) foams at different densities (Gibson & Ashby, 1997).

The tensile stress-strain response of foams differs to that observed in compressive load cases. At first, the response is linear in small strain regimes up to approximately 5%, and the apparent modulus E^* is identical to the compressive modulus. In open-cell foams, the response is dominated by the bending of cell edges, whereas in closed-cell foams, the influence of face-stretching and internal gas pressure is added. Then follows a nonlinear elastic regime which is caused by the alignment of cell walls or edges with the force axis, as shown in Figure 2.14. (Gibson & Ashby, 1997)

As described by (Warren & Kraynik, 1991), the structure's tensile stress σ^* can be described with:

$$\frac{\sigma^*}{E_s} = 1.1 \cdot \left(\frac{\rho^*}{\rho_s}\right)^2 \cdot \varepsilon + 3.74 \cdot \left(\frac{\rho^*}{\rho_s}\right)^2 \cdot \varepsilon^2 + 0.0343 \cdot \left(\frac{\rho^*}{\rho_s}\right)^2 \cdot \varepsilon^3 \quad (13)$$

Once no additional alignment is possible, the stress-strain response is mainly determined by plastic yielding of the material. As stated by (Gibson & Ashby, 1997), it linearly relates to the relative density with:

$$\frac{\sigma^*}{\sigma_y} \approx \frac{\rho^*}{\rho_s} \quad (14)$$

Failure occurs once the material's ultimate tensile strength is reached, and the fracture propagates one cell at a time throughout the foam as shown in Figure 2.15. The tensile test response of Polyvinyl Chloride (PVC) foams of increasing densities are depicted in Figure 2.16 next to their compressive stress response for easier visualization of their behaviour differences.

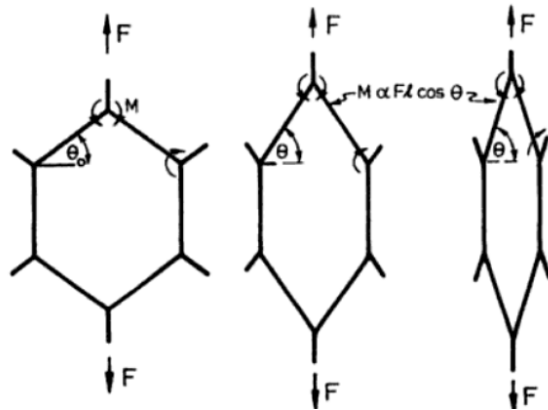


Figure 2.14: Example of edge alignment in hexagonal unit cell at increasing tensile strains, adapted from (Gibson & Ashby, 1997).

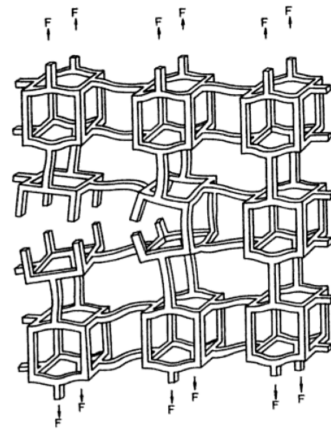


Figure 2.15: Crack propagation through open-cell foam structure caused by tensile load (Gibson & Ashby, 1997).

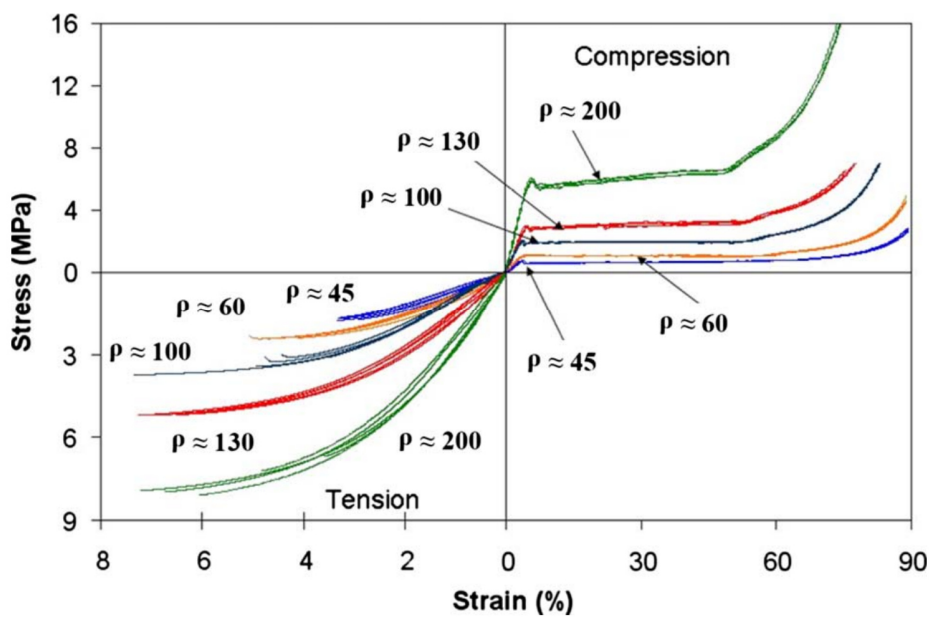


Figure 2.16: Tensile and compressive stress response of PVC foam at different densities. (Walter et al., 2009)

Finally, the energy absorption W of cellular structures per unit volume in compression over the strain ϵ is given by:

$$W = \int_0^\varepsilon \sigma(\varepsilon) d\varepsilon \quad (15)$$

With the properties of stochastic foam structures adequately described, the section continues with the descriptions of surface-based and graph-based lattices.

2.1.2 Surface-Based Lattices

A subcategory of cellular structures are surface-based lattices. They possess regular, repeating unit cells composed of walls akin to closed-cell foams. Honeycomb structures such as those shown in Figure 2.1 (top) and Figure 2.17 (left and middle) can be thought of as extruded sections with the cells being closed only in two dimensions, while the third is open. On the other hand, they may also be composed of angled, straight surface sections arranged in a closed-cell structure, such as shown in Figure 2.17 (right).

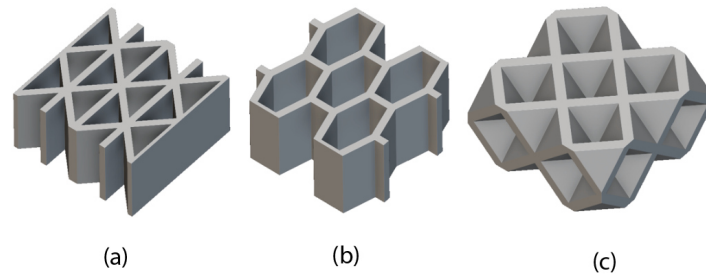


Figure 2.17: Examples of surface-based unit cells: (a) triangular honeycomb, (b) hexagonal honeycomb, (c) Face-Centred Cubic.

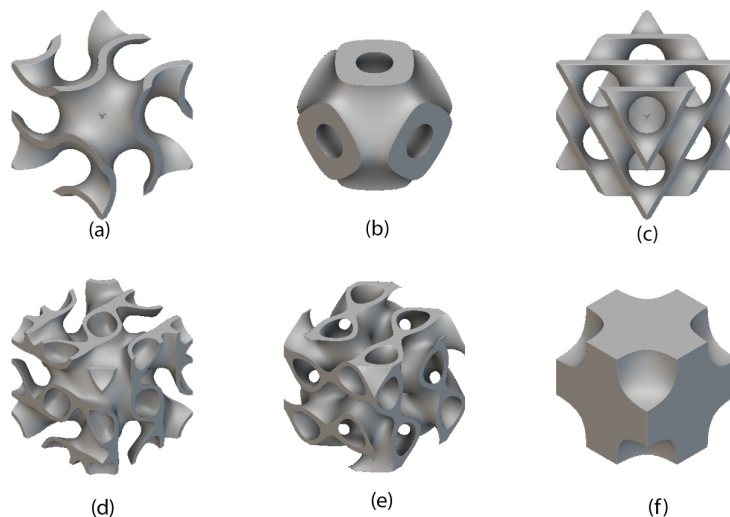


Figure 2.18: Examples of TPMS unit cells: (a) Gyroid, (b) Schwarz, (c) Diamond, (d) Lidinoid, (e) SplitP, (f) Neovius.

Another subcategory of surface-based lattices are the Triply Periodic Minimal Surfaces (TPMS) which are intensely researched in recent scientific literature. Examples of TPMS unit cells are shown in Figure 2.18. They are based on mathematical formulae which locally minimize the surface area and possess zero mean curvature at any point (Maskery et al., 2018). The resulting smooth shape with no sharp corners entails favourable stress distributions without any concentrations in the main structure as shown in Figure 2.19. For example, the equation for the Gyroid structure as given by (J. Feng et al., 2022) is:

$$\begin{aligned} \sin(\omega_x x) \cdot \cos(\omega_y y) + \sin(\omega_z z) \cdot \cos(\omega_x x) \\ + \sin(\omega_y y) \cdot \cos(\omega_z z) = C \end{aligned} \quad (16)$$

Equation (16) refers to cartesian coordinates, but the lattices can also be defined for cylindrical or spherical systems, providing other lattice patterns. Adding scalar fields to the equation (i.e. altering C) can result in constant or locally varying thickness changes, while frequency modulation of the function parameters ω_i allows control over the number of unit cells per axis. In addition, their mathematical description also allows for smooth transitions between unit cell types as shown in Figure 2.20.

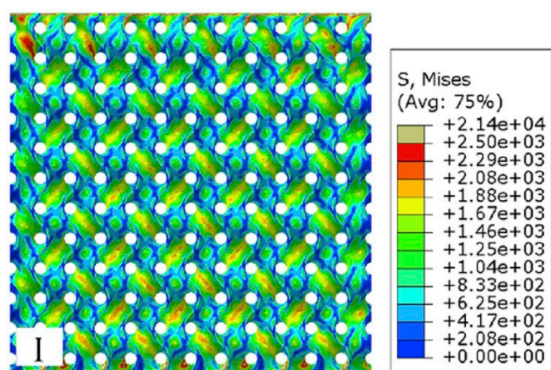


Figure 2.19: Von Mises stress distribution of a Gyroid TPMS lattice in compression, adapted from (Al-Ketan et al., 2020).

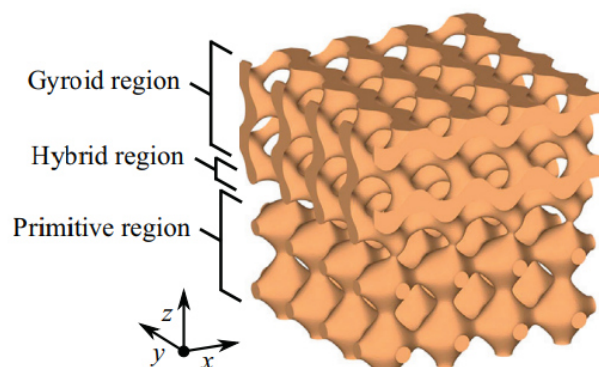


Figure 2.20: TPMS lattice with smooth transition from Gyroid to Schwarz Primitive lattice type. (Maskery et al., 2018)

The existence of TPMS lattices is not restricted to the mathematical domain, but they also occur in biological environments. For example, wing scales of the *callophrys rubi* butterfly possess a Gyroid structure (Gan et al., 2016; L. Han & Che, 2018) as shown in Figure 2.21, and Diamond structures can be found in the exoskeleton scales of the *lamprocyphus augustus* weevil (L. Han & Che, 2018) as depicted in Figure 2.22.

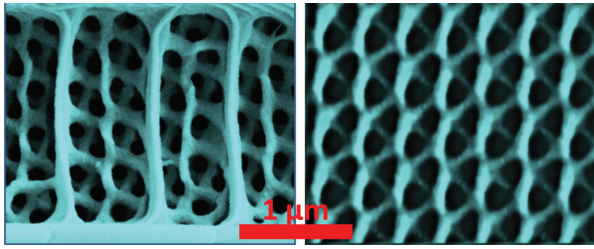


Figure 2.21: Gyroid lattice structure in butterfly wing scales, adapted from (Gan et al., 2016).

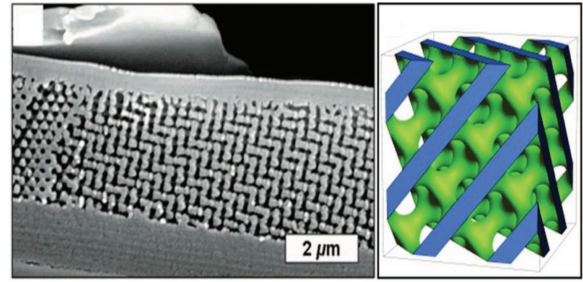


Figure 2.22: Diamond lattice structure found in weevil scales. (L. Han & Che, 2018)

The TPMS lattices possess useful properties for certain engineering purposes. Although the structures do not find wide-spread use yet, numerous studies investigate their potential applications in a wide array of domains. Most TPMS types have open unit cells and the useful property of dividing the occupied space into two separate volumes. They are therefore well-fit for use as heat exchangers as demonstrated by (Röver et al., 2023) and (Qureshi et al., 2021). Other use cases include the absorption of sound (W. Yang et al., 2020) or microwaves (Y. Feng et al., 2021), chemical microreactors (Baena-Moreno et al., 2021), compressive energy absorption (Maskery, Aboulkhair, et al., 2017), porous scaffolds for the growth of engineered bone tissue (Lehder et al., 2021) and implants (Zhu et al., 2019).

Due to their cellular composition, the physical properties of TPMS lattices can also be described by the equations for foams given in the previous section as corroborated by (Al-Ketan et al., 2020; X. Chen et al., 2022; Gibson & Ashby, 1997; Maskery et al., 2018; Qiu et al., 2023). Their behaviour both in tension and compression matches that of foams rather well with minor distinctions. At low relative densities, their compressive stress-strain response shows a similar behaviour (see Figure 2.23 left). First, a linear regime is traversed until the cells start to plastically deform or crack, and the plateau phase begins. Depending on the cell size and relative density, the cell layers may collapse successively as visible from the subsequent stress peaks and drops in the plateau regime. As soon as all cells have completely collapsed, the densification regime dominated by the base material's properties begins. At higher densities (Figure 2.23 right), the linear elastic portion becomes much more significant. Here, the plateau region is reached at a much higher stress, and cell layers cease to collapse successively due to their increased wall thickness. The lattice then tends to fail more like a solid by cracking (Abueidda et al., 2019) and shear banding (X. Chen et al., 2022; Qiu et al., 2023).

Similar to Eq. (16), both graph-based and surface-based lattice structures in compression are commonly evaluated by their specific energy absorption (SEA), which is the weight-normalized energy absorption (see (Ajdari et al., 2011; Habib et al., 2018; Maskery, Aboulkhair, et al., 2017; Tancogne-Dejean et al., 2016)). It is a well-suited method to compare the performance of unit cell types and lattice structures of differing mass.

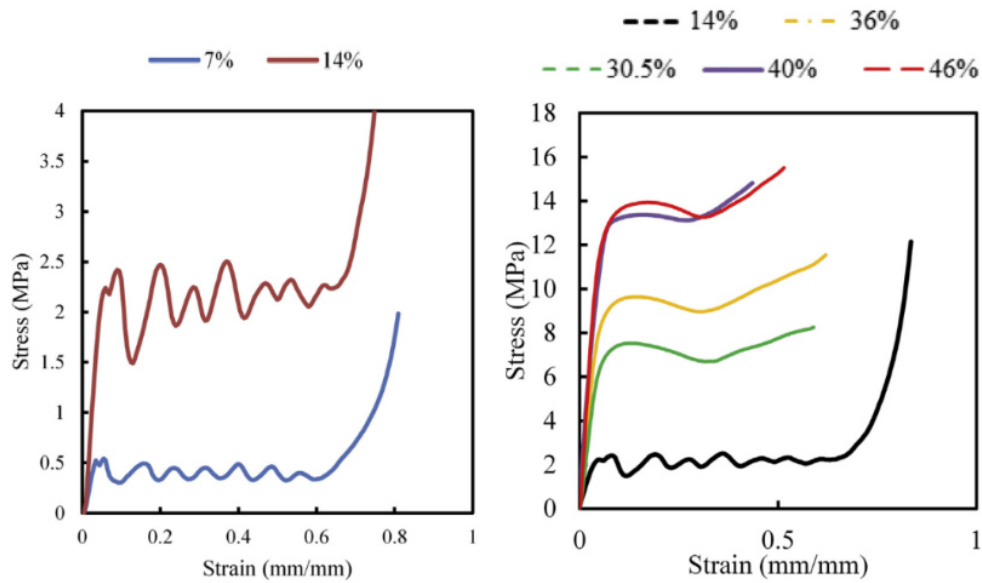


Figure 2.23: Compressive stress-strain response of cubic Gyroid structure made of PA2200 with 4x4x4 unit cells at different relative density ratios from 7% to 46%, adapted from (Abueidda et al., 2019).

2.1.3 Graph-Based Lattices

The third category of cellular structures are graph-based (also called beam-based) lattices. They either consist of random beam arrangements such as Voronoi or tetrahedral lattices, which much resemble open-cell foams, or structured lattices with regularly distributed unit cells (Tamburrino et al., 2018). An example of a naturally occurring graph lattice structure is the skeleton of Radiolaria shown in Figure 2.24. In research, many different unit cells were developed from biological structures, crystal lattice structures or by combining multiple unit cell types into one (Helou & Kara, 2018), some of which are depicted in Figure 2.25.

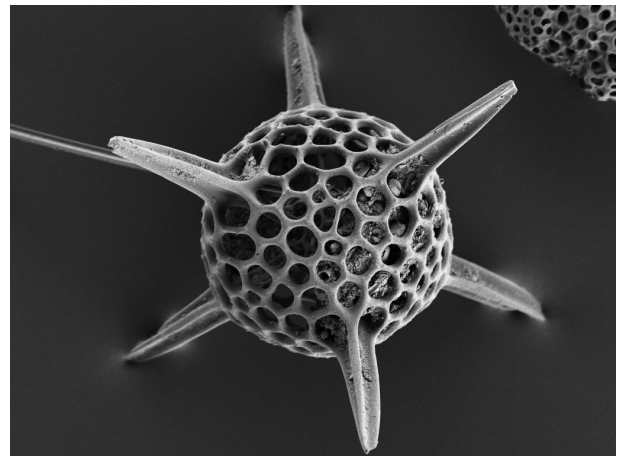


Figure 2.24: Graph-based lattice structure in Radiolaria skeleton. (Radiolaria - Geology Is the Way, n.d.)

Other engineered unit cells allow specific motion behaviour such as twisting under load and freely definable Poisson ratios as discussed in (Surjadi et al., 2019). The Re-entrant unit cell falls into the category of auxetic structures, meaning that it possesses a negative Poisson ratio. It is essentially a hexagon whose top and bottom nodes are moved towards the face centre. When compressed, its free sides move towards the centre, letting it shrink in all dimensions. Auxetic structures can be especially performant in dynamic energy absorption applications due to this behaviour, such as in sports protection equipment (Z. Chen et al., 2020; Hou et al., 2018; Sanami et al., n.d.).

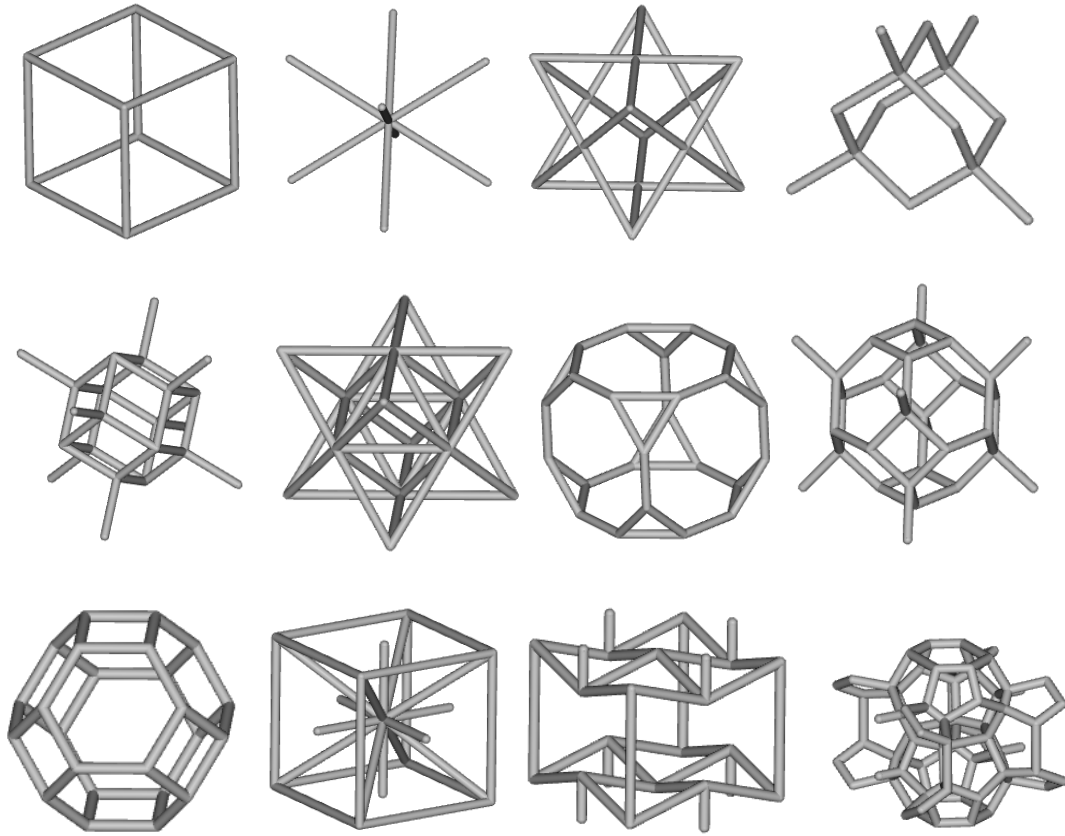


Figure 2.25: Selection of graph unit cells. First row: Simple Cubic, Body Centred Cubic, Face Centred Cubic, Diamond. Second row: Fluorite, Octet, Truncated Cube, Truncated Octahedron. Third row: Kelvin cell, Isotruss, Re-entrant, Weaire-Phelan.

Stochastic graph lattice structures appear to be much more common in nature compared to regular ones, but both types are heavily researched in current studies. Similar to foams and surface-based lattices, they are well-suited for lightweight load-bearing applications and compressive energy absorption tasks (Nazir et al., 2019), with other uses including implants (Mahmoud & Elbestawi, 2017) with potential for improved osseointegration (Y.-T. Wang & Hsu, 2023) and lightweight, breathable orthotics (Badini et al., 2023). Graph lattices can more reliably achieve lower relative densities than surface-based lattices due to their unit cell composition occupying less space. Consequently, the latter may be difficult to produce at a certain point since the potentially very thin wall thicknesses can become unmanageable for current manufacturing methods.

Graph unit cells can be divided into stretch-dominated and bending-dominated types which behave differently in large strain compressive load cases. According to (Deshpande et al., 2001), the deformation type is determined by Maxwell's rule defined as follows for two (17) and three (18) dimensions:

$$M = b - 2 \cdot j + 3 \tag{17}$$

$$M = b - 3 \cdot j + 6 \tag{18}$$

Here, b is the number of struts and j the number of joints. If $M < 0$, then the unit cell simply collapses under load in case of pin joints. It's then considered a *mechanism* rather than a structure. In case of fixed joints, its struts are bent, hence the bending-dominated denomination. If $M = 0$, the cell is stretch-dominated as the cell cannot simply collapse even with freely rotating joints. The struts are mainly loaded in compression and tension even with fixed joints, hence stretch-dominated. If $M > 0$, then the cell is overconstrained. Self-stresses occur in an unloaded state stemming from slightly different strut lengths, the cell is also considered stretch-dominated. A visualization of the strut arrangement for 3D lattice cells is shown in Figure 2.26. A generalized formulation of Maxwell's rule should be used for the overconstrained type, which is described by Deshpande et al. as:

$$b - 3 \cdot j + 6 = s - m \quad (19)$$

where s is the number of self-stress states and m the number of mechanisms. Their exact definitions and further information can be found in (Pellegrino & Calladine, 1986). A statically and kinematically determinate lattice exhibits $s = m = 0$, but Maxwell's rule only implies that $s - m = 0$ is required when $b - 3j + 6 = 0$, not that both s and m need to be zero.

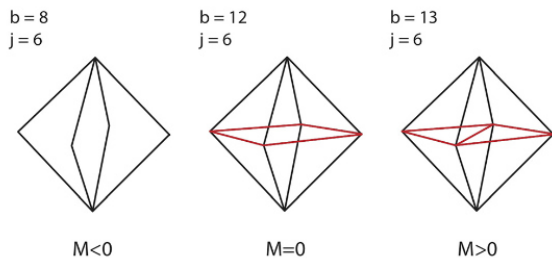


Figure 2.26: Maxwell's rule for 3D unit cells: bending-dominated cell (left), stretching-dominated cell (middle) and overconstrained cell (right). (Tamburrino et al., 2018)

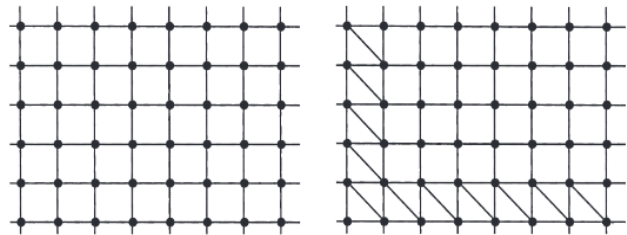


Figure 2.27: Non-rigid (left) and rigid (right) infinite 2D lattices. (Deshpande et al., 2001)

As described by Deshpande et al., Maxwell's rule is a necessary but not sufficient condition when expanded to a network of cells, i.e. a lattice. Considering an infinitely large, pin-jointed lattice in two dimensions, the number of struts is $b \approx j \times Z/2$, where Z is the average number of struts per node. The study lays out that the value of Z needs to be four in the two-dimensional case and six in three dimensions in order for the lattice to be rigid. Figure 2.27 shows 2D lattices to visualize this concept. The unit cell of the first lattice would be considered bending-dominated, hence not rigid. Arranged in a network, however, Z is four and the Maxwell criterion is zero, indicating rigidity, but the lattice still can collapse since it allows one mechanism and one state of self-stress according to the authors. The second lattice with added diagonal struts in border cells also has a Z -value of four but does not allow either a mechanism or state of self-stress.

In compression, graph lattices also show a very similar behaviour to foams and surface-based lattices (Choy et al., 2017; Ling et al., 2019; Xiao & Song, 2018; L. Yang et al., 2013) as can be seen

in Figure 2.28. At first a linear stress-response occurs, then a long plateau followed by a steep densification phase. Bending-dominated unit cell types differ from stretch-dominated ones, they possess a lower apparent elastic modulus E^* as well as a lower apparent yield strength σ_y^* .

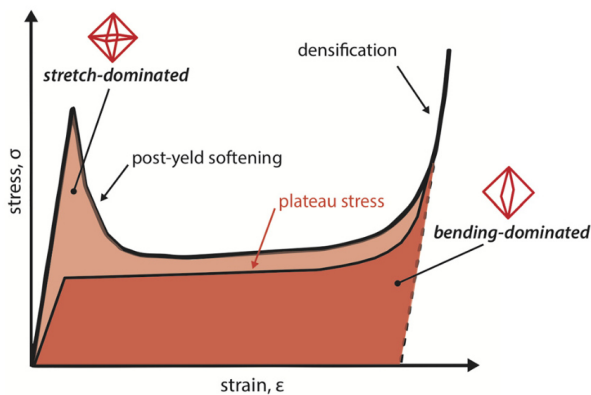


Figure 2.28 Compressive stress-strain behaviour of stretch-dominated and bending-dominated lattices. (Tamburrino et al., 2018)

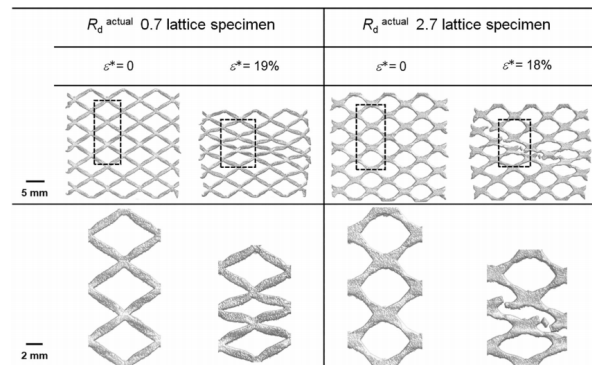


Figure 2.29: Shear band formation in BCC lattice composed of Al-12Si. (Liu et al., 2021)

The relative density also has a strong influence on failure mode, strength, and specific energy absorption similar to foams and surface-based lattices. The specific unit cell type also plays a significant role. Some permit an even, consecutive layer collapse behaviour very similar to the one seen from a TPMS structure in Figure 2.23 on the left. The influence of brittle base materials, certain lattice types and strut/node diameter combinations favour failure modes such as shear band formation as shown in Figure 2.29. Here, the layers do not collapse perpendicular to the compression direction, but diagonally across its cells. According to (Liu et al., 2021), the failure is initiated by stiff nodal connections due to material accumulation at the nodes, rendering the struts comparatively thin, and due to tensile cracks at stress concentrations in the struts.

2.1.4 Functionally Graded Lattice Structures

Functionally Graded Lattice Structures (shortened to FGLS) expand on regular lattice structures having uniform properties by locally varying their thickness, cell size, cell type, or other characteristics. Such lattice structures are commonly found in nature, where the local changes are dictated by an external condition such as a stress field. An example is the trabecular bone structure as depicted in Figure 2.30. Here, the cell size varies according to the local stress magnitude with smaller cell sizes (i.e. higher relative density) near the cortical bone as well as in high load areas near the femoral head. Larger cell sizes (i.e. lower relative density) are present in low load areas further away from the bone's walls, and in low load areas. Additionally, the cell walls are oriented such that they follow the principal stresses' directions for improved load bearing capacity. (J. Zhang et al., 2023)

In use cases where foams and regular lattice structures show high performance, FGLS can outperform them even further. The principal reason is that FGLS have a more advantageous material distribution: material is present where it is needed and absent where it is not. Locally changing cell

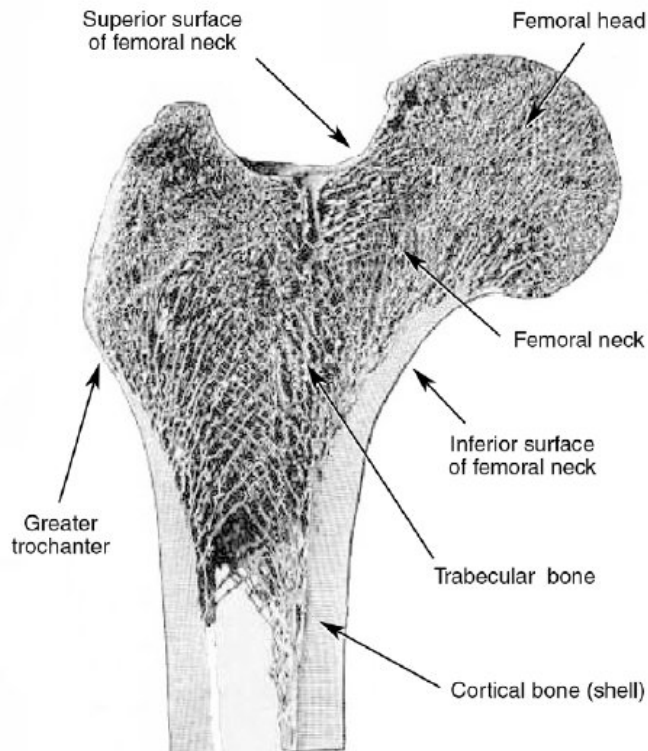


Figure 2.30: Cross-section of a human femur showing solid cortical shell and trabecular, lattice-like bone structure with orientations and densities varying as function of local conditions. (Voo et al., 2004)

wall orientations can contribute to further improvements, as demonstrated by the trabecular bone structure described previously. Both properties render them very well-suited for low-weight structural applications, however they also excel in impact energy absorption tasks thanks to their compression behaviour. The compression starts occurring in low-density regions first and progresses throughout the structure towards increasing relative density regions. In some cases, the reaction force curve of graded lattices in compression is marked by noticeable peaks occurring in the plateau phase, indicating the consecutive collapse of the cell layers (Al-Saedi et al., 2018). Graded lattices show lower reaction forces in the beginning of the compression phase and higher overall energy absorption, both desirable properties for impact absorption applications (Niknam & Akbarzadeh, 2020). FGLS achieve higher stiffness-to-weight ratio

and higher specific energy absorption levels in structural and impact energy absorption applications (Noronha et al., 2023). While the Gibson & Ashby model for describing uniform lattice structures is commonly used for graded lattices as well, refinements of the equations and assumptions are also a topic of research (Jalali et al., 2024).

Researchers have begun implementing the concept in artificial structures through various approaches. Many make use of manual adaptations, focusing on the unit cell size or its wall and beam thickness as shown in Figure 2.31 and Figure 2.32. One can choose to alter the lattice's relative density by changing only one option, or to keep it constant by altering both properties simultaneously. The property gradient can be defined manually setting a stepwise (Xiao & Song, 2018) or continuous property change (Al-Ketan et al., 2020) in one or multiple axes (J. Yang et al., 2022). Certain studies make use of Topology Optimization to alter the unit cell shape (Kazemi et al., 2020; C. Zhang et al., 2021). Others apply Topology Optimization to achieve hierarchical, lattice-like structures with large size differences between neighbouring cells (Y. Han & Lu, 2018; W. Wang et al., 2023). Another avenue is to locally change the lattice's unit cell composition as shown in Figure 2.33 (Pham et al., 2019).

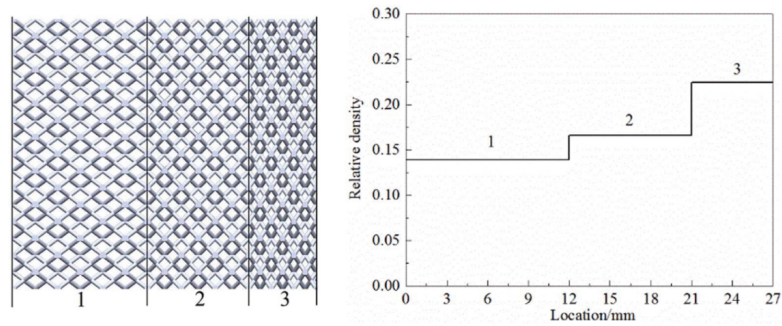


Figure 2.31: Stepwise density grading of graph lattice via unit cell height alteration. (Xiao & Song, 2018)

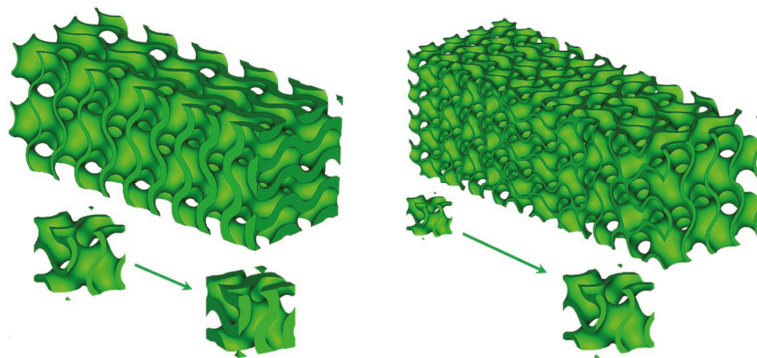


Figure 2.32: Continuous grading of TPMS Gyroid lattice via thickness alteration (left) or cell size alteration (right). (Al-Ketan et al., 2020)

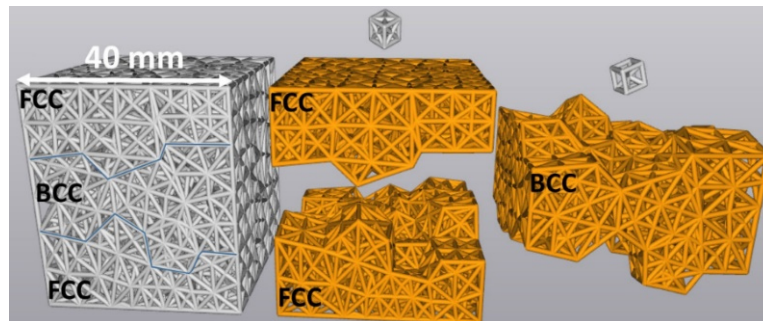


Figure 2.33: Damage-resistant lattice containing varying unit cell types (Face-Centred Cubic (FCC) and Body-Centred Cubic (BCC)) separated into regions mimicking metallic crystals, adapted from (Pham et al., 2019b).

Since uniform lattice structures offer good performance in compressive energy absorption tasks, numerous studies investigating the behaviour of graded lattices have been published as well. A large portion consider cuboid structures with manually applied thickness gradients in one or two axes (Ajdari et al., 2011; Bai et al., 2020; Choy et al., 2017; Daynes et al., 2017; Hou et al., 2018; Maskery, Hussey, et al., 2017; Niknam & Akbarzadeh, 2020; Rahman et al., 2021; Tao & Leu, 2016; Wu et al., 2018; J. Yang et al., 2022). Both in quasi-static and dynamic load cases, the lattice structures with thickness gradient generally achieve higher specific energy absorption levels than ungraded lattices. Fewer

publications on the influence of unit cell height gradients are available. An example is provided by (Xiao & Song, 2018), where the authors investigate two cuboid lattice structures with a stepwise (c.f. Figure 2.31) and continuous layer height change in quasi-static and high-speed dynamic compressive load tests. Both times, the graded structures significantly outperformed the uniform ones. In (Khosroshahi et al., 2018) and (Khosroshahi et al., 2019), the authors introduced a conformal lattice into a spherical helmet shape as energy absorption device. Different configurations of Simple Cubic and Tetrahedral unit cells with varying layer numbers are studied in combination with a cell size gradient as depicted in Figure 2.34. The simulative assessments indicate that lattice configurations with low relative density may achieve lower peak accelerations than an Expanded Polystyrene liner.

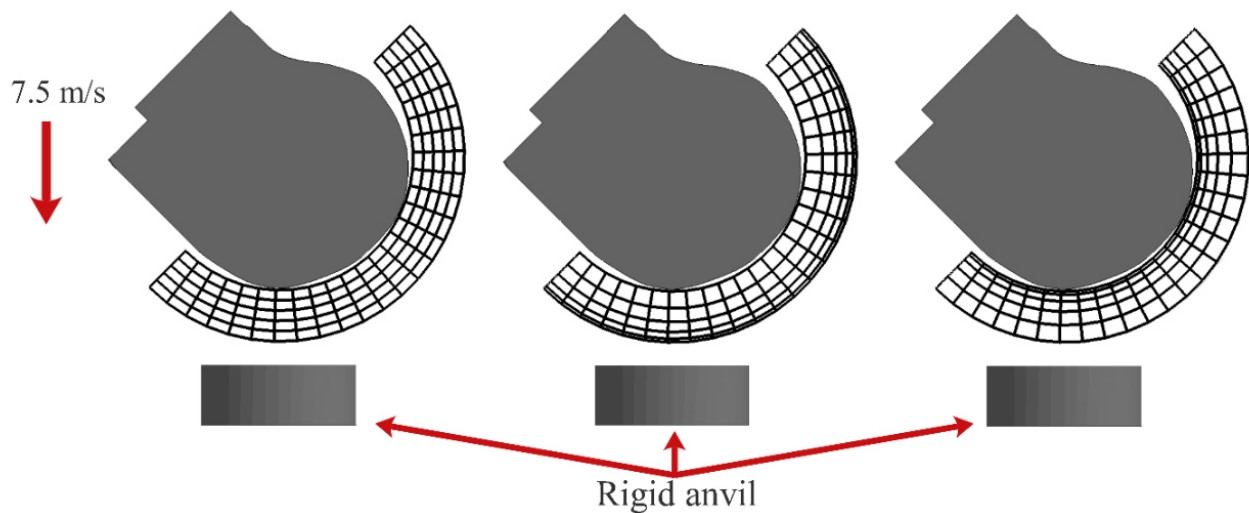


Figure 2.34: Drop test setup of simplified helmet geometry with size graded lattice liner. (Khosroshahi et al., 2018)

More elaborate property gradients can be achieved by optimization routines. Researchers frequently have to rely on custom-written scripts interfacing with the respective simulation solvers since most commercial solutions do not offer sufficient lattice optimization options, as will be laid out in section 2.3. For example, the structural, fluid transport and thermal performance of a heat exchanger with a graph lattice was optimized in 2D and 3D by (Takezawa et al., 2019) through local alteration of the strut thickness (c.f. Figure 2.35). In the investigation by (Dong et al., 2020), the stiffness of a lattice structure with solid skin is maximized in Altair OptiStruct via beam thickness alterations. A free-size optimization method is developed and applied to a TPMS lattice by (Simsek et al., 2021) to exclude resonance frequencies in a certain spectrum (c.f. Figure 2.36). The lattice strut size and their nodal position are locally optimized via the procedure developed by (W. Chen et al., 2018) to maximize the lattice's stiffness in various structural load cases. Similar optimization approaches are pursued by (Daynes et al., 2017; Fernandes & Tamijani, 2021; Li et al., 2020; Wu et al., 2019) through custom optimization routines as depicted in Figure 2.37 and Figure 2.38.

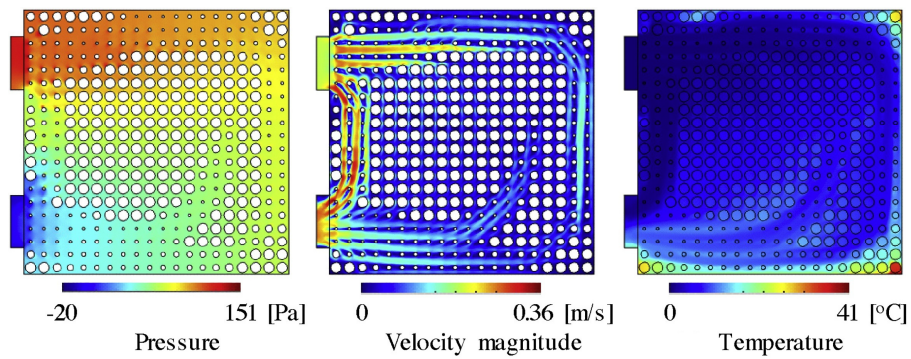


Figure 2.35: Pressure, velocity, and temperature in lattice heat exchanger after optimization, adapted from (Takezawa et al., 2019).

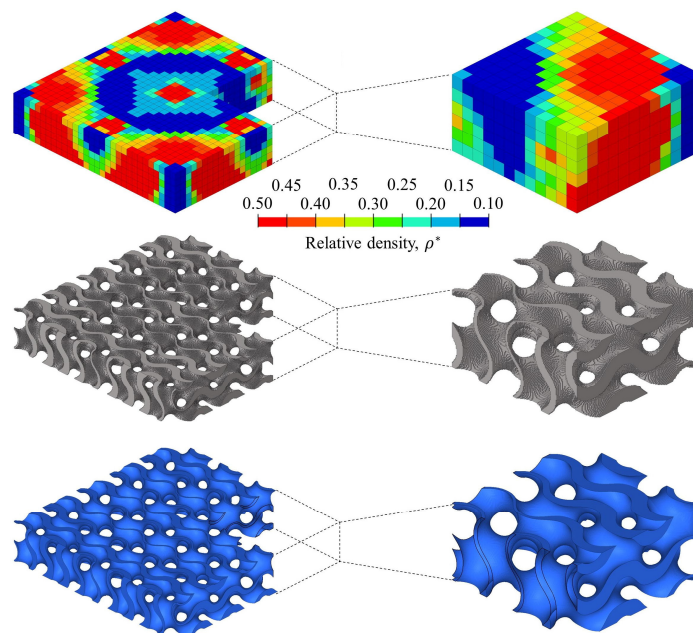


Figure 2.36: Relative density, voxel representation and mesh representation of TPMS lattice after optimization, adapted from (Simsek et al., 2021).

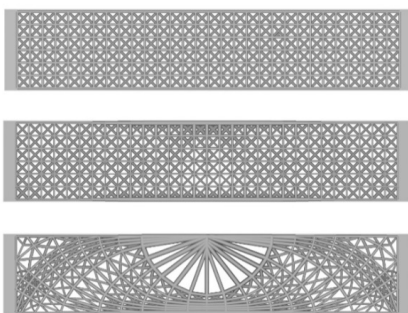


Figure 2.37: Optimisation of strut-based lattice in a three-point bending case with beams following principal stress directions, adapted from (Daynes et al., 2017).

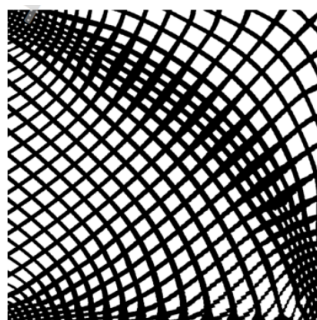


Figure 2.38: Anisotropic lattice graded in unsupported bending load case, adapted from (Li et al., 2020).

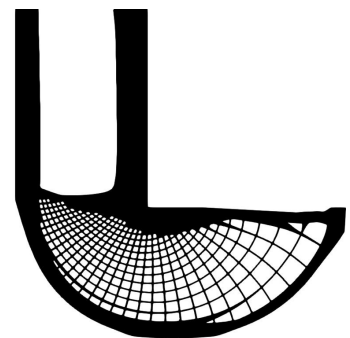


Figure 2.39: Compliance-based optimization result of L-shaped bracket (Fernandes & Tamijani, 2021).

Considering the fact that lattice structures are very well-suited for compressive energy absorption tasks, few studies have explored their optimal configuration. For instance, one study by (Gorgularslan et al., 2021) carried out a strut size optimization of three lattices with three unit cell types under a static compressive load. A custom structural solver and optimization routine was developed by the authors to minimize the lattice's compliance while constraining the total relative density, maximum stress, and strut diameters. The considered load case was chosen such that both the geometry and material can be considered to be linearly elastic. The optimized structures were then subjected to large-strain compression in a secondary load case. Here, a commercial explicit FEA solver was employed to take geometric and material nonlinearities into account. While the structures were not specifically optimized for this use case, increased energy absorption levels were observed in two out of three unit cell types, while the third showed decreased energy absorption capacities.

In the publication by (Hou et al., 2018), a lattice structure is investigated in a dynamic, low-speed impact scenario. Its unit cells are parameterized and optimized for maximum energy absorption. The parameterization of the geometry permits the use of a commercial explicit FEA solver, since it is a built-in software capability. No external custom-written optimization scripts were therefore required. The results report that the optimized structure outperforms the uniform one, however both the unit cell height as well as the width were parameterized and altered. Hence the structure's overall size and mass changed, and the results are not entirely comparable with the initial design.

In summary, the range of applications and grading approaches is vast since FGLS deliver improved performance compared to conventional structures. Yet, the geometries considered in the reviewed studies tend to be simplistic and do not adequately represent the complexities encountered in common engineering parts. Regarding graded lattice structures in compression, it becomes clear that the reported improvements vary greatly. Materials, unit cell types, gradient styles, relative densities, and compression levels are not consistent between each study, and comparisons cannot readily be made. Since very few of those studies included lattice optimizations, the best-performing thickness gradient for each considered load case is mostly unknown, and potential performance increases remain largely unexplored. It is assumed that the comparatively low number of publications treating lattice optimizations is due to inadequate parameterization and optimization options available in commercial structural solvers. Circumventing the restrictions by building a custom solver in addition to the optimization routine itself is complex, as nonlinearities such as accurate elastic-plastic material behaviour and contact interactions are not trivial to implement. Applying a manual gradient is simple and already can provide decent improvements over ungraded lattices. This lessens the need for further investigations if the results are deemed sufficient at this point.

2.1.5 Industry Applications of Functionally Graded Lattice Structures

FGLS have yet to be implemented on a large scale in industrial settings, illustrating that they remain existent mostly in research domains rather than in actual applications. As will be laid out in section 2.3, the main reason are software limitations hindering their effective design and optimisation, but advancements are made in recent times. A few examples of FGLS in appliances are presented here, with them partly being showcase parts or proofs of concept for software or AM machine manufacturers. The domain is rapidly evolving and numerous new appliances incorporating lattice

structures are regularly presented at industrial trade shows such as the annual Formnext trade show (*Formnext - Hub for Additive Manufacturing*, n.d.).

The clothes manufacturer Adidas, in cooperation with the AM machine and materials producer Carbon 3D, presented shoe soles incorporating a graded lattice made of a resin and polyurethane blend (see Figure 2.40). Its goal was reducing the number of single parts for production, having precise control over its cushioning and movement behaviour, as well as improving its thermal and cleaning capabilities. (*Carbon 3D Print Lattice Innovation — The Adidas Story*, n.d.)

Having switched from foam-based cushioning to 3D-printable polyurethane, the bicycle and components manufacturer Specialized developed a saddle incorporating graded lattice structures (c.f. Figure 2.41). The main goal was to reduce pressure at the rider's contact points with the saddle, while simultaneously reducing the part's weight and maintaining sufficient stiffness in non-contact areas. (*S-Works Romin EVO with Mirror*, n.d.)



Figure 2.40: Graded lattice in shoe sole by Adidas and Carbon 3D. (*Carbon 3D Print Lattice Innovation — The Adidas Story*, n.d.)



Figure 2.41: Specialized Mirror saddle with size-graded lattice. (*S-Works Romin EVO with Mirror*, n.d.)

A fuel-cooled oil cooler for aerospace applications was designed by HRL Laboratories using Computational Fluid Dynamics analysis. It is composed of high-performance, 3D-printable aluminium alloy to increase its internal surface area and heat transfer rate significantly compared to standard design methods (c.f. Figure 2.42). A locally varying Gyroid structure was chosen since TPMS lattices inherently separate the volume they occupy into two discrete domains. (*How NTopology Was Used to Design, Analyze and Print a Fuel-Cooled Oil Cooler*, n.d.)

Cobra Aero designed a drone engine block incorporating a spatially varying lattice structure for air-cooling, replacing previously used external cooling fins (c.f. Figure 2.43). This step led to reduced manufacturing lead times, improved cooling capacity and part number reduction through consolidation. (Cobra Aero et al., 2020)



Figure 2.42: Heat exchanger with TPMS structure by HRL Laboratories. (How NTopology Was Used to Design, Analyze and Print a Fuel-Cooled Oil Cooler, n.d.)

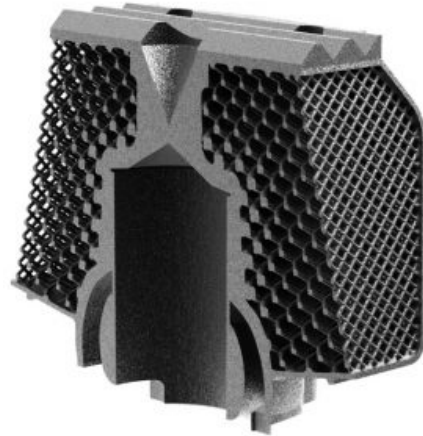


Figure 2.43: Cobra Aero drone engine block with lattice heat exchanger. (NTop Cross Section of a Drone Engine Cylinder Designed in NTop Platform by Cobra Aero - MANUFACTUR3D, n.d.)

In the medical domain, 3D printed titanium implants have become a readily applied tool to replace and reinforce various bone structures or joints. Functionally graded lattices, providing locally controllable part porosity and compliance, are implemented to aid osseointegration and to adapt the implant's behaviour to the patient's individual needs (c.f. Figure 2.44).



Figure 2.44: Titanium orthopaedic implant with controllable porosity and surface roughness to aid osseointegration. (Medical Additive Complex Structures - Titanium Complex Medical Structure Manufacturer, n.d.)

2.1.6 Summary

Cellular structures, i.e., foams and lattices, are ubiquitous in nature and can be subcategorized into randomly structured foams or lattices with regular composition. Their properties render them well-suited for a wide range of tasks such as low weight load-bearing structures, fluid transport, heat exchange, filtering, impact energy absorption and others. Similarly, they are advantageous for engineering purposes with analogous goals in mind. The Gibson & Ashby model describes their

structural behaviour particularly well by relating their properties to the relative density. It is therefore often used for this purpose in research publications and literature. Advances in manufacturing methods have allowed the incorporation of property gradients as they are found in nature to achieve further performance improvements. Manually defined property gradients in lattice structures permit the detailed control over their local behaviour, resulting in tailor-made appliances. Both industrial applications and research publications on the topic make heavy use of this approach, but they do not make use the full potential of FGLS yet. Due to the lack of adequate interfaces and optimization options in commercial physical solver software, custom optimization scripts were commonly applied in publications in conjunction with simplified geometries.

2.2 Additive Manufacturing Techniques

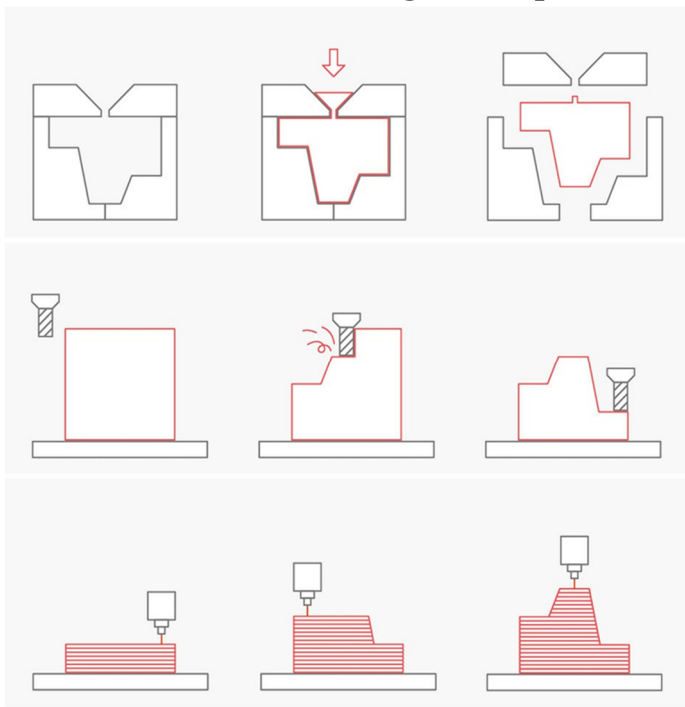


Figure 2.45: Manufacturing processes (top to bottom): formative, subtractive and additive, adapted from (Redwood et al., 2018)

can be extracted. In subtractive manufacturing, material is removed from a solid block whereas additive manufacturing does the opposite by adding material where necessary to produce a part. The majority of AM techniques operate by adding layers in a planar fashion, essentially being 2.5D printing, but non-planar printing is possible with specific movement instructions on common machines (Nisja et al., 2021) or with robotic arms (Puzatova et al., 2022). The additive techniques' principles are depicted in Figure 2.45.

AM technologies are classified according to their base material's state with several differing subcategories. AM enables new dimensions of design freedom opened up in terms of shape, design iteration speed and ease of use (Diegel et al., 2019), making it a staple tool of engineering, electronics, biomedical and numerous other domains for prototyping as well as end-use parts (Bhatia & Sehgal,

Additive Manufacturing (commonly known as 3D printing) is a rapidly growing manufacturing domain spanning low volume and low-cost hobbyist usage up to large budget, large format industrial production of serial parts, including rocket nozzles and fuel tanks. Although AM started gaining the industry's interest over the last 20 years, the main usage and innovation boost came after several patents expired between 2013 and 2015 (*3d Printer Patents | UpCounsel 2021, n.d.*), giving rise to a multitude of new printer manufacturers, types, and scales. Its working principle sets it apart from the two traditional manufacturing techniques. Formative manufacturing is characterized by filling a mould with a liquid base material. After its solidification, the mould is removed, and the finished part

2023). A short overview of the functional principles of additive manufacturing techniques deemed most suitable for this project shall be presented in the following section.

The influences on an additively manufactured part's geometric accuracy and its physical properties are numerous and include aspects such as the part's digital representation, its mesh discretization, quality, base material storage, quality and age, process parameters relating to slicing and tool pathing, machine wear and maintenance, postprocessing steps such as support structure removal, sand blasting etc. A comprehensive range of influential parameters is represented in Figure 2.46 based on the Laser Powder Bed Fusion process. It provides an illustration of the range and number of steps that can influence the final part's performance, and is mostly applicable to other AM processes as well.

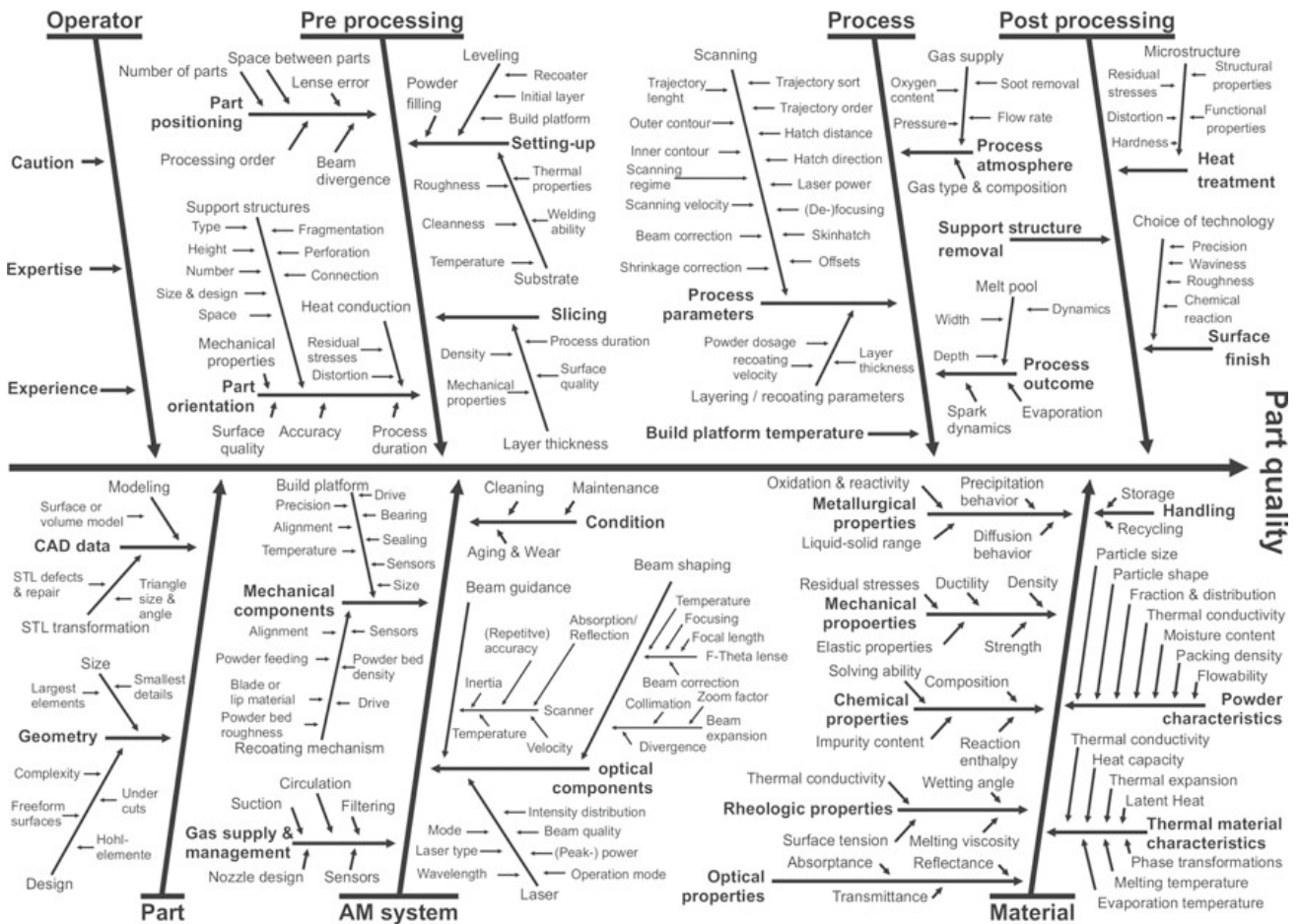


Figure 2.46: Ishikawa diagram of manufacturing parameters influencing a part's quality. (Diegel et al., 2019)

2.2.1 Preprocessing

In order to prepare a part for additive manufacturing, it has to exist in a digital CAD file format first. It is converted from a boundary representation to a mesh representation wherein the body's surfaces are approximated using triangular or rectangular elements. A finer mesh can represent curved surfaces more accurately with the trade-off of larger file sizes. The resulting file is commonly saved as STL, OBJ or 3MF file. It is then imported into a slicer software which splits the part into planar layers and defines the tool head's path or laser lighting pattern, depending on the chosen manufacturing

type, before sending the file to the machine for production. Since additively built parts are successively produced with a finite height step, they are discretized and lose some of their geometrical fidelity. Smooth curves and angled sections are broken up into sections, resulting in a cross-section resembling stair steps as depicted in Figure 2.47. This step is common to all planar AM techniques.

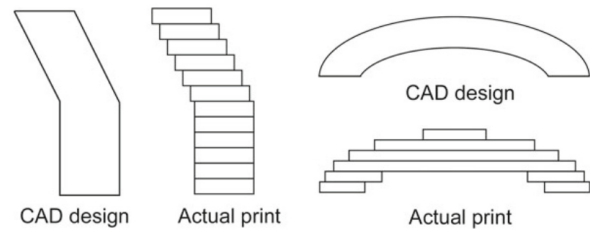


Figure 2.47: Stair-stepping resulting from discretized build process of Additive Manufacturing. (Diegel et al., 2019)

2.2.2 Fused Deposition Modelling

As described by (Diegel et al., 2019), Fused Deposition Modelling (FDM) operates by melting thermoplastic material from a filament spool and extruding it through an extrusion head fitted with a heater cartridge and nozzle. The extrusion head and heated bed move relative to each other in the XY plane, following a path predetermined by a slicing software while the extruder fills the required surface areas with material. The first layer is laid down on a build plate, with the plate being lowered (or the extrusion head being raised) to lay down a new material layer on the previous one. The principle is depicted in *Figure 2.48* and *Figure 2.49*. The nozzle orifice commonly has a diameter of 0.2mm-1mm with layer heights ranging from 0.05mm-0.8mm, usually 25-80% of the orifice diameter. Squishing the material into an oblong shape during extrusion, it ensures adequate layer adhesion and surface covering. The building process entails the risk of warping due to internal stress build up during cooling. Large parts tend to cool non-uniformly which cause the layers to curl upwards, possibly detaching the print from the build platform or causing a failure by delaminating.

The manufacturing method also limits the feasible build angle, as the extruded material starts to lack support from the layer directly underneath. Most FDM printers manage a so-called overhang angle of 45° above which support structures are required for the print to succeed (Diegel et al., 2019). Overhangs perpendicular to the build plate and below a certain distance threshold can be directly bridged without support structures, but they require special care to be successful. Support structures need to be removed after finishing the printing process, hence they should not be surrounded by tight geometries or be fully enclosed.

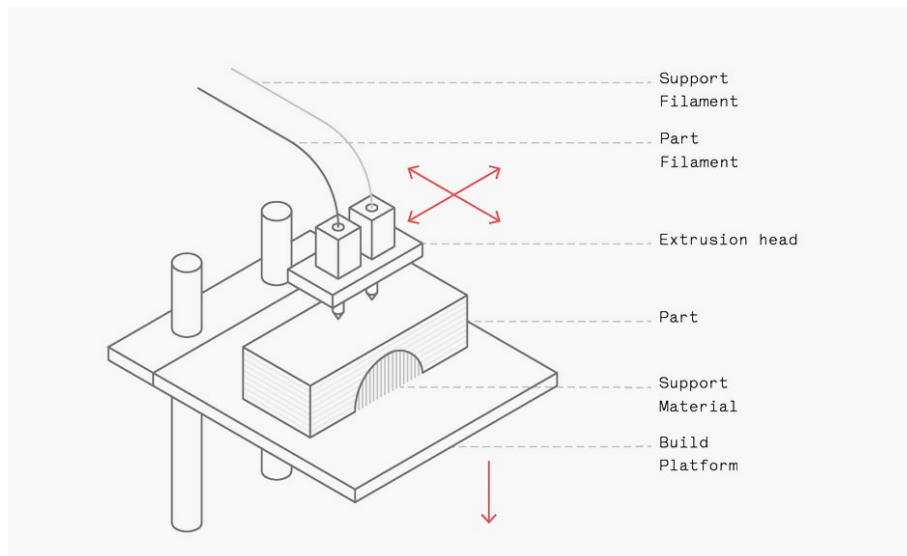


Figure 2.48: Working principle of Fused Deposition Modelling printing process. (Redwood et al., 2018)

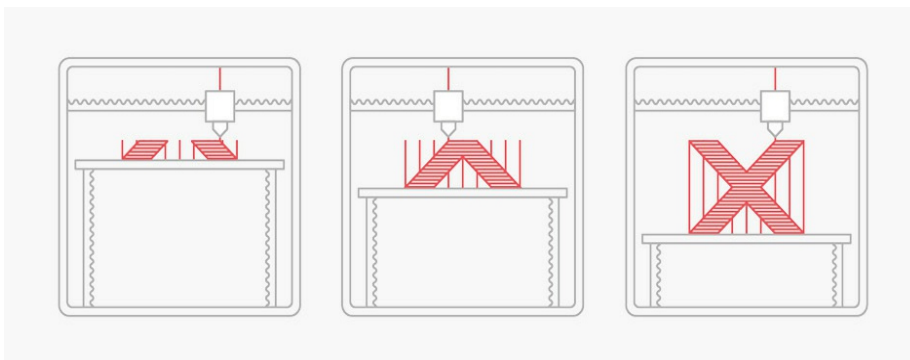


Figure 2.49: Layer-wise part building process, adapted from (Redwood et al., 2018).

Parts produced by FDM printers usually do not consist of solid material. The interior structure is occupied by porous infill, often in a uniform planar grid or triangle pattern to save on printing time and material (c.f. Figure 2.50). The manufacturing process entails that a new, hot layer is laid down on cold material, such that the layers are only held together by adhesion. This significantly lowers the tensile strength in the build direction, causing anisotropic material properties (Ahn et al., 2003). In addition, the oblong outer shape of a layer line creates a notch between each layer interface on the outer surface. The part orientation, layer filling pattern, infill type and density, top/bottom layer count and wall thickness play a significant role in determining a part's final strength and its failure mode (Alvarez C. et al., 2016; Pandzic et al., 2019). In addition, polymers tend to absorb moisture during storage in ambient conditions, potentially degrading the material properties and lowering the print success rate. (Kim et al., 2016)



Figure 2.50: Examples of increasing infill densities with prismatic pattern. (Diegel et al., 2019)

The material selection for FDM machines skews towards easy-to-use polymers such as Polylactic Acid (PLA), Polyethylene Terephthalate Glycol (PETG) or Acrylonitrile Butadiene Styrene (ABS) to easily produce visually-pleasing parts which do not require engineering-grade strength, heat and chemical resistance, or toughness. However, significant advances have been made to enable engineering grade materials with a wide range of properties to be printed on FDM machines as well, opening up the possibility to print Thermoplastic Polyurethane (TPU), Polycarbonate (PC), Polyether Ether Ketone (PEEK), Polyether Ketone

Ketone (PEKK), Polyamide (PA), Polypropylene (PP), and variations thereof such as fibre-filled materials containing carbon or glass fibre strands.

Certain manufacturers like Markforged (*Markforged Homepage*, n.d.) and Desktop Metal (*Desktop Metal Homepage*, n.d.) offer metal-filled filaments to be used in a closed ecosystem with a dedicated printer, debinding and sintering stations, in order to additively manufacture metal parts without the added complexity of Powder Bed Fusion technology. More information regarding the Metal X system can be found in the Addendum in section 7.6. Other materials, like BASF Ultrafuse (*BASF Ultrafuse Metal Filaments*, n.d.) or Virtual Foundry Filamet (*The Virtual Foundry Filamet*, n.d.) are printed on standard open source FDM machines, with debinding and sintering performed with any compatible setup. Alternatives to the material filament rolls are coming up as well, such as pellet-based printers with an extrusion screw (*Pollen AM*, n.d.), or high viscosity UV-reactive resin deposition and curing with printer setups that are otherwise identical to FDM machines (*Massivit*, n.d.).

2.2.3 Light Polymerisation

As described by (Diegel et al., 2019), light polymerisation techniques rely on directing an ultraviolet light source onto liquid resin and solidifying it in the process. The resins are thermoset polymers ranging from rubber-like flexible options to engineering grade strengths, with special variants such as ceramic- or metal-filled resins (Corbel et al., 2011). Light sources can be a directed laser whose path covers the required solid surface or an LCD screen illuminating the slice all at once. Both methods are called Stereolithography which is shortened to SL. Alternatively, a projector can be used as light source with the technique being referred to as Digital Light Processing (DLP). The techniques allow manufacturing comparatively small feature sizes, as the level of details is governed mostly by the size of the laser dot or screen pixel (Davoudinejad et al., 2018). Layer heights commonly range from 0.025mm-0.1mm. Resin printers often possess only one single movable axis raising and lowering the build plate into the resin vat, building the part hanging from the platform as shown in *Figure 2.51*. This motion stirs the resin between layer changes and detaches the cured layer from the FEP (Fluorinated Ethylene Propylene) film, which commonly constitutes the barrier between the liquid

resin and the light source. With Light Polymerization AM, parts are usually not built directly on the build plate but are raised and supported. For overhangs and detached material areas that are not yet connected to the remaining part, support structures are needed as well to successfully complete a print and prevent warping due to gravity. After completion, the part is washed in isopropyl alcohol to remove excess resin and cured with UV light until the material is fully hardened.

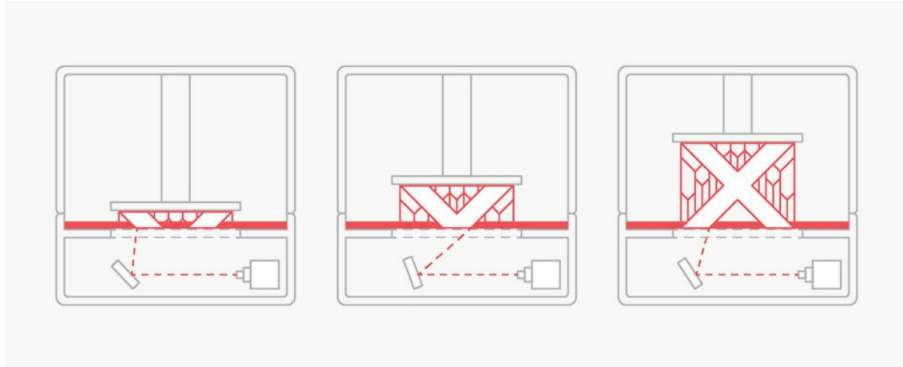


Figure 2.51: Working principle of light polymerisation technique, adapted from (Redwood et al., 2018).

2.2.4 Powder Bed Fusion

Powder Bed Fusion (PBF) builds parts from granular material by selectively solidifying it across the exposed powder surface (Diegel et al., 2019). Its categories are subdivided depending on their solidification method and the material to which it is applied. The solidification can be accomplished by two main methods, either by melting the material via directed energy heating the powder, or by applying a liquid binding material. After each layer completion, the build plate is lowered and a new layer of powder is reapplied, restarting the cycle as depicted in *Figure 2.52*. The former process is carried out by applying energy via a laser in case of Selective Laser Melting (SLM) used for metals and ceramics (Yap et al., 2015), and Selective Laser Sintering (SLS) methods used for polymers (Kumar, 2003). Alternatively, an electron beam is used in case of the Electron Beam Melting (EBM) method, which is mainly used for metals (Körner, 2016). It sinters or completely melts the material in the targeted zone. The method using liquid binder material is generally known as Binder Jetting (BJ) and resembles the working principle of an office paper printer. A multi-nozzle head moves above the powder surface, applying binding liquid where required to fuse the powder in order to form a solid part (Ziaee & Crane, 2019). The powder is essentially selectively glued together. Binder jetting can be applied to polymer and metal materials; however, metal parts require an additional sintering step to fully solidify.

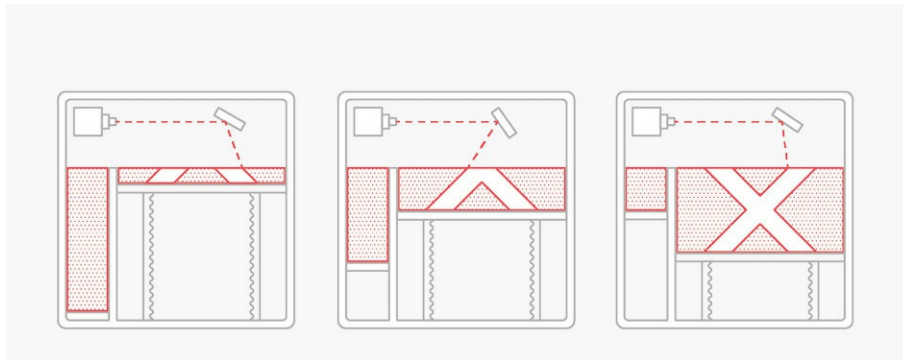


Figure 2.52: Working principle of laser-based powder bed fusion process, adapted from (Redwood et al., 2018).

The Multi-Jet Fusion (MJF) process developed by Hewlett-Packard (HP) combines characteristics of the SLS and binder jetting methods. As described by (O'Connor et al., 2018), the powder material is doused with a fusing agent on the inside of the part, and a detailing agent applied to the part's edges for improved surface quality. Applying heat energy solidifies the part and it is continued to be built layer by layer similar to other AM processes. Contrary to binder jetting, the material is not simply glued, but fused by polymerization which improves the achievable material properties. Its working principle is shown in Figure 2.53.

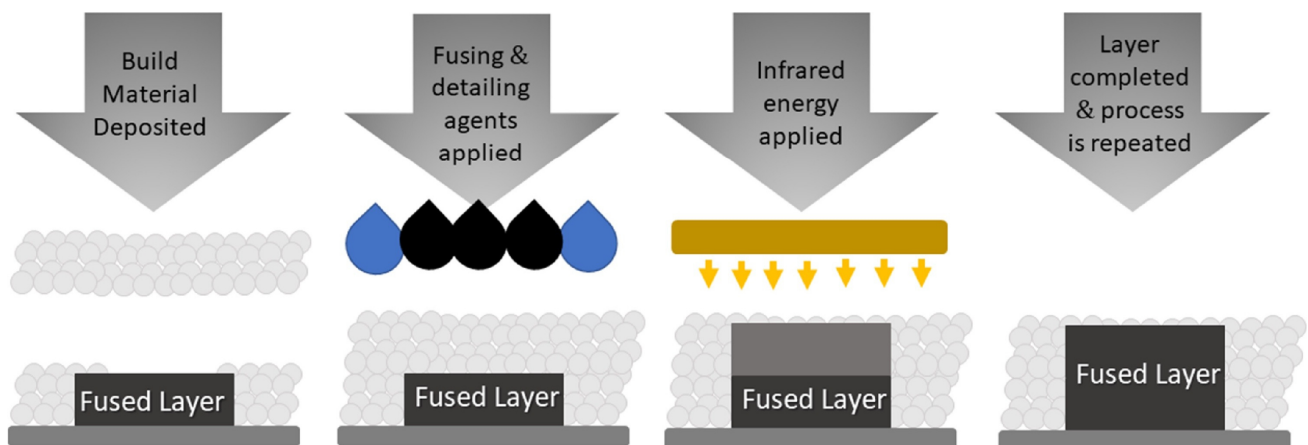


Figure 2.53: Schematic depiction of the Multi Jet Fusion manufacturing process. (O'Connor et al., 2018)

The different PBF technologies enable the production of relatively large part quantities with high accuracy, allowing the use of a large range of material options. They generally do not require the use of support structures since the parts are supported by their surrounding powder during the building process (Diegel et al., 2019). However, metal PBF methods may need anchor points to act as heat sinks and fixation spots to reduce thermal warping.

A wide range of materials is available for the different PBF methods, and an overview is given by (Singh et al., 2020). A commonly used polymer is Polyamide in varying compositions and with optional supplements such as chopped carbon fibre for improved mechanical properties. Offering relatively easy printing, low thermal warping tendencies and versatile material properties, it is readily used for prototyping and end-use parts. Other options include flexible and rubberlike materials or

ceramics. Metals such as aluminium, stainless steel, titanium, tungsten along with precious metals can be processed as well. The size, cost and efforts involving pre- and postprocessing of PBF printing machines mostly prohibit their private use, making them almost exclusively accessible to businesses and research institutes (Diegel et al., 2019).

2.2.5 Suitable Additive Manufacturing Methods for Lattice Geometries

Manufacturing FGLS poses as much of a challenge as the computational design, and each manufacturing method's characteristics must be considered along with detailed material behaviour modelling. Review studies examining the process of additively manufacturing lattice structures are given in (Helou & Kara, 2018; Seharing et al., 2020).

The main issues in FDM printing that apply to all geometries are the need for support structures, material properties being strongly dependent on printing parameters, part anisotropy due to the manufacturing method, as well as the available material selection (Mohamed et al., 2015). Above certain threshold angles, support structures in and around the lattice are necessary for the print to succeed. They can be difficult or impossible to remove depending on the printed structure, causing some print jobs to become impractical on an extrusion machine. This holds true especially when manufacturing graph-based lattice structures irrespective of their surrounding geometry. Although adjustments to the printing angle relative to the lattice structure can lead to support-free lattices, this technique is not always feasible. On the other hand, TPMS lattices result in continuous printing surfaces after the slicing process and are generally self-supporting, they are thus much more forgiving during printing. As Mohamed et al. state, parameters such as part orientation, layer height, number of walls, top/floor layers, extrusion width, infill patterns and percentages strongly influence the material properties of the finished part. Polymer parts loaded in a perpendicular direction to the printing plane can lose up to half their ultimate tensile strength compared to parts loaded parallel to it (Ahn et al., 2003). Metal parts see a noticeable dependence on directionality as well (Gong et al., 2019). They can exhibit significant surface defects stemming from geometrical discretization in the build direction, poor surface finish at support structure interfaces or overhangs, and holes caused by the Z seam, material retraction at layer changes or slicing inaccuracy. These defects can cause significant weak points in geometries exhibiting small feature sizes such as graph lattices and need to be accounted for during the design phase.

Light Polymerisation processes share the need for support structures with extrusion techniques to a lesser degree, but their materials show much lower dependency on printing orientation (Shanmugasundaram et al., 2020). Low layer heights in combination with high resolutions in the XY plane allow for small feature sizes, high dimensional accuracy, and smooth surface finishes of printed parts. However, large parts with low rigidity can be distorted during prints due to their own weight and suction forces between the part and the transparent plastic film on the bottom of the resin vat. Drain holes are required to remove liquid resin trapped inside hollow parts to prevent cracks during the curing process, weakening the structure. Usually, latticed parts are completely solid and consequently do not need drain holes, but the UV light might not reach every spot of the lattice during the curing process. The process is generally well-suited to manufacture graph-based and surface-based lattices as long as they are open-cell. The machines tend to be restrictive in build size, offering only 80-150mm in X and

Y axes and 150-200mm in the Z axis. However, larger machines are coming to the market in increasing numbers.

Powder Bed Fusion processes are widely used in industrial additive manufacturing processes as they possess significant advantages. A large material selection of many engineering polymers and metals can be used, and they do not require support structures as the part is held from all sides by the surrounding powder (Diegel et al., 2019). Metal parts need to be fused to a build surface with anchor structures being attached for heat dissipation and thermal warping prevention. On the other hand, polymer parts can be positioned almost arbitrarily in the build chamber, though some orientation guidelines need to be considered in order to prevent thermal warping and to achieve smooth surface finishes. PBF processes boast low layer heights and high XY resolutions, resulting in small printable feature sizes. Manufacturing hollow parts requires the use of drain holes to remove excess powder, which can be a laborious process. Polymer parts produced with PBF also possess anisotropic material properties, although to a lower extent than those produced with FDM. Metal parts generally show only little dependency on build orientation (Yap et al., 2015). Generally, PBF methods are well-suited for lattice structure manufacturing of graph-based and surface-based unit cell types, as long as they are open-cell.

In conclusion, all three AM techniques can be used to produce lattice structures, but the optimal solution depends on the requirements at hand. Fused Deposition Modelling offers low-cost productions, large build volumes as well as easy material handling and postprocessing, but can be limiting for graph-based lattices. In the special case of metal extrusion processes, special care during sintering and support structure removal must be applied to prevent warping, delamination and fracture. Light Polymerisation and Powder Bed Fusion processes offer the highest resolutions, the best surface finish and little to no support requirements, making them the preferred options among the three. Further considerations such as part size, minimum feature size, material requirements and the necessity for powder or resin evacuation holes decide between Light Polymerization and PBF methods.

2.2.6 Summary

Choosing an appropriate Additive Manufacturing method for lattice structures depends on numerous factors pertaining to the required material, the specific method, and the targeted lattice type. The lattice's density additionally influences the part's manufacturability since thin features or difficult material evacuation paths can exclude certain manufacturing methods. The appropriate options must therefore be analysed for each application individually. A decision matrix ranking the relevant AM method properties regarding the production of lattice structures is given in Table 2.1. As can be seen by the total marks of each method, the results are rather close. Each method's strengths and weaknesses therefore have to be considered for the case at hand.

Table 2.1: Decision matrix ranking the different Additive Manufacturing properties for the production of lattice structures with rankings of 1 = worst and 5 = best.

Property	FDM	Light Polymerization	PBF
Accuracy	3	5	4
Minimum feature size	3	5	4
Material selection	4	3	5
Support requirement	3	4	5
Excess material evacuation	5	3	2
Material anisotropy	2	4	4
Build size	5	2	4
Surface quality	2	5	4
Total	27	31	32

2.3 Lattice Design and Simulation Software

Before the emergence of adequate design software, lattice design and optimization was commonly carried out via custom-written scripts. It allows for design and optimization freedom as well as efficient execution of large-scale optimization of abstracted lattice geometries. On the other hand, handling and exporting the resulting lattices for production remains a nontrivial task. Several examples of studies relying on scripting of the lattice generation or optimization are given in section 2.1.2-2.1.4. When using conventional CAD software, lattices must usually be generated manually, severely limiting their potential. Parametric design and grading of the lattice's thickness is generally feasible with this approach, however due to the boundary representation method used in CAD software, subsequent modifications to its size or other properties are prone to failure and may be unfeasible. Redesigning the lattice from the beginning or omitting some features, like radii between beams, might be necessary to succeed. Recent feature additions to CAD software (e.g. in PTC Creo (*PTC Creo*, n.d.)) allow implementing simple, regular lattices with a thickness gradient in the design phase, but other variables such as cell size or mixed types are not available. Rhinoceros 3D (*Rhino3D*, n.d.) makes use of its parametric plugin Grasshopper, offering a large array of control options which allow for more advanced lattice design options. Simulation suites such as Ansys SpaceClaim (*Ansys Spaceclaim*, n.d.) with its Mechanical solver (*Ansys Mechanical*, n.d.) and Altair OptiStruct (*Altair OptiStruct*, n.d.) also strive to break into the domain by offering lattice optimization functionalities, but they remain limited in their use. For instance, Figure 1.2 shown in the introduction section depicts a bracket after a lattice optimization performed with OptiStruct, however there is no possibility to extract the geometry for production without purchasing a license of Materialise 3-matic (*Materialise 3-Matic*, n.d.). A non-exhaustive overview of reviewed options for digital lattice design in an engineering context is listed in Table 2.2.

2. Fundamentals & State of the Art

Table 2.2: Overview of reviewed software options for lattice generation. Ratings: ★☆☆ = basic, ★★☆☆ = fair, ★★★☆☆ = good.

Software	Lattice design	Simulation options	Export options
<i>Altair Inspire Structure (Altair Inspire, n.d.)</i>	★★★☆☆	★★★★★	★★★☆☆
<i>Autodesk Fusion 360 (Autodesk Fusion 360, n.d.)</i>	★★★☆☆	★★☆☆☆	★★☆☆☆
<i>Altair OptiStruct (Altair OptiStruct, n.d.)</i>	★★☆☆☆	★★★★★	★★☆☆☆
<i>Altair Sulis (Altair Sulis, n.d.)</i>	★★★☆☆	★★☆☆☆	★★☆☆☆
<i>Ansys Spaceclaim (Ansys Spaceclaim, n.d.) & Mechanical (Ansys Mechanical, n.d.)</i>	★★☆☆☆	★★★★★	★★★☆☆
<i>Autodesk Meshmixer (Meshmixer, n.d.)</i>	★★☆☆☆	★★☆☆☆	★★☆☆☆
<i>Autodesk Netfabb (Autodesk Netfabb, n.d.)</i>	★★★☆☆	★★☆☆☆	★★☆☆☆
<i>Autodesk Within Medical (Autodesk Within Medical, n.d.)</i>	★★★☆☆	★★★★★	★★☆☆☆
<i>Materialise 3-matic (Materialise 3-Matic, n.d.)</i>	★★★☆☆	★★☆☆☆	★★☆☆☆
<i>nTop (NTop, n.d.)</i>	★★★★★	★★☆☆☆	★★★★★
<i>PTC Creo (PTC Creo, n.d.)</i>	★★☆☆☆	★★☆☆☆	★★☆☆☆
<i>Rhinoceros 3D (Rhino3D, n.d.) & Grasshopper (Grasshopper, n.d.)</i>	★★★☆☆	★★☆☆☆	★★★☆☆
<i>Simpleware CAD (Simpleware CAD, n.d.)</i>	★★★☆☆	★★☆☆☆	★★★☆☆

Lattice design suites such as nTop, Altair Sulis and Altair Inspire increasingly move towards using implicit body representation techniques. nTop is among the first software suites in the lattice design realm opting for this route, with the initial release in 2015 (then called nTopology Essentials). Others follow suit, such as Altair Sulis (released in 2020 as Gen3D), Altair Inspire introducing implicit body generation with its version 2023.0 release, and Fusion 360 with their support for implicit body import for additive and subtractive manufacturing preprocessing planned for release in early 2024.

The implicit modelling method is an alternative approach to digital 3D body representation in engineering and computer graphics environments. Traditional CAD software suites utilize a boundary representation method, i.e. surfaces, vertices and splines define the outer bounds of a volume body. While this allows for quick and efficient creation of simple geometries by combining primitive bodies, revolutions, extrusions etc., it is severely limiting in some domains. Operations such as filleting at overlapping edges, fixing duplicate edges, Boolean operations, morphing, hollowing, and many other examples can pose insurmountable problems for a CAD software suite. Implicit design approaches lattices with a mathematics-based method instead of relying on vectors, edges, vertices and surfaces. The implicit representation treats bodies as signed distance functions, where the boundaries of a body have zero value, the inside of the body's domain is a negative scalar field decreasing linearly to the centre, and the outside a positive scalar field increasing linearly as depicted in *Figure 2.54* on the left (Allen, 2019). Using this approach, operations such as scaling a body can be as simple as adding a constant value to the body's implicit function as shown in *Figure 2.55*.

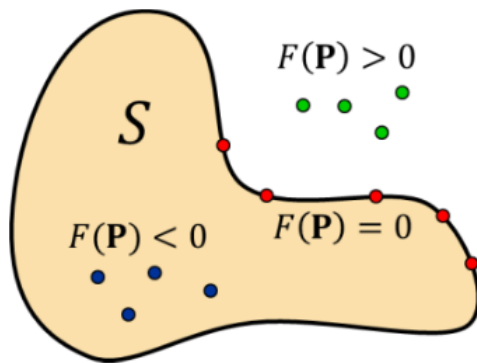


Figure 2.54: Implicit representation of a body with local values F as function of the points P 's position on the inside, outside and on the body's border. (Allen, 2019)

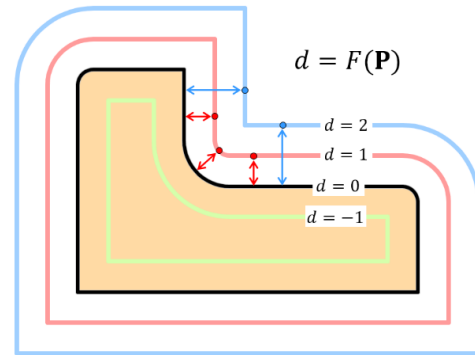


Figure 2.55: Implicit scaling operation achieved by adding a constant value to the implicit function. (Allen, 2019)

The concept is further explained with Figure 2.56. The left side depicts a rectangle created with the boundary representation method, i.e. four corner nodes connected by four lines, whereas the right image shows its implicit representation. The borders are delimited by the two functions $x^2 - 4 < 0$ and $y^2 - 1 < 0$. A point inside both regions is thus inside the rectangle if both conditions are met. One possible implicit function fulfilling these criteria can be $F(x, y) = \max \{x^2 - 4, y^2 - 1\}$. Any volumetric body or operation can be expressed mathematically this way, enabling quick and versatile geometry manipulation: integrating varying lattices in a body, shelling, smoothing, perforating, texturing, Boolean operations etc. The processes are nearly unbreakable, unlike the boundary representation method which struggles with complex operations on intricate geometries. They are also field-driven, meaning that properties can be defined as a function of stress, position, temperature, or user-defined function to gain more control over the design.

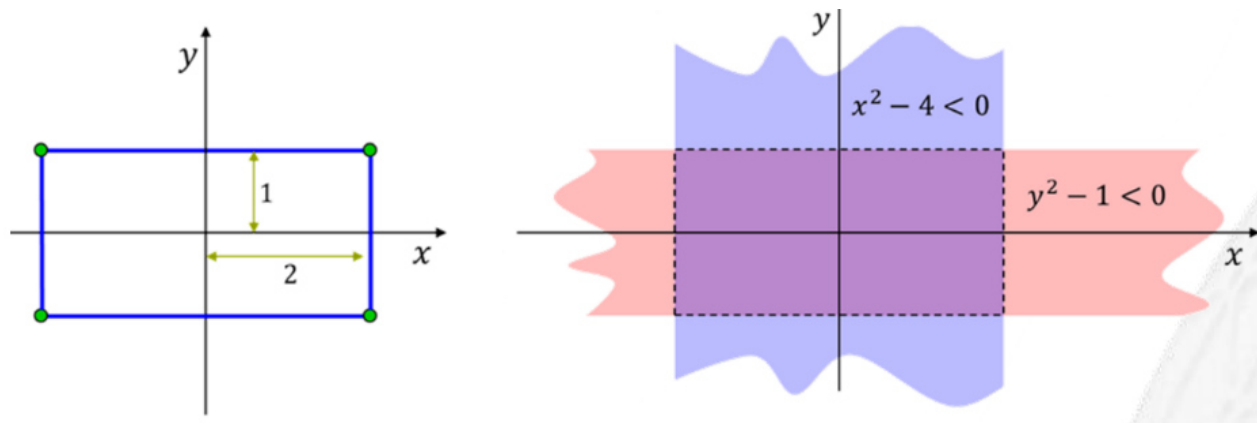


Figure 2.56: Boundary representation of a 2D rectangle (left) and its implicit representation (right), adapted from (Allen, 2019).

Of the options listed in Table 2.2, nTop is the most versatile and offers the most comprehensive set of options. At the start of the thesis, it was the only viable solution and therefore chosen for the projects at hand. An example demonstrating the power of implicit modelling is nTop's ability to control the lattice properties introduced in a cantilever beam under a bending load as shown in Figure 2.57. The beam geometry is replaced by a lattice structure, and its von Mises stress field is used to drive a Simple

Cubic lattice's local thickness – high stress regions are assigned a larger diameter, low stress regions a lower diameter. The assignment is based on a mapping function requiring upper and lower thickness limits. A second example depicts how the stress field can drive the local beam thickness in conjunction with the cell size of a Voronoi lattice using the same approach.

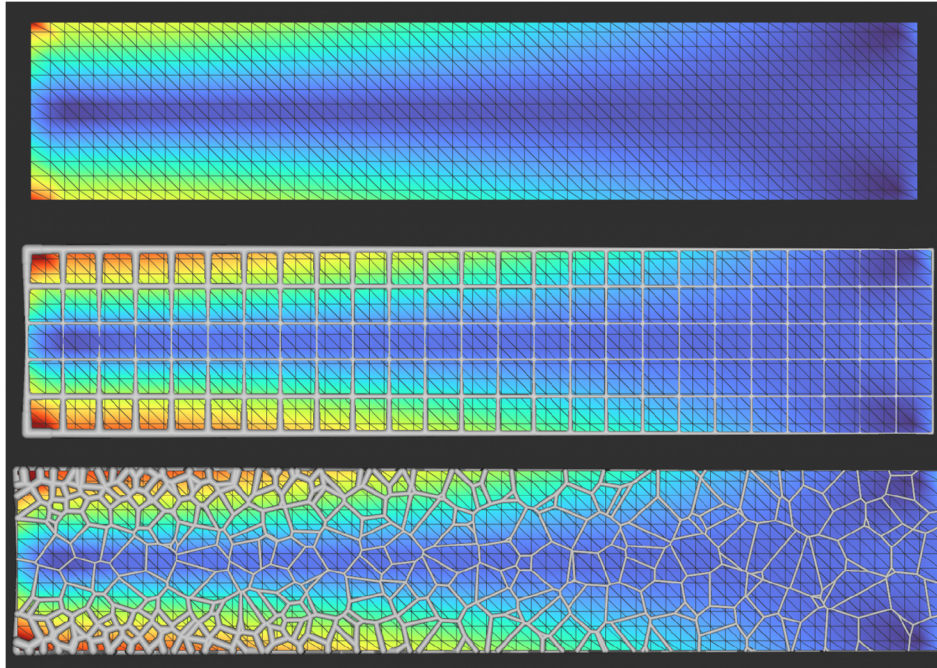


Figure 2.57: Examples of applying a functionally graded lattice to a cantilever beam.

While this gives the user a wide range of control, the process is not an optimization but rather a manual alteration of the lattice's properties. A mapping function must be defined to translate a stress value to a lattice thickness or cell size value. An nTop update in April 2023 introduced the option of performing true optimizations of 1D graph lattices via the material density field gained from a Topology Optimization. The feature is still in the beta phase as of December 2023.

Several options for performing FE analyses of the devised lattice structures are available. nTop features an FE module of its own offering analyses of linear static structural cases, buckling, modal, or thermal investigations. However, dynamic analyses or nonlinearities such as contact or material plasticity are not available, severely limiting its utility for complex models and load cases. It further offers the option of lattice homogenization. The directional stiffness of a unit cell is determined via an FE analysis and applied to a complete lattice structure of the same unit cell type. Each unit cell can then be represented by a single anisotropic hexahedral element replacing multiple beam, shell, or solid elements, thereby greatly reducing the required computational efforts. Examples of the directional stiffness representation of a few unit cells are depicted in *Figure 2.58*. This approach cannot consider any nonlinearities either. The consequence is therefore the necessity to export the lattice geometries for use with adequate FE solvers.

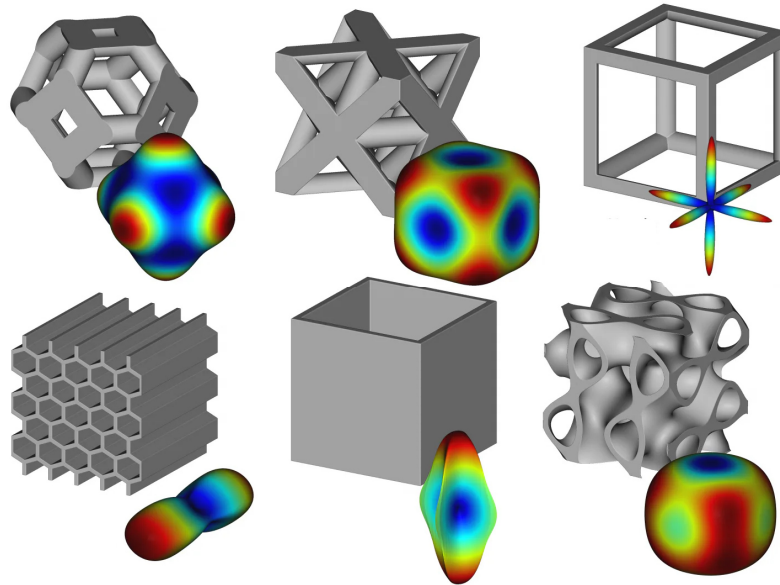


Figure 2.58: Examples of unit cells and their equivalent, homogenized directional stiffness properties, adapted from (Johnathan, 2020).

Preparing lattice geometries for FE analyses requires a potent preprocessor such as Altair HyperMesh due to the intricate meshes. Extensive corrective mesh operations are often required to remedy intersections and element quality issues of 2D and 3D meshes exported from nTop. Altair's solvers OptiStruct and RADIOSS were chosen to be used for simulating the models produced during this project due to their extensive capabilities, along with HyperStudy for the optimization procedure. Other FE suites could have been utilized as well, but Altair's suite was already available to the university at the start of the project.

One of the main hinderances of dealing with lattice geometries is the file exchange between software packages. While handling geometries inside of nTop is generally simple, the file formats to import and export results are limited. Importing well-defined solid geometries in nTop as STEP, IGES or any other popular CAD file format poses no problem. However, it suffices that the body is only described as closed surface and not as a solid for the workflow to break down. Conversely, exporting a lattice geometry as CAD file is practically not feasible except for very simple bodies. The conversion process from an implicit body to a description based on vertices, lines, splines, and surfaces is complex and fragile. The only viable options for higher complexities are either to export the geometries as surface based meshes (such as STL, OBJ, PLY) or FE meshes containing shell, beam and/or solid elements. Meshed geometries usually require significant clean-up before they can be remeshed or run with external FE solvers and are difficult to alter in case of geometry changes. Whenever applicable, a simpler exchange method can be achieved by exclusively using beam and shell elements. Thin-walled TPMS lattices can readily be represented using shell elements, whereas thick-walled TPMS structures can be exported as hollow shell elements and filled with solid elements later in the preprocessor. Beam-based lattices can be exported using the relatively new 3MF file format specifically developed for this task. It is intended to include more information than STL while also being structured in a simplified manner to enable a more streamlined connection between geometry creation tools and additive manufacturing. It can represent 1D beam elements in addition to triangular

and quadrilateral elements for surface descriptions, but it is not yet supported by FE preprocessors such as HyperMesh.

Beam-based lattices with uniform thickness distribution can be exported as 1D FE beam mesh, allowing easy handling. However, beam lattices with non-uniform thicknesses can only be exported from nTop via their own LTCX file format that is not supported elsewhere. Fortunately, it is merely an XML file in ASCII format and thus human-readable. During the course of the thesis projects, a script was written in MATLAB to convert the LTCX file to an input file for OptiStruct. It offers the choice of sorting the diameter values into a fixed number of bins to reduce the amount of element properties required, or to keep all of them (see Addendum, section 7.1). This specific script was written with the optimization approach of the beam lattice in mind, which is described in the publication in section 4.1. Here, the lattice splitting was performed in nTop, so the size adaptation after the optimization step could be performed there before exporting the STL file for manufacturing.

On the other hand, a subsequent project required to reimport the lattice to nTop after its optimization in Altair RADIOSS. Here, the lattice splitting is performed in HyperMesh after the lattice was exported from nTop. A second MATLAB script was therefore devised (see Addendum, section 7.2). It reads the RADIOSS input file used for the optimization and outputs several LTCX files, each containing one region of the split lattice. It can then be reassembled in nTop and thickened according to the optimization results. The lattice splitting is in principle also entirely feasible in nTop. However, the script was written with the idea in mind that mesh morphing would be applied during the optimization studies, too. The resulting morphed lattice could not have been replicated accurately in nTop, thus importing the simulation results to nTop was deemed necessary. The aforementioned project is found in section 4.6.

In any case, reimporting results back to nTop or adapting an existing lattice in nTop is a mandatory step. It is not yet possible with simple means such as first-party tools to create an STL file from 1D FE beam elements for additive manufacturing. Although FE meshes can be imported directly to nTop, it does not allow any manipulation or extraction of the mesh for further steps.

3 Research Methodology & Objectives

In this chapter, the research goals are refined based on the conducted literature review and identified gaps. Subsequently, the proposed research methodology is presented including key research questions. The scope of the research is outlined and ultimately, the proposed lattice optimization method is outlined.

3.1 Research Objectives

As laid out in Chapter 2, numerous research papers about lattice structures focus on suitable materials, manufacturing methods, lattice types, bioinspired and newly created unit cell geometries, and application domains. The studies agree that lattice structures are advantageous in numerous tasks, and that graded lattices can outperform uniform lattices at equal weight. However, publications tend to concentrate on simplified geometries such as cubes in compression or cantilever beams under bending loads in standard test conditions. These approaches do not necessarily represent the complex geometries and load cases experienced by mechanical parts as found in the automotive or aerospace domains. Furthermore, lattice property gradients are commonly applied manually. They rarely deviate from the option of changing the unit cell height or thickness either linearly or in stepwise intervals. If optimization routines are used to alter local lattice properties, they frequently make use of custom-written optimization scripts. These routines heavily involve the user and are not in line with engineering workflow requirements regarding flexibility, usability, and results extraction. The aim of this thesis is therefore to efficiently implement FGLS in mechanical parts under consideration of engineering requirements. The research gaps are summarized in Table 3.1.

Table 3.1: Research gaps determined from literature research.

Research Gaps
RG1: Potential performance gains of engineering parts with FGLS are largely unexplored, so far mostly synthetic tests of simple geometries were studied.
RG2: No optimization method for arbitrary goals and physics is available that is compatible with engineering tools and restrictions, such as FEA tools and manufacturing methods.
RG3: FGLS are advantageous for impact energy absorption tasks, but very few studies researched their optimal thickness distribution.

The project's aim is to enable and simplify the implementation of FGLS in mechanical designs. More exactly, in designs with a realistic level of complexity as found in the industry. Four objectives emerge from this aim. First, a generalized workflow shall be developed that allows the efficient design, optimization, and manufacturing of FGLS using existing engineering tools whenever possible. This entails that adequate design and simulation tools must be determined. Next, the parts need to be assessed via means of simulative and physical testing to assess their performance. The parts evidently must be physically produced to do so, hence adequate AM production methods and materials have to be determined. The manufacturing methods available in the AM laboratory of the University of Luxembourg should preferably be used to allow fast design iterations and full control over the production settings. Table 3.2 summarizes the four research objectives.

Table 3.2: Objectives guiding the research direction.

Research Objectives
RO1: Find software suites capable of designing, simulating, and optimizing lattice structures.
RO2: Develop an optimization method compatible with common simulation suites.
RO3: Perform simulative and experimental assessments of the optimized lattice structures.
RO4: Find an adequate AM method and material selection for production of the lattice structures.

3.2 Research Methodology

The research methodology encompasses multiple steps guided by the research objectives as shown in Figure 3.1. The task begins with a thorough literature research determining the general properties of lattice structures, current research topics, adequate use cases, available software, and knowledge gaps. This information is assembled and assessed to decide on potential avenues. Material tests are performed to obtain detailed information about their properties, aiding in building accurate simulative models. Simultaneously, their suitability for lattice production can be partly assessed. The developed optimization method is applied to implement FGLS in two real-world applications. Their performance is assessed via simulative and physical testing. As laid out in Chapter 2, lattice structures excel in lightweight structural tasks and compressive energy absorption applications. Therefore, the appliances considered in this thesis adhere to the same categories.

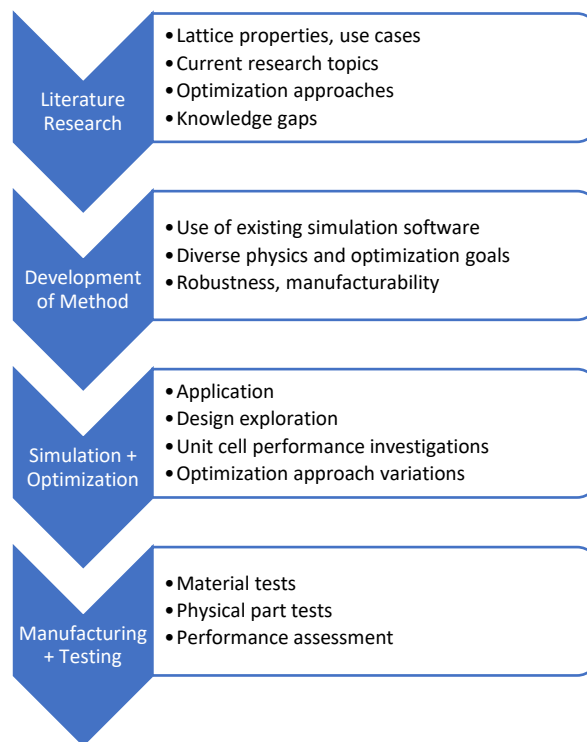


Figure 3.1: Primary and secondary research methodology steps.

The results of the thesis facilitate the transition of FGLS from a research novelty to a usable and valuable concept employed in engineering appliances. It does so by providing answers to the following leading research question:

Table 3.3: Leading research question derived from research gaps.

Leading Research Question
RQ1: How can FGLS be designed and optimized in mechanical parts with consideration of engineering requirements?

The aforementioned engineering requirements are modelled after industry requirements, where ease of use, flexibility and time constraints are major decision factors. The following aspects are guiding the method's properties:

- Compatibility with existing engineering software
- Possibility to simulate wide range of nonlinear physical phenomena (structural, thermal, fluid dynamics...) and optimization goals
- Simple geometry extraction to ensure and facilitate manufacturing
- Robust and repeatable workflow structure for fast design iterations?
- Creation of conformal lattice gradients for improved performance
- As little need for custom scripting as possible

From the leading research question and these requirements spring the supplemental research questions listed in Table 3.4:

Table 3.4: Supplemental research questions originating from application requirements.

Supplemental Research Questions
RQ2: How well do FGLS perform in realistic mechanical appliances?
RQ3: How can FGLS be modelled and simulated adequately?
RQ4: How can the computational effort of lattice optimization studies be reduced?
RQ5: Which unit cell types are suitable for the considered tasks?

Two applications, chosen to play to the strengths of FGLS in lightweight structural and energy absorption tasks, demonstrate the design and optimization approach. The first is a hollow bicycle crank arm, shown in Figure 3.2, fitted with a lattice structure optimized for maximum rigidity. The second application revolves around a bicycle helmet, shown in Figure 3.3, equipped with an energy-absorbing lattice replacing the commonly used foam liner. The lattice's thickness is optimized to reduce the wearer's injury risk as much as possible. The applications are chosen since they stem from an approachable domain familiar to a wide range of people. In addition, their size and targeted choice of materials allow to manufacture them locally entirely or partially. An auxiliary study explores the optimal thickness distribution of a cuboid lattice (c.f. Figure 3.4). in large strain compression to achieve the highest specific energy absorption. Its findings support the investigation of the lattice helmet model. Two material investigations are conducted to provide the required data for the simulations. The respective publications are included in Chapter 4, and an overview summarizing which paper answers which research question is provided in Table 3.5.

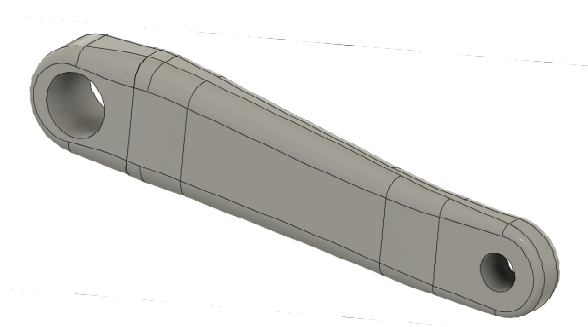


Figure 3.2: Bicycle crank arm geometry used for first investigation.



Figure 3.3: Bicycle helmet geometry used for second investigation.

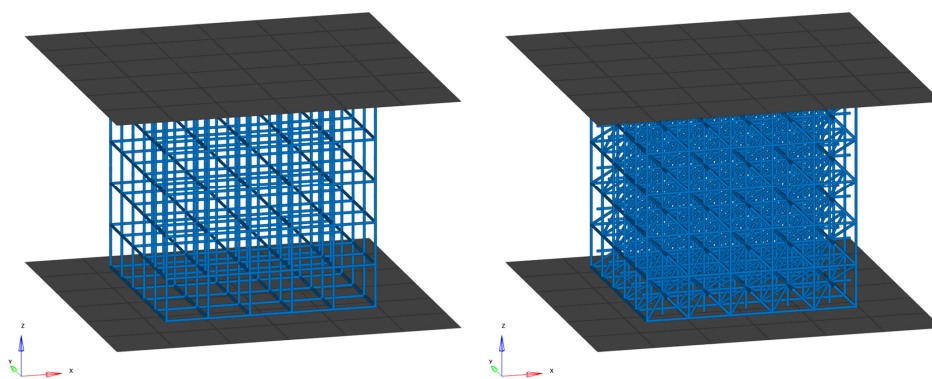
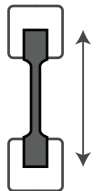
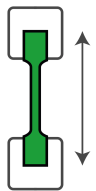
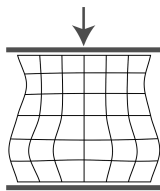


Figure 3.4: Cuboid lattice structures in compression used for auxiliary investigation.

Table 3.5: Overview of publication connections to research questions.

					
(Decker et al., 2020)	(Kedziora et al., 2022)	(Kedziora et al., 2023)	(Decker et al., 2023)	(Decker & Kedziora, 2023a)	(Decker & Kedziora, 2023b)
RQ1, RQ2, RQ3, RQ5	RQ3	RQ1, RQ2, RQ3	RQ3	RQ1, RQ3, RQ4	RQ1, RQ2, RQ4, RQ5

3.3 Scope

This thesis focuses on the creation of a lattice design, optimization, and manufacturing workflow suitable for engineering purposes, along with the improvement and assessment of appliances containing functionally graded lattice structures. It therefore requires a holistic approach covering the entire process from design inception, geometry creation, lattice type selection and evaluation, FEA

modelling, optimization method, material selection, manufacturing method, and physical testing. The selectable variety of material, method, appliance, and technique combinations is exceedingly vast, therefore a low-level investigation on each one's specific aspects or detailed behaviours is not feasible within this frame. Rather, a high-level view of the design chain with two applied examples is targeted to achieve the presented goal.

3.4 Lattice Optimization Method & Application

The proposed method aims to offer true spatial optimization for lattice structures regardless of the optimization goal or use case. Simultaneously, it retains the versatility and usability of engineering methods by allowing the consideration of complex modelling features (e.g. crash modelling, material failure, buckling) and ensuring the possibility to extract the results for production. It makes use of established simulation and optimization tools to remain versatile. For demonstration purposes, the simulation suite Altair HyperWorks with its structural solvers OptiStruct (implicit solver for non-/linear static and dynamic models) and RADIOSS (explicit solver for highly nonlinear dynamic models of short duration) are used in conjunction with their general optimization suite HyperStudy. The simulation tools are generally interchangeable with any other appropriate contender.

First, a short overview of finite element representation and their property handling by solvers must be laid out. After having chosen a suitable part for consideration and creating its accompanying lattice in nTop, it is exported in a file format readable for structural simulation solvers for the model setup. Different geometrical discretization methods are possible for geometries. Thick-wall geometries that are roughly the same size in every dimension are generally modelled by solid elements (see Figure 3.7). Thin-wall geometries with large spans in two dimensions and a thin third dimension are represented by shell elements (see Figure 3.6 and surface lattice in Figure 3.8), while geometries that are thin in two dimensions and large in the third can be modelled via beam elements (see Figure 3.5 and the strut lattice Figure 3.9). Surface lattices are usually thin enough to be modelled by shell elements, while strut lattices are best modelled by beam elements. Solid elements can generally be used for these purposes as well, but due to the complexity of the geometry, a very large number of elements must be used, which increases computational efforts. Furthermore, solid elements do not lend themselves well to the optimization procedure presented in this project, as will be evident later.

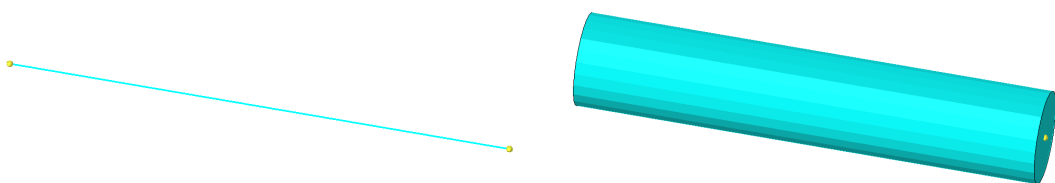


Figure 3.5: Beam element without (left) and with thickness property representation (right).

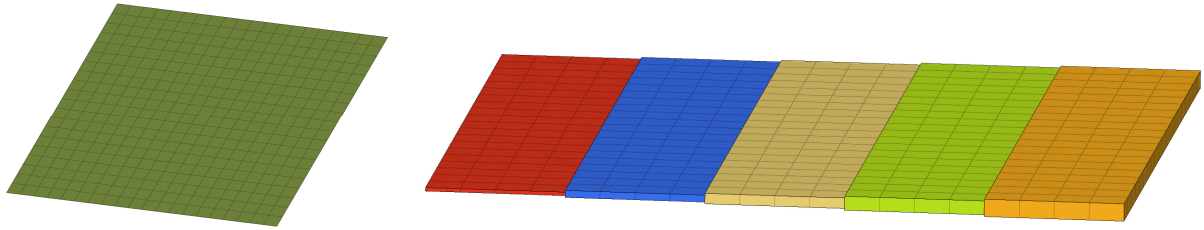


Figure 3.6: Shell element representation without thickness representation (left) and with discrete thickness steps (right). The colours of the elements in the right image correspond to their respective property collector, underlining that they have different thickness properties.

Solid elements do not possess such a thickness property, but rather discretize the geometry entirely by their shape. Consequently, they cannot be used with this approach. In principle, shape optimization of the element nodes on the outside of a lattice part could achieve the same, but this is also impractical in many regards.

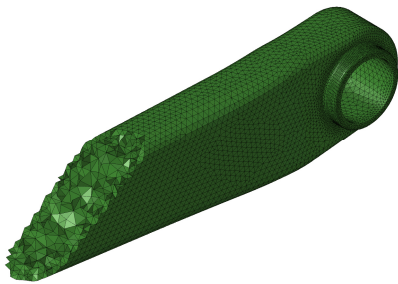


Figure 3.7: Thick body of a bicycle crank arm modelled with solid tetrahedral elements.



Figure 3.8: Surface lattice represented by shell elements (green), with the thicker surrounding body being modelled with solid elements.

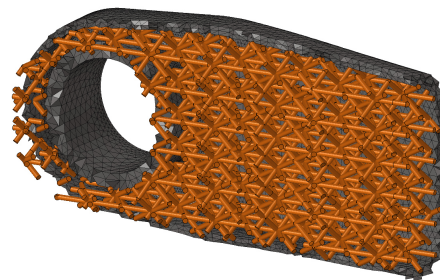


Figure 3.9: Graph lattice represented by beam elements.

Beam and shell elements simplify the original geometry they intend to model by reducing the real dimensions of a part. Shell elements model plate-like geometries only by their middle surface since these elements themselves do not possess any thickness. Similarly, beam elements represent long and slender structures like a pole only by its middle axis, such that it is reduced to a line. Both element types are assigned a thickness property that is a separate entity from the element. The beam elements additionally require a cross-section property defining information about their shape (circular, quadratic, hexagonal etc.). Elements with the same properties are grouped together, each group having only one thickness value. This entails that there can be no continuous thickness variation in a part

modelled by these element types, only discrete steps. While continuous thickness variations can be approached in principle by applying many small steps, it quickly becomes impractical and should be avoided.

With this in information mind, parts of the structure of a solver input file also must be explained. A solver input file is a human-readable text file containing all the information of a simulation model, such as the node coordinates, element connectivity, boundary conditions etc. An example of a beam element property assignment is shown in Figure 3.10, where the thickness value is marked in red.

```

/PROP/INT_BEAM/4
prop_lattice
# Isect 5 Ismstr 4
# Dm Df
# NIP Iref Y0
# 0 0 0.0
# NITRS L1 1.0
# 9

/PROP/INT_BEAM/8
property8
# Isect 5 Ismstr 4
# Dm Df
# NIP Iref Y0 Z0
# 0 0 0.0 0.0
# NITRS L1 L2
# 9 {varname_8, %8.3f}

```

Figure 3.10: Beam element property section of input file, with the numerical value of thickness property marked in red (left) and its replacement variable definition (right).

This input file can be passed to a general optimization program such as Altair HyperStudy. It is not restricted to working with a specific solver or program. It can handle any input file, call a solver or other program, run it, and read its output. In short, it takes complete and automatic control over the solver. In HyperStudy, the variables to be altered for a screening or optimization run are defined via the input file. Their numerical value is substituted by a placeholder (compare Figure 3.10 left and right), where HyperStudy replaces the original numerical value with a different one chosen by the optimization algorithm. HyperStudy then runs a multitude of simulations in a loop during which it reads and interprets the output variables defined by the user, alters the variables accordingly, runs them again and so on until the optimization goal is met. The goals and constraints can be defined almost arbitrarily depending on the physics at hand: maximum stiffness at a given weight, minimizing peak acceleration, maximum energy absorption during compressive loading, minimizing weight at a given stiffness, maximizing heat transfer, minimizing displacement during vibrations etc.

Numerous optimization algorithms and approaches can be chosen based on the desired goals and requirements. Standard or global gradient-based response surface search methods, gradient-free methods such as the Genetic Algorithm, Multi-Objective Optimizations for treating opposing optimization goals and Design Exploration studies are available. One of the most useful tools to reduce computation time is the concept of Design of Experiment (DOE) studies together with response surface fit methods. In a DOE study, the model behaviour is observed and analysed by altering selected variables. Their values are specifically chosen such that the design space is adequately covered while limiting the amount of required solver runs. Additionally, the risk of confounding the effects of variables which change simultaneously is minimized. Each variable's influence is assessed and quantified. Next, a response surface fit is built which approximates the actual model's behaviour based on existing data. This response surface can then be used to optimize the model's parameters instead of executing a multitude of solver runs. This allows to perform an optimization in seconds rather than hours or days, however a response surface fit can only be built if the model behaviour is reasonably

predictable. Highly nonlinear models are not always suitable, in which case it must be optimized by executing a solver run for each iteration.

Now that the optimization route is established, the lattice geometry to be analysed must be prepared for spatial thickness altering. As mentioned, the thickness value of shell or beam elements can only be applied to groups of elements. Therefore, the lattice must be split into easily manageable chunks. The splitting operation can be performed by a simple manual separation of elements into different groups, either in Altair HyperMesh or in nTop. A second method is to split the lattice with the aid of a programming script and a field function. The procedure is demonstrated with the aid of three applications. The first is a bicycle crank arm optimized for maximum stiffness in a typical load case. The second is an auxiliary model of a lattice cube in large-strain compression. The third is a bicycle helmet optimized for minimum injury risk during a crash event. The optimization and lattice splitting method is applied to each with gradually increasing complexity levels.

The first analysis treats the implementation and optimization of a graph lattice structure in a hollow bicycle crank arm with realistic geometry. Its thickness is optimized for maximum rigidity with consideration of stress and mass constraints (c.f. section 4.1). The initial investigation serves to test the methods' suitability for the task, hence a simple manual splitting approach of the beam mesh performed in HyperMesh was chosen. The elements are grouped such that planar symmetry is inherently considered as indicated by their group colours. The investigation is continued and refined with the same crank geometry now incorporating a shell lattice (c.f. section 4.3). It is separated into discrete regions in HyperMesh through a TCL/TK script (see Addendum, section 7.4). A field function segregates the elements into bins following the expected stress field produced from the considered load case. The lattices resulting from these approaches are shown in Figure 3.11.

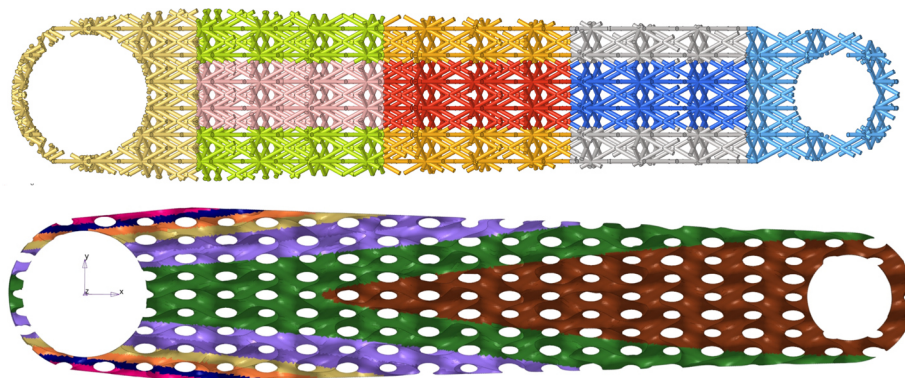


Figure 3.11: Manual (top) and scripting-aided splitting (bottom) of lattice geometry.

After having split the lattice in a suitable fashion, different options for their thickness values can be chosen. The simplest is to only define upper and lower thickness boundaries and let the optimization routine run its course, as was the case with the aforementioned study investigating the crank arm. While this potentially gives the best result, it also requires the highest amount of computational effort. Every single lattice group is treated as an optimization variable, and the thickness may take on any value in its range. An alternative is to restrict the thickness values to discrete values, i.e. dividing the thickness range into n steps. For example, the value may be allowed to change between 1mm and 2mm with steps of 0.05mm. To further reduce the number of optimization variables, one can make use of

any planar or cyclic symmetry present in the geometry as shown in Figure 3.11. The discrete regions can either be put in the same group in HyperMesh, or alternatively be linked in HyperStudy such that they are assigned the same thickness value.

Linking different regions via a mathematical function can further reduce the number of optimization variables. One such example can be the linking of neighbouring lattice regions via a function taking into consideration their relative position. The thickness can then be defined as a linear, quadratic, power law, or other function such that only two or three optimization variables need to be considered. The computational efficiency can be greatly increased without sacrificing parts of the model complexity. This concept is explored in the second analysis (c.f. 4.5, where a cuboid lattice is split into ten separate regions. Each region's thickness is controlled by a function where the independent variable is the lattice's distance from the origin as depicted in Figure 3.12. The investigation serves as demonstration for an avenue to reduce computation time, and to explore the optimal thickness distribution of such a lattice in large-strain compression. The structure is optimized for maximum specific energy absorption, and its maximum weight is constrained to that of a uniform lattice for comparability.

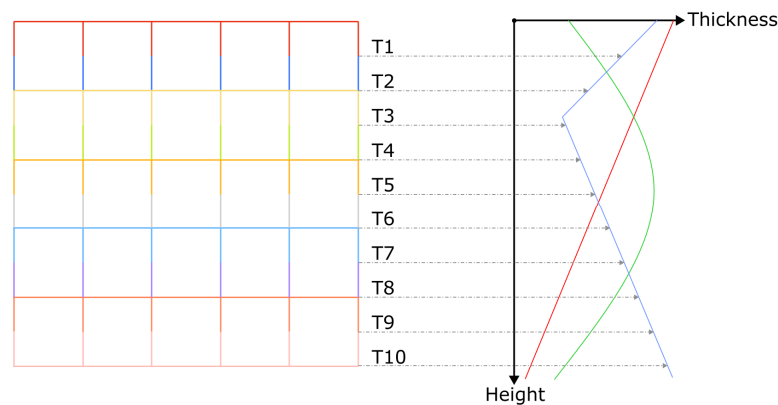


Figure 3.12: Regions of lattice structure being linked via mathematical function to reduce computational efforts during optimization.

The last investigation assembles the previously acquired knowledge and applies it to a realistic bicycle helmet in a crash scenario. Replacing the commonly used foam liner, a conformal lattice is introduced as energy absorption device (c.f. section 4.6). It is split in HyperMesh via a TCL-TK script segregating the beam elements based on their distance from an ellipsoid surface (see Addendum, section 7.3) such that the splitting pattern resembles the helmet's shape as shown in Figure 3.13. In addition, the lattice's thickness distribution is governed by a quadratic function taking into account each lattice group's distance from the model's origin point. The thickness distribution is optimized such that the wearer's injury risk is minimized.

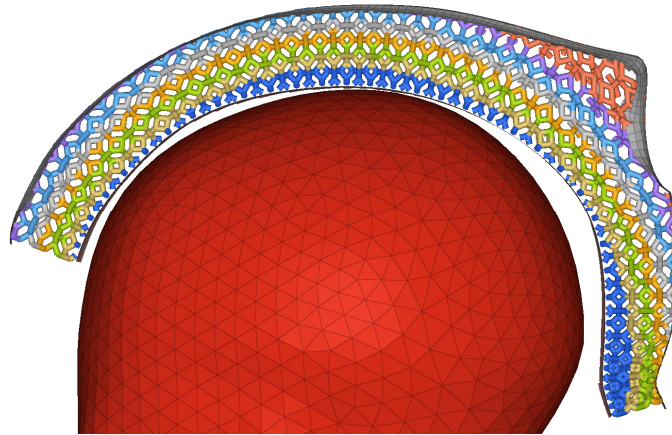


Figure 3.13: Helmet with segregated lattice whose thickness is governed by a quadratic function.

The method is summarized in the flowchart given in Figure 3.14. A CAD model is imported to nTop where it is hollowed and fitted with a lattice. The lattice is exported to HyperMesh as STL or FE mesh and prepared for the simulation. If the lattice was not already split in nTop, it is performed here. The lattice's elements are grouped into their respective components and exported to a solver input file upon completion of the preprocessing step. It is imported into HyperStudy, the lattice's thickness values are parameterized, and computational tasks such as DOE runs, potentially response surface fits, as well as optimization runs are performed. The results then have to be reassembled in nTop to create geometry files for manufacturing. If the lattice was initially split in nTop, the resulting lattice thickness values can simply be applied there. If the splitting was performed in HyperMesh, a conversion script is required to produce a lattice file readable by nTop. Afterwards, an STL file of the optimized geometry can be exported to a slicer of choice for manufacturing.

The structure of nTop's user interface allows a workflow resembling visual programming, where different design operations are linked by function blocks. In conjunction with template models built in nTop, HyperMesh, HyperStudy, and the conversion scripts for importing and exporting, most of the operations can be entirely automated. Very little user input is then required, for example to change the lattice type or density in nTop, to assign the correct components and FE properties in HyperMesh, and to parameterize the solver input files in HyperStudy. Different lattice designs can then be quickly iterated, simulated, and optimized.

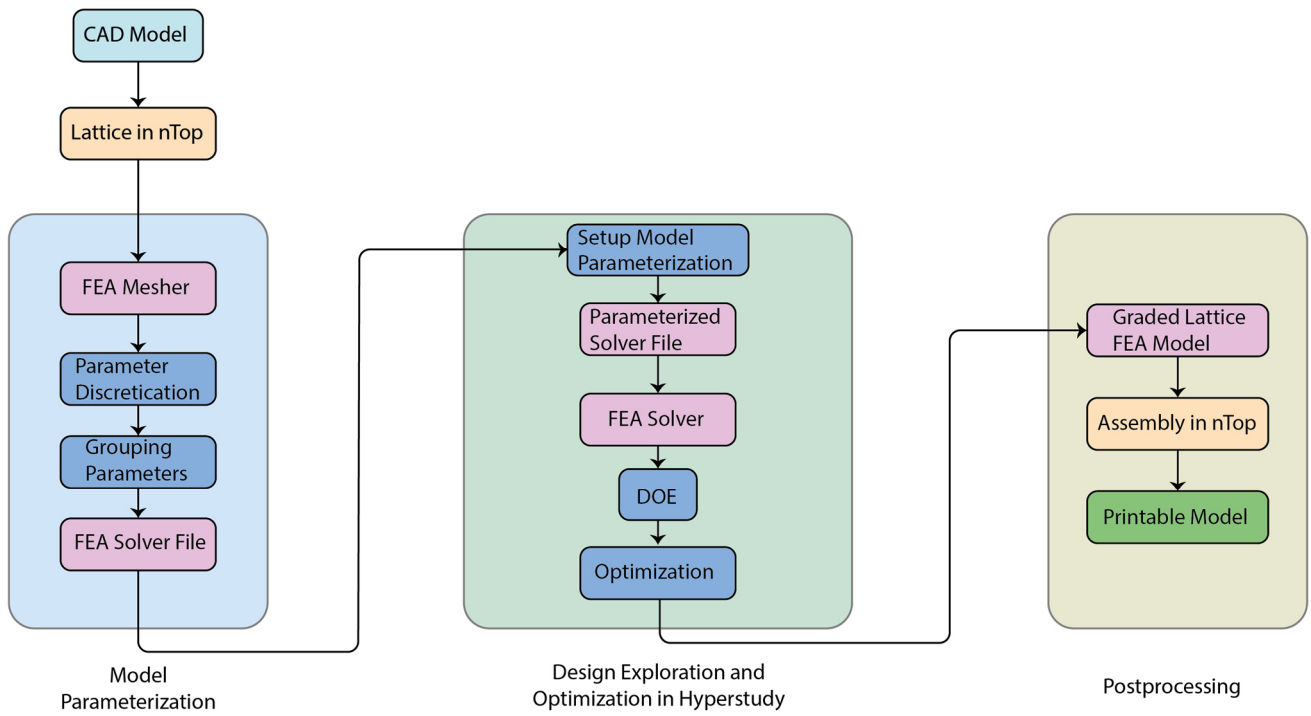


Figure 3.14: Flowchart outlining the optimization method and its components.

4 Publications

The following section presents the publications produced during the course of the doctoral studies in chronological order. Each publication is preceded by a summary of its motivation, achievements, and advancements over existing literature.

4.1 Graded Graph Lattice in a Bicycle Crank Arm

This publication titled *Practical Implementation of Functionally Graded Lattice Structures in a Bicycle Crank Arm* (Decker et al., 2020) serves as a first test and demonstration of the devised workflow and lattice optimization method, which are expanded upon in subsequent projects. The literature review conducted at the initial stage of the doctoral studies (c.f. Chapter 2) revealed that the majority of publications in the lattice research space focused largely on investigations of synthetic tests with simplistic lattice-filled geometries or only concentrated on lattice optimisation procedures with no regard for manufacturing. Therefore, the aim was to expand on these studies by considering a realistic workflow from the CAD design stage, introduction of a lattice structure to the part, its optimisation with engineering tools, to the manufacturing of the physical part.

The part and material choice was taken under consideration of the local manufacturing possibilities with the Markforged Metal X additive manufacturing system installed at the University of Luxembourg. It was not yet operational at the time of writing and publishing; the scope of the paper was thus limited to its simulative aspects. Material properties of 17-4 precipitation-hardened steel as reported by the manufacturer's data sheet were utilized as no studies covering its tensile and fatigue properties were available at that time due to the system's novelty. A bicycle crank arm was chosen for this study as it fits the Metal X's build volume and sintering oven size. It is compared to a commercially available aluminium crank arm produced by Shimano (model FC-R450-453). Using an aluminium or titanium variant for production of the lattice crank would have been preferred for better comparability, but these options were not available for the Markforged system during the project's course.

The hollowed crank geometry was filled with every suitable lattice type available in nTop. Each model was simulated in a linear static load case following the EN ISO 4210-8 standard. The two best-performing lattice types (Face-Centred Cubic and Re-entrant) were chosen for the optimization step based on their resulting crank displacement ranking. Before the optimization, the influence of the lattice's orientation and cell size on the maximum displacement were investigated via manual alterations (see section 7.5 in the addendum for additional pictures) and applied. After having found the best combination, each lattice was manually split into separate, symmetric regions. The beam elements' thickness parameters were then used as optimization variables in Altair HyperStudy and optimized for maximum stiffness with weight and stress restrictions. A Design of Experiment (DOE) study was executed to create a surface fit used for the optimization step to save on computational time. For validation of the model, the optimized geometries were meshed with solid elements and compared. As a result, the crank arms with optimized lattice structures achieved a 64% (Face-Centred Cubic) and 67% (Re-entrant) higher stiffness-to-weight ratio than the aluminium crank arm.

The author contributed to this paper by creating the optimization method, performing the design, analysis, and lattice optimization study, conducting data analysis and visualization, writing the original document draft, performing the review and editing, and presenting the work at the conference.

Practical Implementation of Functionally Graded Lattice Structures in a Bicycle Crank Arm

THIERRY DECKER, SLAWOMIR KEDZIORA, CLAUDE WOLF

Faculty of Science, Technology and Communication
University of Luxembourg, 6 rue Coudenhove-Kalergi
L-1359 Luxembourg City, Luxembourg

Abstract: Functionally graded lattice structures (FGLS) were studied thoroughly for the past years, mostly focusing on specific synthetic tests in the context of additive manufacturing while rarely being actually applied outside of this specific domain. This paper examines a way to practically implement them in a commonly used appliance and study their potential for its improvement. A bicycle crank arm was chosen for this purpose, and a solid aluminium reference model (Shimano FC-R450-453) is used as a performance baseline. The novel design is composed of a hollow body containing a beam-based, non-stochastic, functionally graded lattice structure and is planned to be manufactured on a Markforged Metal X system using 17-4 PH stainless steel. It aims to increase the total stiffness under EN ISO 4210-8 norm loading conditions compared to the reference model while limiting mass and stress values to acceptable degrees. Two crank arm variants, containing a face-centred cubic (FCC) and re-entrant auxetic lattice respectively, are optimised by locally altering their beam radii in eight separate regions. The displacement at the load application point is minimised using Altair OptiStruct and HyperStudy. The reference crank, weighing 213g, exhibits a deflection magnitude of 7.1mm in the most demanding load case while the newly designed and optimised versions only showed displacements of 2.52mm (FCC lattice, 340g) and 2.58mm (re-entrant lattice, 339g) respectively. In addition, the stress distribution was significantly enhanced compared to the reference model, as the latter would not pass the fatigue tests required by the norm. This demonstrates that FGLS, in combination with high-strength materials and additive manufacturing, can increase the performance of many parts, although in this case, with a trade-off in terms of its mass. In future projects, it might be considerably reduced by utilising alternative lattice types lattices or other materials while preserving the benefits of FGLS.

Keywords: Additive Manufacturing, Functionally Graded Lattice Structures, Design Exploration, Finite Element Method, Cellular Structures

1 Outline

1.1 Introduction

Additive manufacturing (AM) is being adopted rapidly across many scientific and industrial domains as it enables completely new design approaches, material blends, and manufacturing flexibility. It democratizes manufacturing rendering it available to small businesses and, in the case of plastic AM machines, even to individual persons thanks to its easy accessibility and steadily decreasing costs. High-performance metals, ceramics, fiber reinforced plastics, and even biological materials fit for AM are researched heavily, gradually improving their properties and ease of use. Furthermore, novel artificial structures like cellular solids emerged mimicking light-weight, porous configurations commonly found in nature, e.g., in cancellous bone or fungi mushrooms. They can be constituted of beams or surface-based unit cells and were coined functionally graded lattice structures (FGLS) as they exhibit locally varying mechanical properties adapted to the requirements. They fall in the category of mechanical metamaterials, the behaviour of which is mostly defined by their structural layout rather than their base material. These can be tailored to exhibit specific characteristics like exceptionally high strength-to-weight ratio, energy absorption, negative Poisson's ratio [1] (in that case called auxetic structures), or negative thermal expansion coefficient [2]. Although many scientific analyses study the behaviour of FGLS and demonstrate their potential, they predominantly focus on synthetic assessments like vibration [3], impact [4], compression [5], or heat exchanging properties [6]. This situation makes reports on their implementation of real-world parts scarce, which this paper aims to remedy. Our hypothesis is that combining FGLS with high-performance materials in a common mechanical appliance can significantly improve its performance compared to a generic solid counterpart produced by conventional manufacturing means. For this purpose, a bicycle crank arm was chosen. The aim is to design a crank arm fit for use on mountain bikes with a functionally graded lattice structure core surpassing the stiffness of a conventional crank arm. It is to be optimised for maximum stiffness while limiting stress and weight values to acceptable levels. The widespread use of bicycle cranks makes them an approachable demonstrator, and their size is suitable for the AM machine at hand: a Markforged Metal X system.

1.2 State of the art

While unit cells and their composition as FGLS currently are a vibrant research topic, their properties are largely investigated in an isolated manner rather than holistically and their industrial use is still a rare occurrence. Comprehensive overviews are provided in [2], [7] and [8]. Custom-written code or elaborate, manual CAD operations are often used to generate specific lattices since only few software suites exist to handle the needs of researchers and engineers alike, mostly offering a limited number of options to manipulate lattice properties [7]. Relevant software suites like Autodesk Netfabb or Ansys SpaceClaim mainly offer basic lattice creation and modification tools with optional local density grading capabilities. A novel, more advanced approach is pursued by nTopology Platform providing significant advantages in terms of its lattice manipulation capabilities, ease of use and design iteration speed [9]. Industrial case studies show potential for improvement in performance and weight in various applications (see [10], [11], [12] and others). Lattice structures in additively manufactured parts also start to be applied in bicycling appliances. Some examples include polymer saddles [13], titanium crank arms with varying wall thicknesses [14], or frames consisting of steel or titanium lugs combined with carbon fiber reinforced polymer tubes [15]. The lattices used in these cases appear to be uniform in nature rather than functionally graded.

2 Materials and Procedure

2.1 Materials

Inexpensively produced bicycle crank arms are commonly forged using 6061-T6 aluminium, as is assumed to be the case with the chosen Shimano crank model. The new crank design containing the lattice will, in a first iteration, be made of 17-4 PH stainless steel available for the Markforged Metal X system at hand. This choice was made as it was the only complete property dataset available for base materials provided by Markforged. Aluminium or titanium would have been the preferred material for this endeavour, but are not yet available for the Markforged Metal X system. The mechanical properties of 17-4 PH SS manufactured via SLM have been investigated thoroughly (see [16], [17]); however, at the time of writing and to the authors' knowledge, no independent studies confirming the material data provided by Markforged seem to be publicly available. Table 1 specifies the material properties used hereafter.

Property	17-4 PH SS as sintered	Aluminium 6061-T6
Ultimate Tensile Strength [MPa]	1050	310
0.2% Yield Strength [MPa]	800	276
Elongation at Break [%]	5	17
Tensile Modulus [GPa]	140	68.9
Density [g/cm ³]	7.5 – 7.8*	2.7
Poisson's ratio [∕]	0.27**	0.33

Table 1: Material data of Markforged 17-4 PH SS [18] and aluminium 6061-T6 [19]. *For FE models, a density of 7.8 g/cm³ is chosen. **No Poisson's ratio is given by Markforged and is thus substituted by the value provided in [20].

2.2 Lattice design and optimisation procedure

The solid aluminium crank arm model used for reference is a Shimano FC-R450/453, originally mounted to a Giant Anyroad 2 bicycle from 2015. It was mainly chosen as its shape, partly resembling a C-beam, is typical for models produced at high volume and low cost. The crank models for this paper were designed in Autodesk Fusion 360, whereas the lattice structures are generated in nTopology Platform. It allows for fast lattice generation and manipulation as it does not rely on a boundary representation approach for bodies like traditional CAD software suites, but is based on mathematical functions [9]. To determine a suitable lattice structure, the new hollowed steel crank is analysed by replacing its void space with a non-stochastic, beam-based volume lattice and tracing its displacement magnitudes during a typical bicycling loading condition. The performance of each fitting lattice-type available in nTopology Platform is tested separately via the built-in FEA module. The script-like structure of its functionalities allows for quick design changes without repeating tasks like Boolean operations on bodies, meshing, or connecting nodes of solid and beam meshes manually for each design variant. Thus, these tests are exclusively conducted in nTopology Platform. In an initial approach, all lattices exhibit a uniform beam diameter, constant cell size and the lattice orientations coincide with the cartesian coordinate system at hand. The two stiffest lattices showing a weight reduction of at least 80% compared to the negative body, if it were wholly occupied by steel, are retained for further analyses. To gain a marginal weight advantage, their cell sizes are subsequently increased along the longitudinal (Y) crank axis as it is expected not to affect the stiffness drastically. Afterwards, the lattices are rotated about the Y-axis to determine the orientation offering the lowest total compliance. Subsequently, the lattices are partitioned into eight regions, the radii of which are individually optimised for minimal compliance using Altair HyperStudy. As a final verification step, the optimisation results are implemented on both crank arm variants fully discretised by solid elements. Instead of optimising every single beam diameter, as is feasible within Altair OptiStruct, only eight regions have been chosen. Postprocessing becomes very resource-intensive as the number of individual diameter values increases, it is, therefore, preferable to limit them to a sensible amount. In addition, exporting these results for actual manufacturing is only feasible with the third-party software Materialise 3-matic, which is not available to the authors at the moment of writing.

3 Model Description

3.1 CAD Models

3.1.1 Aluminium crank model

The digital replication of the available Shimano crank arm (see Fig. 1) amounts to a weight of 213g, whereas the physical model weighs approximately 225g. For simplification purposes, the exact thread geometry for mounting the pedal as well as the spline joint geometry were neglected. Both are modelled as cylinders causing most of the weight difference between the real and replicated model. The surrogate cylinder diameter for the pedal mount thread is equal to 12.954mm (0.51 inches), i.e., the chosen minor diameter of a

9/16"x20 tpi UN 2B thread common for pedals. The diameter of the cylinder replacing the shaft mount spline is equal to 22mm, i.e., the outer diameter of the shaft geometry. The cylinder centres are 170mm apart – a dimension commonly referred to as the crank length in cycling jargon.

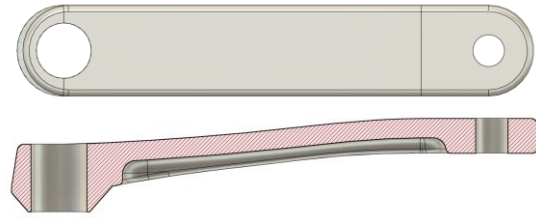


Fig. 1: Front and section view of aluminium crank model with its shaft bore (left side) and pedal bore (right side).

3.1.2 Hollow steel crank model

The new design follows the same dimensions and spacing for functional surfaces as the Shimano model, but is rendered hollow with a wall thickness of 1.6mm (cf. Fig. 2). It is assumed that lower values might compromise manufacturability; thus, a conservative approach is chosen. At the pedal and shaft mounting cylinder surfaces, the thickness is increased to 3mm for strength purposes resulting in a total mass of 276g. A negative body of the inner volume is created via Boolean subtraction in order to generate the volume lattice in nTopology Platform and to track the relative weight reduction. The negative body, weighing 604g, is sectioned into 8 regions for the purpose of generating separate beam sections for the optimisation procedure.

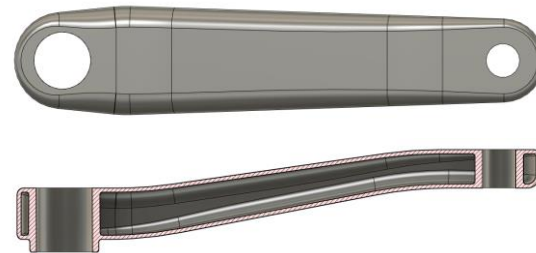


Fig. 2: Front and section view of hollow steel crank model.

3.1.3 Volume lattices

The lattices selected for further analyses consist of re-entrant auxetic and face-centred cubic unit cells. Fig. 3 illustrates the volume lattices, replacing the negative body, with their sectioning and naming scheme after manual alterations were performed. The sectioning is carried out such that the lattices always remains symmetrical about the Y plane, meaning that sections on opposing sides of the lattice exhibit the same beam diameter. Thereby, the number of regions per lattice type to be optimised is kept at a manageable level. Since the lattice's spatial extent along the Z-axis is small compared to its other dimensions, sectioning is only performed along the X and Y axes.

3.2 Load cases

All crank models are loaded according to EN ISO 4210-8 for mountain bikes (see [21]). The forces are induced at a distance of 65mm from the crank's outer surface simulating the cyclist's force acting on the pedal centre, termed point P. The shaft mounting cylinder is rigidly constrained to emulate the shaft connection. Load case 1 defines a force of 1500N acting perpendicularly to the horizontally positioned crank arm. According to the norm, a gear reduction between the smallest chain wheel (front) and the largest sprocket (rear) may be considered, which reduces the applied force proportionally. A gear ratio of 0.8 was chosen in this instance,

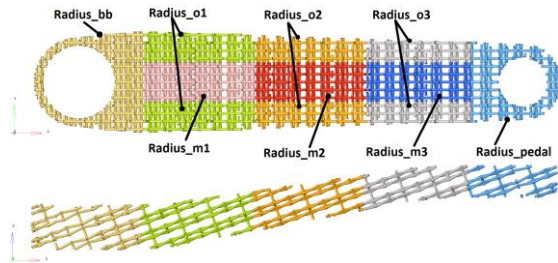


Fig. 3a: Front and top views of re-entrant volume lattice.

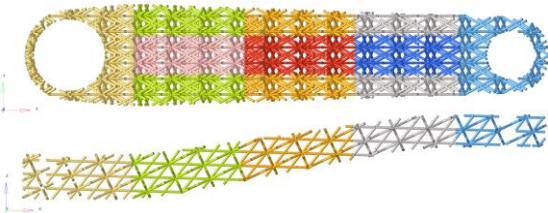


Fig. 3b: Front and top views of face-centred cubic volume lattice.

yielding a force of 1200N. Load cases 2 and 3 specify a force of 1800N acting on the crank without considering any gear reductions, while the crank arm is rotated to angles of 45° and 30° to the horizontal plane, respectively. Although load cases 2 and 3 are intended as fatigue tests with 50.000 load cycles, they are conducted as static tests. Including a fatigue assessment would surpass the scope of this paper, and no fatigue data for 17-4 PH SS produced by this particular manufacturing method is available at the time of writing.

3.3 FEA Models

3.3.1 Model setup in nTopology Platform

In order to create a suitable lattice structure, the negative crank body is replaced by a volume lattice. The hollow crank body is meshed using circa 298.000 second-order tetrahedral elements with an element edge length of 1mm, ensuring the presence of at least two elements across thin walls. The lattice is discretised by second-order one-dimensional beam elements without subdivisions, i.e. all lattice nodes are connected by one single beam element. To determine a suitable lattice configuration, the displacement response of the steel crank body is logged while its lattice properties are altered sequentially. All FE models are carried out as linear static analyses, no nonlinear geometrical or material behaviour is considered. Load case 1 is applied for this initial testing setup. Since the system behaviour remains entirely in the linear domain, its response to the lattice modifications is assumed to be qualitatively similar for the other two load cases and can, in consequence, be extrapolated. In order to connect the beam and solid meshes, all beam element nodes within a distance of 0.5mm to the solid body are coupled.

3.3.2 Model setup in Altair OptiStruct

Using HyperMesh, the aluminium crank model is meshed with 485.000 second-order tetrahedral elements while the hollow steel crank body is discretised by approximately 328.000 second-order tetrahedral elements. Edge lengths range from 0.4mm to 2mm with at least two elements across thin solid walls. Identically to the models in nTopology Platform, the lattice meshes constitute of second-order beam elements with a circular cross-section and no subdivisions. They were exported to HyperMesh/OptiStruct by means of a custom MATLAB script directly converting them to an OptiStruct input file. All calculations are executed as linear static analyses as well. Regarding the boundary condition interfaces, the nodes on the shaft mounting cylinder surface are rigidly constrained (RBE2 connection) at its centre while the node at point P is coupled via an interpolating connection (RBE3), distributing the load to the nodes on the pedal mounting cylinder surface. In the case of the

hollow crank models, all beam element nodes within a search distance of 2mm to the crank body are coupled to it by a tie contact. All six degrees of freedom are tied to the movement of the contact master surface on the interior surface of the crank. The slave node adjustment algorithm is set to automatic mode and the contact discretisation type to node-to-surface.

3.4 Numerical optimisation in Altair HyperStudy

To determine the ideal local radii dimensions for the lattices to be analysed, both hollow crank models previously set up in OptiStruct are subjected to an optimisation analysis in Altair HyperStudy. In order to reduce the extent of this paper, only load case 2 is considered for the optimisation since it induces the highest displacement magnitude. For each of the two lattice variations, the beam radii are established as input variables, starting with a uniform radius of 0.5mm and an allowable continuous range of 0.4mm to 1mm. These limits are chosen for ease of manufacturability and to prevent blending of thick beams at their junctions. Four output responses are defined: the maximum displacement magnitude at point P, the total mass, as well as stress values of the solid and beam meshes. To avoid taking outlier stress values into consideration, the mean von Mises stress value plus four times its standard deviation is defined as output response for both lattice and solid bodies. This approach ensures that approximately 99.9936% of all stress values fall inside the specified limit. In this particular case, the outlier values stem from physically not valid stresses caused by the contact interface between the lattice and solid body. A Design of Experiment (DOE) study is conducted using the *Modified Extensible Lattice Sequence* (MELS) method for design space exploration with 50 runs as recommended by HyperStudy. In order to cut calculation time, a response surface using the *Fit Automatically Selected by Training (FAST)* option is then generated to feed into the subsequent optimisation. For the latter, the *Global Response Search Method* (GRSM) is used. The optimisation goal is to minimise the displacement magnitude, while the total mass is limited to 360g. This corresponds to an approximate mass increase of 30% compared to the hollow steel cranks mass without a lattice component. In addition, the stress responses are constrained to the desired upper bound of 320MPa, i.e., 40% of the yield strength as a conservative estimate of the materials' fatigue strength. Values of 400MPa are still deemed acceptable in postprocessing of the final models. For all optimisation constraints, the *Standard Constraint Enforcement* option is active accepting results within 0.5% of the specified limits. The optimised values based on the response surface are verified in OptiStruct as a blend of solid and beam elements before proceeding to the last step.

3.5 Crank models fully discretised by solid elements

In two final analyses, the crank bodies as well as the lattices are completely discretised by solid elements and simulated using Altair OptiStruct in order to check their performance when issues at the contact interfaces between beam and solid elements are eliminated. Following the optimisation step, the optimised beam radii values are applied to the lattices in nTopology Platform, which are then merged with the hollow crank body using a 0.25mm fillet at their boundaries. Surface meshes with 0.25mm element edge length are generated by voxelizing the resulting bodies. The voxel meshes are then smoothed, exported as STL files and remeshed in HyperMesh to reduce the element count while preserving acceptable element quality. Both model variants are subsequently discretised by approximately 3 million second-order tetrahedral elements. The load case and load step setups are identical to the previous models, but element quality checks are disabled as the geometrical complexity hinders high-quality tetrahedral meshing without a substantial time investment.

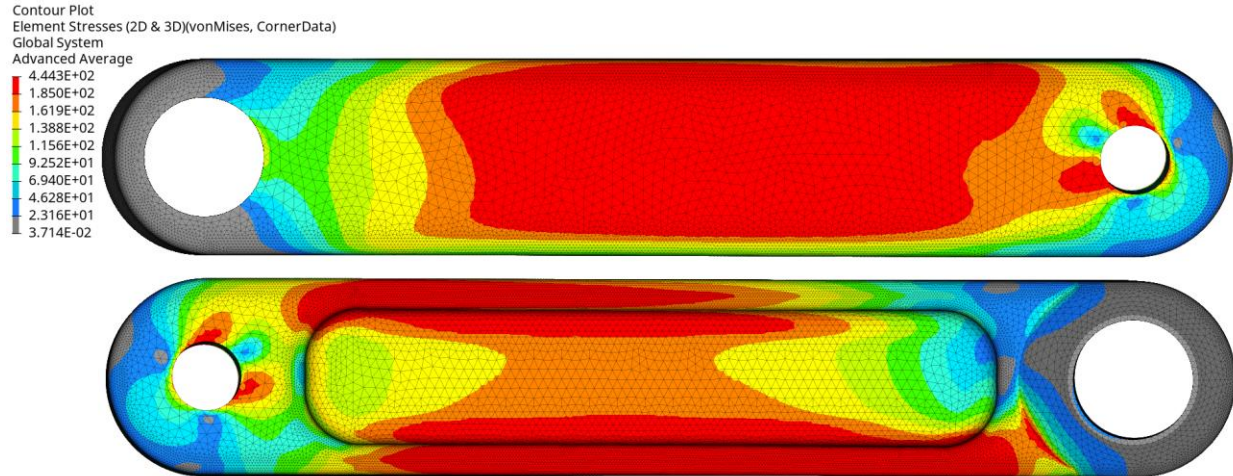


Fig. 4: Von Mises stress distribution of aluminium crank for load condition 2. Red zones show stress values above fatigue strength.

4 Results and discussion

4.1 Solid aluminium crank

The solid aluminium reference crank model calculated in OptiStruct shows the largest displacement magnitude of 7.1 mm at point P for load case 2. Significant portions of the crank body show stress values above the fatigue strength of 6061-T6 aluminium, cf. Fig. 4. According to tests conducted in [22], its fatigue stress limit at 50,000 load cycles amounts to approximately 185 MPa. Small regions even surpass its yield strength of 276 MPa.

4.2 Steel crank

4.2.1 Manual lattice alterations

Note: The displacement values of a point on which the remote loads are applied cannot be probed in the software version of nTopology Platform used for this study. The values in the following subsection thus report the maximum displacement magnitudes of the crank body, not of point P.

Starting out the lattice tests with load case 1 and a uniform unit cell with an edge length of 6 mm, the re-entrant auxetic and face-centered cubic (FCC) lattices show the least amount of displacement while offering more than 80% weight reduction compared to the solid negative body. This is equivalent to a maximum lattice weight of 120.8 g providing a suitable starting point for further weight reduction during the subsequent optimisation process. Both the FCC and re-entrant crank variants show a total deflection of 0.712 mm with a weight reduction of 84% and 81%, respectively. Evidently, the completely solid steel crank arm shows the lowest displacement of 0.255 mm, whereas the variant without any inner structure exhibits the highest displacement at a value of 0.797 mm. Testing shows that increasing the unit cell edge length in multiples of 6 mm up to 30 mm along the longitudinal axis offers marginal weight savings without significantly compromising the crank stiffness. The approach with 12 mm longitudinal edge length is chosen for further procedure as greater values might influence manufacturability. Rotating the lattice about its Y-axis yielded the best results at an angle of -25 degrees for the re-entrant and -20 degrees for the FCC lattice. The displacement magnitude of the FCC crank variant drops to 0.69 mm while it is reduced to 0.677 mm for the re-entrant variant. In OptiStruct, these values translate to displacement magnitudes of 0.667 mm for the re-entrant crank variant and 0.686 mm for the FCC crank variant, respectively. The displacement magnitude at the loading point P amounts to 1.57 mm for both crank variants.

4.2.2 Numerical optimisation results

The initial and optimised system response values for local beam radii, displacement, stress and mass for both steel crank variants are detailed in Table 2. They are not based on the response surface, but

on the verification models under consideration of load case 2 since it causes the greatest displacement values of all three load cases. All the design constraints are satisfied by the optimisation procedure, and although the solid and beam stress values of both models were slightly altered during the procedure, only partial improvements were achieved.

System response	Re-entrant		FCC	
	Initial	Final	Initial	Final
Radius_bb [mm]	0.50	0.47	0.50	0.64
Radius_o1 [mm]	0.50	0.52	0.50	0.54
Radius_o2 [mm]	0.50	0.50	0.50	0.49
Radius_o3 [mm]	0.50	0.43	0.50	0.43
Radius_pedal [mm]	0.50	0.47	0.50	0.49
Radius_m1 [mm]	0.50	0.41	0.50	0.40
Radius_m2 [mm]	0.50	0.40	0.50	0.59
Radius_m3 [mm]	0.50	0.46	0.50	0.40
Displacement [mm]	2.59	2.61	2.57	2.55
Solid stress [MPa]	311.7	313.5	309.8	307.9
Beam stress [MPa]	248.5	261.8	221.7	223.2
Mass [g]	369	357	355	360

Table 2: System response values in load case 2 for both crank variants before and after optimization.

4.2.3 Crank models fully discretised by solid elements

The final displacement magnitudes are slightly lower in comparison to the previous models, amounting to 2.58 mm for the re-entrant lattice crank variant and 2.52 mm for the FCC lattice crank variant. Locations exhibiting high stress values generally coincide well with the previous results, though the stress concentration issues occurring at the contact interfaces naturally were eliminated. The upper stress limit of 320 MPa is locally surpassed, specifically near the pedal and shaft bores models as displayed in Fig. for the crank variant with re-entrant lattice. The high stress regions at the aforementioned locations are slightly less pronounced in the crank variant with the FCC lattice. Stresses in the re-entrant crank variant do not exceed 400 MPa except at locations with bad element connections at some beams junctions, which are due to the smoothing and remeshing procedure. Thus, they are not physically valid and can, therefore, be neglected. The FCC variant, on the other hand, displays three regions at beam junctions near the pedal mounting area where the von Mises stress values surpass 400 MPa, reaching up to 490 MPa as shown in Fig. 6. Both models show stress singularities at the edge of the boundary condition interface of the pedal mounting cylinder, which are physically not valid as well. The total crank weights

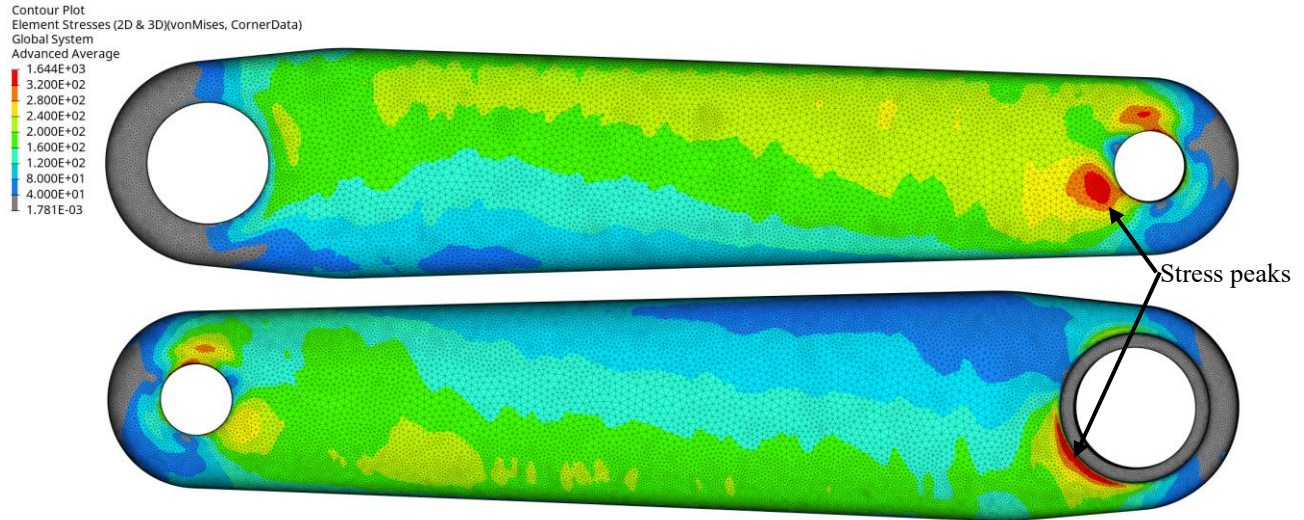


Fig. 5: Von Mises stress distribution of final crank version with re-entrant lattice. Stress values surpassing 320MPa are coloured in red.

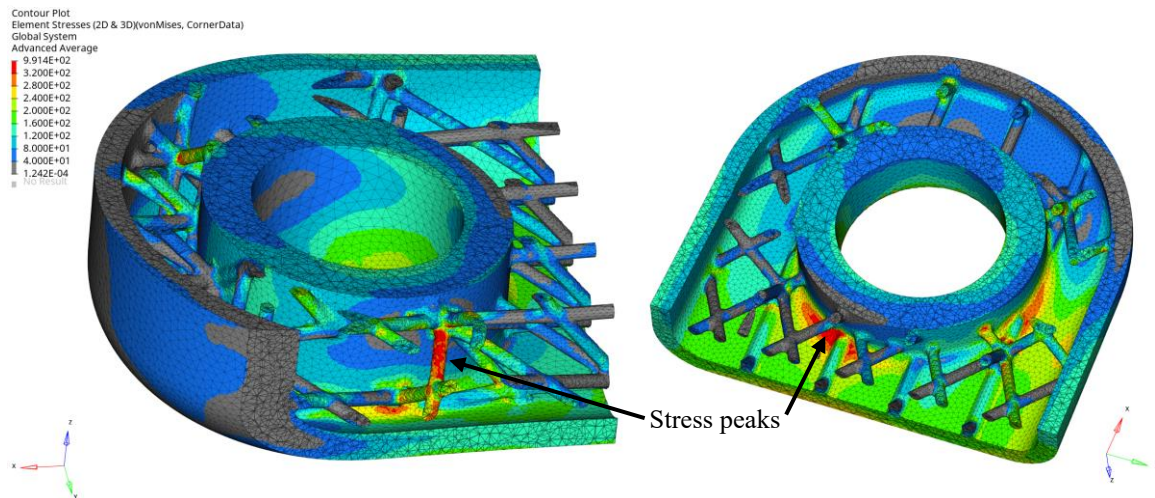


Fig. 6: Von Mises stress peaks of up to 490MPa at pedal bore of final crank variant with FCC lattice. Stress values surpassing 320MPa are coloured in red.

amount to 339g for the re-entrant variant and 341g for the FCC variant. The weight differences to the previous models consisting of solid and beam elements are due to the fact that previously overlapping beam and solid elements are now merged.

4.3 Test prints using FDM

To assess whether the lattice structures are indeed manufacturable using AM, test prints were conducted on an Ultimaker 2 Extended+ FDM machine using the finalised version of the FCC crank variant.

Prints using a 0.4mm nozzle and PLA filament showed significant stringing issues and poor beam surface quality at first, especially on their underside. Adjusting the part orientation almost vertically, lowering the print speed, enabling retraction and combing options and, most importantly, reducing the layer height to 0.06mm as well as using a 0.25mm nozzle amongst other minor adjustments netted acceptable results after approximately 80h of printing time as depicted in Fig. 7. Evidently, FDM and ADAM techniques are not entirely comparable and the results of these tests cannot be simply



Fig. 7: FDM test print of final crank variant with FCC lattice, accomplished on an Ultimaker 2 Extended+ using a 0.25mm nozzle and PLA filament.

extrapolated to the Markforged Metal X system. However, the material deposition method is quite similar and the tests might point to difficulties that might occur, especially concerning issues with printing orientation and the need for support structures which are inherently more pronounced in ADAM.

4.4 Discussion

The solid 6061-T6 aluminium crank model was digitally recreated and analysed under EN ISO 4210-8 load conditions. Afterwards, the performance of the redesigned hollow crank made of 17-4 PH steel containing an optimised functionally graded lattice structure was compared to the original one. Analysis of the original crank reveals significant structural flaws; large regions with stresses exceeding the material's fatigue strength with a displacement of 7.11mm at the load application point are formed in the most demanding load case. Some locations also surpass its yield strength and the crank arm would inevitably fail a real test. Following up with analyses of the hollow steel cranks, manual lattice manipulations conducted in nTopology Platform permitted a displacement value decrease of 3.2% for the FCC crank variant and 5.2% for the re-entrant lattice, respectively. The subsequent optimisation step, utilising blends of solid and beam elements in the discretised models, did not succeed in further increasing the total stiffness but adapted the beam diameters to the local stresses. The final models, which were fully discretised by solid elements omitting the contact interfaces and beam elements, are able to slightly improve upon the displacement magnitudes and stress values. Merging the lattice and crank to a single body also reduced the weight of both variants to approximately 340g, undercutting the initial goal of 360g. Displacement values of both variants are further reduced to 2.58mm (re-entrant) and 2.52mm (FCC), respectively. Though the chosen stress limit of 320 MPa could not entirely be met, the crank variant with the re-entrant lattice did not surpass the secondary limit of 400MPa. Small regions in the FCC lattice exhibited stresses of up to 490MPa which might become problematic during a fatigue test. In total, a displacement value decrease of approximately 65% was achieved compared to the aluminium crank, albeit at the detriment of a 59% weight increase.

Prospective topics for future work encompass material property validation, physical printing in metal, testing and exploration of material alternatives like heat-treated stainless steel, titanium, or aluminium to reduce the crank weight. A conceivable alternative to all-metal models may be blends of metal lattices encased in carbon fibre shells such that a continuous fibre can be used. In addition, lattices based on triply periodic minimal surfaces (TPMS) will be analysed in the same context in an upcoming paper. Other potential topics include tapered beams as well as conformal or Voronoi lattices which better adapt to the geometries and can provide more control over local lattice properties. Their basis may be stress vector fields sourced from solid models to influence the exact beam orientation and thicknesses. Additionally, the drive-side crank arm with its direct chainwheel mount, as it is common on today's cranks, and a suitable shaft geometry will be designed for the concluding assembly and tests.

5 Conclusions

This paper shows the practical application of beam-based FGLS on a bicycle crank using a blend of manual adjustments and numerical optimisation methods. Theoretically, the implementation of functionally graded lattice structures in a crank arm in combination with high-performance materials can indeed significantly improve the stiffness of a common bicycle crank. This statement nonetheless holds limited validity. The material properties of 17-4 PH stainless steel produced using ADAM technology are not yet evaluated, and the physical model ultimately has to be tested to support these assertions. Its manufacturability is unexplored and might be hindered by software restrictions of Eiger.io, the preprocessor software provided by Markforged, since it prohibits user control over support structures at the time of writing. Furthermore, a more

in-depth exploration of the initial lattice properties, like conformal lattices adapting to a body's surface, blends of different lattice types, cell sizes, or orientations mimicking crystal microstructures like in [23], might have yielded superior results. Future functionalities allowing more control over non-stochastic beam-based lattices to be added to nTopology Platform may provide further potential as well. Though nTopology Platform does offer a utility to create conformal lattices based on CAD faces, its capabilities are not yet sufficient to attain a suitable design with the complex geometry at hand.

References

- [1] L. Yang, D. Cormier, H. West, O. Harrysson, and K. Knowlson, "Non-stochastic Ti-6Al-4V foam structures with negative Poisson's ratio," *Materials Science and Engineering A*, vol. 558, pp. 579–585, 2012, doi: 10.1016/j.msea.2012.08.053.
- [2] J. U. Surjadi *et al.*, "Mechanical Metamaterials and Their Engineering Applications," *Advanced Engineering Materials*, vol. 21, no. 3, pp. 1–37, 2019, doi: 10.1002/adem.201800864.
- [3] W. P. Syam, W. Jianwei, B. Zhao, I. Maskery, W. Elmadih, and R. Leach, "Design and analysis of strut-based lattice structures for vibration isolation," *Precision Engineering*, vol. 52, no. May 2017, pp. 494–506, 2018, doi: 10.1016/j.precisioneng.2017.09.010.
- [4] K. Davami, M. Mohsenizadeh, M. Munther, T. Palma, A. Beheshti, and K. Momeni, "Dynamic energy absorption characteristics of additively manufactured shape-recovering lattice structures," *Materials Research Express*, vol. 6, no. 4, 2019, doi: 10.1088/2053-1591/aaf78c.
- [5] R. Mahshid, H. N. Hansen, and K. L. Højbjerg, "Strength analysis and modeling of cellular lattice structures manufactured using selective laser melting for tooling applications," *Materials and Design*, vol. 104, pp. 276–283, 2016, doi: 10.1016/j.matdes.2016.05.020.
- [6] K. J. Maloney, K. D. Fink, T. A. Schaedler, J. A. Kolodziejska, A. J. Jacobsen, and C. S. Roper, "Multifunctional heat exchangers derived from three-dimensional micro-lattice structures," *Int J Heat Mass Transf*, vol. 55, no. 9–10, pp. 2486–2493, 2012, doi: 10.1016/j.ijheatmasstransfer.2012.01.011.
- [7] M. Helou and S. Kara, "Design, analysis and manufacturing of lattice structures: An overview," *International Journal of Computer Integrated Manufacturing*, vol. 31, no. 3, pp. 243–261, 2018, doi: 10.1080/0951192X.2017.1407456.
- [8] A. Nazir, K. M. Abate, A. Kumar, and J. Y. Jeng, "A state-of-the-art review on types, design, optimization, and additive manufacturing of cellular structures," *International Journal of Advanced Manufacturing Technology*, vol. 104, no. 9–12, pp. 3489–3510, 2019, doi: 10.1007/s00170-019-04085-3.
- [9] G. Allen, "nTopology Modeling Technology," 2019.
- [10] "Printing the future: Cobra Aero rethinks designing for additive manufacturing with nTopology | Association for Unmanned Vehicle Systems International." <https://www.auvsi.org/printing-future-cobra-aero-rethinks-designing-additive-manufacturing-ntopology> (accessed Sep. 14, 2020).
- [11] M. Vlahinos and R. O. Hara, "Unlocking Advanced Heat Exchanger Design and Simulation with nTop Platform and ANSYS CFX," 2020.
- [12] N/a, "Streamlining additive manufacturing for spinal implants," 2019.
- [13] "S-Works Power Saddle with Mirror." <https://www.specialized.com/us/en/power-saddle-mirror> (accessed Jul. 28, 2020).

- [14] “Bastion reveals 3D-printed parts for Australia’s 2020 Olympic track campaign | Cycling Smarter.com.” <https://cyclingsmarter.com/bastion-reveals-3d-printed-parts-for-australias-2020-olympic-track-campaign/> (accessed Jul. 28, 2020).
- [15] “MOORHUHN 129 - huhncycles.” <https://huhncycles.com/MOORHUHN-129> (accessed Jul. 28, 2020).
- [16] A. Yadollahi, N. Shamsaei, S. Thompson, and A. Elwany, “Fatigue Behavior of 17-4 PH Stainless Steel Fabricated Using Selective Laser Melting,” no. August, 2015, doi: 10.13140/RG.2.1.3996.2323.
- [17] P. D. Nezhadfar, R. Shrestha, N. Phan, and N. Shamsaei, “Fatigue data for laser beam powder bed fused 17-4 PH stainless steel.pdf.”
- [18] Markforged, “Material datasheet 17-4 PH Stainless Steel,” 2018.
- [19] Matweb, “6061-T6 Matweb,” *MatWeb*, pp. 1–2, 2015.
- [20] Desktop Metal, “17-4 PH Stainless Steel,” *Www.Desktopmetal.Com*, p. 1, 2018.
- [21] “Cycles - Safety requirements for bicycles - Part 8: Pedal and drive system test methods (ISO 4210-8:2014, Corrected version 2014-11-01).” Comité Européen de Normalisation.
- [22] S. Bai, X. Li, Z. Xie, Z. Zhou, and J. Ou, “A wireless fatigue monitoring system utilizing a bio-inspired tree ring data tracking technique,” *Sensors (Switzerland)*, vol. 14, no. 3, pp. 4364–4383, 2014, doi: 10.3390/s140304364.
- [23] M. S. Pham, C. Liu, I. Todd, and J. Lertthanasarn, “Damage-tolerant architected materials inspired by crystal microstructure,” *Nature*, vol. 565, no. 7739, pp. 305–311, 2019, doi: 10.1038/s41586-018-0850-3.

4.2 Material Properties of Steel Produced with Metal FDM

The publication titled *Strength Properties of 316L and 17-4 PH Stainless Steel Produced with Additive Manufacturing* (Kedziora et al., 2022) serves as continuation of the previous study. Two steel variants produced with metal FDM as well as two variants manufactured with SLM are investigated: Markforged 17-4 Precipitation Hardened (PH) stainless steel produced on the Metal X system and BASF Ultrafuse 316L stainless steel produced on an Intamsys Funmat HT are compared to two 316L stainless steel materials produced on an EOS M290 (with heat treatment) and Renishaw AM400, respectively. The metal FDM materials were chosen since they are potential candidates for local production of the crank model shown in the first publication.

The samples' printing orientation was defined to be parallel to the build direction such that loads occur in their weakest plane, therefore testing the worst-case loading scenario. The paper reports their properties in detail by investigating tensile strengths, fatigue properties, Charpy impact strengths, surface roughness and hardness measurements, and includes microscopy imagery. They are compared to a large array of literature results encompassing investigations of 17-4 PH and 316L steels produced with metal FDM, SLM, metal injection moulding (MIM) and wrought material. The paper expands on previous publications by performing a wide array of tests covering the metal FDM steel materials, and first reports on fatigue and impact tests.

Aside from the much larger result deviations compared to their SLM counterparts, their reported fatigue and impact strengths indicate issues stemming from the production method itself that become clearly noticeable when loading the samples in their weakest orientation. Both materials produced with metal FDM do not reach the manufacturer's stated strengths in the tests and exhibit very large result spreads. Markforged's 17-4 material breaks at an average strain of 0.4% during tensile testing. Both the Markforged and BASF material were brittle to the point of not putting up any measurable resistance during the Charpy impact tests. Their fatigue strengths were also severely below the SLM material samples. The microscopy images of fractured samples after different tests show weak bonding between layers, potentially originating from incomplete sintering. Literature results investigating their density indicate the presence of sharp voids which stem from neighbouring oblong layer lines as well as high surface roughness, both acting as stress risers and severely affecting the samples' fatigue strength. In contrast, none of these issues are present in the investigated SLM samples which show consistent test results with little deviations and fully melted material structure.

Since the material compositions as well as the debinding and sintering methods used for metal FDM production are comparable to those utilized for MIM, a comparison based on literature results was compiled. It was established that using the metal FDM process results in higher material porosity, more pronounced anisotropy, and generally lower strengths.

The author contributed to this paper by executing part of fatigue testing, performing data analysis and the literature review, and writing part of the original paper draft.

Article

Strength Properties of 316L and 17-4 PH Stainless Steel Produced with Additive Manufacturing

Slawomir Kedziora ^{1,*}, Thierry Decker ¹, Elvin Museyibov ¹, Julian Morbach ², Steven Hohmann ², Adrian Huwer ² and Michael Wahl ²

¹ Faculty of Science, Technology and Medicine, University of Luxembourg, Campus Kirchberg, 6 rue Coudenhove-Kalergi, L-1359 Luxembourg, Luxembourg

² Trier University of Applied Sciences, Umwelt-Campus Birkenfeld, Campusallee, 55768 Hoppstädten-Weiersbach, Germany

* Correspondence: slawomir.kedziora@uni.lu; Tel.: +352-466-644-5590

Abstract: The number of additive manufacturing methods and materials is growing rapidly, leaving gaps in the knowledge of specific material properties. A relatively recent addition is the metal-filled filament to be printed similarly to the fused filament fabrication (FFF) technology used for plastic materials, but with additional debinding and sintering steps. While tensile, bending, and shear properties of metals manufactured this way have been studied thoroughly, their fatigue properties remain unexplored. Thus, the paper aims to determine the tensile, fatigue, and impact strengths of Markforged 17-4 PH and BASF Ultrafuse 316L stainless steel to answer whether the metal FFF can be used for structural parts safely with the current state of technology. They are compared to two 316L variants manufactured via selective laser melting (SLM) and literature results. For extrusion-based additive manufacturing methods, a significant decrease in tensile and fatigue strength is observed compared to specimens manufactured via SLM. Defects created during the extrusion and by the pathing scheme, causing a rough surface and internal voids to act as local stress risers, handle the strength decrease. The findings cast doubt on whether the metal FFF technique can be safely used for structural components; therefore, further developments are needed to reduce internal material defects.

Keywords: additive manufacturing; Charpy impact energy; fatigue properties; tensile strength; BASF Ultrafuse; Markforged



Citation: Kedziora, S.; Decker, T.; Museyibov, E.; Morbach, J.; Hohmann, S.; Huwer, A.; Wahl, M. Strength Properties of 316L and 17-4 PH Stainless Steel Produced with Additive Manufacturing. *Materials* **2022**, *15*, 6278. <https://doi.org/10.3390/ma15186278>

Academic Editor: Andrea Di Schino

Received: 28 July 2022

Accepted: 5 September 2022

Published: 9 September 2022

Publisher's Note: MDPI stays neutral with regard to jurisdictional claims in published maps and institutional affiliations.



Copyright: © 2022 by the authors. Licensee MDPI, Basel, Switzerland. This article is an open access article distributed under the terms and conditions of the Creative Commons Attribution (CC BY) license (<https://creativecommons.org/licenses/by/4.0/>).

1. Introduction

Metal additive manufacturing (AM) is rapidly gaining adoption throughout engineering industries, with many research resources being directed at developing new methods and usable material types. While powder bed fusion (PBF) methods such as selective laser melting (SLM) [1] and binder jetting (BJ) are well-established due to the excellent achievable part quality, they are also costly and complex in their use [2]. Advances were made to enable metal AM with more straightforward approaches centered on material extrusion methods using a filament containing polymer-metal blends similar to materials used in metal injection molding (MIM) [2,3]. MIM is a traditional process for producing high complexity parts in which powder metal mixed with binder material is shaped and solidified using injection molding. Then, the parts are subjected to a binder removal step (debinding), and finally, they are sintered to the full-density parts. On the other hand, the metal extrusion printing method is similar to the well-established fused filament fabrication (FFF) method [1,4] for polymers, also known as fused deposition modeling (FDM), with subsequent debinding and sintering steps.

In the metal FFF technology, everything starts with a CAD model that is sent to slicer software via a STereoLithography (STL) file. Next, the filament containing metal powder

with polymer binder is deposited layer by layer through a nozzle onto the build plate (green part). During the slicing step, the geometry is scaled by a specific factor to account for part shrinkage during sintering. In the subsequent debinding step, the green state part is immersed in a solvent to dissolve a portion of the binder, and the debinded part is obtained (brown part). The debinding time is a function of cross-sectional area, wall thickness, and infill density; that process can take several hours to days. A grey state part is obtained after the total polymer removal by thermal debinding affected by a heating strategy [5]. In the later sintering step, the grey part is sintered to a fully dense solid part within an atmosphere of a specific gas mixture at a defined overpressure and a temperature profile. The sintering process can take several hours with the parameters depending on the sintered material.

The main benefits of the metal FFF technology are that it allows the creation of complex parts without adding powder-release channels, meaning it does not require removing unsintered, loose powder from internal cavities, and it is very cost-competitive [2]. Unfortunately, the technology also introduced constraints. Internal structures (infill) are limited by minimum infill requirements due to the material strength of brown parts. The used nozzle size determines the minimum part thickness, and the maximum thickness of any part feature is limited to prevent excessive debinding times. Aspect ratios, defined as the ratio of a feature's maximum to minimum geometry, should be less than 8:1 [6].

Only some metal alloys are available for printing at the moment. Significant shrinkage during the sintering process from 14% to 23% was reported [7], depending on printing orientation and material. It was found that the material will exhibit anisotropic behavior [8] and have a mesh of crack-like defects related to the printing orientation [9]. Printed parts have significant porosity [3], causing low strength. In addition, a restriction on the size of printing parts limits this technology; the printer's area, furnace volume, and sintering technology restrict the size [10].

Nevertheless, the metal extrusion AM method can help produce small parts with closed-cell infill, creating lightweight components. Therefore, the mechanical properties of common printable steel alloys (316L and 17-4 PH) can interest engineers and researchers.

The other AM method employed in the presented development is SLM technology. Selective laser melting (SLM) is a unique technology that belongs to the powder bed fusion (PBF) methods, producing objects with complex geometry from metal powders (typically in a range of 30–50 μm) [11] with mechanical properties similar to bulk materials.

SLM requires that a 3D CAD model shall be created and sent to slicer software to generate a code that controls the printer's laser beam. The laser beam melts the powder material layer line by line, the build plate is lowered, a subsequent powder layer is deposited onto the last layer, and the powder is melted again to build the part's geometry. These steps are repeated until almost fully dense parts are manufactured. The employed materials can be metal powder alloys, including stainless steel, tool steel, cobalt-chromium alloys, titanium, and aluminum.

The SLM process is controlled by processing parameters [12], such as laser power, scanning speed, scan line spacing, layer thickness, scanning strategy, working atmosphere, the temperature of the powder bed, and material-based input parameters.

The SLM technology is used to produce parts of complex geometric shapes, often with thin walls allowing the creation of high-strength structural elements, inaccessible for traditional mechanical manufacturing methods due to the geometric complexity. The SLM technology can be used at all stages of product development, from design concepts to low-volume production [12]. Dimension quality of the finished products is so high that the subsequent mechanical finishing processing can be neglected in some cases.

As with every manufacturing method, SLM has some disadvantages. Porosity levels can be an issue in applications where gas-tightness is crucial, for example, in high-pressure valves where leakage through the wall is unacceptable. There are constraints on the geometries of printed parts [13]; for example, the SLM method requires avoiding part

overhanging with an angle limit of 45° with reference to the build platform. Often, final parts require post-processing, such as de-powdering support removal and surface grinding.

It is important to recall an essential element to understand the test strength properties of 3D printed specimens, that printed materials are anisotropic due to variation of build orientations and used printing strategies [14,15]. Therefore, predefined build orientations are typically used during printing, as shown in Figure 1, to compare different strength test data. The presented orientation nomenclature is applied in the whole text of the article.

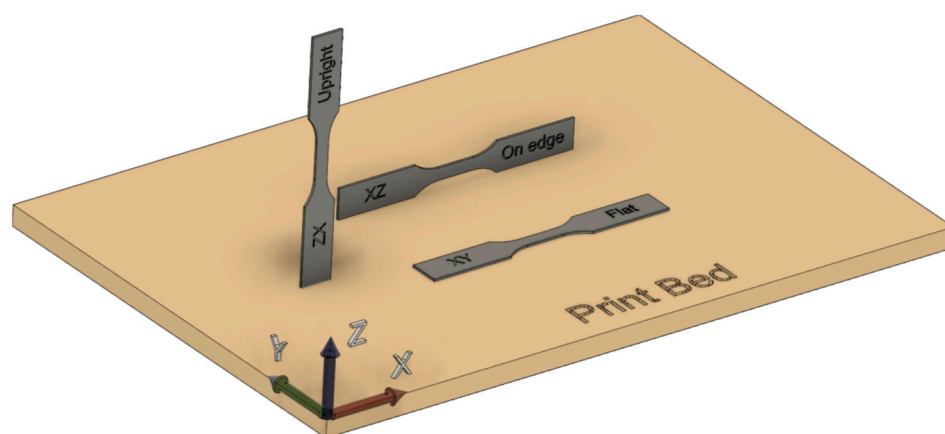


Figure 1. Printed specimen and predefined build orientations.

As outlined above, the SLM and metal FFF technologies are desirable to researchers and engineers who want to create competitive next-generation products and further develop the technology. Researchers need data on the strength of the printed materials to take advantage of these brand-new printing technologies. The advantages of the metal FFF have led to intense interest in the technology in the last years, with many studies investigating the parts' attainable mechanical properties. Extensive lists of references are presented in Tables 10–12, with the literature test data. Unfortunately, fatigue test data are rare, and the existing articles do not fully answer whether the metal FFF can be used for structural parts safely with the current state of technology.

Therefore, the authors focus on proving the hypothesis that FFF-printed steel materials have significantly worse structural properties than the same SLM-printed steel alloy, leading to the further supposition that the metal FFF technique is currently not advisable as a structural component in mechanical engineering.

In addition, the presented paper aims to fill an existing gap in the literature regarding the fatigue properties of 316L and 17-4 PH stainless steel alloys produced by the metal FFF method. So, a comparison of the mechanical properties, including strength parameters, hardness, roughness, and impact strength of materials produced in both ways, is presented to prove our hypothesis and thereby determine the scope of possible applications and contribute to the further development of FFF technology. The fatigue and impact data are of particular interest, as these mainly determine the material's applicability in service conditions.

2. Materials and Methods

Two groups of specimens were built using the two aforementioned 3D printing technologies. Additionally, two SLM printers (EOS M290, Krailing, Germany, and Renishaw AM 400, Wotton-under-Edge, UK) were used to print 316L stainless steel (Table 1). Two materials were selected for the metal FFF process due to their prevalence in the metal FFF domain: BASF Ultrafuse 316L and Markforged 17-4 PH (Table 1). The BASF 316L specimens were produced on an Intamsys Funmat HT printer with parameters shown in Table 2; debinding and sintering took place in an external supplier as part of a service offered by BASF. A catalytic debinding process was used in which green parts were exposed to

gaseous nitric acid (HNO₃) in a nitrogen atmosphere and heated. The sintering process was performed in a pure hydrogen atmosphere, according to BASF.

Table 1. Chemical composition of printed materials, (weight) wt %.

Elements	EOS 316L ¹		Renishaw 316L [16] ²		Ultrafuse BASF 316L [17]		17-4 PH [18]	
	Min	Max	Min	Max	Min	Max	Min	Max
Fe	balance		balance		balance		balance	
C	-	0.03	-	0.03	-	0.07	-	0.07
Co	-	0.1	-	-	-	-	-	-
Cr	16	18	16	18	16	18.5	15	17.5
Cu	-	0.075	-	-	-	-	3.0	5.0
Mn	-	2.0	-	2.0	-	2.0	-	1.0
Mo	2.0	3.0	2.0	3.0	2.0	2.5	-	-
N	-	0.01	-	0.01	-	0.11	-	-
Nb	-	-	-	-	-	-	0.15	0.45
Ni	10	14	10	14	10	13	3.0	5.0
O	-	0.1	-	0.1	-	-	-	-
P	-	0.04	-	0.045	-	0.045	-	0.04
Si	-	1.0	-	1.0	-	1.0	-	1.0
S	-	0.03	-	0.03	-	0.03	-	0.03

¹ Data from AnyShape (<https://any-shape.com/>) based on a made test. ² Data according to EN1.4404 Stainless Steel (X2CrNiMo17-12-2).

Table 2. Printing settings for the BASF Ultrafuse 316L specimens.

Printing Parameter	Value
Nozzle size, mm	0.4
Retraction distance, mm	0.5
Retraction speed, mm/s	45
Layer height, mm	0.15
Nozzle temperature, °C	250
Print bed temperature, °C	100
Chamber temperature, °C	100
Oversizing factors: X, Y, Z, %	21.35, 21.35, 26

The 17-4 PH specimens were manufactured using the Markforged Metal X system with the settings shown in Table 3. The debinding and sintering processes were performed in-house with the default parameters recommended by Markforged.

Table 3. Printing settings for the Markforged 17-4 PH specimens.

Printing Parameter	Value
Nozzle size, mm	0.45
Layer height, mm	0.125
Print bed temperature, °C	115
Metal hotend temperature, °C	220
Chamber temperature, °C	48
Oversizing factors: X, Y, Z, %	19.5, 19.5, 20

A 100% infill was applied for both materials, although a different printing strategy was employed because various slicers were used to generate the G-code. It is worth noting here that the slicer Eiger (<https://www.eiger.io/>) of Markforged is very restricted in terms of changing print parameters to ensure the best quality of printed parts; however, it introduces significant limitations for users.

The 316L SLM steel specimens were printed on an EOS M 290 printer and a Renishaw AM 400 printer with parameters presented in Table 4. All EOS M 290 specimens were

printed by AnyShape (<https://any-shape.com/>), and they applied a stress relief heat treatment at 700 °C for two hours, a standard procedure for all their printed parts. The other specimens were printed onsite at the University of Luxembourg and the Trier University of Applied Sciences.

Table 4. SLM process parameters used on EOS M 290 and Renishaw AM 400 printer.

Printing Parameter	EOS M 290	Renishaw AM 400
Layer height, μm	40	40
Laser power, W	*	180
Focus Diameter, μm	100	70
Hatch distance, mm	*	0.11
Shielding gas	Argon	Argon
Oxygen content, %	*	0.15

* Data not provided by AnyShape (www.any-shape.com) due to their confidentiality.

The recommended manufacturing settings for fully dense parts were used for all materials. All specimens were built vertically (ZX), the worst-case scenario for specimens in tensile loading cases, especially for the metal FFF specimens [14]. For each type of test and material, ten samples were used to balance the reliability of test results and the test costs.

Tensile testing followed the standard [19] using the tensile machine MTS 20/M with a load cell of 100 kN. A constant elongation speed of 10 mm/min and a data sampling frequency of 227 Hz were employed during all tests. The tests were conducted at an ambient temperature of 23 °C. The flat dog bone specimens have an overall length of 110 mm, 38 mm gauge length, and 3 mm thickness, as shown in Figure 2.

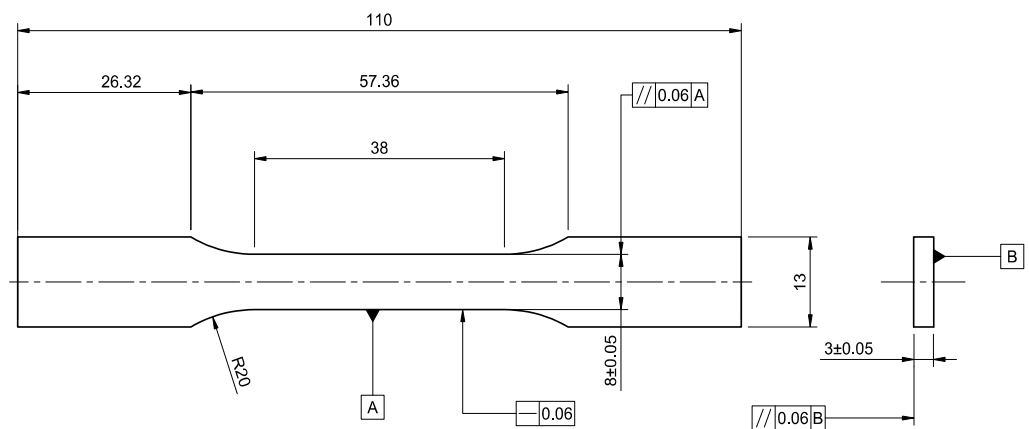


Figure 2. Tensile specimen design according to the standard [19], units: mm.

Axial fatigue tests were performed following the standard [20], which involves metallic materials fatigue testing axial force-controlled method with a stress ratio $R = 0.1$ and a constant test frequency of 30 Hz. The tests were performed using an Instron 8872 universal testing machine with a load cell of 25 kN. The tests were conducted at an ambient temperature of 23 °C. The specimens have a nominal gauge width of 6 mm, a thickness of 4 mm, a gauge length of 24 mm and a nominal length of 144 mm, as shown in Figure 3.

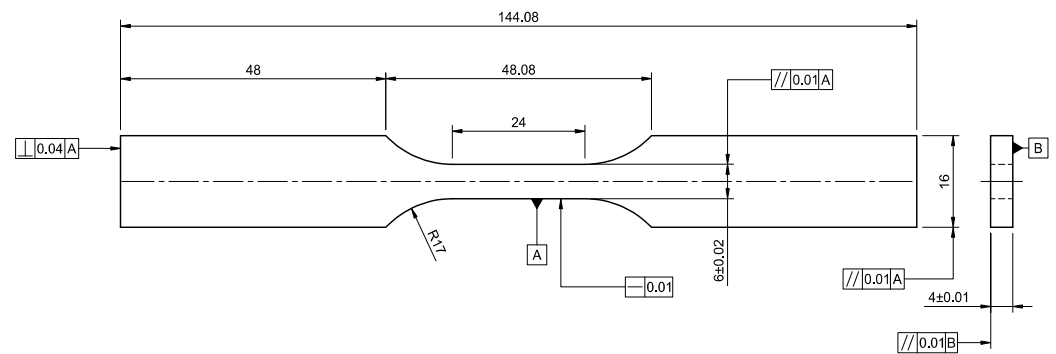


Figure 3. Fatigue specimen design according to the standard [20], units: mm.

The surface roughness of the fatigue specimens was measured using the TESA Rugosurf 10 G roughness gauge. Measurements were made in the middle of the specimens and in the longitudinal direction on the flat and side specimen surfaces. Two parameters of the surface roughness were measured R_a and R_z .

The hardness of all fatigue specimens was measured using the HB Brinell 2.5/187.5 scale since the tested material was not surface hardened. A ball diameter of 2.5 mm was used with a proof force of 1839 N and a proof time of 15 s [21]. The hardness test was completed using an Instron Wolpert DIA-TESTOR 722 at the ambient temperature of 23 °C. The ball diameter of 2.5 mm results in a relatively large imprint of 1.3 mm on the sample's surface, giving an average hardness result over the surface. The measurements were performed after tests of the fatigue specimens. Both fractured parts of a specimen were measured in the proximity of the fracture. Then, an average hardness value was calculated for all specimens per the tested materials. Furthermore, due to the surface texture of the printed specimens, small areas were ground manually such that the ball impression was made visible, and the impression diameters were measured using a digital microscope in two perpendicular directions.

Charpy impact tests were also performed for specimens printed in ZX orientation (vertical) with a V notch, as shown in Figure 4. The test was performed according to the standard [22] using AMSLER Pendelschlagwerk Typ RKP 450 at an ambient temperature of 23 °C. Ten specimens of each material batch were analyzed. The impact occurred on the surface lying on the opposite side of the incised notch.

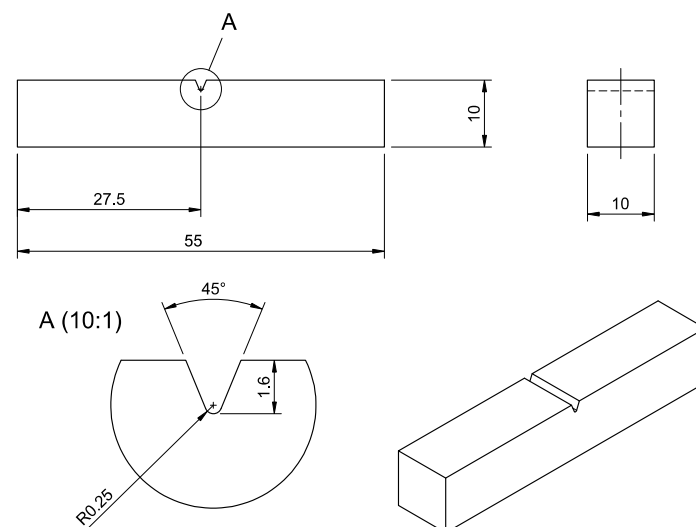


Figure 4. Charpy specimen design with the V notch according to the standard [22], units: mm.

3. Results

3.1. Tensile Tests

The tensile test results are summarized in Table 5 and Figure 5, and the envelope stress–strain diagrams are shown in Figure 6. The metal FFF specimens do not achieve the strength values specified by the filament manufacturers shown in Table 6. However, it should be emphasized that for the case of 17-4 PH stainless steel, Markforged published data only in (XY) build orientation, the most favorable one in the context of the strength.

Table 5. Results of tensile tests (mean ± standard deviation).

Parameters	Markforged 17-4 PH	BASF Ultrafuse 316L	EOS M 290 316L (HT)	Renishaw AM 400 316L
Yield strength, R_e , MPa	441.0 ± 55.4	152.9 ± 61.3	375.2 ± 22.4	443.1 ± 15.7
Tensile strength, R_m , MPa	495.9 ± 77.0	314.0 ± 41.7	533.2 ± 1.1	570.8 ± 4.4
Elongation at break A , %	0.4 ± 0.1	10.2 ± 5.0	38.2 ± 0.1	38.4 ± 0.1
Young’s modulus, E , GPa	142 ± 65	160 ± 22	190 ± 18	129 ± 17

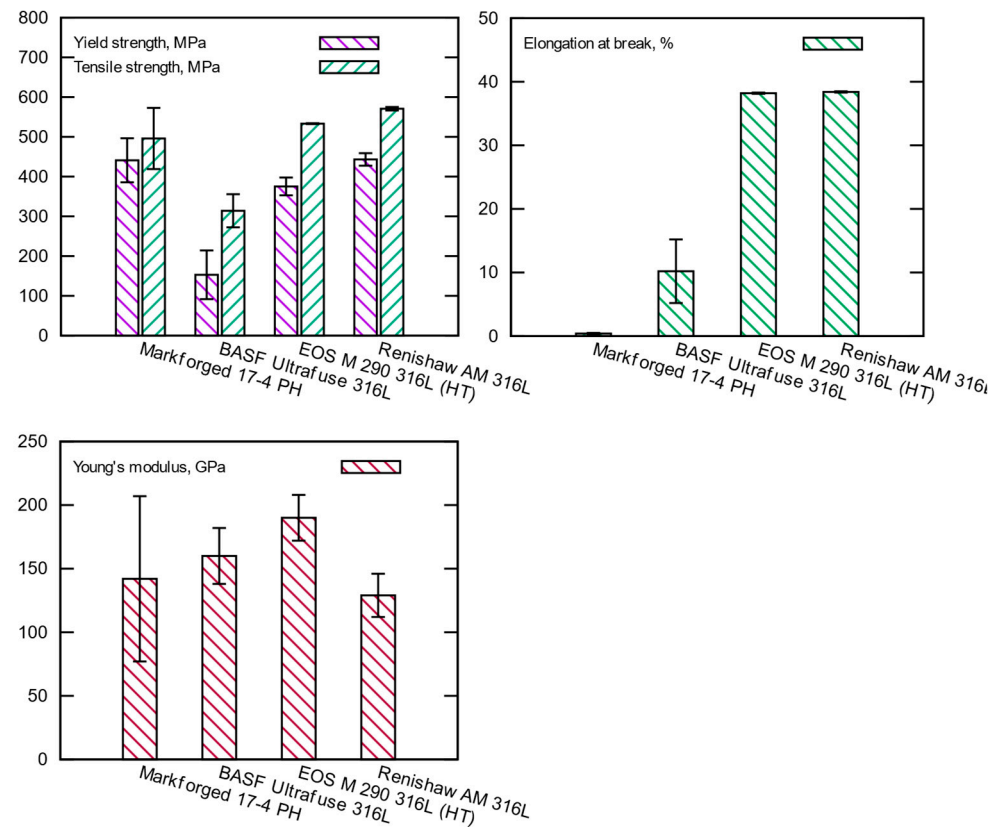


Figure 5. Results of tensile tests (mean with +/− standard deviation).

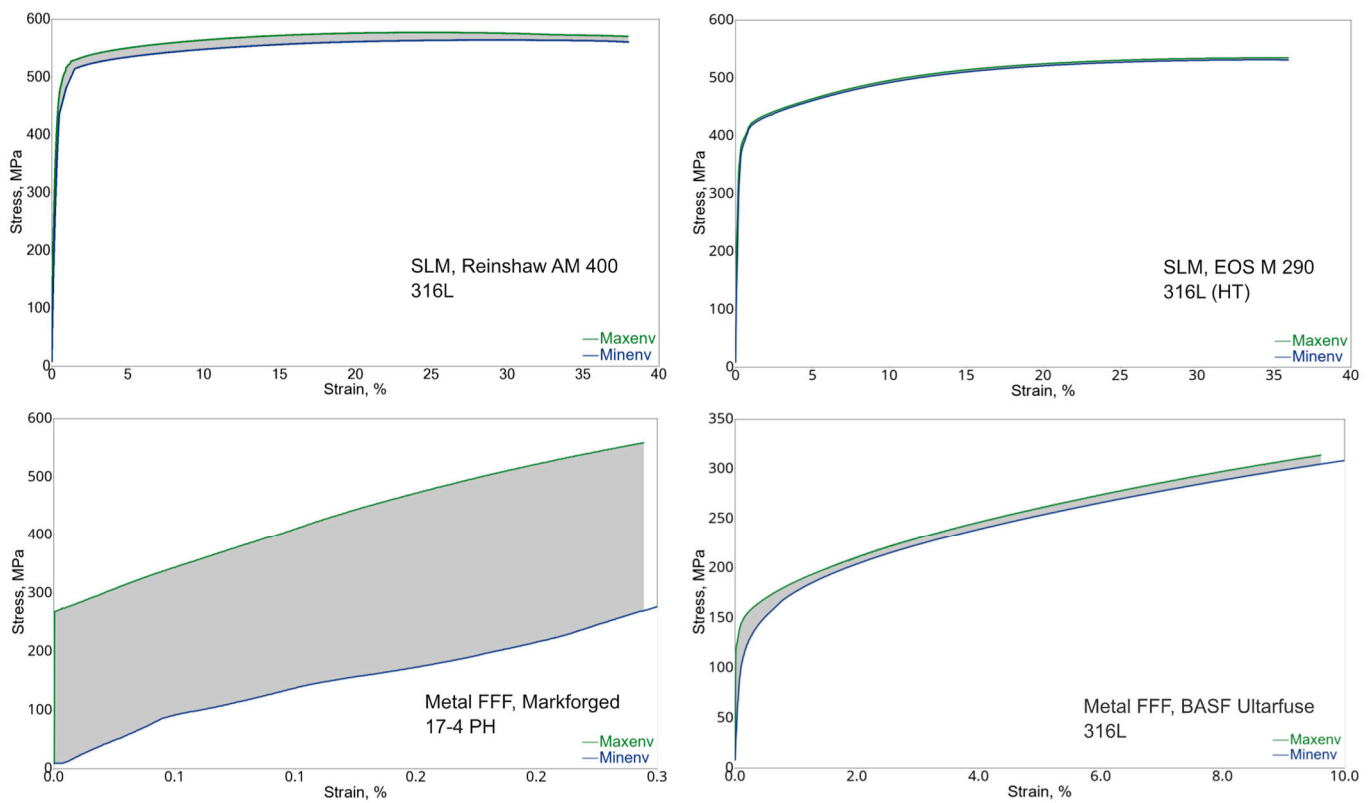


Figure 6. Envelope stress–strain curves (engineering stress versus engineering strain). Plots were created based on performed tensile tests considering all specimens.

Table 6. Material properties as indicated by the manufacturer’s data sheets.

	Markforged 17-4 PH (XY) ¹ [18]	BASF Ultrafuse 316L (XY/ZX) [17]	EOS M 290 316L ² (XY/ZX) [23]	Renishaw AM 400 316L (XY/ZX) [16]
R_m , MPa	800	251/234	530/470	547/494
R_e , MPa	1050	561/521	640/540	676/624
A , %	5	53/36	40/54	43 ^{+/-2} /35 ^{+/-8}
E , GPa	140	-	-	197/190
ρ , density g/cm ³	7.44	7.85	≥ 7.97	7.99
a_{eN} , impact strength, J/cm ²	-	111/-	-	-
Hardness	30, HRC	128/128, HV10	-	198/208, HV0.5

¹ No values for the Z direction are given by the manufacturer. ² Values for as-built samples without heat treatment.

For 17-4 PH stainless steel, considerable standard deviations for all strength parameters were obtained, and the large spread of the test results confirms Figure 6, where envelope curves of the obtained material characteristics are present. It should be noted that the spread of the curves is alarmingly large. The measured tensile strength of 441 MPa is much lower than the expected value of 800 MPa. The 17-4 PH batch reached elongation at a break of 0.4%, much lower than the value of 5% given by Markforged, with a significant standard deviation of 0.1%. It means that the material was very brittle and had massive properties spread. The material behavior was confirmed by studying the specimens after tests—they did not have a necking portion, a characteristic deformation before a fracture for ductile materials. The fracture of those specimens is characterized by delamination between the printed layer (see Figure 7a–e), and that failure mechanism was consistent for all 17-4 PH specimens. The fractures always happened between the printed layers (formed by printed lines), with evidence that gaps (air voids) between the layers were present after sintering (see Figure 7c–e).

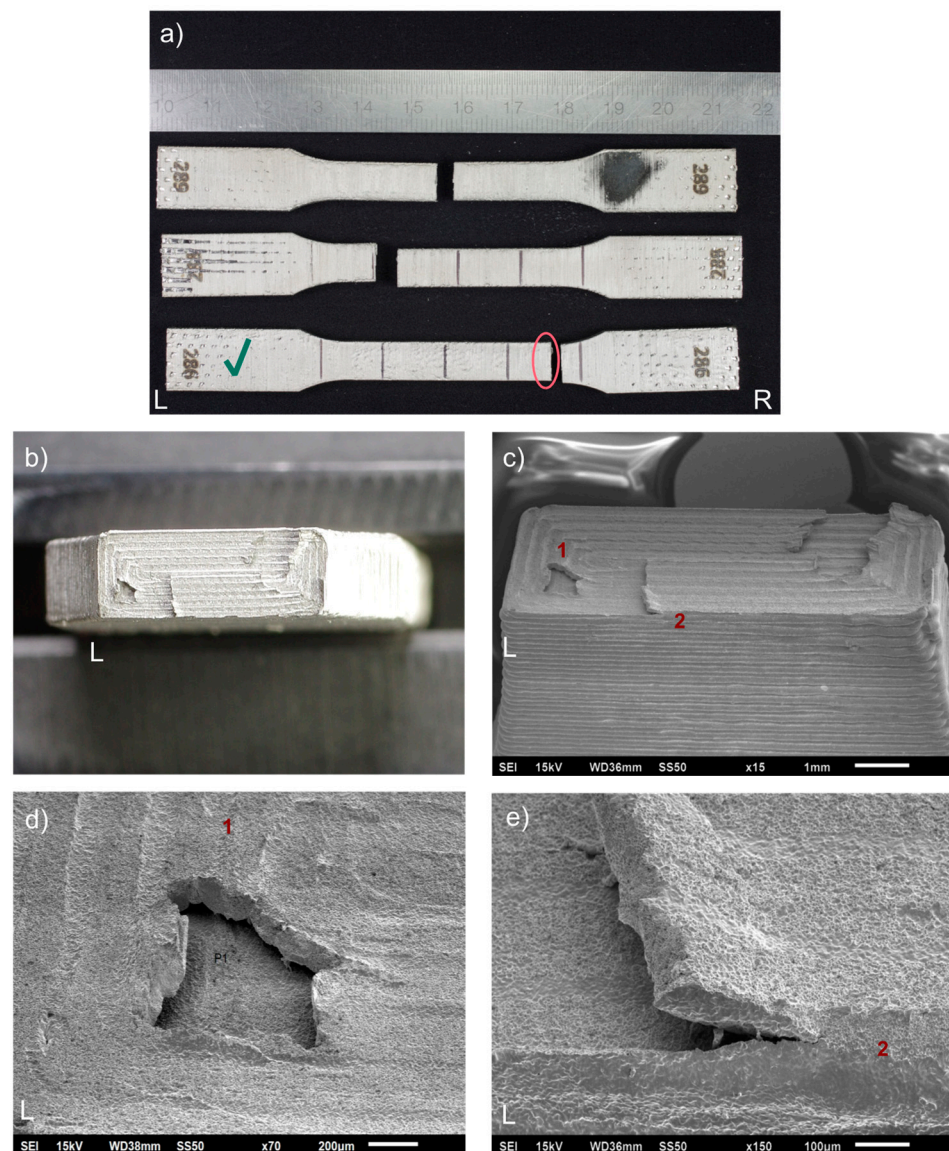


Figure 7. Fractures of tensile test 17-4 PH specimens presented as: (a) fractured specimens; (b) fracture surface, left side (optical microscope image), specimen 286; (c) fracture surface, left side (SEM image), specimen 286; (d) local delamination of a printed layer in the fracture, feature 1 (SEM image), specimen 286; (e) local delamination of the printed layer, feature 2 (SEM image), specimen 286. The samples have been numbered, which are visible in the figure. The letters L and R stand for the left-hand and right-hand sides of the sample in the figure. A green check mark means the specimen whose fracture faces were shown.

Likewise, the BASF Ultrafuse 316L specimens fractured at the low elongation at break of 10.2% compared to a value of 36%, indicated by BASF (Table 6). The measured tensile strength of 314 MPa is much lower than the expected value of 521 MPa.

The yield strength and elongation at break values show considerable standard deviations, but the spread of the measured material characteristics is much smaller than for 17-4 PH specimens. The specimen fractures were typical for brittle material with a tiny necking portion. Interestingly, the fracture mechanism was the same as for 17-4 PH steel, namely, delamination of the printed layer, as shown in Figure 8. However, the phenomenon's intensity is less visible than for the 17-4 PH specimens.

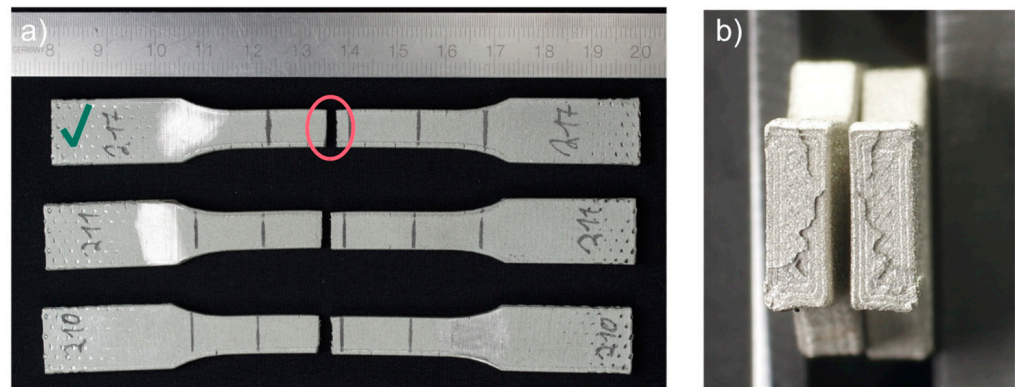


Figure 8. Fractures of tensile test BASF Ultrafuse 316L specimens presented as: (a) fractured specimens; (b) optical microscope image of the fracture surfaces, specimen 217. The samples have been numbered, which are visible in the figure. The letters L and R stand for the left-hand and right-hand sides of the sample in the figure. A green check mark means the specimen whose fracture faces were shown.

In contrast to the metal FFF specimens, the SLM samples show excellent consistency, as seen from the material characteristics' envelope curves and low standard deviations (Figure 5). Both batches of specimens printed on EOS M 290 and AM 400 show slightly lower strength than those published by the material suppliers (see Table 6). The measured elongation at break of 38.4% for the AM 400 specimens is greater than a value of 35% given by the printer manufacturer but in the specified tolerance. In contrast, the sample produced on EOS M 290 shows the elongation at break of 38.2%, which is smaller than the published value of 54%. It should be noted that the EOS M290 specimens were heat treated.

The SLM specimens show the typical ductile steel characteristic without an evident yield strength, meaning without a plasticity range with strain hardening at constant stress (Figure 6). The heat-treated material reveals lower strength than the material as printed without increased ductility. The fracture surfaces of both batches confirm that the SLM specimens presented typical indicators of the highly ductile materials during the tensile test, namely, clearly visible necking of the specimens (see Figure 9a,b). Extensive plastic deformation (necking) was observed in all SLM specimens before fracture.

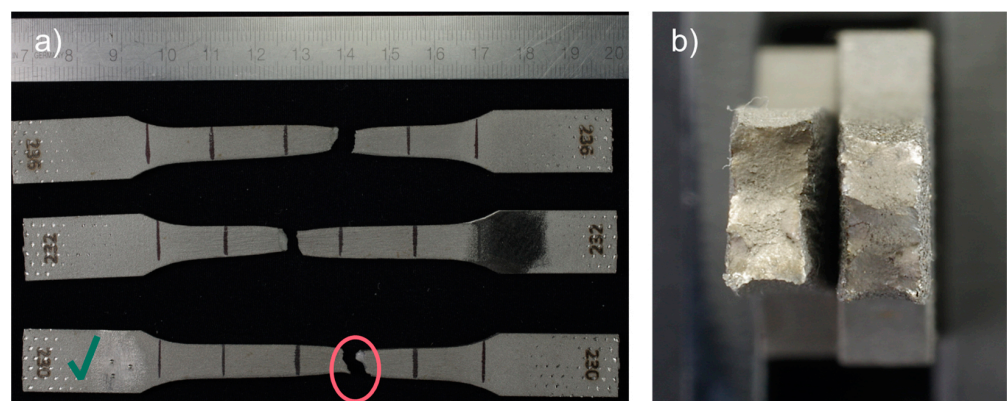


Figure 9. Fractures of tensile test EOS M 290 316L (HT) specimens presented as: (a) fractured specimens; (b) optical microscope image of the fracture surfaces, specimen 230. The samples have been numbered, which are visible in the figure. The letters L and R stand for the left-hand and right-hand sides of the sample in the figure. A green check mark means the specimen whose fracture faces were shown.

Table 5 reveals the significant difference in strength between the SLM and metal FFF samples for 316L stainless steel. Regarding the ultimate tensile strength, the discrepancy is 256.8 MPa to the detriment of the metal samples FFF. The same trend is observed for the yield strength decreasing by 290.3 MPa. Significant differences can be observed in the elongation at break; the reduction is 0.262 to the detriment of the metal FFF sample. So, the structural performance of the SLM specimens exceeds the metal FFF specimens. Even the theoretically stronger 17-4 PH steel showed lower strength when printed by the FFF metal technique compared with 316L printed by the SLM method. Additionally, the 17-4 PH samples were exceptionally brittle compared to all 316L samples.

Returning to the relationship between the curves in Figure 6, it is evident that the 17-4 PH samples show a very large scatter in the stress–strain curves. In view of the observed broken samples, it must be considered that we are dealing with the existence of partially incompletely sintered material layers. That effect can also be seen for BASF Ultrafuse specimens, but the level of the gaps between the layers is much smaller.

The best results were obtained for the SLM specimens, especially for EOS M 290 printer with the heat treatment, where the spread between 10 stress–strain curves is negligible. The rupture in the samples appears to be homogeneous in structure with very pronounced plastic deformation before fracture, as shown in Figure 9. The same type of failure was observed for all SLM specimens.

3.2. Roughness and Hardness Tests

Surface roughness results are presented by the two parameters Ra and Rz. Ra is the arithmetic mean deviation of surface roughness value within a sampling length, and Rz is the sum of the height of the tallest peak and the deepest valley of a profile within a sampling length. Therefore, for Rz, extremes have a much more significant influence on the final results than for Ra. Rz can be used to check whether the profile has protruding peaks that might affect a part function, and Ra is meaningful for stochastic surface roughness of machined parts.

Table 7 and Figure 10 illustrate the results of a measurement of the surface roughness of the fatigue specimens. Two measurements were made on a flat and a side along the sample. The measurements were in the center of the specimens. As shown in the table, the results indicate that the metal FFF samples exhibit higher roughness values than their SLM counterparts in both measurement locations. For the flat orientation, the SLM 316L samples had approximately a mean Ra roughness of 4.1 μm , the BASF Ultrafuse 316L samples reached a mean Ra of 7.3 μm , and the Markforged 17-4 PH batch had a mean Ra of 8.2 μm . For the side orientation, the SLM 316L samples had a mean Ra of 4.8 μm , while the BASF Ultrafuse batch had a mean Ra of 7.5 μm , and the Markforged 17-4 PH specimens were as high as a mean Ra of 16.6 μm . The high Rz values of the FFF metal samples indicate that high surface profile extremes characterized their surfaces.

Table 7. Average and standard deviation (mean \pm standard deviation) of the surface roughness of fatigue specimens.

Roughness	Measurement Direction	Markforged 17-4 PH	BASF Ultrafuse 316L	EOS M 290 316L (HT)	Renishaw AM 400 316L
Ra, μm	Flat, along a sample	8.15 \pm 0.85	7.34 \pm 1.02	4.05 \pm 0.43	4.07 \pm 0.79
Rz, μm	Flat, along a sample	47.67 \pm 5.64	43.09 \pm 4.56	24.54 \pm 2.95	25.51 \pm 4.96
Ra, μm	Side, along a sample	16.55 \pm 1.22	7.49 \pm 1.15	3.73 \pm 0.38	5.78 \pm 0.65
Rz, μm	Side, along a sample	77.84 \pm 9.12	46.23 \pm 6.41	22.58 \pm 2.71	36.95 \pm 3.55

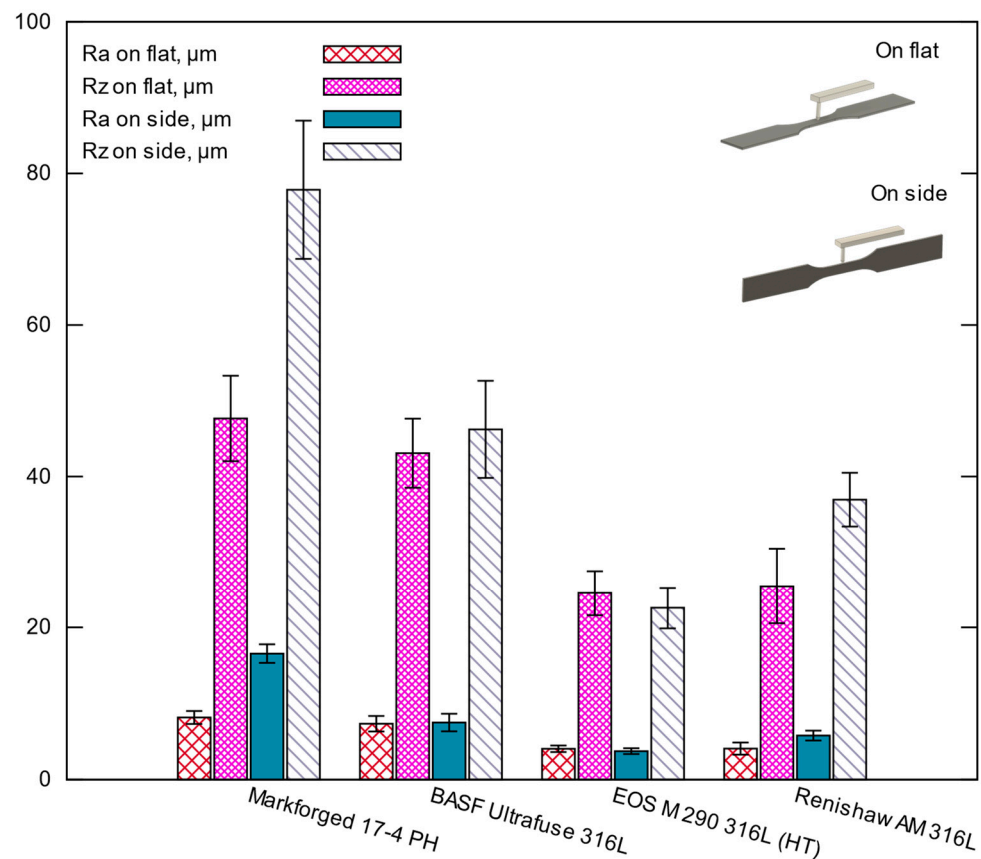


Figure 10. Results of roughness tests (mean \pm standard deviation).

Table 8 contains the harnesses measurement of the fatigue specimens. The highest hardness was measured for 17-4 PH samples with a mean of 261 HB and the lowest for BASF Ultrafuse 316L samples with a mean of 126 HB. The most significant standard deviation of 17.4 HB for the ten samples tested was for 17-4 PH. The measured hardness values mean that all materials are soft.

Table 8. Average and standard deviation (mean \pm standard deviation) of the hardness of fatigue specimens close to fractures.

HB 2.5/187.5	Markforged 17-4 PH	BASF Ultrafuse 316L	EOS M 290 316L (HT)	Renishaw AM400 316L
	261 \pm 17.4	126 \pm 6.2	213 \pm 9.7	217 \pm 10.6

3.3. Fatigue Tests

The results of the fatigue tests are presented in Figure 11 as an S-N plot on a log-log scale. The test results for all group specimens are at least highly correlated; in other words, the data with their group closely resemble a power trendline. What is striking in this figure is the curve for EOS M 290 samples. One test point (22,762,694 cycles; 341 MPa) deviates significantly from the power trendline trend of the other points; this is due to an insufficient number of test samples in the 1–2 million cycles range.

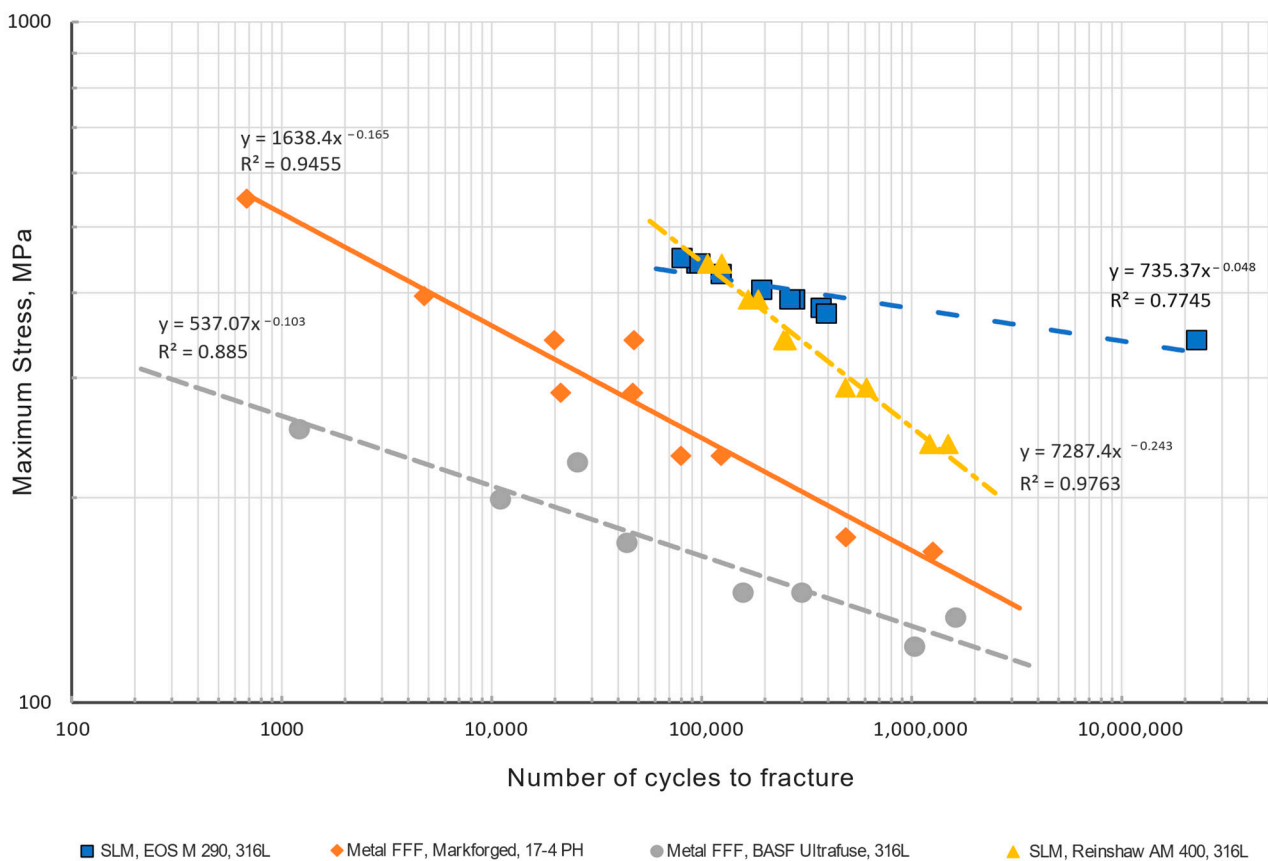


Figure 11. S-N curves for tested specimens; cycling tensile test with $R = 0.1$. (Two specimens of Ultrafuse 316L were broken in the grips, and their results were excluded.).

The graph shows that the greatest fatigue strength is for the SLM 316L specimens printed on the EOS M 290 printer and then heat-treated, whereas the worst is for the BASF Ultrafuse 316L specimens printed via the metal FFF method. The difference is significant; for example, for 1×10^6 cycles, the difference is 87 MPa. What stands out in this figure is the different curve slopes for those specimens. Interestingly, the slope of the SLM 316L specimens printed on the Renishaw AM 400 printer has a curve slope one order of magnitude larger.

Further analysis of the roughness in Table 7 and Figure 10 reveals that the EOS M 290 316L specimens had the lowest average R_a roughness value of about $4 \mu\text{m}$, while for BASF Ultrafuse 316L, R_a was $7.5 \mu\text{m}$. Furthermore, the hardness between those specimens was also different, with 213 HB for the EOS M 290 batch and 126 HB for the BASF Ultrafuse specimens see Table 8. Comparing the two results confirms the well-known tendency for fatigue strength of materials to increase with decreasing roughness and increasing hardness. The results also indicate that the lower fatigue strength for the Renishaw SLM specimens is influenced by the mean R_a roughness value of $5.8 \mu\text{m}$ and lack of heat treatment after printing which is usually made to remove internal residual stresses (stress relief) [24].

Looking at Figure 11, it is apparent that the 17-4 PH specimens have a low fatigue strength compared with the tested SLM 316L specimens, which is a surprise considering the tensile strength shown in Table 6. The most striking result to emerge from the data in Table 7 is that very high R_a roughness of $16.6 \mu\text{m}$ measured on a side along with the sample for the Markforged 17-4 PH specimens, which is 2.21 times greater than for the BASF Ultrafuse ones. Such difference in the roughness directly influences the fatigue strength results.

Further analysis of a fracture of the Markforged 17-4 PH specimens shows that the fracture mechanism is based on delamination of the printed layers, as seen in Figure 12b,c.

For the metal FFF specimens, beach (clamshell) marks were not observed on fatigue fracture surfaces. Macroscopically, the fracture surface is flat with evidence of the printing layers' delamination and perpendicular to the applied stress. The presented specimen does not show necking; therefore, the fracture may be considered a brittle fatigue fracture. It is incontestable that there were voids between the printer layers, which were sources of crack initiations. All specimens from this group had the exact failure mechanism. An analogous fracture mechanism was detected in the Ultrafuse 316L specimens but with less evident delamination between the printed layers (see Figure 13). Those specimens had an almost imperceptible necking part. Furthermore, it should be noted that the fatigue fracture surfaces for all metal FFF specimens are like the tensile test failure surfaces.

Turning to the experimental evidence on the SLM fatigue specimens (Figures 14 and 15), the fatigue fractures are not flat looking at them macroscopically. They have a flat portion perpendicular to the applied stress and the other part with a very expressive necking. The flat parts originated during fatigue cycles—fatigue zone A_f , and the other part A_c is the remaining material fractured catastrophically (final fracture). The ratio between those areas depends on the applied stress level. If the ratio, $A_f/A_c < 1$ it is a case of the fracture in the low cycle fatigue regime, whereas when the ratio, $A_f/A_c \geq 1$ is the fracture in a high cycle fatigue regime [25]. As seen in the Renishaw AM400 specimen, the ratio $A_f/A_c = 3.62$ corresponds to 1,492,546 cycles, whereas for the EOS M 290 specimen, the ratio is 1.13, corresponding to 392,641 cycles.

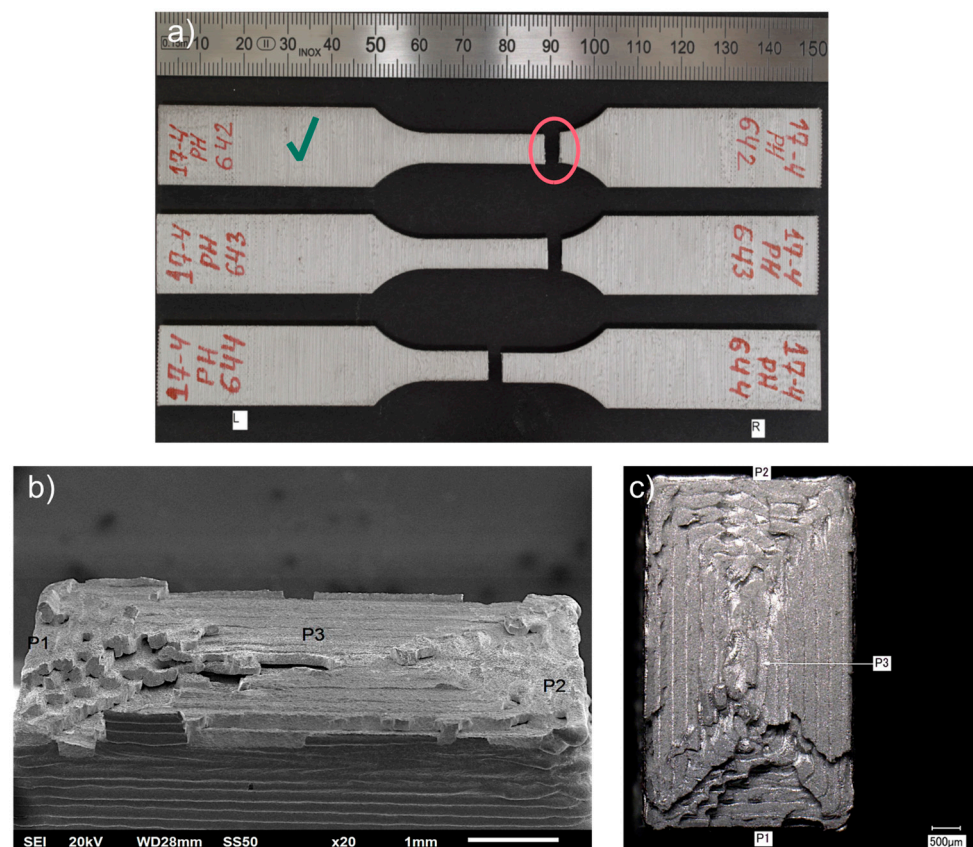


Figure 12. Fatigue fractures of Markforged 17-4 PH samples: presented as: (a) fractured specimens during the fatigue test; (b) fracture surface (SEM image), left side, specimen 642, at 4770 cycles; (c) top view of fracture surface (SEM image), left side, specimen 642, at 4770 cycles. The samples have been numbered, which are visible in the figure. The letters L and R stand for the left-hand and right-hand sides of the sample in the figure. A green check mark means the specimen whose fracture faces were shown.

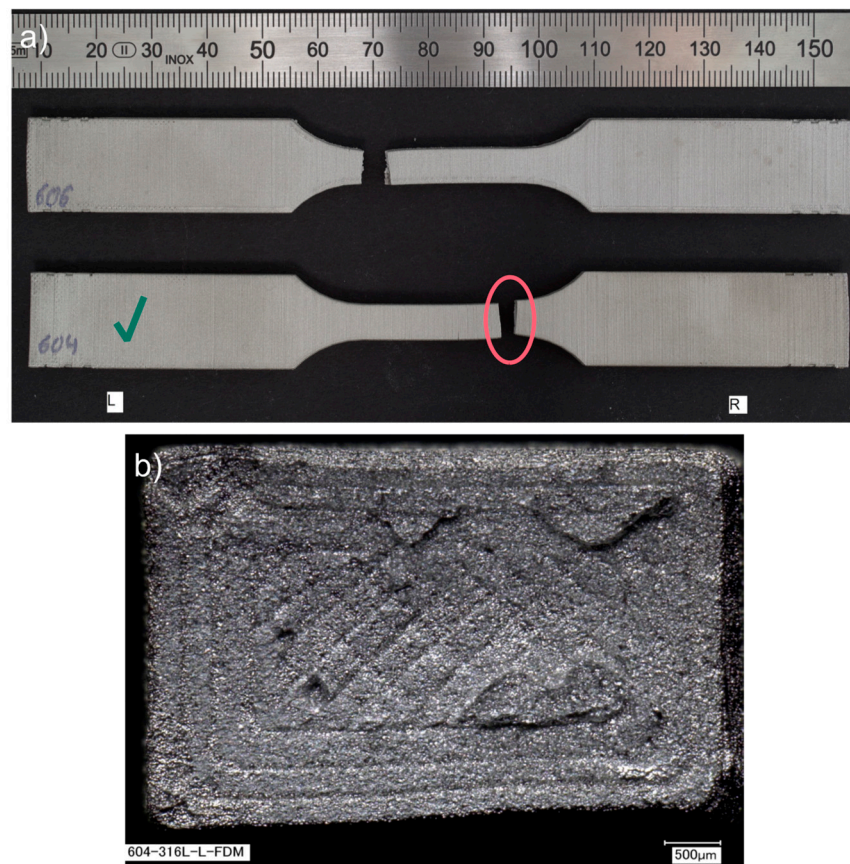


Figure 13. Fatigue fractures of BASF Ultrafuse 316L samples presented as: (a) fractured specimens during the fatigue test; (b) fracture surface (SEM image), left side, specimen 604, at 44,058 cycles. The samples have been numbered, which are visible in the figure. The letters L and R stand for the left-hand and right-hand sides of the sample in the figure. A green check mark means the specimen whose fracture faces were shown.

Additionally, beach (clamshell) marks were not observed on fatigue fracture surfaces. One must remember that the non-occurrence of beach markings means continuous crack growth during load cycling, which is common in fatigue tests of samples at constant load amplitudes. Therefore, while it is reasonable in many cases to identify fatigue as a cause of failure based on beach markings on the fracture face, this should not always be completed [25]. Due to the lack of beach marks, it is challenging to recognize the location of the crack origin; however, on closer analysis of the fatigue fracture face, it is possible to approximate the crack origin based on the radial groove pattern.

For both groups of the SLM specimens, the described failure mechanism was observed, as one can see in Figures 14 and 15. One difference between the two is the noticeably larger necking part for the EOS M 290 samples than for the Renishaw AM400 316L samples, apart from the apparent discrepancy between the test stress levels in the presented specimens that manifests itself in different values of the ratio A_f/A_c .

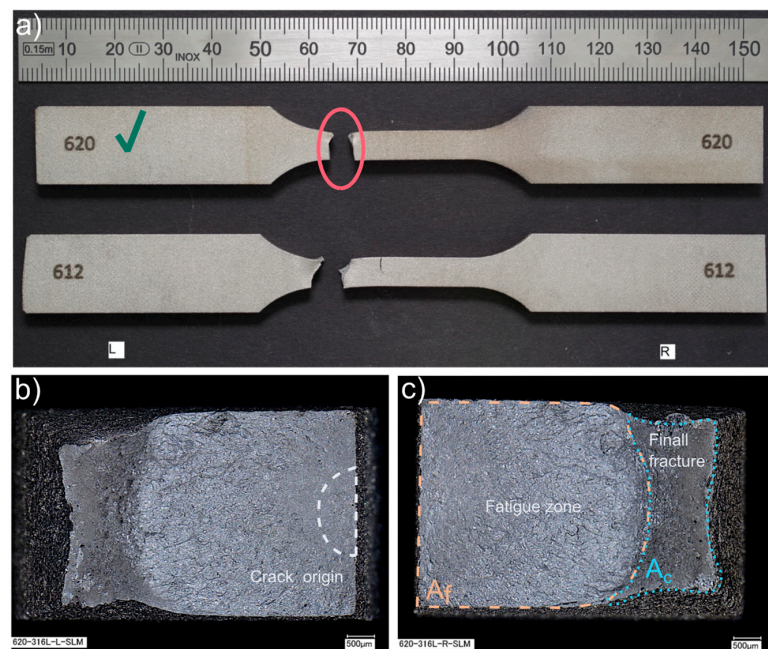


Figure 14. Fatigue fractures of Renishaw AM400 316L samples presented as: (a) fractured specimens during the fatigue tests; (b) fracture surface (SEM image), left side, specimen 620, at 1,492,546 cycles; (c) fracture surface (SEM image), right side, specimen 620, at 1,492,546 cycles. The samples have been numbered, which are visible in the figure. The letters L and R stand for the left-hand and right-hand sides of the sample in the figure. A green check mark means the specimen whose fracture faces were shown.

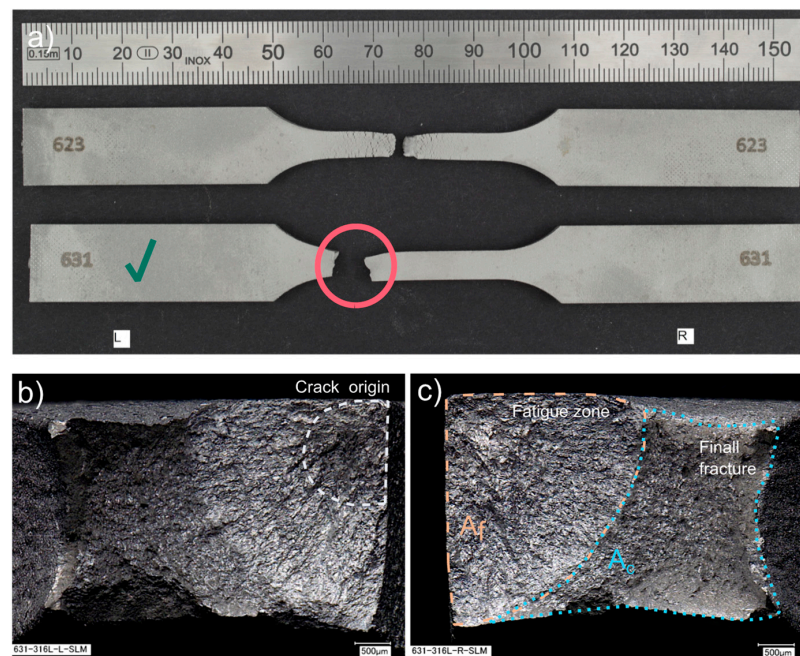


Figure 15. Fatigue fractures of Renishaw EOS M 290 316L samples: (a) fractured EOS M 290 316L specimens during the fatigue tests; (b) fracture surface (SEM image), left side, specimen 631, at 392,641 cycles; (c) fracture surface (SEM image), right side, specimen 631, at 392,641 cycles. The samples have been numbered, which are visible in the figure. The letters L and R stand for the left-hand and right-hand sides of the sample in the figure. A green check mark means the specimen whose fracture faces were shown.

3.4. Charpy Test

The metal FFF specimens of both steel types failed to generate an unmeasurable impact resistance; hence, no results can be reported. The fractures were confined to the printing plane, indicating poor inter-layer bonding. Some portions of the adjacent layer (printing lines) experienced sufficient cohesive strength to be not detached from their original layer. No apparent plastic deformation of the cross-section is visible. One can see a distinct printing pattern on fracture surfaces (Figure 16).

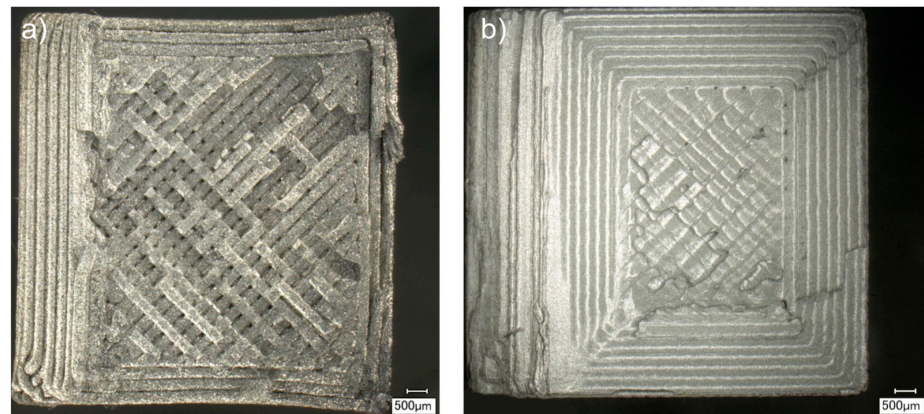


Figure 16. Fractured faces of the Charpy test metal FFF specimens presented as: (a) fractured surface (SEM image) of Ultrafuse BASF 316L specimen; (b) fractured surface (SEM image) of Markforged 17-4 PH specimen.

In contrast, the SLM specimens showed significant resistance and ductility, indicating good layer bonding. The absorbed impact energy was 202 J (standard deviation: 16.4 J) for the Renishaw specimens and 223 J (standard deviation: 17.3 J) for the EOS specimens. The samples demonstrated fractures with large plastic deformations and rough surfaces (see Figure 17).

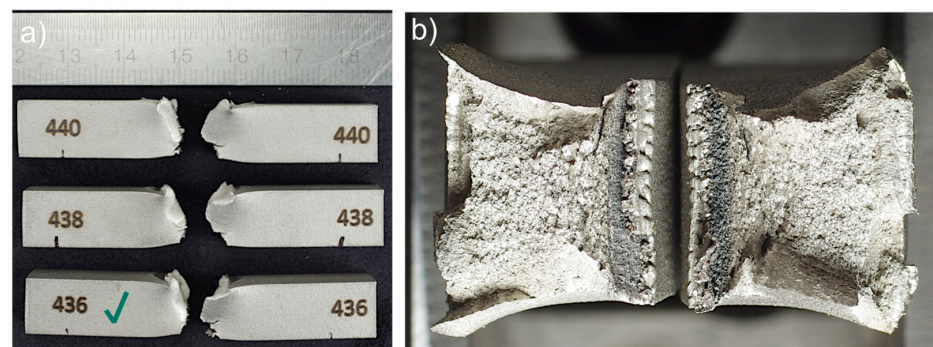


Figure 17. Fractures of Charpy test EOS M 290 specimens presented as: (a) fractured Charpy EOS M 290 specimens; (b) fracture surface (optical microscope image) of the EOS M 290 316L, specimen 436. The samples have been numbered, which are visible in the figure. The letters L and R stand for the left-hand and right-hand sides of the sample in the figure. A green check mark means the specimen whose fracture faces were shown.

4. Discussion

4.1. Test Results

The presented test data support the hypothesis that the metal FFF printed steel materials (316L alloy) have a significantly lower structural performance than the same steel alloy printed using the SLM method. A yield strength reduction of 59% compared to the heat-treated material was determined, and a 65% reduction in comparison with the non-heat-treated material. A drop in the tensile strength of 41% is observed compared

to the heat-treated material and 45% to the non-heat-treated one. The same trend can be seen for the elongation at break. The reduction is 73% compared to heat-treated and non-heat-treated materials, meaning that the material printed via the metal FFF loses ductility significantly due to insufficient bonding of the printed layers observed after a fracture.

Another important discovery is that the fatigue strength for the FFF and SLM specimens of 316L stainless steel differs significantly. For example, for 1×10^6 cycles, the discrepancy is 56% between the metal FFF and heat-treated specimens and 34% compared to the non-heat-treated one, to the detriment of the metal FFF process. What is surprising is that the proposed heat treatment drastically improves the fatigue strength of the SLM specimens. Looking at surface roughness in Table 7, one can see that the metal FFF 316L specimens had a maximum Ra of 7.5 μm and the SLM specimens had a maximum Ra of 5.8 μm . This greater roughness led to a lower fatigue life as well.

The current study found a significant difference in the repeatability of test results to the detriment of the metal FFF technology. The low repeatability for the metal FFF specimens can be seen particularly evident in Figure 6 with the maximum and minimum enveloped curves of the material characteristics and in Table 5, looking at the standard deviations. This finding is valid for all metal FFF specimens.

The most unexpected finding is that the internal defects (voids) between the printed material layers formed by the printed lines determined the strength of the metal FFF samples so severely. The authors expected that effect but not to the measured extent. The phenomenon (delamination of the printed layers caused by air gaps between the extruded lines [7,14,26] while loading) is striking in all test types carried out and for all specimens. This was most evident in the Charpy tests, where no results could be obtained due to the specimens' negligible impact resistance (Table 9). For the SLM specimens, this problem did not exist. Consequently, the greatest energy absorption was measured for the Renishaw AM 400 samples at 223.3 J, which is 9.4% more than for the EOS M 290 specimens, and both sample groups showed typical fracture for ductile materials with large plastic deformation, as revealed in Figure 17.

Table 9. Average and standard deviation (mean \pm standard deviation) of measured impact energy.

Markforged 17-4 PH, J	BASF Ultrafuse 316L, J	EOS M 290 316L (HT), J	Renishaw AM 400 316L, J
Not measurably small	Not measurably small	202.4 \pm 17.3	223.3 \pm 18.0

The degrading effect of high roughness on fatigue strength properties is well known, so roughness control is crucial for structural components. This is also reflected in the standard [20], listing the roughness as a factor influencing fatigue test results. For this reason, our fatigue test samples were also subjected to the roughness test.

The current study found that the surface Ra roughness for the metal FFF 316L specimens is much greater than for the SLM specimens, with a maximum measured difference of 101%. Moreover, the surface roughness can vary much between the metal FFF printers. For example, for the Markforged specimens, the roughness measured on the side of the specimens and along a sample was Ra = 16.6 μm , and for the BASF Ultrafuse samples, only 7.5 μm . A possible explanation for this might be those different printing parameters, printing strategies, and filaments. An example of the surface texture of the specimen can be seen in Figure 7c. A high value of Rz for those FFF specimens confirms the presence of high extremes (peaks and valleys) on their surfaces.

The most surprising aspect of the roughness data is a significant difference in the roughness for the Markforged 17-4 PH specimens depending on the measurement locations. The measurement performed on a flat, along a sample, gives a mean Ra of 8.2 μm but on the side, along a sample, gives a mean Ra of 16.6 μm . An explanation for this might be the type of filament properties used and the printing strategy. The build orientation may also come into play, as thin and tall structures tend to wobble during printing as they are

dragged sideways by the lateral forces exerted by the nozzle, resulting in an uneven surface structure. The drag forces may vary drastically depending on the layer height, material properties, and printing speed.

The very high roughness of the metal FFF samples means that the fracture initiation occurs very quickly, which translates into reduced fatigue strength. This trend is seen in our test results.

The tests made for 17-4 PH stainless steel printed using the metal FFF confirms all findings for the metal FFF 316L samples. The material is very brittle with low strength caused by the presence of internal defects (Figure 7)—voids between the printed layers, which is more evident than for 316L. Those defects also cause low fatigue strength (Figure 12). Due to the randomness of the printed layer delamination, the material's properties have varied greatly, as shown in Figure 6—the large scatter taken up by the minimum and maximum envelope curves. Thus, the most prominent finding to emerge from the test results is that applying the metal FFF technology for structural parts is risky now, but the technology still offers a high potential for further development in the direction of reducing the internal defects of the printed parts.

Contrary to expectations, this study shows a significant difference between the E-modulus for the SLM specimens printed using the different printers (see Table 5). The measured E-modulus for the EOS M290 specimens was 160 GPa, which was 19% greater than for the AM 400 specimens. The heat treatment of the first samples could explain a slight difference, but the 19% variation is unusual. One would have to focus on determining the modulus precisely and see what causes such a significant difference in results. The authors presume that a discrepancy in porosity can explain the observed effect. Another difficulty is the limited literature data on the E-modulus with which a comparison can be made (Table 10).

Table 10. Overview of tensile properties for 316L stainless steel produced using metal FFF, SLM and MIM.

Method	Infill, Print Direction %	Build Orientation, Notes	Porosity ⁷ %	R_e MPa	R_m MPa	A %	E GPa	Source
FFF	100	XY	-	251	561	53	-	[17]
FFF	100	ZX	-	234	521	36	-	[17]
FFF	100 ¹	XY	-	148	444	43	157	[27]
FFF	100	ZX	-	114	206	13	117	[27]
FFF	100	XY	1.5	167	465	31	152	[28]
FFF	100 ²	XY	8.2	-	421	43	-	[7]
FFF	100 ²	ZX	7.3	-	107	2.5	-	[7]
FFF	100 ²	XZ	8.5	-	356	28	-	[7]
MIM	N/A	-	5.3 ⁶	175 ⁶	520 ⁶	50 ⁶	-	[29]
MIM	N/A	water atomized	4	170	460	29	-	[30]
MIM	N/A	gas atomized	2	205	560	58	-	[30]
MIM	N/A	-	2 ⁶	180 ⁶	520 ⁶	40 ⁶	185 ⁶	[31]
SLM	100	XZ	2	412	577	35	139	[32]
SLM	100	ZX	2	365	469	17	78	[32]
SLM	100	XY	0.7	500	630	39	-	[33]
SLM	100	ZX	0.7	500	625	47	-	[33]
SLM	100 ³	ZX	2.3	512	622	20	-	[34]
SLM	100 ³	XY	2.3	430	509	12	-	[34]
SLM	100 ⁴	ZX	1.9	536	668	25	-	[34]
SLM	100 ⁴	XY	1.9	449	528	12	-	[34]
SLM	100 ⁵	XY	-	320	574	50	180	[35]
Wrought	N/A	hot rolled	-	241	621	59	185	[35]

¹ Full density strategy [3]; ² rectilinear infill pattern [15]; ³ single melt pattern [16]; ⁴ checkerboard melt pattern [16]; ⁵ print in the Y-direction; ⁶ typical values; ⁷ porosity is defined as (1—relative density). Where: R_e —yield strength, R_m —tensile strength, A —elongation at break, E —Young's modulus.

4.2. Comparison with Literature

4.2.1. Tensile Test Considerations

Comparing results from metal FFF and MIM specimens is particularly interesting, as the base material composition and the debinding methods are similar [4]. The tables (Tables 10 and 11) show that the printed materials are anisotropic and have lower strength and E-modulus than MIM materials. The elongations at break measured in ZX builds orientation show that the printed material is much more brittle than MIM. This phenomenon is explained in the metal FFF technology by the presence of structural defects perpendicular to the layer direction (Z) [4]. The authors [7] deduced that the bead's orientation perpendicular to the layer direction (Z) increased the average metal particle distance in the layer direction, which could also cause the higher linear shrinkage in this direction. Additionally, if the metal particle distances between those layers are too large, it would cause voids after the sintering process. During tensile tests, these voids oriented perpendicularly to the tensile direction act as stress concentrations leading to poor mechanical properties. For the SLM process, it can be explained that weak interfacial layers for vertically built samples are parallel to cracks, providing more accessible paths for shear bands coalescence and void growth under tension loading than horizontally built ones [36]. Additionally, it has been reported that specimens fabricated in the vertical direction typically contain extensive porosity compared to horizontal directions [37]. Therefore, the presented investigation focuses on analyzing the built-in ZX direction specimens, making a conservative assessment of the mechanical properties of the printed materials.

As it can be seen from the presented literature data, the porosities of the specimens produced by metal FFF are greater than those created by SLM, which can be one of the elements causing the much lower strength of the metal FFF specimens. An unfavorable shape of structural defects and their distribution in the samples reduce the mechanical properties of the FFF samples. As reported [26], the existence of pores showed a significant impact on tensile fatigue strength because large pore-induced voids that contain subcracks near the surface of the sample contribute to the fast failure of the tensile fatigue specimen.

The reported literature data shows that for 316L steel, the best tensile strength results are achievable for SLM in XY build orientation with a slightly lower value of 561 MPa, than for wrought material with 621 MPa, although the largest elongation at the break is reported for the wrought material at 59%. The tendency for the 17-4 PH stainless steel is different in the relevant literature. The highest tensile strength of 1068 MPa (without heat treatment) is stated for metal FFF in the XY build orientation, similar to SLM and wrought material, while the greatest elongation at the break is reported for the SLM sample at 61%. However, the elongation at break for all metal FFF samples is much lower than for other specimens. The lowest strength values with minimum elongation at break are reported for high porosity samples for both materials. The literature data for both materials reveal that MIM specimens show closer strength results to metal FFF specimens, although MIM specimens are more ductile and have high E-modulus comparable with wrought material. The tensile test results of 316L specimens manufactured with SLM show higher yield and tensile strengths than their metal FFF counterparts, while for the 17-4 PH specimens, the yield strength is comparable with the SLM and MIM samples and much lower than for the wrought material.

The variation in the physical properties of the specimens produced by different technology sections can be explained in terms of microstructures developed in the considered manufacturing processes [35]. The microstructure is a very broad concept and includes porosity, pore shape, crack density, dislocation density, grain size, etc. Due to a massive variety of microstructures between those specimens, particularly in porosity and type of internal structural defects, a significant difference in strength is observed.

Table 11. Overview of tensile properties for 17-4 PH stainless steel produced using metal FFF, SLM and MIM.

Method	Infill, Print Direction %	Build Orientation, Notes	Porosity %	R_e MPa	R_m MPa	A %	E GPa	Source
FFF	100 ¹	XY	9.8	443	497	0.79	108	[27]
FFF	100 ¹	ZX	-	412	494	0.95	103	[27]
FFF	100 ²	XY	2.7	604	776	7.7	176	[38]
FFF	100 ²	XY	2.7	605	776	5.9	176	[38]
FFF	100 ⁴	XY aligned in Y	6.5 ⁵	580	794	2.7	128	[39]
FFF	100 ⁴	XY aligned in X	6.5 ⁵	600	795	3.2	131	[39]
FFF	100 ⁴	ZX	6.5 ⁵	647	701	0.76	134	[39]
FFF	100 ⁴	XY	-	688	1068	4.97	138	[9]
FFF	100 ⁴	XZ	-	650	815	0.86	189	[9]
FFF	100 ⁴	ZX	-	615	727	0.98	131	[9]
FFF	100	XY	1.4	746	1034	4.9	176	[40]
FFF	100	XZ	2.6	689	978	4.2	163	[40]
FFF	100	ZX	2.3	668	745	0.8	159	[40]
FFF	100 ⁴	XY	4	800	1050	5	140	[18]
FFF	100 ⁴	XY/H900	4	1100	1250	6	170	[18]
MIM	N/A	Heat-treated	4	965	1140	12	-	[41]
MIM	N/A	1038 °C @0.5 h	-	992	1018	13.4	199	[42]
MIM	N/A	H900	-	1387	1414	12.5	223	[42]
MIM	N/A	As sintered	3.2	730 ³	900 ³	6 ³	-	[29]
MIM	N/A	H900	3.2	965 ³	1070 ³	6 ³	-	[29]
SLM	N/A	ZX	-	830	887	61	133	[43]
SLM	N/A	ZX/H900	-	1050	1117	17	189	[43]
SLM	N/A	XZ	-	493	1058	19	-	[44]
SLM	N/A	XY/650 °C @1 h	-	428	1281	15	-	[44]
SLM	N/A	XY	-	535	1029	18	-	[44]
SLM	N/A	ZX	-	494	979	18	-	[44]
SLM	N/A	ZX/650 °C @1 h	-	483	1298	15	-	[44]
SLM	N/A	XY	-	635	1048	9.8	-	[36]
SLM	N/A	ZX	-	635	942	4	-	[36]
Wrought	N/A	-	-	980	1060	8	200	[45]
Wrought	N/A	-	-	1000	1103	5	-	[20]

¹ Closed triangular cell path [3]; ² printed in ZX and XY; ³ typical values; ⁴ metal X Markforged pathing arrangements [39]; ⁵ maximum porosity as a percentage of the area [39]. HXXX—means age-hardening treatment at XXX °F for 4 h air quenching.

The test results (Figure 6 and Table 5) are in accord with recent studies (Tables 10 and 11), indicating that the materials 316L and 17-4 PH printed using the metal FFF process have much lower strength in the context of yield and tensile strength than the material printed using the SLM method. The elongation at break results also supports previous research, which shows a significant reduction of ductility of the material printed by the metal FFF method due to internal defects and porosity. In contrast, the elongation at the break of 0.4% revealed in the 17-4 PH stainless steel study is lower than those found in the literature, but within the range of values presented by other authors. The obtained test results of the E-modulus for the metal FFF specimens do not differ much from the literature data.

Consistent with the literature, the material printed using the SLM method shows excellent mechanical properties, which can be compared with wrought material (Tables 5, 10 and 11). The obtained strength properties are in a range reported by other authors.

4.2.2. Fatigue Test Considerations

An overview of the fatigue properties of 316L and 17-4 PH alloys is provided in Table 12. The fatigue behavior of the materials as wrought and from the metal FFF and SLM manufacturing methods has been evaluated thoroughly, but studies investigating fatigue

of MIM 17-4 PH appear to be rare in the literature. Moreover, differing manufacturing, post-processing, and testing conditions render direct comparisons difficult.

No study has investigated the fatigue properties of 17-4 PH stainless steel produced using the metal FFF method. Only one paper concerning fatigue testing of BASF Ultrafuse 316L (metal FFF) at three tensile stress levels is available at the time of writing, in which the endurance limit is determined to lie between 80–100 MPa at $R = 0.1$ [26]. The authors indicate the build direction XY of the specimens with a porosity value of 4.4%. They explained these low tensile fatigue strength results as partially due to the unmachined rough surface that facilitates the fast crack creation as well as the existence of internal pores. Indeed, as-built metal FFF specimens exhibit a higher surface roughness as built than SLM and MIM specimens [2,31,35].

Similarly, the porosity is typically the greatest for metal FFF than SLM and MIM, as seen in Table 12. Porosity and roughness data induce that the best results for the endurance limit are achieved for wrought material for both analyzed alloys. As can also be seen in the presented overview, the heat treatment significantly increases the endurance limit for SLM and wrought specimens.

In summary, comparing all the mentioned studies, it is apparent that these significant variations of the mechanical properties are a function of the printing parameters, which confirms the finding from [53]. It can be concluded that the fatigue performance of 3D printed parts depends on the quality of the microstructural morphology, which is driven by porosity, distribution of pores and defects, and their shapes. The resulting material imperfections depend on the printing parameters and the used material. Therefore, wrought material performed the best in reviewed articles (minimum defects), with the machined/HIPed SLM specimens being close. Hot Isostatic Pressing (HIP) post-treatment is an exciting method to reduce porosity. It improves the mechanical properties and microstructure [53] of the 3D printed parts by applying high isostatic gas pressure at elevated temperatures.

Table 12. Overview of high cycle fatigue properties for 316L and 17-4 PH stainless steels.

Alloy	Method	Infill %	Surface/Porosity %	Build Orientation, Notes	Max Stress MPa	Life Cycles	R	Source
316L	FFF	100	as sintered/4.4	XY	80 ¹	* 1.0×10^6	0.1	[26]
316L	FFF	100	as sintered/4.4	XY	100 ¹	1.04×10^5	0.1	[26]
316L	FFF	100	as sintered/4.4	XY	120 ¹	1.05×10^4	0.1	[26]
316L	MIM	-	as produced/4	water atomized	90 ¹	* 3.32×10^6	0.1	[30]
316L	MIM	-	as produced/2	gas atomized	135 ¹	* 1.0×10^7	0.1	[30]
316L	SLM	-	Rz < 0.2 μm	H900	280 ¹	3.0×10^6	-1	[46]
316L	wrought	-	Rz < 0.2 μm	1100 °C, water	210 ¹	* 1.0×10^7	-1	[46]
316L	wrought	-	Polished	-	438 ²	1.0×10^7	-1	[47]
316L	wrought	-	Ra = 0.2 μm	1038 °C, air	220 ¹	* 1.0×10^6	-1	[48]
316L	wrought	-	Ra = 0.2 μm	1038 °C, air	165 ¹	* 2.0×10^7	0.1	[48]
17-4	MIM	-	as sintered/4	H1000	414 ²	* 1.0×10^7	-1	[49]
17-4	MIM	-	as sintered/2	H1000, HIP	448 ²	* 1.0×10^7	-1	[49]
17-4	SLM	100	Ra < 0.7 μm	ZX	225 ¹	1.5×10^5	-1	[50]
17-4	SLM	100	Ra < 0.7 μm	ZX/H900	280 ¹	* 1.0×10^6	-1	[50]
17-4	SLM	100	Ra = 8.38 μm	ZX/CA-H1025	311 ¹	* 1.0×10^7	-1	[51]
17-4	SLM	100	Ra = 0.015 μm	ZX/CA-H1025	480 ¹	* 1.0×10^7	-1	[51]
17-4	SLM	100	Ra = 0.013 μm	ZX/CA-H1025	541 ¹	1.266×10^6	-1	[51]
17-4	SLM	100	Ra = 0.011 μm	ZX/HIP	560 ¹	5.0×10^6	-1	[51]
17-4	SLM	100	as produced	ZX	271 ¹	* 5.0×10^8	-1	[52]
17-4	SLM	100	as produced	ZX/HIP	243 ¹	* 5.0×10^8	-1	[52]
17-4	SLM	100	Machined	ZX	340 ¹	* 5.0×10^8	-1	[52]
17-4	wrought	N/A	as produced	H900	355 ¹	* 5.0×10^8	-1	[52]
17-4	wrought	N/A	Ra = 0.01 μm	H1025	750 ¹	8.91×10^5	-1	[51]

¹ Tensile fatigue test. ² Rotating beam fatigue tests, * runout fatigue test—a test specimen that just will not fail in the given amount of time. HXXX—means age-hardening treatment at XXX °F for 4 h air quenching.

The existing limited literature data do not allow a direct comparison of the test results obtained for metal FFF and SLM samples. The problem is a lack of literature data or different test and material conditions. However, as can be seen, the results obtained for SLM samples (Figure 11) do not differ significantly from those observed by other authors (Table 12). The test results also show the tendency to increase fatigue strength with heat treatment or surface roughness reduction, similar to the literature data.

4.3. Final Assessment

The presented study focused only on two materials, so that the comparisons may be somewhat limited. However, the whole spectrum of tests was conducted for ten specimens per test and per material. This approach gives confidence to the obtained results. To produce specimens, the authors used two different printers per the employed technologies to see an influence of a particular printer. To enhance the outcome of the analysis, it would be beneficial to add the measurement of the porosity by employing CT (computed tomography) scanning of the specimens so the internal defects can be seen and assessed. Unfortunately, this was not possible for the presented project.

The presented results and observations support our hypothesis that FFF-printed steel materials have significantly worse structural properties than the same SLM-printed steel alloy. The main reason for this is the variability of the material properties and the meager impact resistance caused by the characteristics of the metal FFF technology. The findings cast some doubt on whether the metal FFF technique can currently be safely used for structural components. In this case, a better solution is to use SLM technology instead.

5. Conclusions

This study aimed to evaluate the properties of the material (BASF Ultrafuse 316L stainless steel) printed using the FFF method and to compare it with the material produced through SLM. Additionally, 17-4 PH stainless steel specimens made via the metal FFF additive manufacturing (Markforged Metal X) were tested to determine the mechanical properties.

The findings clearly indicate that due to the low repeatability of material properties, and low impact resistance, we currently do not recommend using the metal FFF method to produce any structural parts.

Material printed using the SLM method shows excellent mechanical properties, which can be compared with wrought material. We recommend applying a heat treatment for the SLM parts after printing to improve fatigue resistance. Moreover, the static strength parameters of 316L stainless steel printed via the SLM technique are surprisingly repeatable.

The findings indicate that further development of the metal FFF technology is required to improve the connection between the extruded lines by eliminating air gaps during printing and optimizing the sintering process. Those gaps are a cause of inferior mechanical properties, especially evident in the printed orientation ZX. In the case of 316L stainless steel, a yield strength reduction of 59% compared with the SLM heat-treated specimens and 65% with the non-heat-treated specimens was determined. A tensile strength drop of 41% was measured with the heat-treated samples and 45% with the non-heat-treated samples.

Fatigue strength of 316L is lower for the metal FFF specimens than for the SLM ones; for 1×10^6 cycles, the discrepancy is 34% between the metal FFF and SLM non-heat-treated specimens. For the SLM heat-treated specimens, the difference is more significant and reaches the value of 56%.

Additionally, the scattering of tensile test results of the metal FFF specimens is substantial due to the randomness of the occurrence of internal defects. Furthermore, those defects cause the metal FFF specimens to have no measurable Charpy impact resistance when printed in ZX orientation.

The strength results are abysmal for 17-4 PH stainless steel, where internal defects make the material weak (low static and fatigue strength) and very brittle, with significantly varying material properties caused by internal defects.

The mean Ra surface roughness of 7.4 μm of the 316L FFF specimens was more significant than the SLM specimens, with a mean Ra of 4.4 μm . The Markforged 17-4 PH specimens had a maximum mean Ra roughness of 16.6 μm . Moreover, a significant Ra roughness difference was observed depending on measurement locations ranging from 8.2 μm to 16.6 μm , most probably caused by printing parameters and the build orientation.

Author Contributions: S.K. wrote the manuscript and collected the test results, data interpretation, and test planning. T.D. wrote the manuscript and data interpretation. E.M. conducted the printing and fatigue, and roughness tests. J.M. conducted sample printing. S.H. did microscope analysis of samples and tensile, Charpy, and hardness tests. A.H. conducted sample printing at the University Trier of Applied Sciences. M.W. revised the manuscript and project management. All authors have read and agreed to the published version of the manuscript.

Funding: European Union from the Regional Development Fund (Interreg V A Greater Region Program), German Ministry of Economic Affairs, Transport, Agriculture and Viniculture Rhineland-Palatinate.

Institutional Review Board Statement: Not applicable.

Informed Consent Statement: Not applicable.

Data Availability Statement: Data available on request due to restrictions eg privacy or ethical.

Conflicts of Interest: The authors declare no conflict of interest.

Abbreviations

AM	Additive manufacturing
BJ	Binder jetting
CAD	Computer-aided design
CT	Computed tomography
FDM	Fused deposition modeling
FFF	Fused filament fabrication
HIP	Hot isostatic pressing
MIM	Metal injection molding
PBF	Powder bed fusion
SEM	Scanning electron microscope
SLM	Selective laser melting

References

1. Spencer, O.O.; Yusuf, O.T.; Tofade, T.C. Additive manufacturing technology development: A trajectory towards Industrial Revolution. *Am. J. Mech. Ind. Eng.* **2018**, *3*, 80–90. [[CrossRef](#)]
2. Munsch, M.; Schmidt-Lehr, M.; Wycisk, E. Binder Jetting and FDM: A Comparison with Laser Powder Bed Fusion and Metal Injection Moulding. In *Metal Additive Manufacturing*; Inovar Communications Ltd.: Shrewsbury, UK, 2018; Volume 4, p. 159.
3. Galati, M.; Minetola, P. Analysis of density, roughness, and accuracy of the atomic diffusion additive manufacturing (ADAM) process for metal parts. *Materials* **2019**, *12*, 4122. [[CrossRef](#)] [[PubMed](#)]
4. Suwanpreecha, C.; Manonukul, A. A review on material extrusion additive manufacturing of metal and how it compares with metal injection moulding. *Metals* **2022**, *12*, 429. [[CrossRef](#)]
5. Kan, X.; Yang, D.; Zhao, Z.; Sun, J. 316L FFF binder development and debinding optimization. *Mater. Res. Express* **2021**, *8*, 116515. [[CrossRef](#)]
6. Desktop Metal Inc. *BMD Design Guide*; Desktop Metal, Inc.: Cambridge, MA, USA, 2022.
7. Kurose, T.; Abe, Y.; Santos, M.V.; Kanaya, Y.; Ishigami, A.; Tanaka, S.; Ito, H. Influence of the layer directions on the properties of 316l stainless steel parts fabricated through fused deposition of metals. *Materials* **2020**, *13*, 2493. [[CrossRef](#)] [[PubMed](#)]
8. Alkindi, T.; Alyammahi, M.; Susantyoko, R.A.; Atatreh, S. The effect of varying specimens' printing angles to the bed surface on the tensile strength of 3D-printed 17-4PH stainless-steels via metal FFF additive manufacturing. *MRS Commun.* **2021**, *11*, 310–316. [[CrossRef](#)]
9. Bjørheim, F.; Lopez, I.L.T. Tension testing of additively manufactured specimens of 17-4 PH processed by Bound Metal Deposition. *IOP Conf. Ser. Mater. Sci. Eng.* **2021**, *1201*, 012037. [[CrossRef](#)]
10. GmbH, B.D.P.S. User Guidelines for 3D Printing Metal Parts. Available online: <https://forward-am.com/material-portfolio/ultrafuse-filaments-for-fused-filaments-fabrication-fff/metal-filaments/ultrafuse-316l/> (accessed on 28 July 2022).

11. Poprawe, R.; Hinke, C.; Meiners, W.; Schrage, J.; Bremen, S.; Merkt, S. SLM Production Systems: Recent Developments in Process Development, Machine Concepts and Component Design. In *Advances in Production Technology*; Springer International Publishing AG: Cham, Switzerland, 2015; pp. 49–65.
12. Yadroitsev, I.; Smurov, I. Selective laser melting technology: From the single laser melted track stability to 3D parts of complex shape. *Phys. Procedia* **2010**, *5 Pt B*, 551–560. [[CrossRef](#)]
13. Kokkonen, P.; Salonen, L.; Virta, J.; Hemming, B.; Laukkanen, P.; Savolainen, M.; Komi, E.; Junttila, J.; Ruusuvoori, K.; Varjus, S. *Design Guide for Additive Manufacturing of Metal Components by SLM Process*; VTT Technical Research Centre of Finland: Espoo, Finland, 2016; p. 131.
14. Abe, Y.; Kurose, T.; Santos, M.V.; Kanaya, Y.; Ishigami, A.; Tanaka, S.; Ito, H. Effect of layer directions on internal structures and tensile properties of 17-4PH stainless steel parts fabricated by fused deposition of metals. *Materials* **2021**, *14*, 243. [[CrossRef](#)]
15. Messimer, S.L.; Rocha Pereira, T.; Patterson, A.E.; Lubna, M.; Drozda, F.O. Full-density fused deposition modeling dimensional error as a function of raster angle and build orientation: Large dataset for eleven materials. *J. Manuf. Mater. Process.* **2019**, *3*, 6. [[CrossRef](#)]
16. Renishaw. SS 316L-0407 Powder for Additive Manufacturing. Available online: [https://www.renishaw.com/resourcecentre/en/details/Data%20sheet:%20SS%20316L-0407%20powder%20for%20additive%20manufacturing\(75792\)?lang=en](https://www.renishaw.com/resourcecentre/en/details/Data%20sheet:%20SS%20316L-0407%20powder%20for%20additive%20manufacturing(75792)?lang=en) (accessed on 10 May 2022).
17. BASF. Technical Data Sheet for Ultrafuse 316L. Available online: https://www.ultrafuseff.com/wp-content/uploads/2019/07/Ultrafuse_316L_Technical_Data_Sheet_TDS.pdf (accessed on 30 May 2022).
18. Markforged. 17-4 PH Stainless Steel. Available online: <https://static.markforged.com/downloads/17-4-ph-stainless-steel.pdf> (accessed on 10 May 2022).
19. DIN EN ISO 6892; Metallic Materials—Tensile Testing—Part 1: Method of Test at Room Temperature. DIN: Berlin, Germany, 2020.
20. ISO 1099:2017; Metallic Materials—Fatigue Testing—Axial Force—Controlled Method. International Organization for Standardization: Geneva, Switzerland, 2017.
21. ISO 6506-1; Metallic Materials—Brinell Hardness Test—Part 1: Test Method. In Part 1: Test Method. International Organization for Standardization: Geneva, Switzerland, 2014.
22. ISO 148-1:2016; Metallic Materials—Charpy Pendulum Impact Test—Part 1: Test Method. 3rd ed. International Organization for Standardization: Geneva, Switzerland, 2016; p. 29.
23. EOS. EOS Stainless Steel 316L Material Data Sheet. Available online: https://www.eos.info/03_system-related-assets/material-related-contents/metal-materials-and-examples/metal-material-datasheet/stainlesssteel/material_datasheet_eos_stainlesssteel_316l_en_web.pdf (accessed on 10 May 2022).
24. Chao, Q.; Thomas, S.; Birbilis, N.; Cizek, P.; Hodgson, P.D.; Fabijanic, D. The effect of post-processing heat treatment on the microstructure, residual stress and mechanical properties of selective laser melted 316L stainless steel. *Mater. Sci. Eng.* **2021**, *821*, 141611. [[CrossRef](#)]
25. Milella, P.P. *Fatigue and Corrosion in Metals*; Springer Science & Business Media: Berlin/Heidelberg, Germany, 2013. [[CrossRef](#)]
26. Jiang, D.; Ning, F. Additive manufacturing of 316L stainless steel by a printing-debinding-sintering method: Effects of microstructure on fatigue property. *J. Manuf. Sci. Eng.* **2021**, *143*, 091007. [[CrossRef](#)]
27. Tosto, C.; Tirillò, J.; Sarasini, F.; Cicala, G. Hybrid metal/polymer filaments for Fused Filament Fabrication (FFF) to print metal parts. *Appl. Sci.* **2021**, *11*, 1444. [[CrossRef](#)]
28. Gong, H.; Snelling, D.; Kardel, K.; Carrano, A. Comparison of stainless steel 316L parts made by FDM-and SLM-based additive manufacturing processes. *JOM* **2018**, *71*, 880–885. [[CrossRef](#)]
29. ASTM International. *ASTM B883-19*; Standard Specification for Metal Injection Molded (MIM) Materials. ASTM International: Geneva, Switzerland, 2019; Volume ASTM B883-19.
30. Zhang, Y.; Feng, E.; Mo, W.; Lv, Y.; Ma, R.; Ye, S.; Wang, X.; Yu, P. On the Microstructures and Fatigue Behaviors of 316L Stainless Steel Metal Injection Molded with Gas- and Water-Atomized Powders. *Metals* **2018**, *8*, 893. [[CrossRef](#)]
31. Heaney, D.F. *Handbook of Metal Injection Molding*; Woodhead Publishing: Sawston, UK, 2018.
32. Lavery, N.; Cherry, J.; Mehmood, S.; Davies, H.; Girling, B.; Sackett, E.; Brown, S.; Sienz, J. Effects of hot isostatic pressing on the elastic modulus and tensile properties of 316L parts made by powder bed laser fusion. *Mater. Sci. Eng. A* **2017**, *693*, 186–213. [[CrossRef](#)]
33. Montero Sistiaga, M.; Nardone, S.; Hautfenne, C.; Van Humbeeck, J. Effect of heat treatment of 316L stainless steel produced by selective laser melting (SLM). In Proceedings of the 27th Annual International Solid Freeform Fabrication Symposium-An Additive Manufacturing Conference, Austin, TX, USA, 8–10 July 2016; pp. 558–565.
34. Suryawanshi, J.; Prashanth, K.G.; Ramamurty, U. Mechanical behavior of selective laser melted 316L stainless steel. *Mater. Sci. Eng.* **2017**, *696*, 113–121. [[CrossRef](#)]
35. Eshkabilov, S.; Ara, I.; Sevostianov, I.; Azarmi, F.; Tangpong, X. Mechanical and thermal properties of stainless steel parts, manufactured by various technologies, in relation to their microstructure. *Int. J. Eng. Sci.* **2021**, *159*, 103398. [[CrossRef](#)]
36. Mahmoudi, M.; Elwany, A.; Yadollahi, A.; Thompson, S.M.; Bian, L.; Shamsaei, N. Mechanical properties and microstructural characterization of selective laser melted 17-4 PH stainless steel. *Rapid Prototyp. J.* **2017**, *23*, 280–294. [[CrossRef](#)]
37. Wang, F. Mechanical property study on rapid additive layer manufacture Hastelloy® X alloy by selective laser melting technology. *Int. J. Adv. Manuf. Technol.* **2012**, *58*, 545–551. [[CrossRef](#)]

38. Watson, A.; Belding, J.; Ellis, B.D. Characterization of 17-4 PH Processed via Bound Metal Deposition (BMD). In *Proceedings of TMS 2020 149th Annual Meeting & Exhibition Supplemental Proceedings*; Springer: Cham, Switzerland, 2020; pp. 205–216.
39. Henry, T.C.; Morales, M.A.; Cole, D.P.; Shumeyko, C.M.; Riddick, J.C. Mechanical behavior of 17-4 PH stainless steel processed by atomic diffusion additive manufacturing. *Int. J. Adv. Manuf. Technol.* **2021**, *114*, 2103–2114. [[CrossRef](#)]
40. Suwanpreecha, C.; Seensattayawong, P.; Vadhanakovint, V.; Manonukul, A. Influence of specimen layout on 17-4PH (AISI 630) alloys fabricated by low-cost additive manufacturing. *Metall. Mater. Trans.* **2021**, *52*, 1999–2009. [[CrossRef](#)]
41. Harmer, S. *ASM Handbook Vol. 7 'Powder Metal Technologies and Applications'*; ASM International: Almere, The Netherlands, 2000; Volume 43, p. 22.
42. Jui-Hung, W.; Chih-Kuang, L. Tensile and fatigue properties of 17-4 PH stainless steel at high temperatures. *Metall. Mater. Trans.* **2002**, *33*, 1715–1724. [[CrossRef](#)]
43. Nezhadfar, P.D.; Shrestha, R.; Phan, N.; Shamsaei, N. Fatigue behavior of additively manufactured 17-4 PH stainless steel: Synergistic effects of surface roughness and heat treatment. *Int. J. Fatigue* **2019**, *124*, 188–204. [[CrossRef](#)]
44. Luecke, W.E.; Slotwinski, J.A. Mechanical properties of austenitic stainless steel made by additive manufacturing. *J. Res. Natl. Inst. Stand. Technol.* **2014**, *119*, 398–418. [[CrossRef](#)]
45. Desktop Metal, I. 17-4 PH Stainless Steel. Available online: www.desktopmetal.com (accessed on 15 May 2022).
46. Werner, T.; Madia, M.; Zerbst, U. Comparison of the fatigue behavior of wrought and additively manufactured AISI 316L. *Procedia Struct. Integr.* **2022**, *38*, 554–563. [[CrossRef](#)]
47. Celik, A.; Arslan, Y.; Yetim, A.F.; Efeoglu, I. Fatigue behaviour of duplex treated AISI 316L stainless steel. *Metall. Mater.* **2007**, *45*, 35–40.
48. Strizak, J.; Tian, H.; Liaw, P.; Mansur, L. Fatigue properties of type 316LN stainless steel in air and mercury. *J. Nucl. Mater.* **2005**, *343*, 134–144. [[CrossRef](#)]
49. Marshall, T.P. Injection molding of 17-4 PH stainless steel. *SAE Trans.* **1984**, *93*, 27. [[CrossRef](#)]
50. Yadollahi, A.; Shamsaei, N.; Thompson, S.M.; Elwany, A.; Bian, L.; Mahmoudi, M. Fatigue Behavior of Selective Laser Melted 17-4 PH Stainless Steel. In *Proceedings of the 2015 International Solid Freeform Fabrication Symposium*, Houston, TX, USA, 13–19 November 2015.
51. Molaei, R.; Fatemi, A.; Phan, N. Multiaxial fatigue of LB-PBF additive manufactured 17–4 PH stainless steel including the effects of surface roughness and HIP treatment and comparisons with the wrought alloy. *Int. J. Fatigue* **2020**, *137*, 105646. [[CrossRef](#)]
52. Concli, F.; Fraccaroli, L.; Nalli, F.; Cortese, L. High and low-cycle-fatigue properties of 17–4 PH manufactured via selective laser melting in as-built, machined and hipped conditions. *Prog. Addit. Manuf.* **2021**, *7*, 99–109. [[CrossRef](#)]
53. Al-Maharma, A.Y.; Patil, S.P.; Markert, B. Effects of porosity on the mechanical properties of additively manufactured components: A critical review. *Mater. Res. Express* **2020**, *7*, 122001. [[CrossRef](#)]

4.3 Graded Shell Lattice in a Bicycle Crank Arm

The publication titled *Application of Functionally Graded Shell Lattice as Infill in Additive Manufacturing* (Kedziora et al., 2023) builds on the first paper which described the implementation and optimization procedure of a functionally graded graph lattice structure in a bicycle crank arm. Now, the method is refined and expanded upon by incorporating a lattice splitting method based on scripting. The resulting separation closely matches expected stress field of the crank under a bending load. Furthermore, after obtaining detailed material properties from the preceding tests, the structure's manufacturability is considered more strictly during the design phase. Two Gyroid shell lattices with differing unit cell sizes are investigated. Similar to the original investigation, a DOE study is performed, and its resulting model behaviour is approximated by a response surface fit. The fit is then used for the Multi-Objective Optimization (MOO) approach to reduce the required computation time. The MOO study minimizes the crank's displacement and its mass while respecting a stress limit. Since the MOO approach gives a set of solutions, one result with an adequate deflection value and lattice thickness was chosen. The lowest acceptable lattice thickness value was chosen to be 0.5mm such that it remains manufacturable with the Markforged Metal X system. The part's mass limit is identical to the one imposed in the first investigation, i.e. 360g. The optimized Gyroid lattice model reaches the highest stiffness-to-mass ratio of all the investigated crank models incorporating a graph or surface lattice structure. It is greatly outperforming the aluminium crank arm with a relative improvement of almost 110%. At the same time, it is also able to respect the imposed stress limitation as opposed to the aluminium model.

A prototype was produced with the Markforged Metal X system to prove its manufacturability after Markforged enabled the possibility to manually manipulate support structure settings in Eiger.io (see section 7.6). Although the prototype showed no visible cracks on its external surface, its weight indicated manufacturing issues. At 344g, it only reached 89% of its expected mass. Numerous voids were noted on the internal Gyroid lattice structure where its overhangs surpassed a certain angle, rendering the structure not fully solid. The slicer's restrictions delayed the production significantly, and at this stage the project had to progress to subsequent tasks. The prototype was therefore not physically tested. Nevertheless, the study proved the feasibility of implementing, designing, and optimizing a functionally graded lattice structure in a mechanical part while considering engineering constraints. Additional prototype pictures produced with different materials can be found in section 7.7 of the Addendum.

The author contributed to this paper through the development of the concept and methodology in conjunction with Slawomir Kedziora, as well as by reviewing the original manuscript draft.

Article

Application of Functionally Graded Shell Lattice as Infill in Additive Manufacturing

Slawomir Kedziora ^{*}, Thierry Decker  and Elvin Museyibov 

Faculty of Science, Technology and Medicine, University of Luxembourg, 6 rue Coudenhove-Kalergi, L-1359 Luxembourg, Luxembourg; thierry.decker@uni.lu (T.D.); emuseyibov94@gmail.com (E.M.)

* Correspondence: slawomir.kedziora@uni.lu; Tel.: +352-466-644-5590

Abstract: The significance of lightweight designs has become increasingly paramount due to the growing demand for sustainability. Consequently, this study aims to demonstrate the potential of utilising a functionally graded lattice as an infill structure in designing an additively manufactured bicycle crank arm to achieve construction lightness. The authors seek to determine whether functionally graded lattice structures can be effectively implemented and explore their potential real-world applications. Two aspects determine their realisations: the lack of adequate design and analysis methods and the limitations of existing additive manufacturing technology. To this end, the authors employed a relatively simple crank arm and design exploration methods for structural analysis. This approach facilitated the efficient identification of the optimal solution. A prototype was subsequently developed using fused filament fabrication for metals, enabling the production of a crank arm with the optimised infill. As a result, the authors developed a lightweight and manufacturable crank arm showing a new design and analysis method implementable in similar additively manufactured elements. The percentage increase of a stiffness-to-mass ratio of 109.6% was achieved compared to the initial design. The findings suggest that the functionally graded infill based on the lattice shell improves structural lightness and can be manufactured.

Keywords: functionally graded lattice structure; infill; design exploration; finite element method; bicycle crank arm; additive manufacturing



Citation: Kedziora, S.; Decker, T.; Museyibov, E. Application of Functionally Graded Shell Lattice as Infill in Additive Manufacturing. *Materials* **2023**, *16*, 4401. <https://doi.org/10.3390/ma16124401>

Academic Editors: Alexander Yu Churyumov and Rubén Paz

Received: 24 April 2023

Revised: 28 May 2023

Accepted: 8 June 2023

Published: 15 June 2023



Copyright: © 2023 by the authors. Licensee MDPI, Basel, Switzerland. This article is an open access article distributed under the terms and conditions of the Creative Commons Attribution (CC BY) license (<https://creativecommons.org/licenses/by/4.0/>).

1. Introduction

The significance of lightweight designs has become increasingly paramount due to the growing demand for sustainability. Consequently, this study aims to demonstrate the potential of utilising a functionally graded lattice as an infill structure in designing an additively manufactured bicycle crank arm to achieve construction lightness. The bicycle crank arm (Figure 1) is a part where lightness is essential and self-evident since the vehicle is powered by human muscle power, and minimal energy input is desired.

With this publication, the authors aim to demonstrate that designing and manufacturing parts with optimised internal infills as a functionally graded shell structure using metal Fused Filament Fabrication (FFF) technology is possible. Such a solution does not currently exist, and its creation could contribute to the further development of this new printing technology. In addition, the authors want to prove that this can significantly improve the structural lightness of the fabricated parts. Thus, the authors' efforts were principally targeted at answering the following questions:

- How to represent the geometry of a 3D printed object with a functionally graded infill efficiently?
- How to identify an optimal design among many viable options, and how to include manufacturing constraints?
- Does the developed part fulfil functional requirements?
- How to validate its structural performance theoretically?

- Is manufacturing the part with a functionally graded infill feasible with the metal FFF technology?

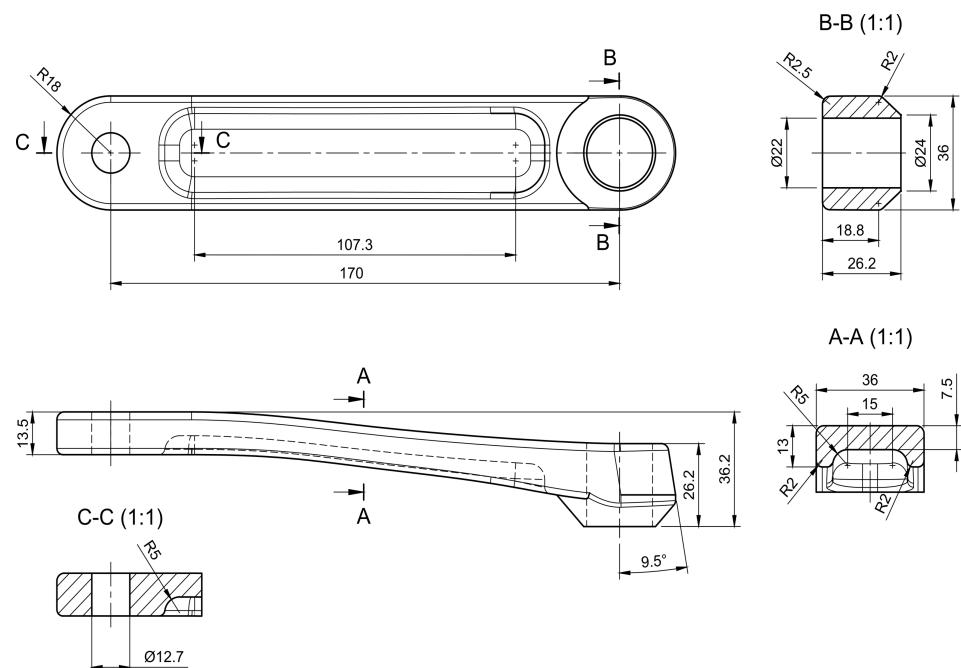


Figure 1. CAD model of crank arm created based on Shimano FC-R450/453 crank arm.

To answer these questions accurately, the authors conducted the entire process of designing and analysing a new part for specific loads, including manufacturing constraints, and then created a prototype. In order to achieve this, three elements must be in place: practical design tools, a structural analysis methodology and a reliable manufacturing method. These three components form an inseparable process that aims to create a lightweight crank arm with an optimised functionally graded shell lattice as the infill.

Thus, this project's primary outcome is a robust design and simulation process for additive manufacturing targeting the metal FFF method with the infill as functionally graded lattices. The metal FFF is often called the Material Extrusion Method (MEX). It characterises that wire-shaped metal-containing plastic (filament) is plasticised in a nozzle and selectively put locally layer by layer, building a 3D part, which is washed and sintered, receiving a finished metal part [1]. A main benefit of the metal FFF technology in the project's context goal is the possibility of creating parts without adding powder-release channels for loose powder from internal cavities, as required in powder bed fusion processes.

Any internal structure of the 3D printed objects, called an infill, was an optimised item. The infill usually has regular structures determined in slicing software as a total volume percentage. The infill structures determine the mechanical properties of the printed parts and impact the printing process [2]. More material in the infill leads to a more robust but heavier object and extends the print time.

As the infill, very promising structures are shell-based lattices because of their stiffness, strength, and printability, supported by the literature review. Therefore, the authors implemented one in the crank arm. Many researchers have been working on the mechanical responses of the lattice structures in recent years [3–9]. However, their projects have focused mostly on specimens or simple parts with basic load cases—compression and/or tension. Unfortunately, attempts were missing to show how to benefit from those structures as the infill in functional parts with complex stress states that cannot be simplified to only tension or compression. The shown work fills this gap by demonstrating a real part's investigation/optimisation process. As a result, the authors used a Gyroid shell lattice for the internal functionally graded infill, mainly considering its stress concentration-free characteristic, sufficient stiffness, and printability.

It should also be noted that there are solutions where an open lattice is a part of the structure. The paper's authors [10] show this structure with the example of a suspension arm analysed using lattice structure optimisation. They concluded that strength improvement and weight reduction could be reached using various types of lattice structure and topology optimisation.

Further, the article text presents the background research to explain the applied methodology and to present the status quo. Next, in the Section 2, the analysis method is described with the level of detail required to reproduce the analyses. The authors also present assumptions that were made, models, and material properties, giving all data. Subsequently, in the Sections 3 and 4, obtained results and comparison with existing designs highlight the achieved improvements. Findings are discussed, focusing on structural performance, part lightness, and the developed method. Lastly, the authors summarised the work in the Section 5 and proposed further directions for the planned investigations.

1.1. Lightweight Constructions

Lightweight constructions are characterised by low material density and unique methods of shaping and specific manufacturing, and all are implemented to achieve maximum stiffness at a given weight and strength. Lightweight and ultra-light structures are critical due to reducing machines' energy consumption and sustainability. The main obstacle to the increased use of lightweight parts is cost pressure in individual industrial sectors [11–13]. However, the future of creating new lightweight products looks very encouraging because of the increasing demand for such products in the last few years. This trend is fostered by the rapidly developing new additive manufacturing production technology.

Understanding natural structures is fundamental to designing lightweight designs effectively. In nature, lightweight objects have been ubiquitous for millions of years and have improved over time due to the evolutionary process. Natural creative processes based on the efficient use of resources have built structures unrivalled for us in many ways. For instance, in the bones of living beings, there is a mechanism causing the bone structure to grow primarily in locations with high cycling strain and disappear where the strain is low [14]—that remodelling occurs in bone mass and architecture because of stimuli obtained from its mechanical environment. That mechanism creates structures with different densities depending on external loads. Plants have also developed lightweight structures through natural evolution; bamboo is an excellent example. The bamboo stem has an optimal solution for strength and stability in specific environmental conditions. Bamboo is a nature-designed functionally graded material because the fibres' volume fraction increases radially from the inner to the bamboo stem's outer surface [15].

However, engineers can achieve structural lightness through a variety of techniques: lightweight and high-strength materials, new design and analysis methods, and modified or new manufacturing technology. The decision on which strategy to use depends on various aspects of the specific development needs. This project aimed to mimic nature in design (biomimicry) by using exploration methods in the design phase and the metal FFF in manufacturing.

1.2. Additive Manufacturing

Additive Manufacturing (AM) processes give engineers the most design freedom and produce physical objects from a computer model with few design restrictions, depositing layer-by-layer material systematically until the whole object is created without any shaping tools. AM technologies have several methods: binder jetting, directed energy deposition, material extrusion, material jetting, powder bed fusion, sheet lamination, and vat polymerisation. A brief review of the entire AM technology can be found in the article [16].

A specific metal AM technology was chosen for the project: metal fused filament fabrication (FFF). This technology allows us to maximise benefits from the optimised internal lattice structure. The primary advantage of this approach is that it facilitates the generation of intricate infill patterns without necessitating the incorporation of power-

release channels. This obviates the need to extract unsintered, loose powder from internal cavities created by the internal structures. Most significantly, this method is highly cost-competitive [1].

This process belongs to the extrusion method, and it is based on a standard FFF method for polymers, also known as Fused Deposition Modelling (FDM). In this method, metal powder bound in plastic is printed layer by layer into the object's shape. The object size is scaled up to compensate for shrinkage during sintering. At that stage, the printed part is soft and brittle (green part). The printed part can then go through a washing stage to remove the binder or directly to the sintering process. Finally, the object is sintered in a furnace to fuse the metal powder into solid metal. The metal part is created as the process's results and can be post-processed like any other metal part. The technology is still in development, and some issues exist, such as print size restriction, support structure requirements, available materials and the printed object strength [17].

1.3. Infill as Functionally Graded Structure

Functionally Graded Materials (FGMs) are materials endowed with spatial variations in the physical properties and chemical compositions, which act as functional qualities. The FGM idea was proposed in the 1980s by Japanese researchers [18], who developed a new class of composite materials for aerospace applications dealing with very high-temperature gradients. FGMs can be artificially created or formed by natural evolution. The examples of bones and bamboo show natural functionally graded materials [15]. Designed FGMs are used nowadays in different industries: machinery [19], medicine (implants) [20], aerospace [19], etc. FGMs are very often cellular materials, which include foams and lattices. Their cellular characteristic can be observed differently depending on the scale: nano (1 Å–1 µm), micro (0.1 µm–1 mm), and meso (0.1–10 mm). In the presented work, the internal structure—the infill has functionally graded properties through the variable thickness. However, their variations are on a millimetres scale, and therefore it would be better to name them Functionally Graded Structures (FGS) [7] instead of FGMs. Using mesoscale is determined by the current capability of metal (FFF) technology.

Designing functionally graded structures requires complex optimisation methods with considerable effort because of a high dimensionality of a model representation causing high computational costs [21]. However, as shown in [21,22], it is feasible to design and create functionally graded materials efficiently. The authors showed in the article [21] the novel general structural optimisation method—the particle swarm optimisation (PSO), a nature-inspired optimiser, for parts with functionally graded material properties. Their numerical simulations presented that the proposed approach is practical, flexible, and computationally efficient for FGM optimisation problems. The developed optimiser outperformed a classical mathematical programming-based optimiser, and the proposed approach is applicable to FGM objects with 2D and 3D geometries and any heterogeneous feature tree structure as a model of FGM variations. In the book [22], the authors give an excellent overview of FGM detailed material mechanics, modelling, applications, and manufacturing methods.

In the research area of FGS, there is a recent article [23] in which the authors propose a new approach for generating bone-like porous structures. The paper proposes a novel formulation for generating porous structures based on structural optimisation considering the optimum design from a mechanical perspective and analysing it through detailed parameter studies. The method is an extended voxel-wise topology optimisation algorithm, which maximises the mechanical stiffness by optimising the distribution of a given amount of material in a specified design domain under a given set of external loads. The authors successfully show the optimised 2D and 3D infill, including a manufacturing constraint—a minimum feature size. The authors did not focus on manufacturing constraints such as overhangs, avoidance, and closed voids containing unsintered powder occurring in the process of Selective Laser Sintering (SLS) for plastic materials. The work showed that it is possible to generate the optimised infill for bone-like structures in conjunction with SLS printing technology.

The next exciting work related to the presented project is the article [2], wherein the authors investigated numerically and tested 2D and 3D biologically inspired infill patterns in cylindrical tubes. The infills were defined in a geometrical form of Gyroid, Schwarz D, and Schwarz P surfaces. The authors found that 2D (honeycomb) infills, such as rectangular or hexagonal lattices, are unsuitable for structural applications with complex 3D geometry because of the resulting imposed anisotropy. In the case of loaded and supported classical structural elements (when a 2D infill pattern is aligned with the principal stress orientation), 2D infills may outperform 3D infills. The authors also proposed optimising the local infill density based on the actual stress fields and performance requirements, modifying an infill wall thickness to achieve uniformly distributed stress. That idea was similarly realised in the presented work, showing that it is feasible for metal FFF printing. Inspired by these articles, we used a general, robust and affordable method of analysis of the functionally graded infill of the crank arm, namely design exploration.

1.4. Design Exploration

Design Exploration (DE) or Design Space Exploration (DSE) [24] is a computer-assisted approach to arriving at an optimal design solution. Design space exploration must be performed carefully because a large complex system may admit millions, sometimes billions, of design alternatives. Therefore, a manual approach to DSE is unachievable. It comprises the following elements: a representation of design space, an analysis equipped with computer-assisted techniques for discovering potential design candidates, and an exploration method for exploring many design candidates [25]. Therefore, various procedures are included in the design exploration; they are the design of experiments (representation), response surface modelling with optimisation (analysis), and data mining (exploration method). These tools enable us to explore, understand, and improve the design before a conceptual phase of product development. The authors used the DE for the presented problem to obtain a set of optimal designs. The implementation of DE is described fully in Section 2.6 to avoid limitations here.

1.5. Lattice Types

Various researchers have investigated different types of lattices/cellular materials and their applications, including structural components [26], energy absorption [27], heat exchange [28], and biomaterials [20]. In the context of application in lightweight structures, it is known that the best option for lightweight constructions is to use stretching-governed lattice structures (strut-lattice types) based on Maxwell's stability criterion [29,30]. The necessary condition for strut-lattice systems to be stretching-dominated lies within the connectivity that the structure's unit cell satisfies Maxwell's criterion for static determinacy [29]. The stretching-governed structures are expected to be about three times as strong as the bending-governed ones [29]. As shown in [29], the deformation of most foams, whether open or closed cells, is bending-dominated.

The presented investigation work was preceded by an analysis of strut-lattice implementation in the identical crank arm, as presented in the article [31]. This article shows the practical application of beam-based functionally graded lattice structures using a blend of manual adjustments and numerical optimisation methods similar to those presented in the current work. Theoretically, the conclusions were that implementing the functionally graded lattice structures (strut-lattice) in the crank arm, combined with high-performance materials, significantly improves the typical bicycle's stiffness crank arm. However, the result holds limited validity due to the uncertain material properties of stainless steel 17-4 PH produced via 3D printing technology.

The article [2] is an example where the authors analysed the infill as a Triply Periodic Minimal Surface (TPMS) in the form of Gyroid, Schwarz D, and Schwarz P surfaces. They are minimal 3D surfaces, meaning a surface that locally minimises its area and has a mean curvature equal to zero at every point [2]. TPMS structures are periodic, continuous, non-self-intersecting, and infinite. Some of these surfaces are known enough to have names

associated with them, such as Schwarz primitive, Schwarz diamond, Schwarz hexagonal, Schwarz crossed of parallels, Neovius, and Gyroid.

The Gyroid surface and shell lattices based on the Gyroid structure were discovered by Schoen [32]. The 3D model of the TPMS Gyroid surface geometry can be described using the following expression Equation (1).

$$\cos(\omega \cdot x) \cdot \sin(\omega \cdot z) + \cos(\omega \cdot y) \cdot \sin(\omega \cdot x) + \cos(\omega \cdot z) \cdot \sin(\omega \cdot y) = t \quad (1)$$

where x , and y are spatial coordinates, $\omega = 2\pi/l$, l is the unit cell's length, and t is the level parameter of the isosurface, which can effectively control the relative density of the gyroid surface [32].

A Gyroid-based structure characterises low-stress concentrations due to zero mean curvature (no joints or discontinuities exist) [33]. Moreover, it has no planes of symmetry and no embedded straight lines, which is beneficial when filling complex geometry regions. Moreover, as shown in [34], the Gyroid infill is nearly isotropic, simplifying its implementation into design and optimisation workflows. Low anisotropy under compression of the Gyroid infill structure was also confirmed by [35]. Moreover, it was noted that the inner Gyroid structure and pattern are more relevant than the material used to build the structural part. In recent years, TPMS-based lattices have been proposed for various engineering applications: body implants, functionally graded structural lattices, heat exchangers and lightweight structures for mechanical components [36]. Furthermore, functional grading TPMS lattice can be used with a proper design to mimic the structure of natural systems [37,38]. Therefore, we assumed that the Gyroid lattice infill is an excellent choice for a 3D-printed infill of complex lightweight parts.

1.6. Crank Arm Design and Analysis

The crank arm design was a topic for various authors. They have used it for investigations with Finite Element Analysis (FEA) and structural optimisation [39–42]. Most of the time, the crank arms had a standard form known from the daily usage of bicycles. However, one can see an innovative crank arm design for additive manufacturing in [40] designed using topology optimisation to maximise stiffness at minimum mass by employing a finite element method. In the context of manufacturing, crank arms are primarily designed for forging and casting for purely economic reasons. However, for high-tech applications, they are made of carbon fibre composites. Materials for the crank arm are typical for lightweight structures, such as aluminium alloys, high-strength steel alloys, carbon fibre composites, and titanium. Nonetheless, bicycle crank arms are manufactured mainly of aluminium, fibre composite, and steel alloys. Material selection depends on bike types, targeted customer groups' applications, and manufacturing costs. Due to the variety of materials, the stiffness-to-weight ratio of the cranks is highly variable.

2. Materials and Methods

2.1. Analysis Method

Several tools to design 3D models exist, but not all can effectively create components with a lattice structure, mainly because of a lack of robust lattice generation methods and their proper representation in existing CAD systems. The manual process of building lattice models using existing CAD software is always very cumbersome. However, the software—nTopology (nTop), version 3.45.4. [43] can give some freedom in the design of the lattices, but exporting to CAD can be done only via mesh formats such as the Standard Triangle Language (STL) format, which is very inconvenient for further integration with other solids. We selected nTop software for the project since it has all the needed lattice generation capability and a sufficient interface to export the lattice model. However, due to the limitations of the simulation and optimisation routines implemented in the version of nTop software available at the time, our optimisation problem could not be performed in nTop. Therefore, Altair HyperMesh and HyperStudy software and programming were employed. The developed process is presented graphically as the flowchart in Figure 2.

The design process started with creating a 3D CAD model; then, a Gyroid infill lattice was created employing nTop. Next, a shell body and the generated infill were served to build a finite element model in HyperMesh. After that, the FEA model was an input for the design exploration (DE) module, resulting in an optimum design of the lattice infill according to a defined optimisation problem. In the last step, the infill as the optimum graded lattice and the shell body were combined into one solid body using HyperMesh and nTop, resulting in an STL file of the print-ready model.

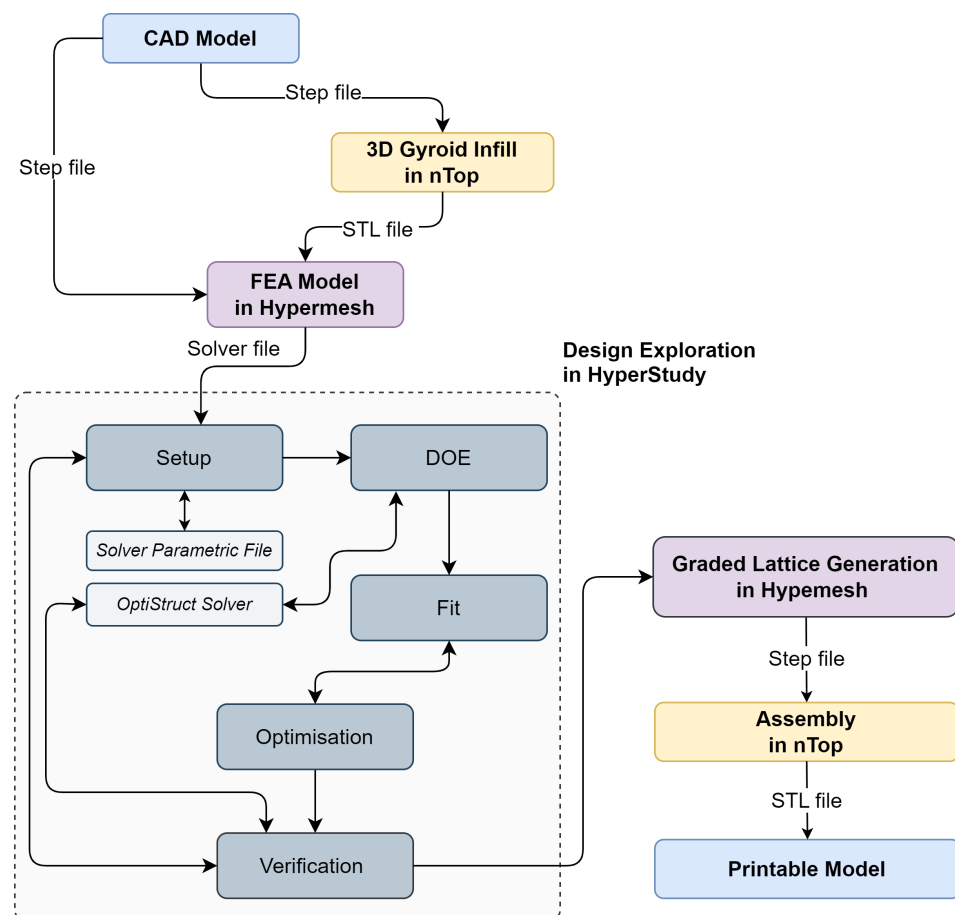


Figure 2. Flowchart of design method of the crank arm with the graded lattice infill.

In order to compare the results of the optimised design with reference models, additional FEA models were analysed. So, four models were built using the same loads and boundary conditions as in the case study. These reference objects were a hollow crank arm model with no infill and two models from a previous publication [31], which have the exact dimensions as the optimised one but two different infills made of a Face-Centred Cubic (FCC) and (Re-entrant) strut-lattice and as well as the original Shimano FC-R450/453 geometry model made of aluminium.

2.2. Loading and Assessment Criteria

Typical loading of the crank arms coming from pedalling is dominated by bending in two perpendicular planes and torsion. The loading is standardised by an ISO standard [44], and for design purposes, it is split into two loading groups—two fatigue load cases. Depending on the bicycle application, a vertical force of 1300 N or 1800 N is required by that standard with minimum test cycles of 100,000 or 50,000. The load is applied on a pedal with an offset of 65 mm from the outboard face of the crank arm. The direction of the crank arm with respect to the horizontal plane is 30° or 45° depending on the load case, as shown in Figure 3. The greatest fatigue force of 1800 N of the 45° load case is defined

for mountain and racing bicycles with cycling requirements of 50,000 and 100,000 cycles, respectively. For the 30° load case, only a force of 1800 N is required with 50,000 cycles. The obligatory load values of the standard appear conservative compared to the test data shown in the article [45]—a 34-year-old healthy man can generate during 2 min on a bicycle power of 200 W with a rotational crank speed of 50 rpm. Therefore, he generates a torque of 38.2 Nm and considering the crank arm length of 170 mm, it translates to the force at the pedal of 225 N. The observed significant difference in the forces can be explained by the desire to ensure safety under all conditions, for example, when the force is applied dynamically by jumping on the pedal. In the presented work, only one fatigue load at 45° (Figure 3) with a maximum force of 1800 N is analysed since it is the most severe case for this crank arm.

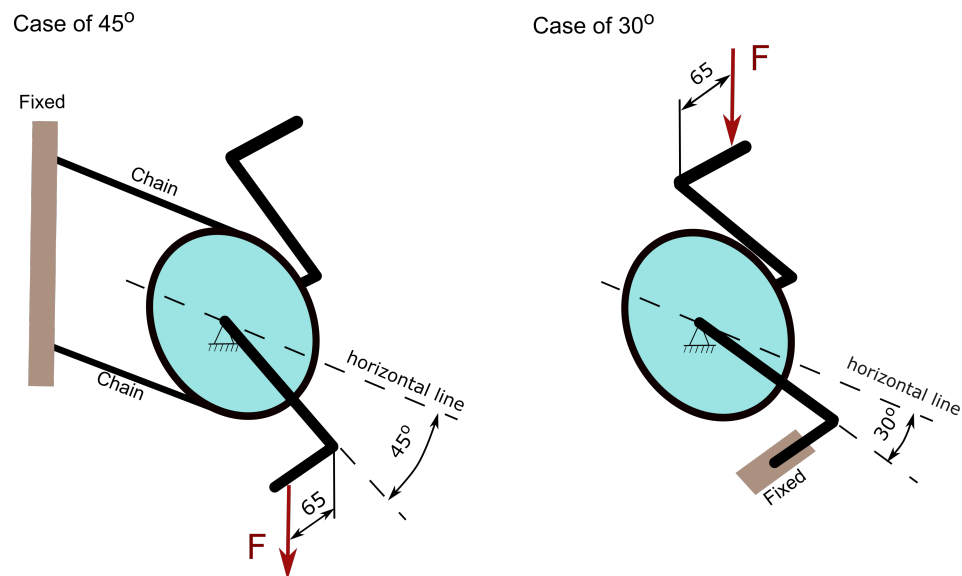


Figure 3. Load configurations defined by the standard [43].

Detailed fatigue analysis can significantly complicate the whole design exploration process, causing the optimisation results to be incorrect because of a mesh-sensitive fatigue model and difficulty in result interpretation. Moreover, the fatigue endurance of a printed object significantly depends on the printing process parameters [17]. Consequently, a simplified assessment criterion was defined by a von Mises stress limit of stainless steel 17-4 PH of 360 MPa. The authors accepted that the chosen limit of von Mises stress is sufficient, considering the printed material strength [17] and the fact that the infill has extra small fillets of 0.35 mm that were not present in the FEA models because their implementation was practically impossible due to the complexity of the infill geometry. Nevertheless, fillets were applied in the stage of the infill assembly with the crank arm body in nTop software for printing preparation.

2.3. Infill as Surface-Lattice Structures

The selected lattice structure is the Gyroid TPMS with two different cell sizes: $10 \times 10 \times 10$ mm (X, Y, Z) and $18 \times 8 \times 10$ mm (Figure 4). The authors used the shell lattice with two unit cell sizes and varying thicknesses. As a result, optimal spatially varying shell lattice structure thickness was found to create the functionally graded infill. The cell size has been chosen to achieve a self-supporting infill structure and avoid closing the cell because of its size in the printed element. As a rule of thumb, an overhang that extends at a 45° angle requires extra support to make it possible to print the structure. Reorientation of the printed object during printing can help to minimise the overhangs. Nevertheless, the proposed infill ensured a print without extra internal support. Unfortunately, the cell size selection limits possible design candidates for the infill.



Figure 4. Internal shell-lattice as gyroid surface: (a) $10 \times 10 \times 10$ mm lattice (X, Y, Z); (b) $18 \times 8 \times 10$ mm lattice.

The initial thickness pattern was identical for both lattice types. The pattern Equation (2) was selected based on the assumption that the crank arm must be symmetric and cantilever bending with torsion is the dominant loading. The defined pattern corresponds approximately to the stress distribution during pure bending. Generally, any thickness pattern is possible, but the choice limits potential solutions. The pattern distribution is displayed in Figure 5. The thickness variability has been limited to 8 design variables to minimise the computational time. The thickness parameters were obtained by dividing a thickness range specified by Equation (2) into eight groups, and the average group thickness was assigned to all group elements. Each variable had a continuous allowable range of variation of 0.5–1.5 mm. The minimum thickness was driven by the resolution of a 3D printer nozzle, while the maximum thickness was restricted by the desire to achieve a recognisable post-print structure of the lattice infill. Too small a cell size could cause a complete closing of the space in the cells in some parts of the infill where maximum thickness could be required.

The initial thickness distribution function shown in Figure 5 is defined as follows by the equation:

$$T(x, y) = 0.685 - 0.001 \cdot x + (0.003 - 3.331 \cdot 10^{-5} \cdot x + 1.172 \cdot 10^{-7} \cdot x^2) \cdot y^2 \quad (2)$$

where x , and y are spatial coordinates and $T(x, y)$ -thickness distribution in mm.

The crank arm design was chosen to be a shell body with a thickness of 1.6 mm with the presented functionally graded infill. The shell body thickness was selected, considering that a printer nozzle size for metal FFF technology can be 0.4–0.6 mm. A thinner wall can cause manufacturing problems with the proper representation of the wall thickness. A thicker wall can lead to an unwanted increase in the mass of the printed object.

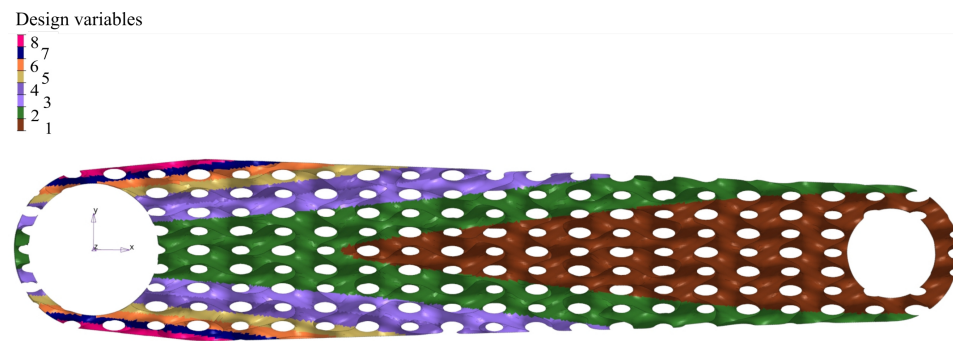


Figure 5. Initial 2D distribution of thickness of shell-lattice, design variables based on Equation (2) and then discretised in 8 groups.

2.4. Manufacturing Constraints

Manufacturing constraints can depend on the specific metal FFF technology. Currently, there are some available commercial solutions; the first one is Markforged with Metal X system [46], the second one is BASF with Ultrafuse material [47], the third one is Virtual Foundry [48], and the last one is Desktop Metal Studio System [49]. In the presented project, the Markforged Metal X system was used to produce a prototype part, and consequently, the following manufacturing constraints need to be considered in the design process:

- The material strength of the green parts determines the required support structure and limits the possible types of internal shell lattice structures.
- The sintering process limits the size of the printed parts and forces to use of support structures.
- The printed material and nozzle size determine the minimum thickness of a printed object.
- Metal X technology offers only some materials to print: 17–4 PH stainless steel, H13 tool steel, A2 tool steel, D2 tool steel, Inconel 625, and copper, whereas 316L stainless steel, titanium Ti6Al4V and aluminium are not yet available for this system.
- A substantial shrinkage after sintering reached approximately 20%, varying in a small range depending on part sizes.
- The material is characterised by high porosity because of the specific production process.
- Materials show strength anisotropy determined by a part orientation during printing.

For the presented project, the authors selected a filament developed by Markforged, stainless steel 17–4 PH (version 2), offering theoretically sufficient strength. As mentioned, bicycle crank arms are manufactured mainly of aluminium, fibre composite, and steel alloys. Therefore, the material selection does not seem unusual for the application.

2.5. 3D Printing, Debinding and Sintering Parameters

The crank arm made of 17–4 PH (version 2) stainless steel was manufactured using the Markforged Metal X system (printing time of 2 d 4 h) with the settings shown in Table 1.

Table 1. Printing settings for the Markforged 17–4 PH (version 2) filament.

Printing Parameters	Value
Nozzle size, mm	0.4
Layer height, mm	0.125
Print bed temperature, °C	115
Metal hotend temperature, °C	220
Chamber temperature, °C	48
Oversizing factors: X, Y, Z, %	19.5, 19.5, 20

The debinding and sintering processes were done in-house with the default parameters developed by Markforged [47]. The Wash-1, a solvent-based debinding system with Opteon

SF-79 liquid, was utilised for debinding the green part for 1 d 8 h. For the sintering, Sinter 1, a tube furnace was employed to produce the 3D-printed crank arm.

2.6. Design Exploration

The design exploration methodology was employed to find the best possible configuration by modifying the design variables in a design space. The DE analysis was conducted using Altair HyperStudy software [50], the Altair OptiStruct [51]—a finite element solver, Multiobjective Optimisation (MOO) [52], and other auxiliary tools for data analysis. To begin this process, eight design variables—the lattice shell thickness pattern were selected, as shown in Figure 5, based on the distribution described by Equation (2). Those variables and other parameters were implemented in an input file of the OptiStruct solver via its parameterisation that allows an optimisation process. Once the finite element model and the design variables were established, design objectives were defined as the crank's mass and its maximum displacement. We decided to use MOO, minimising the objectives with a design constraint defined as von Mises stress of 360 MPa. Since we had set it as multiobjective optimisation with two contradictory objectives to minimise the total mass and the maximum deformation, the design exploration gave not one but a set of optimal solutions.

Once the DE model was set up, a Design of Experiments (DOE) study was employed as prerequisite steps for an approximation stage, fitting a predictive mathematical model to the data to create a response surface model approximation (Figure 2). The DOE study's objective was to distribute the design points uniformly in the design space to feed them into a fitting method to predict the model behaviour accurately. The Modified Extensible Lattice Sequences (MELS) method [53] was employed for the DOE studies. MELS is a quasi-random sequence designed to distribute the design points in space, minimising clumps and voids evenly, and is based on extensible lattice sequences [54]. The fitting process used the Fit Automatically Selected by Training (FAST) method [53], automatically building the best-fitting functions by testing all implemented methods. Then, instead of finite element analysis, that built approximation was utilised to shorten the optimisation process time, avoiding typical problems with limited computation resources. Following appropriate procedures, the multiobjective optimisation step was employed. The Global Response Search Method (GRSM) [53] was used for optimisation. The algorithm generates a few designs, including global sampling, to ensure the right balance of local and global search capability. The response surface is updated with the newly generated designs to improve the model fit. Afterwards, response surface-based optimisation is conducted. As a result of the described process, the non-dominated solutions (Pareto-optimal set) are determined. Here is where the entire analysis process ends, and the optimum solutions were selected, considering other factors that could not be considered during the DE process, such as manufacturing constraints.

2.7. Finite Element Model

We built a crank arm finite element model using two elements: second-order 10-node tetrahedron elements and first-order shell quad elements (Figure 6). The OptiStruct solver was employed to analyse the developed model. Since the deformation of the part is expected to be small with stress below the yield strength, the FE analysis is linear, allowing for a shorter optimisation time. However, the model linearity does not limit the generality of the proposed method in any way. The shell model of the internal lattice infill allowed us to parametrise the models required for the design exploration phase. Contact elements connect the external solid elements with the shell elements of the infill (Figure 6). The initial lattice thickness distribution was defined, as illustrated in Figure 5, applying eight design variables (shell element thickness). For that purpose, a TCL/TK script was developed that assigns a particular thickness to the shell elements with a defined number of the variables based on Equation (2). The reduced number of parameters contributed to the simplicity when optimising and generating a final STL model. However, increasing the variables at the cost of additional modelling complexity is possible.

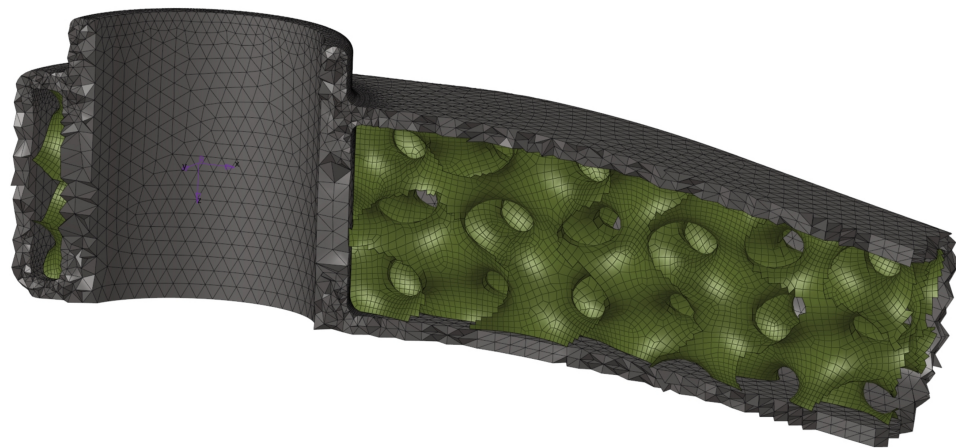


Figure 6. Analysed FE models with $10 \times 10 \times 10$ mm (X, Y, Z) shell-lattice, view of solid and shell elements.

2.7.1. Load and Boundary Conditions

As we described earlier, only the load case of the fatigue at the crank arm location of 45° , with a maximum force of 1800 N, is analysed since it is the most severe case for the designed crank arm. The force was applied using the distributing type 3 rigid body element (RBE3), and the crank arm was fixed using the RBE2 element, as stated in Figure 7. The drive (independent) node of the RBE2 element was created in the centroid of the large hole used to fix the crank arm onto the shaft. All degrees of freedom of that node were fixed.

The force offset of 65 mm from the outboard face of the crank arm was used to simulate a realistic load condition; the force was assumed to be applied to the middle of a pedal.

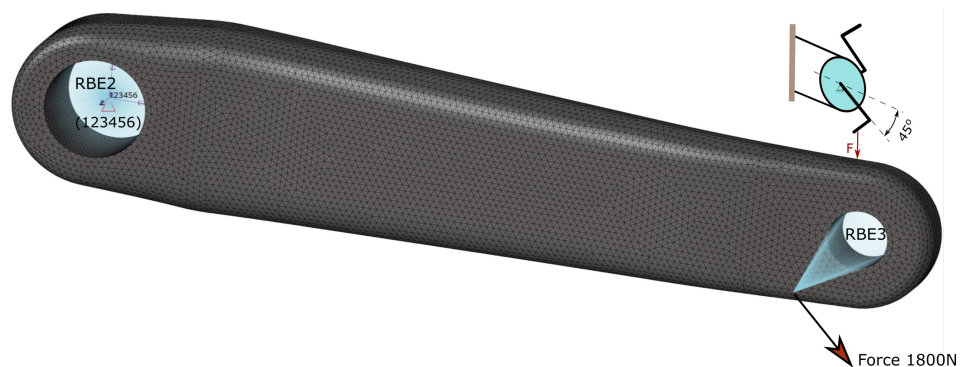


Figure 7. Load and boundary conditions.

2.7.2. Contact

The solid and shell elements are connected via contact elements; all degrees of freedom of nodes of both element types are bounded via a contact penalty algorithm. The Freeze contact interface is used, which enforces zero relative motion on the contact surface, and the rotations at the slave node are matched to the rotations of the master patch. The Freeze contact type is predefined in the OptiStruct solver as one of the offered contact types.

2.7.3. Materials of Models

The mechanical properties of 17–4 PH (version 1) stainless steel as printed are presented in Table 2. The data come from the Markforged document [55] and the articles [17,56], where the properties have been experimentally verified, and as we can see in these publications, the 17–4 PH steel is very brittle as printed with varying strength caused by material defects. In the article [17], the authors argue that applying the metal FFF technology for structural parts is risky. Even so, the choice of FFF metal technology for the current project is enforced,

as it allows parts to be manufactured without trapped metal powder inside the infill. The technology still offers a high potential for further development.

Table 2. Material properties reported in the literature for 17–4 PH (version 1) as sintered.

Parameters	[16]	[54]	[55]
Print direction	ZX (Upright)	XY (Flat)	XZ (On Edge)
Young's modulus, GPa	142	140	189
Poisson' ratio	-	0.272	-
Tensile strength, MPa	496	1050	815
Yield strength, MPa	441	800	650
Elongation at break, %	0.4	5	0.86
Density, g/cm ³	-	7.44	-
Hardness	261 HB	30 HRC	-

Seeing the large spread of material properties and existing anisotropy of material caused by the printing, we decided to select the properties shown in Table 3 for our research and used a linear isotropic material. Additionally, one of the reference models was the original Shimano FC-R450/453, made of a precipitation-hardened aluminium alloy, and its properties are listed in Table 3.

Table 3. Material properties used in the analysis.

Parameters	Stainless Steel 17–4 PH (As-Sintered)	Aluminium 6061–T6
Young's modulus, GPa	170	69
Poisson' ratio	0.27	0.33
Stress limit, MPa	360	-
Density, g/cm ³	7.44	2.7

3. Results

3.1. Design Exploration

The output of the design exploration step is shown in Figure 8. A Pareto plot shows the sets of optimum designs for the defined constraints and objectives. The figure compares the results obtained from the analysis of the two models analysed of the shell-lattice types. The two curves obtained are linear, with Pearson's R coefficient being adequately -0.9986 and -0.9995 for $18 \times 8 \times 10$ mm and $10 \times 10 \times 10$ mm curves, and offset from each other. The curve for the $18 \times 8 \times 10$ mm lattice is shifted to the left of the $10 \times 10 \times 10$ mm lattice curve. The figure shows that the solution with lattice $18 \times 8 \times 10$ mm performs better regarding the stiffness-to-mass ratio. The difference between both lattice types is significant and reduces with the mass decrease since both curves have a different slope. The curve slope of the $18 \times 8 \times 10$ mm lattice is smaller than the second lattice. Looking at Figure 8, it is apparent that there are many different possible solutions; however, the printability without internal support and the print resolution limit the possible design candidates.

The minimum mass of 348.3 g was obtained for the constant thickness of the lattice of 0.5 mm for the lattice $18 \times 8 \times 10$ mm with a maximum displacement of 1.985 mm. Unfortunately, this solution is not the best for manufacturing reasons and print quality; as explained, 0.5 mm thickness is difficult to achieve for the infill during printing. Including the part oversizing because of the post-sintering shrinkage, the wall of 0.5 mm needs to be printed as 0.6 mm. The nozzle size utilised in the experiment was 0.4 mm. Consequently, printing lines with thicknesses that deviate from multiples of the standard line width of 0.4 mm, as defined by the Markforged preprocessor, deteriorate part quality due to poor material connectivity at the point where lines merge. As a result, selecting a structure with a slightly thicker minimum wall thickness to mitigate these line interface issues is a more prudent approach. This would also increase rigidity and facilitate the manufacturing

process of the arm. Thus, to prototype the arm, the authors choose the design that is marked in Figure 8—iteration 61. The selected design has a mass of 385.8 g with a resulting displacement of 1.9 mm. We showed the thickness distribution of the selected solution (iter. 61) in Figure 9a, and in this design candidate, the region of the critical thickness of 0.5 mm is greatly reduced. Considering technological limitations, this distribution was slightly adjusted to the printing prototypes (Figure 9b).

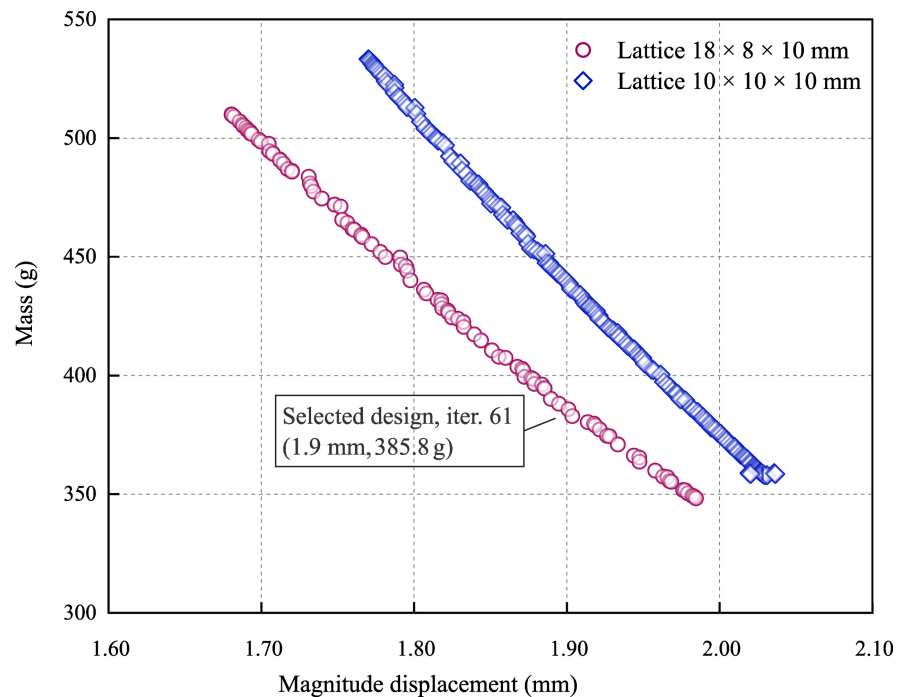


Figure 8. Pareto-optimal set of solutions.

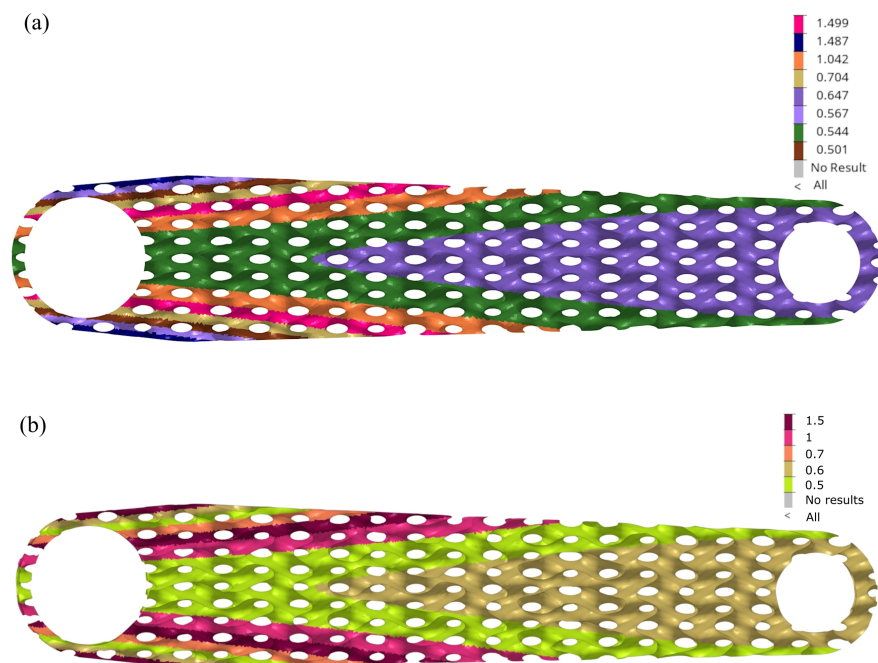


Figure 9. Thickness distribution of shell-lattice of infill: (a) thickness of selected optimum design iter. 61; (b) thickness defined for printed prototypes.

The general thickness distribution is not surprising—it follows approximately a bending stress map in a cantilever beam. However, a specific local perturbation in the distri-

bution is unexpected around the large hole: a sudden decrease in thickness in the lattice’s outer layers and a renewed increase.

3.2. Optimum Solution

Comparing the mass of the analysed crank arms results in Figure 10 and Table 4, the chosen design with shell lattice has 1.81 times greater mass than the reference design and slightly more than the crank arm with the strut-lattices having that ratio of 1.67. It should be remembered that the reference arm (Shimano FC-R450/543) is made of aluminium, and the others are made of stainless steel. Therefore, the obtained ratio of 1.81 is a reasonably good result compared to the specific density ratio of 2.8 between steel and aluminium. The authors added the mass of the hollowed arm with a wall thickness of 1.6 mm, having a ratio of 1.25. However, it must be remembered that the hollowed construction does not meet the criteria for maximum permissible von Mises stresses of 360 MPa.

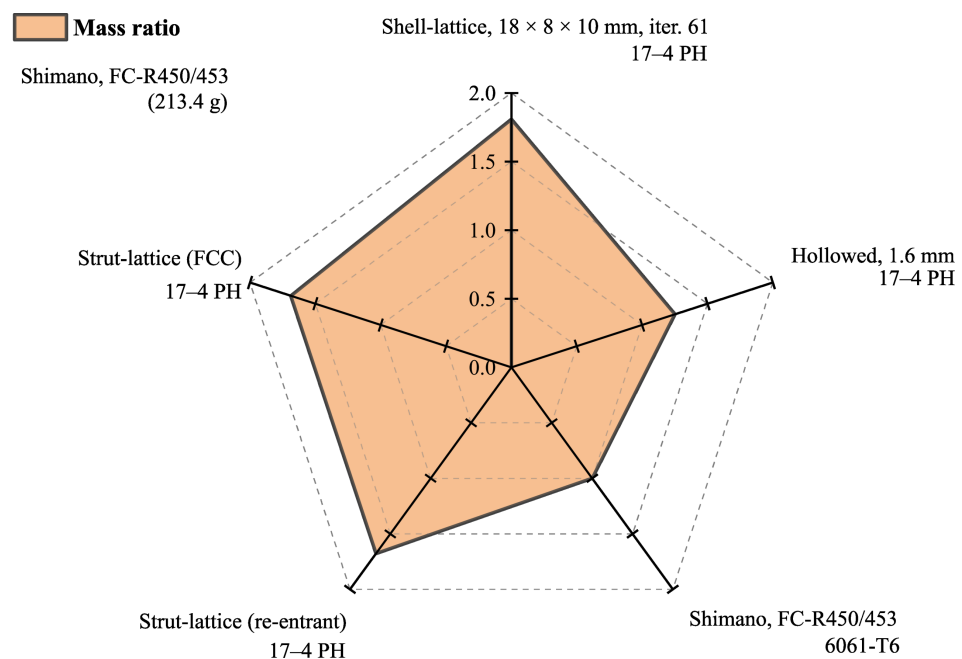


Figure 10. Mass comparison between designs.

Table 4. Results of analysed designs.

Design	Material	Mass, g	Displacement, mm	Stiffness, N/mm	Stiffness-to-Mass, $10^6 \cdot (1/s^2)$
Shimano FC-R450/453	6061-T6	213.4	7.20	250.2	1.172
Strut-lattice (re-entrant)	17-4 PH	357.0	2.61	689.7	1.927
Strut-lattice (FCC)	17-4 PH	360.0	2.55	705.9	1.961
18 × 8 × 10 mm (Iter. 61)	17-4 PH	385.8 *	1.90	947.4	2.456
Hollowed, 1.6 mm	17-4 PH	267.3	2.37	760.5	2.845

* The printed crank arm had 343.8 g.

More exciting results are shown in Figure 11 and Table 4, where the stiffness-to-mass ratio is presented for the same structures. Here, we see that the developed arm with the surface lattice is by far the best in this category, which also respects the stress restriction. The ratio reaches a value of 2.10 compared to the design with the strut-lattices of 1.67, including the reference design of 1. The best overall solution for 2.43 is the hollow design, but it should be remembered that it is excluded because of unacceptable stress levels.

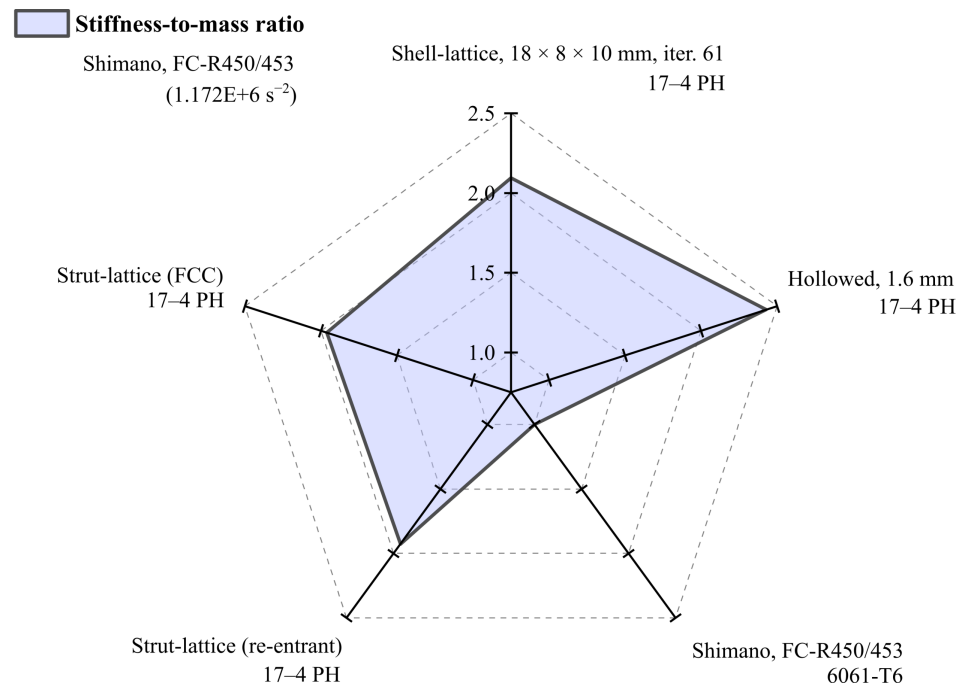


Figure 11. Stiffness-to-mass ratio comparison between designs.

Figure 12 presents the magnitude of displacement of the selected arm design under a defined load, as the evidence shows that the load is dominated by bending in two planes and torsion. For the structural assessment, the maximum displacement of the node at the pedal centre (load application point) was considered.

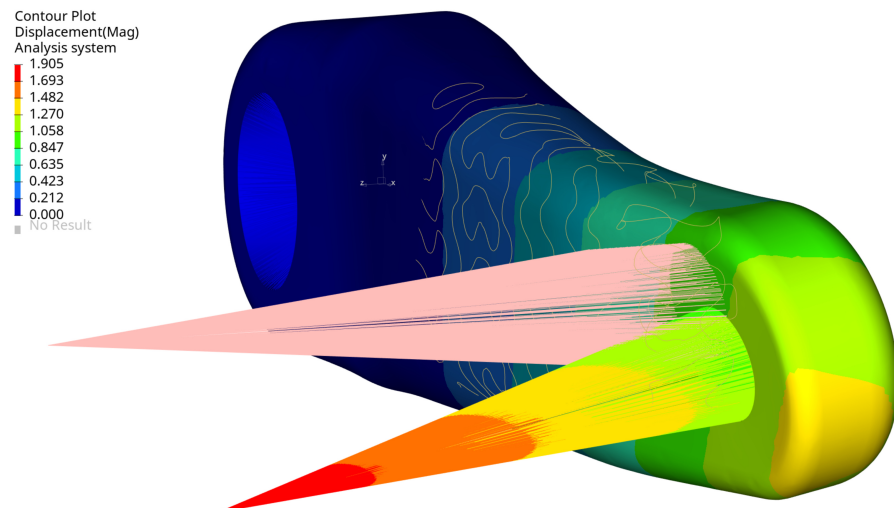


Figure 12. Magnitude of displacements (mm) selected optimal design, iter. 61.

Figure 13 displays the von Mises stress in the crank arm's internal shell lattice for the selected optimal configuration. As can be seen, the stress level is below the defined stress limit of 360 MPa. The results are plotted from the shell elements' external layers (top and bottom). The maximum stress is located around the small hole in the crank arm. There, the load is applied through the RBE3 element. The maximum stress position is not surprising; they should typically be expected around the fixation and the load location. This effect can also be seen in Figures 14 and 15 on the arm's external surface close to the hole used to assemble a pedal. That stress concentration shows the level of von Mises stresses below 333 MPa.

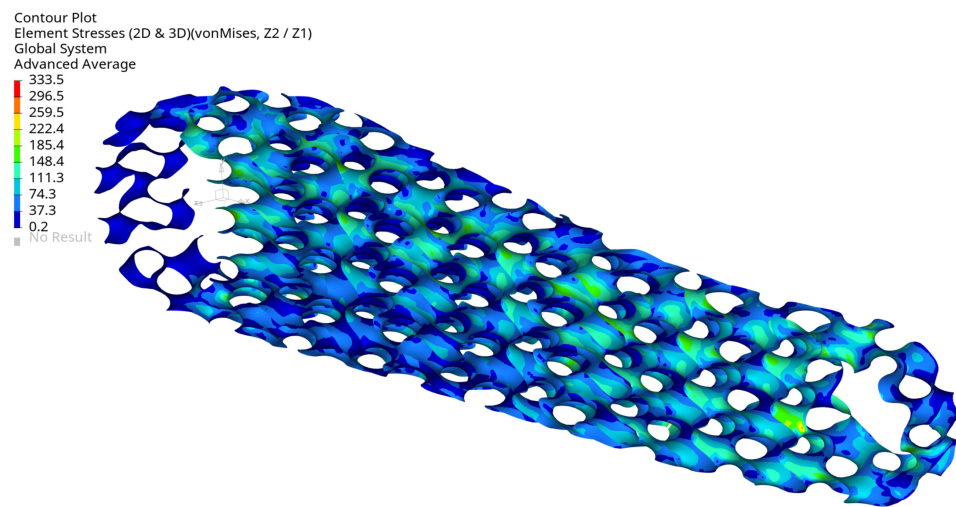


Figure 13. Maximum von Mises stress (MPa) for selected optimal design at maximum load, view 1, iter. 61.

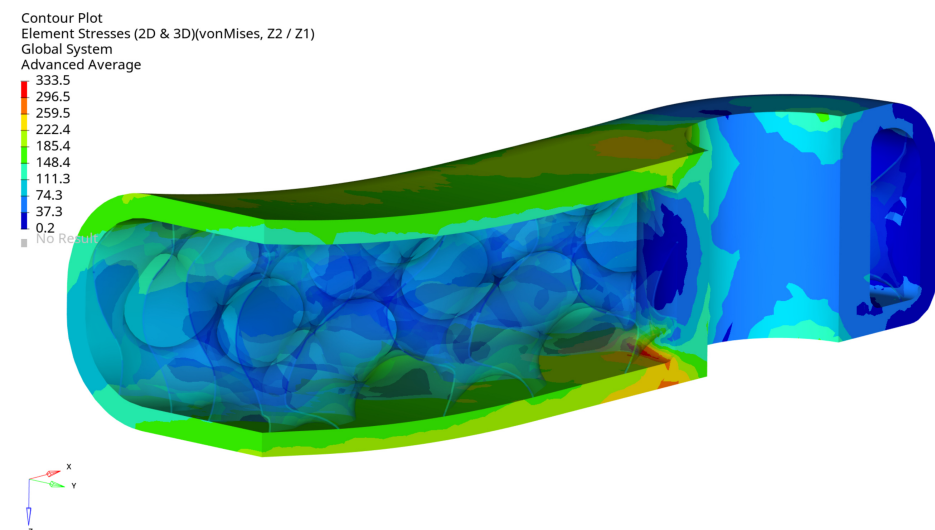


Figure 14. Maximum von Mises stress (MPa) for selected optimal design at maximum load, view 2, iter. 61.

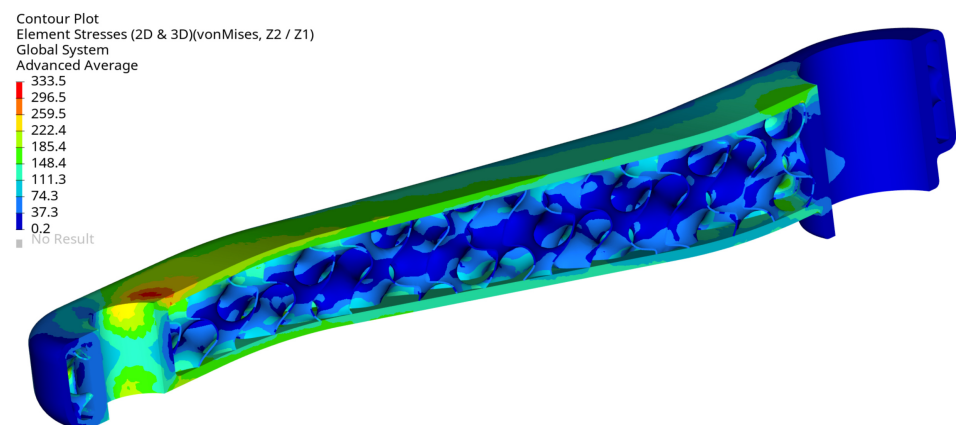


Figure 15. Maximum von Mises stress (MPa) for selected optimal design at maximum load, view 3, iter. 61.

Figure 13 shows that the maximum stress of 333.5 MPa is in the arm's shell part inside the cavity on the radius. The stress level is acceptable, but it is evident that local geometry modifications can reduce the stress in future investigations.

The arm's fixation looks very well designed, the stress level is relatively low, and the design does not need to be modified. The stress level is below 333.5 MPa, and the maximum is located in the radius of the external surface Figure 16. The maximum stress localisation is fully explainable and expected due to how it is fixed and the load type. In reality, lower stresses are expected because the used boundary conditions are simplified, resulting in stiffening the places where the loads have been applied. That effect translates into higher stresses and is created directly by the RBE2 element, which adds locally infinite stiffness to a structure.

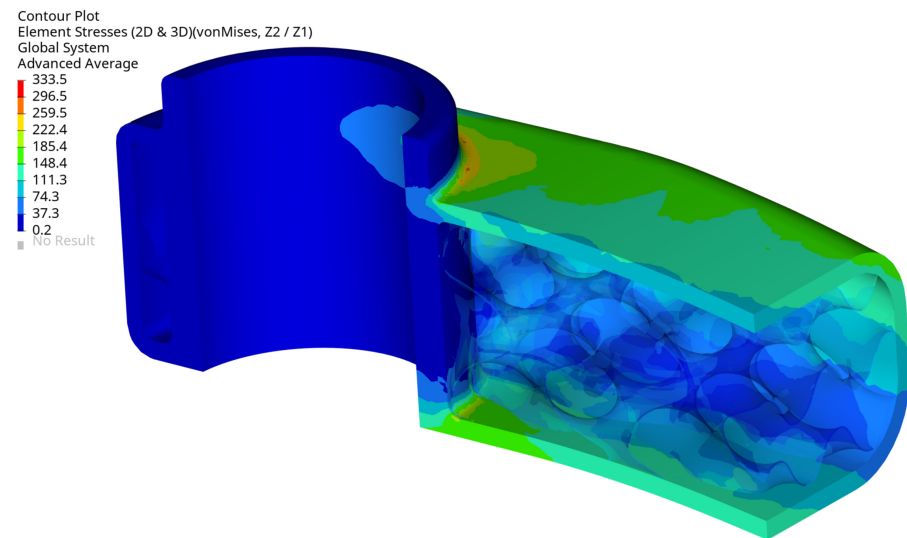


Figure 16. Maximum von Mises stress (MPa) for selected optimal design at maximum load, view 4, iter. 61.

3.3. Prototype

Complex geometry requires many elements to represent the print model properly; therefore, the size of the generated STL file (inter. 61) was huge, about 600 MB. Finally, it was possible to handle the file without significant difficulties. A part of the generated STL model is shown in Figure 17; it reflects the complex internal geometry of the developed infill.

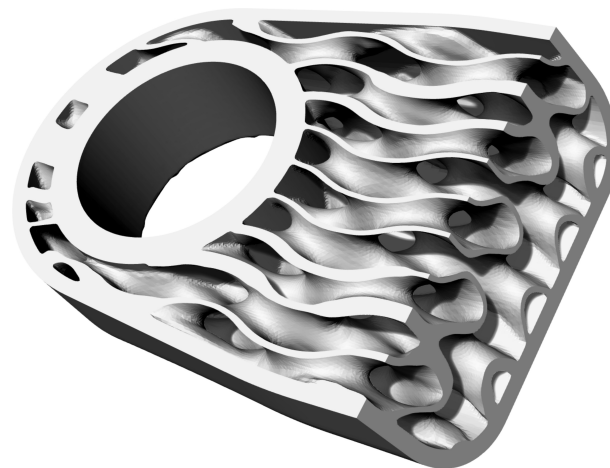


Figure 17. Internal structures, iter. 61, STL model (part of the whole model).

The sintered crank arm (Figure 18d) had a mass of 343.8 g and no visible cracks on its external surfaces. The green part and the sintered one had a typical surface roughness determined by layer-by-layer material deposition of the metal FFF technology, as shown in Figure 18. Interestingly, the measured mass of 343.8 g of the crank arm represented only 89% of the 3D model's mass of 385.8 g, and an explanation of this will be provided later in the article.

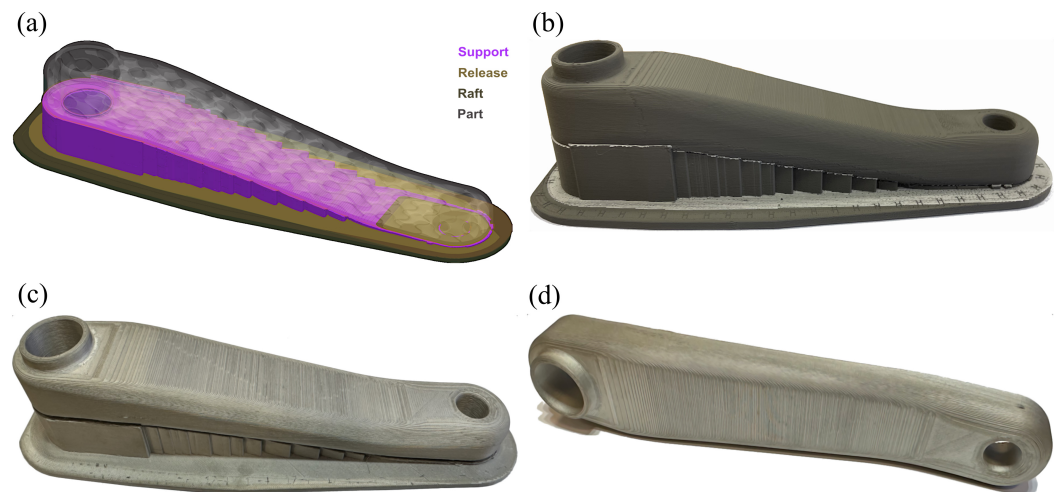


Figure 18. Prototype of the crank arm, iter. 61: (a) model with support and raft structures; (b) green part; (c) sintered part with support structure; (d) sintered part.

The printing and sintering process achieved the crank arm's desired external dimensions, as shown in Figure 19. The external surface of the part has a typical metal FFF technology texture caused by the distribution of material layers while printing.



Figure 19. Views of the printed and sintered crank arm (iter. 61).

Additionally, the infill structures showed the same typical texture of metal FFF parts. However, the infill was not represented entirely correctly; Figure 20a–c shows that unsintered and missing layers caused gaps in the infill, occurring randomly throughout its volume.

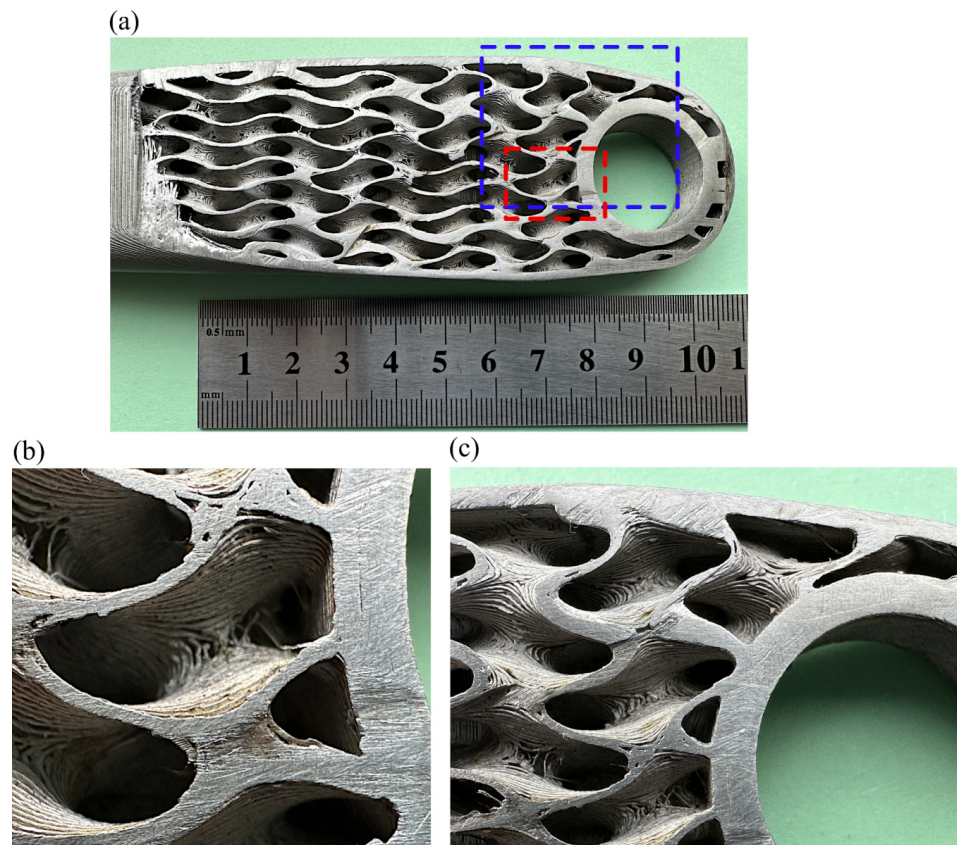


Figure 20. Views of the sintered cut crank arm (iter. 61) showing the internal structure: (a) whole cut section; (b) view of the infill marked by the red rectangle, (c) view of the infill marked by the blue rectangle.

4. Discussion

It was hypothesised that the functionally graded internal shell lattice could be implemented in real mechanical parts and that the applications could benefit from increased stiffness-to-mass ratios. The literature shows that many works are devoted to specimens rather than geometrically complex parts. The presented work shows that it is feasible to design the functionally graded lattice as the infill in the crank arm using the metal FFF technology and existing engineering tools. A novel design and analysis method is proposed. In detail, the authors show how to efficiently represent the crank arm's geometry with the functionally graded infill and how to search the design space for the optimum design. Finally, the optimum configuration was selected considering the manufacturing requirements from the sets of optimum designs for the defined constraints and objectives represented by the Pareto plot in Figure 8. The results show that a satisfactory outcome regarding the stiffness-to-mass ratio is possible. In the presented work, that ratio is much better than the existing reference design (Table 4). A percentage increase of 109.6% was achieved, although the lattice cell was chosen to meet the manufacturing requirements (overhangs and visible lattice structure after sintering). Theoretically, there is room for improvement by selecting a more appropriate cell grid and thickness distribution, but this requires developing a new sophisticated selection strategy that must include aspects of a chosen manufacturing method.

The authors believe the chosen stress limit of 360 MPa for optimisation is appropriate for the given loads and considering the project's objectives. The structural performance of the optimised crank arm was accomplished based on the finite element method for the simplified model without the small fillets in the infill, which makes the assessment more conservative. As the developed finite element model showed, a theoretical assessment of the structural performance of the mechanical elements, such as a crank arm

with the graded internal infill, is feasible. However, because of the considerable strength variability caused by internal material defects shown in work [17], there should be no illusion that metal FFF technology can currently be applied to functional parts. It is hoped that further development into improving the material strength of parts produced by the metal FFF printing process will enable their application. It is particularly important when applied to crank arms, as failures due to fatigue fractures of crank arms can occur in bicycles [57,58]. It is crucial to ensure a safe design, as failure can cause serious injury to the cyclist. Thus, it can be concluded that the designed crank arm currently does not fulfil functional requirements because of safety concerns.

The most important result of the work was the original elaborated method of the structure's design with functionally graded lattice structures. The proposed method can adapt to any structure, boundary conditions, and manufacturing constraints. Design exploration and finite element analysis together can be excellent tools for that problem, as shown in the article. Unluckily, the procedure is required to assume a pattern of the lattice cell distribution; however, it enables us to consider the manufacturing constraints. Additionally, the initial distribution of the lattice thicknesses is recommended to reduce the number of design variables to accelerate optimisation. A dream method would be a design exploration procedure containing a mechanism that gives a graded distribution of grid cells with variable thickness with no initial constraints. It is conceivable that a field defined by an equation, point cloud, or a stress gradient could guide the grid cell size distribution and variable thickness and consider manufacturing constraints. The authors believe it is currently impossible or unnecessary to create such a method; that is confirmed because no one has shown such a working solution for a complex three-dimensional part.

The following important outcome of the project is testing the limits of the metal FFF additive technology. Unexpectedly, the most complicated part of the project was additive manufacturing. Although printing technology opens up space to create complex structures, there are still areas where further development is necessary. The crank arm's example with the complex infill shows the technical limitations of the technology. Here, we can start pointing out the obstacles. Firstly, slicing software cannot always cope with huge data sets. As shown in the project, the STL file format forced the handling of huge model files of hundreds of megabytes for complex geometry parts. Secondly, slicing software is often limiting in its ability to modify support structures manually. For instance, it auto-generates a predefined support structure that needs to be manually changed, which can be very difficult for complex geometry. Thirdly, the metal FFF technology limits printing thin-walled infill structures due to the current material properties and the nozzle size.

An example can be seen in Figure 20, where the defects are observed. Most likely, the faults were caused by the localised material collapse while printing because of the filament properties and insufficient support of the complex thin-walled infill. The last main obstacle is the maximum size of printed objects, often limited to $160 \times 130 \times 300$ mm by Markforged, Metal-X Sinter-2 oven. That constraint is caused mainly by sintering process capabilities. Manufacturing larger objects is workable, but problems during the sintering process are expected. As shown in the paper, the printing time is also an issue because it can be long for parts with thin-walled internal structures reaching dozens of hours. As an example of the difficulties, it is noteworthy that it took the authors about a year to print the prototype shown in Figure 19, and only the latest version of the slicer software Eiger.io [59] and version 2 of 17-4 PH filament made printing possible with shown quality in Figure 20.

As was mentioned, we noticed a significant variation between the masses of the model and the actual printed and sintered parts by 11%. The pure porosity present in the sintered part cannot explain its magnitude. The maximum observed porosity in the metal FFF technology is 6.5% based on the review presented in [17]. Therefore, additional factors must contribute to the mass difference. So, the discrepancy is caused by the inappropriate geometric representation of the internal lattice in the prototype (Figure 20). Thus, the shown manufacturing faults contribute to the observed difference. Unfortunately, a precise

measurement of the infill geometry in the sintered part is unrealistic, so no proof of measurement results can be provided.

Root causes of the observed manufacturing faults of the infill structure are determined by insufficient infill support, the minimum thickness of the infill, and the filament material strength. The orientation of the infill lattice and its size can be optimised using, for example, multi-objective optimisation similar to those proposed by the authors [60], who successfully showed the method to determine the build orientation in the SLM process automatically. The other parameters required, unfortunately, more profound modifications of metal FFF technology. Thus, it can be concluded that manufacturing the part with a functionally graded infill is feasible in the metal FFF technology; however, the selections of the structure infill type and its minimum thickness are crucial for a successful print.

5. Conclusions

This study aimed to demonstrate the feasibility of designing and manufacturing parts with optimised internal infills in the form of a functionally graded shell lattice structure using metal FFF technology. The results indicate that this approach significantly enhances the structural lightness of the fabricated part. The study suggests that using functionally graded lattices based on shell structures as the infill can significantly improve the stiffness-to-mass ratio within a defined stress limit. In this case, a percentage increase of 109.6% was achieved. This supports the idea that mimicking natural materials with functionally graded lattice structures can benefit parts. The presented analysis method shows that it is feasible to identify an optimal design of the graded infill among many viable options with manufacturing constraints. A detailed structural assessment method for the optimised crank arm was also presented. This study proves that the existing technology software, analysis methods, and hardware are developed satisfactorily to support the design process. The evidence suggests that designing the structures with functionally graded lattices is feasible for complex parts, and an example of the methodology was shown. Nonetheless, further advancements in metal FFF technology are necessary because several limitations were encountered while implementing the functionally graded lattice in the design. The restrictions concern additive manufacturing and its technical limitations in software and hardware. The most critical ones concerning 3D printing and sintering complex infill parts are the minimum wall thickness, the maximum part size, and filament materials.

More broadly, development is needed to improve three elements in the future:

- Firstly, work is required to improve the metal FFF technology for printing thin-walled internal structures, with issues relating to nozzle size, printing parameters and printer control algorithms.
- Secondly, improvements are required in metallic filament materials for the metal FFF technology to enhance printability and reduction of post-sintered internal defects, thereby increasing the strength.
- Thirdly, it is recommended to develop methods for generating field-controlled lattice structures and integration in CAD systems that enhance design optimisation and exploration, opening up space for new types of high-performance parts.

Due to the significant strength variability caused by internal material defects shown in the article [17] and possible manufacturing imperfections shown in the presented work, we do not recommend using metal FFF technology for functional parts at this time.

The primary study's strength is the presentation of the in-depth design process of those structures supported by a shown case study of the crank arm and an identification of the current boundaries of metal FFF technology. Thus, the work contributes to the existing design knowledge for additive manufacturing technology by providing detailed design, simulation, and manufacturing methods.

Author Contributions: Conceptualisation, S.K. and T.D.; methodology, S.K. and T.D.; software, S.K.; validation, S.K., E.M. and T.D.; formal analysis, S.K.; investigation, S.K., E.M. and T.D.; resources, S.K.; data curation, S.K.; writing—original draft preparation, S.K.; writing—review and editing, S.K. and T.D.; visualisation, S.K.; supervision, S.K.; project administration, S.K.; funding acquisition, S.K. All authors have read and agreed to the published version of the manuscript.

Funding: This research received no external funding

Institutional Review Board Statement: Not applicable.

Informed Consent Statement: Not applicable.

Data Availability Statement: All data used to support the findings of this study are available from the corresponding author upon request.

Conflicts of Interest: The authors declare no conflict of interest.

Abbreviations

The following abbreviations are used in this manuscript:

AM	Additive Manufacturing
CAD	Computer-Aided Design
DE	Design Exploration
DOE	Design of Experiments
DSE	Design Space Exploration
FCC	Face-Centred Cubic
FDM	Fused Deposition Modelling
FEA	Finite Element Analysis
FFF	Fused Filament Fabrication
FGM	Functionally Graded Materials
FGS	Functionally Graded Structures
GRSM	Global Response Search Method
ISO	International Organisation for Standardisation
MELS	Modified Extensible Lattice Sequences
MEX	Metal Extrusion Method
MOO	Multiobjective Optimisation
nTop	nTopology
PBF	Powder Bed Fusion
SLS	Selective Laser Sintering
TPMS	Triply Periodic Minimal Surface

References

1. Munsch, M.; Schmidt-Lehr, M.; Wycisk, E. Binder Jetting and FDM: A Comparison with Laser Powder Bed Fusion and Metal Injection Moulding. Available online: <https://www.metal-am.com/articles/binder-jetting-fdm-comparison-with-powder-bed-fusion-3d-printing-injection-moulding/> (accessed on 15 October 2022).
2. Podroužek, J.; Marcon, M.; Ninčević, K.; Wan-Wendner, R. Bio-inspired 3D infill patterns for additive manufacturing and structural applications. *Materials* **2019**, *12*, 499. [CrossRef]
3. Abate, K.M.; Nazir, A.; Yeh, Y.P.; Chen, J.E.; Jeng, J.Y. Design, optimization, and validation of mechanical properties of different cellular structures for biomedical application. *Int. J. Adv. Manuf. Technol.* **2020**, *106*, 1253–1265. [CrossRef]
4. Afshar, M.; Anaraki, A.P.; Montazerian, H.; Kadkhodapour, J. Additive manufacturing and mechanical characterization of graded porosity scaffolds designed based on triply periodic minimal surface architectures. *J. Mech. Behav. Biomed. Mater.* **2016**, *62*, 481–494. [CrossRef]
5. Jia, H.; Lei, H.; Wang, P.; Meng, J.; Li, C.; Zhou, H.; Zhang, X.; Fang, D. An experimental and numerical investigation of compressive response of designed Schwarz primitive triply periodic minimal surface with non-uniform shell thickness. *Extrem. Mech. Lett.* **2020**, *37*, 100671–100671. [CrossRef]
6. Lee, D.W.; Khan, K.A.; Abu Al-Rub, R.K. Stiffness and yield strength of architected foams based on the Schwarz primitive triply periodic minimal surface. *Int. J. Plast.* **2017**, *95*, 1–20. [CrossRef]
7. Li, Y.; Feng, Z.; Hao, L.; Huang, L.; Xin, C.; Wang, Y.; Bilotti, E.; Essa, K.; Zhang, H.; Li, Z.; et al. A review on functionally graded materials and structures via additive manufacturing: From multi-scale design to versatile functional properties. *Adv. Mater. Technol.* **2020**, *5*, 1900981. [CrossRef]

8. Maskery, I.; Hussey, A.; Panesar, A.; Aremu, A.; Tuck, C.; Ashcroft, I.; Hague, R. An investigation into reinforced and functionally graded lattice structures. *J. Cell. Plast.* **2017**, *53*, 151–165. [[CrossRef](#)]
9. Yang, L.; Yan, C.; Cao, W.; Liu, Z.; Song, B.; Wen, S.; Zhang, C.; Shi, Y.; Yang, S. Compression–compression fatigue behaviour of gyroid-type triply periodic minimal surface porous structures fabricated by selective laser melting. *Acta Mater.* **2019**, *181*, 49–66. [[CrossRef](#)]
10. Aslan, B.; Yıldız, A.R. Optimum design of automobile components using lattice structures for additive manufacturing. *Mater. Test.* **2020**, *62*, 633–639. [[CrossRef](#)]
11. Czerwinski, F. Current trends in automotive lightweighting strategies and materials. *Materials* **2021**, *14*, 6631. [[CrossRef](#)]
12. Oczóś, K.E. Konstrukcje lekkie–istota, rodzaje, realizacja i zastosowanie. Cz. 1. *Mechanik* **2011**, *84*, 271–272.
13. Oczóś, K.E. Konstrukcje lekkie–istota, rodzaje, realizacja i zastosowanie. Cz. 2. *Mechanik* **2011**, *84*, 377–390.
14. Oftadeh, R.; Perez-Viloria, M.; Villa-Camacho, J.C.; Vaziri, A.; Nazarian, A. Biomechanics and mechanobiology of trabecular bone: A review. *J. Biomech. Eng.* **2015**, *137*, 010802. [[CrossRef](#)] [[PubMed](#)]
15. Sato, M.; Inoue, A.; Shima, H. Bamboo-inspired optimal design for functionally graded hollow cylinders. *PLoS ONE* **2017**, *12*, e0175029. [[CrossRef](#)]
16. Spencer, O.O.; Yusuf, O.T.; Tofade, T.C. Additive manufacturing technology development: A trajectory towards industrial revolution. *Am. J. Mech. Ind. Eng.* **2018**, *3*, 80–90. [[CrossRef](#)]
17. Kedziora, S.; Decker, T.; Museyibov, E.; Morbach, J.; Hohmann, S.; Huwer, A.; Wahl, M. Strength properties of 316L and 17–4 PH stainless steel produced with additive manufacturing. *Materials* **2022**, *15*, 6278. [[CrossRef](#)]
18. Koizumi, M. FGM activities in Japan. *Compos. Part B Eng.* **1997**, *28*, 1–4. [[CrossRef](#)]
19. Saleh, B.; Jiang, J.; Fathi, R.; Al-hababi, T.; Xu, Q.; Wang, L.; Song, D.; Ma, A. 30 years of functionally graded materials: An overview of manufacturing methods, applications and future challenges. *Compos. Part B Eng.* **2020**, *201*, 108376. [[CrossRef](#)]
20. Mahmoud, D.; Elbestawi, M. Lattice structures and functionally graded materials applications in additive manufacturing of orthopedic implants: A review. *J. Manuf. Mater. Process.* **2017**, *1*, 13. [[CrossRef](#)]
21. Kou, X.Y.; Parks, G.T.; Tan, S.T. Optimal design of functionally graded materials using a procedural model and particle swarm optimization. *CAD Comput. Aided Des.* **2012**, *44*, 300–310. [[CrossRef](#)]
22. Miyamoto, Y.; Kaysser, W.A.; Rabin, B.H.; Kawasaki, A.; Ford, R.G. *Functionally Graded Materials: Design, Processing and Application*; Springer Science and Business Media: New York, NY, USA, 2013; Volume 1, pp. 1–339. [[CrossRef](#)]
23. Wu, J.; Aage, N.; Westermann, R.; Sigmund, O. Infill optimization for additive manufacturing–approaching bone-like porous structures. *IEEE Trans. Vis. Comput. Graph.* **2018**, *24*, 1127–1140. [[CrossRef](#)] [[PubMed](#)]
24. Gries, M. Methods for evaluating and covering the design space during early design development. *Integr. VLSI J.* **2004**, *38*, 131–183. [[CrossRef](#)]
25. Kang, E.; Jackson, E.; Schulte, W. An approach for effective design space exploration. In *Foundations of Computer Software. Modeling, Development, and Verification of Adaptive Systems*; Springer: Berlin/Heidelberg, Germany, 2011. [[CrossRef](#)]
26. Pan, C.; Han, Y.; Lu, J. Design and optimization of lattice structures: A review. *Appl. Sci.* **2020**, *10*, 6374. [[CrossRef](#)]
27. Al-Saedi, D.S.J.; Masood, S.H.; Faizan-Ur-Rab, M.; Alomarah, A.; Ponnusamy, P. Mechanical properties and energy absorption capability of functionally graded F2BCC lattice fabricated by SLM. *Mater. Des.* **2018**, *144*, 32–44. [[CrossRef](#)]
28. Zheng, X.; Lee, H.; Weisgraber, T.H.; Shusteff, M.; DeOtte, J.; Duoss, E.B.; Kuntz, J.D.; Biener, M.M.; Ge, Q.; Jackson, J.A.; et al. Ultralight, ultrastiff mechanical metamaterials. *Science* **2014**, *344*, 1373–1377. [[CrossRef](#)]
29. Ashby, M.F. The properties of foams and lattices. *Philos. Trans. R. Soc. A Math. Phys. Eng. Sci.* **2006**, *364*, 15–30. [[CrossRef](#)]
30. Deshpande, V.S.; Fleck, N.A.; Ashby, M.F. Effective properties of the octet-truss lattice material. *J. Mech. Phys. Solids* **2001**, *49*, 1747–1769. [[CrossRef](#)]
31. Decker, T.; Kedziora, S.; Wolf, C. Practical Implementation of Functionally Graded Lattice Structures in a Bicycle Crank Arm. 2020. Available online: <http://hdl.handle.net/10993/46747> (accessed on 28 May 2022).
32. Schoen, A.H. *Infinite Periodic Minimal Surfaces without Self-Intersections*; Report; NASA: Washington, DC, USA, 1970.
33. Abueidda, D.W.; Elhebeary, M.; Shiang, C.S.; Pang, S.; Abu Al-Rub, R.K.; Jasiuk, I.M. Mechanical properties of 3D printed polymeric gyroid cellular structures: Experimental and finite element study. *Mater. Des.* **2019**, *165*, 107597. [[CrossRef](#)]
34. Bean, P.; Lopez-Anido, R.A.; Vel, S. Numerical modeling and experimental investigation of effective elastic properties of the 3D printed gyroid infill. *Appl. Sci.* **2022**, *12*, 2180. [[CrossRef](#)]
35. Silva, C.; Pais, A.I.; Caldas, G.; Gouveia, B.P.P.A.; Alves, J.L.; Belinha, J. Study on 3D printing of gyroid-based structures for superior structural behaviour. *Prog. Addit. Manuf.* **2021**, *6*, 689–703. [[CrossRef](#)]
36. Al-Ketan, O.; Abu Al-Rub, R.K. MSLattice: A free software for generating uniform and graded lattices based on triply periodic minimal surfaces. *Mater. Des. Process. Commun.* **2020**, *3*, e205. [[CrossRef](#)]
37. Zhang, X.Y.; Yan, X.C.; Fang, G.; Liu, M. Biomechanical influence of structural variation strategies on functionally graded scaffolds constructed with triply periodic minimal surface. *Addit. Manuf.* **2020**, *32*, 101015. [[CrossRef](#)]
38. Han, C.; Li, Y.; Wang, Q.; Wen, S.; Wei, Q.; Yan, C.; Hao, L.; Liu, J.; Shi, Y. Continuous functionally graded porous titanium scaffolds manufactured by selective laser melting for bone implants. *J. Mech. Behav. Biomed. Mater.* **2018**, *80*, 119–127. [[CrossRef](#)]
39. Quaresimin, M.; Meneghetti, G.; Verardo, F. Design and optimisation of an RTM composite bicycle crank. *J. Reinf. Plast. Compos.* **2001**, *20*, 129–146. [[CrossRef](#)]

40. McEwen, I.; Cooper, D.E.; Warnett, J.; Kourra, N.; Williams, M.A.; Gibbons, G.J. Design and manufacture of a high-performance bicycle crank by additive manufacturing. *Appl. Sci.* **2018**, *8*, 1360. [CrossRef]
41. Gutiérrez-Moizant, R.; Ramírez-Berasategui, M.; Calvo, J.A.; Álvarez Caldas, C. Validation and improvement of a bicycle crank arm based in numerical simulation and uncertainty quantification. *Sensors* **2020**, *20*, 1814. [CrossRef]
42. Chang, R.R.; Dai, W.J.; Wu, F.Y.; Jia, S.Y.; Tan, H.M. Design and manufacturing of a laminated composite bicycle crank. *Procedia Eng.* **2013**, *67*, 497–505. [CrossRef]
43. nTopology. nTopology, Version 3.45.4. Available online: <https://ntopology.com/ntop-platform> (accessed on 4 April 2023).
44. ISO 4210-8:2023; Cycles—Safety Requirements for Bicycles—Part 8: Pedal and Drive System Test Methods. ISO: Geneva, Switzerland, 2023.
45. Whitt, F.R.; Wilson, D.G. *Bicycling Science*, 2nd ed.; MIT Press: Cambridge, MA, USA, 1982; p. 364.
46. Markforged, T. Metal-X System. Available online: <https://markforged.com/metal-x/> (accessed on 15 March 2022).
47. Basf, T. Ultrafuse FFF. Available online: <https://www.ultrafusefff.com/product-category/metal/ultrafuse-316l/> (accessed on 14 February 2021).
48. Foundry, T.V. Manufacturing Metal 3D Printing Filaments and Materials. Available online: <https://www.thevirtualfoundry.com/> (accessed on 12 September 2022).
49. Desktop Metal Inc. Studio System™ 2. Available online: <https://www.desktopmetal.com/products/studio> (accessed on 12 May 2022).
50. Altair Engineering Inc. HyperStudy Guide, 2022.1. Available online: <https://altairhyperworks.com/product/HyperStudy> (accessed on 3 February 2023).
51. Altair Engineering Inc. OptiStruct, Version 2022.1. Available online: <https://www.altair.com/optistruct/> (accessed on 8 February 2023).
52. Jaimes, A.L.; Martínez, S.Z.; Coello, C.A.C. An introduction to multiobjective optimization techniques. In *Optimization in Polymer Processing*; Chemical Engineering Methods and Technology; Nova Science Publishers: Hauppauge, NY, USA, 2011; pp. 29–57.
53. Engineering, A. Altair HyperStudy Guide, Version 2022.1, DOE Modified Extensible Lattice Sequence. Available online: https://2022.help.altair.com/2022.1/hwdesktop/hst/topics/design_exploration/method_modified_extensible_lattice_sequence_doe_r.htm (accessed on 3 April 2023).
54. Ollar, J. A Multidisciplinary Design Optimisation Framework for Structural Problems with Disparate Variable Dependence. Ph.D. Thesis, Queen Mary University of London, London, UK, 2016.
55. Markforged, T. 17–4 PH Stainless Steel. Available online: <https://static.markforged.com/downloads/17-4-ph-stainless-steel.pdf> (accessed on 9 November 2022).
56. Bjørheim, F.; Lopez, I.L.T. Tension testing of additively manufactured specimens of 17–4 PH processed by bound metal deposition. *IOP Conf. Ser. Mater. Sci. Eng.* **2021**, *1201*, 012037. [CrossRef]
57. Morgan, J.E.; Wagg, D.J. The failure of bike cranks, International Standards, tests and interpretations. *Sport. Eng.* **2002**, *5*, 113–119. [CrossRef]
58. Engineering, M. Component Failure Museum, Bicycle Crank Failure II. Available online: http://technology.open.ac.uk/materials/mem/mem_ccf4.htm (accessed on 15 July 2022).
59. Markforged, T. Eiger.io, Slicer 3.97.0. Available online: <https://www.eiger.io/> (accessed on 9 January 2023).
60. Günaydın, A.C.; Yıldız, A.R.; Kaya, N. Multi-objective optimization of build orientation considering support structure volume and build time in laser powder bed fusion. *Mater. Test.* **2022**, *64*, 323–338. [CrossRef]

Disclaimer/Publisher’s Note: The statements, opinions and data contained in all publications are solely those of the individual author(s) and contributor(s) and not of MDPI and/or the editor(s). MDPI and/or the editor(s) disclaim responsibility for any injury to people or property resulting from any ideas, methods, instructions or products referred to in the content.

4.4 Strength Properties of PBF and SLA Materials

The publication titled *Comparison of strength properties of common Powder Bed Fusion and Stereolithography materials* (Decker et al., 2023) investigates the material properties of four materials manufacturable with two AM methods potentially suitable for producing FGLS in compressive energy absorption tasks, such as for a helmet. The materials and manufacturing methods were chosen since they are either available locally or at nearby suppliers, and theoretically provide adequate properties and build volumes for producing an entire helmet geometry. Formlabs Clear and Tough 2000 resins produced on a Formlabs Form 2 stereolithography printer are examined, along with PA12 produced on a Sinterit Lisa Pro SLS printer as well as PA12 produced on a HP MJF machine. The choices are intended to represent lower cost, commonly available material and manufacturing choices (Formlabs Clear, Sinterit PA12) as well as higher grade materials and manufacturing methods (Formlabs Tough 2000, HP MJF PA12).

The paper analyses the materials' density, tensile properties, Charpy impact strengths, Poisson's ratio determination of the cured resins by Digital Image Correlation (DIC), and fatigue properties of one resin type as well as one PA12 type. Similar to the previous publication, the samples were printed in parallel to the build direction and loaded in their weakest plane to emulate the worst-case scenario. A detailed overview of the material candidates was deemed necessary to progress with subsequent projects where precise knowledge of their stiffness and tensile behaviour was required. The study expands on related publications by determining the density, impact strength and Poisson's ratio for both resin materials as well as fatigue properties of the Tough 2000 resin, which were previously neither reported by papers nor by the manufacturer.

The author contributed to this paper by deciding on the test battery and setup, manufacturing of test samples, performing the tensile and fatigue tests, and executing the Digital Image Correlation study to determine the materials' Poisson's ratios. Further, the author performed the data analysis and visualization, wrote the paper draft, and edited it according to reviewer feedback, and presented the results at the conference.

Comparison of Strength Properties of Common Powder Bed Fusion and Stereolithography Materials

Thierry Decker^{1,a,*}, Slawomir Kedziora^{1,b} and Elvin Museyibov^{1,c}

¹University of Luxembourg, 6 rue Richard Coudenhove-Calergi, L-1359 Luxembourg

^athierry.decker@uni.lu, ^bslawomir.kedziora@uni.lu, ^cemuseyibov94@gmail.com

Keywords: PBF, MJF, SLS, SLA, mechanical properties, additive manufacturing

Abstract. This paper serves as basis for subsequent studies investigating a potential material and manufacturing method selection for producing lattice structures to be used as energy absorption device, such as in novel wearable protective gear. Four additively manufactured plastics from two additive manufacturing methods are examined in detail. Polyamide 12 specimens produced on two Powder Bed Fusion (PBF) machines are compared against specimens produced on a stereolithography (SLA) printer using a standard and an engineering-grade resin. A comprehensive analysis of their mechanical properties is presented by measuring their densities as well as tensile, fatigue, and impact properties. In addition, Poisson's ratio of the resin materials is estimated using Digital Image Correlation (DIC).

Introduction

Additive manufacturing (AM) allows the creation of complex structures such as three-dimensional lattice structures exhibiting high stiffness-to-weight ratio for light-weighting applications [1]–[3], substantial specific energy absorption capabilities in quasi-static or dynamic compression for protective use cases [4]–[6], including specific or even negative Poisson ratios of the structure [7]–[9], or increased heat transfer for cooling applications thanks to large surface areas and guided fluid flow [10]–[12]. Uniform lattice structures are able to perform exceptionally well in a variety of tasks, but the concept can be taken further by altering their structural properties non-uniformly to fit certain needs exactly. So-called functionally graded lattice structures (FGLS) can be tailored for a specific goal, introducing locally varying properties such as strut thickness, cell size, cell type or cell orientation. The choice of application and optimisation goals may be defined almost arbitrarily, adapting the structure for optimal specific energy absorption [13], heat transfer [14], the stiffness-to-weight ratio [15] or even the combined optimisation of structural, fluid flow and heat transfer capabilities [16].

Like graded foams, FGLS were shown to perform exceptionally well when used as compressive energy absorption devices, surpassing lattices with uniform properties in terms of specific energy absorption capabilities [13], [17–21]. They have thus the potential to be implemented as conformal protective liners in wearable gear or padding of sensitive equipment, where uniform expanded foam structures were used previously. Apart from the lattice's geometrical properties, the choice of base material greatly influences its energy absorption properties, as ductile or brittle material behaviour results in vastly different cushioning behaviour [22]. Therefore, it is essential to possess exact material data for detailed studies.

As for the manufacturing of lattice structures, all three major plastics AM methods can be used in conjunction with a vast array of material types, but not all are equally appropriate for this task. Fused Deposition Modelling (FDM) is able to handle surface-based lattices such as Gyroids with relative ease but requires extensive support structures for thin beam-based lattice structures. Stereolithography (SLA) can more easily produce fine structures, such as beam-based lattices, without requiring extensive support structures, though some are almost always required. On the other hand, parts made via Powder Bed Fusion (PBF) methods often can completely forgo support structures as the parts are constantly supported by the surrounding powder during the build process. Therefore, the SLA and PBF technologies are the methods of choice for this paper and the subsequent studies.

Both methods offer vast arrays of printer and material selections covering different application, cost, and property categories. For the PBF systems, Polyamide 12 (PA12) was chosen due to its suitable processability and suitable material properties. Samples from an HP Multi-Jet Fusion (MJF) machine and a Sinterit Lisa Pro Selective Laser Sintering (SLS) are compared to contrast results from two commonly used PBF systems. The Sinterit machine and its PA12 powder are mostly targeted towards small runs of visual prototypes and non-functional parts, whereas the HP systems and their PA12 material are commonly used for small to medium batch production of functional prototypes and end-use parts as evidenced by the material data provided by the manufacturers (see Table 1). As for SLA printing technology, the Formlabs resin and machine line-up were chosen. Their resins are similarly divided into material categories designated for functional and visual purposes, respectively, with the standard resins sharing similar properties apart from their colouration [23]. The standard Clear V4 resin was chosen to be compared to the Tough 2000 V1 engineering-grade resin, which is intended to mimic ABS plastic in its properties [24].

The authors plan to examine the properties and optimisation approaches of beam-based FGLS further in subsequent studies, for which this paper is intended to provide detailed material data. The results are compared to the manufacturers' indications and data from current literature.

Methods and Materials

Materials and Sample Preparation. The Formlabs resin and Sinterit PA12 samples were prepared locally, while the HP PA12 samples were produced by a third-party facility. The Sinterit samples were produced with a Lisa Pro machine using a layer height of 0.125mm, whereas the HP MJF machine applied its standard layer height of 0.08mm. The fresh Sinterit Smooth PA12 powder was mixed with previously used material as required by the manufacturer (see [25]).

As for the SLA parts, both the standard Formlabs Clear V4 and Formlabs Tough 2000 V1 resins are printed on a Formlabs Form 2 printer with a layer height of 0.05mm. The subsequent curing step was performed under the recommended conditions specified by Formlabs (see [23], [24]). All specimens were printed with their longitudinal axis oriented in parallel to the build direction to load the parts in their weakest plane, taking into consideration their anisotropy introduced by the manufacturing process. The build orientation is not as impactful for SLA samples as compared to SLS due to the polymerisation process during printing, but still significant [26], [27].

As indicated by their manufacturers, material properties are summarised in Table 1. To determine the actual material densities, the dimensions and weights of all bending test samples were measured three times each with a micrometre screw (thickness, width), a digital caliper (length) and a Kern precision scale, respectively.

Table 1. Material properties as given in the manufacturer's material data sheets.

	HP PA12 ^a [28]	Sinterit PA12 ^b [25]	Formlabs Clear [23]	Formlabs Tough 2000 [24]
E [MPa]	1800	1470	2800	2200
E_f [MPa]	1730	1160	2200	1900
σ_{UTS} [MPa]	48	32	65	46
ε_{max} [%]	15	10	6.2	48
ρ [kg/m³]	1.01	0.92	-	-
Impact strength	3.5 [kJ/m ²] (Izod, notched)	16 [kJ/m ²] (Charpy, unnotched)	16 [J/m] (Izod, notched)	40 / 715 [J/m] (Izod, notched / unnotched)
Flexural strength [MPa]	70	47	-	65

^aValues given for samples oriented in Z-direction. ^bNo printing orientation was indicated.

Tensile Test and Secant Moduli. The tensile tests were carried out following EN ISO 527 1 on a Form + Test UP 5E universal testing machine with a total of five specimens per material type. A constant speed of 1mm/min was applied, which translates to 1.78%/min initial strain rate. Force and grip displacement are logged and used for engineering stress and strain calculation. Since the grip distance of this machine is relatively short, specimen type 1BA, as defined by EN ISO 527 2 was chosen (see Fig. 1). Per material, the secant modulus of the sample with the largest ultimate strain is derived from the engineering stress and strain values. The load cell's sampling rate was set to 3kHz with subsequent downsampling to 30Hz for postprocessing of the data.

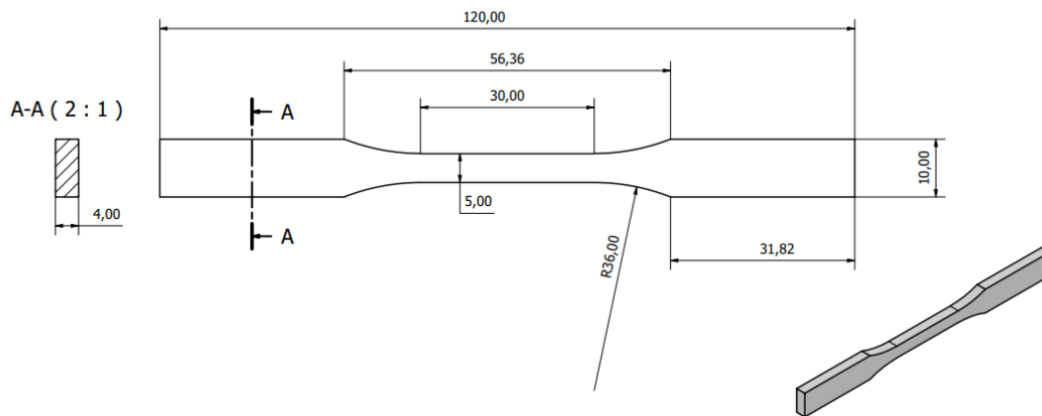


Fig. 1. Dimensions of tensile EN ISO 527-2 1BA test specimen.

Poisson's Ratio Determination. Poisson's ratio of one specimen per resin type was approximated using separate tensile test samples. Poisson's ratio of PBF-based PA12 parts is known and was found to be approximately 0.4 [29], [30], hence no measurements of these materials were performed in this study.

A series of high-resolution photographs taken with a Nikon D700 at ten-second intervals were analysed via the Digital Image Correlation (DIC) tool nCorr for Matlab. The strain rate was set to 0.2mm/min to permit ample time for handling the camera setup. Strains between 0.3% and 1.5% were captured as outlined in EN ISO 527. A fine speckle pattern was applied to the specimens' sides via an aerosol paint can. Black colour was utilised on the Clear specimens and white on the Tough 2000 specimens to improve the contrast for the pattern recognition algorithm (see Fig. 2).

Since the local strain results are available digitally, the ratio was determined at several points in the region of interest. In total, a grid of 20 sample points in horizontal and 100 sample points in a vertical direction was analysed for each picture and subsequently averaged, permitting a more precise estimate.

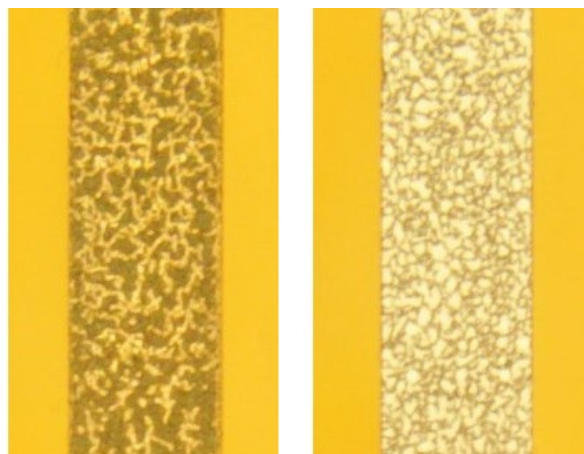


Fig. 2. Black speckle pattern on Clear resin sample (left) and white speckle pattern on Tough 2000 sample (right).

Charpy Impact Test. The Charpy impact strength of eight specimens per material was examined following EN ISO 179 1 with an impact energy of 5J. The specimens were unnotched, 80mm by 4mm by 10mm in dimension and oriented in the edgewise position such that the hammer strikes the side with 4mm thickness.

Fatigue Test. Fatigue testing of one material from the PBF and SLA categories was completed. The choice fell on the toughest material per category as determined by the Charpy impact tests. The fatigue tests followed ASTM D638 14 using Type I specimens (see Fig. 3). A stress ratio R of 0.1 was defined, with a minimum of five stress levels and two specimens per level.

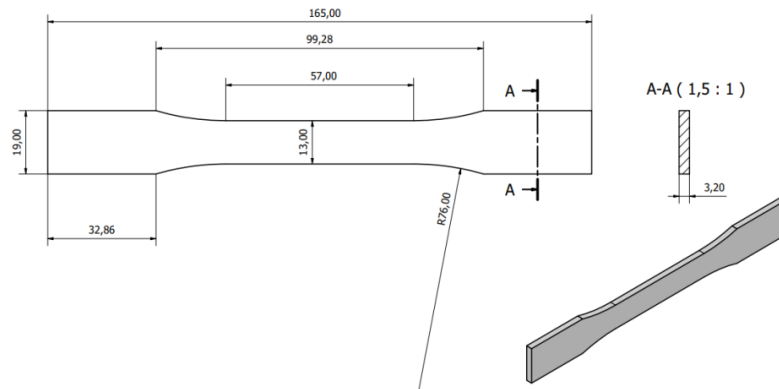


Fig. 3. Dimensions of the ASTM D638 Type I fatigue test specimen.

Results

Density measurement. Measurements showed that the samples of HP PA12 and Formlabs Clear resin were more consistent than the other two material samples. The dimensions of the Sinterit specimens differed strongly from the nominal dimensions and showed the highest standard deviations. Especially their width overshoots the nominal value considerably. The relatively large length deviation of the Formlabs Tough 2000 test pieces seems to stem from a resin build-up and bulging of the first layers. This could have been caused by the lateral movement of the tank during printing, sloshing resin on top of the first layers. Protrusions at the support structures' contact points also remained at this spot but were avoided during measurements. Light warping was present along their longitudinal axes, curling the samples along their broad edge. All these flaws were far less pronounced on the Clear resin samples. The measured densities of Formlabs Clear and Tough 2000 were 1.16 g/cm³ and 1.17g/cm³, respectively. The HP samples achieved 0.94g/cm³, and the Sinterit samples 0.98g/cm³. All dimensions, mass and density measurements are given in Table 2.

Table 2. Measured dimensions, weights and densities.

	HP PA12	Sinterit PA12	Formlabs Clear	Formlabs Tough 2000
Thickness [mm]	4.07	4.36	3.99	3.98
Width [mm]	10.14	10.14	9.95	9.99
Length [mm]	80.19	79.62	80.28	80.69
Mass [g]	3.11	3.45	3.71	3.78
Measured density [g/cm³]	0.94	0.98	1.16	1.17

Tensile Test. The Formlabs Clear resin samples reached the highest ultimate tensile strength (UTS) with 62.3MPa on average at a maximum strain of 7.2%. The largest average strain was achieved by the Formlabs Tough 2000 material with 36% at a UTS of 38MPa. Both PA12 materials showed relatively low ultimate strains, with the HP samples reaching 42.7MPa at 6.2% and their Sinterit counterparts only 22.7MPa at 2% strain on average. Samples from the SLA printer showed relatively little inconsistency in their tensile properties compared to the SLS PA12 samples. Only the

Tough 2000 specimens showed high ductility and visible necking at the failure section, the other material samples broke in a brittle manner. The test results are shown as box plots in Figures 4 and 5.

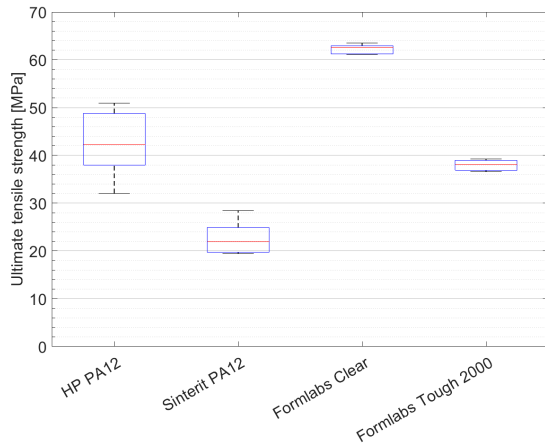


Fig. 4. Ultimate tensile strengths of the tested samples.

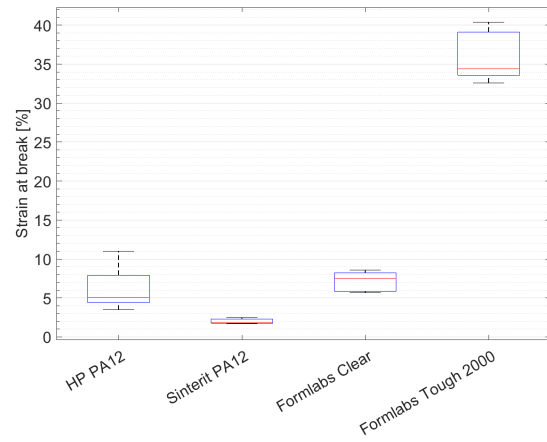


Fig. 5. Strains at break of the tested samples.

Secant Modulus. The secant moduli based on the material sample with the largest maximum strains are shown in Fig. 6. At 0.1% strain, the Formlabs Tough 2000 sample's secant modulus is approximately 1260MPa, followed by the HP PA12 sample with 1480MPa, then Sinterit PA12 with 1555MPa and lastly, the Formlabs Clear sample with 1905MPa. The Sinterit PA12 material exhibits a modulus reduction to 1280MPa at 1% strain compared to its value at 0.1% strain, whereas the other three samples show vastly smaller decreases at this point.

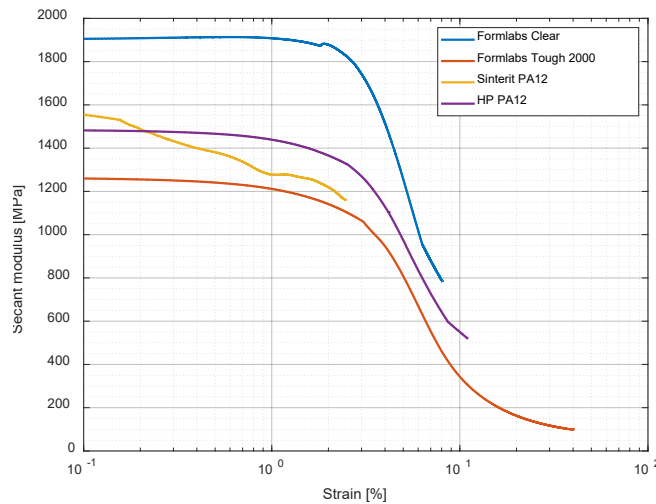


Fig. 6. Secant moduli of the most ductile sample per material type.

Poisson's Ratio Determination. Since unphysical values and fluctuations occurred during the evaluation of the initial stretching range, these results are discarded, and the average Poisson ratio is determined in the range between 0.85%-1.5% strain, i.e. within the last ten pictures of the series. The estimated Poisson's ratio of the Formlabs Tough 2000 material settled at approx. 0.39, with the ratio for the Clear samples remaining around 0.33. Figures 7 and 8 display the average Poisson ratio evolution in the stretching phase as well as the local ratios calculated from the last picture at 1.5% strain.

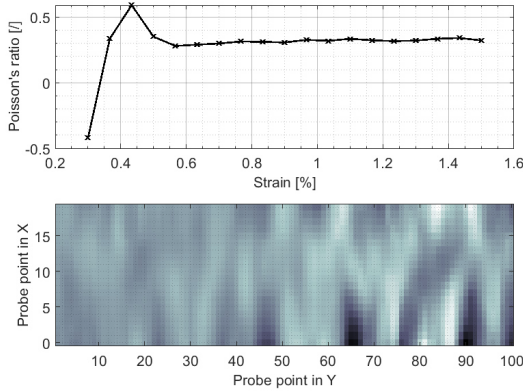


Fig. 7. Top: Evolution of Poisson’s ratio of the Formlabs Clear sample over strain range. Bottom: Local Poisson ratio of the last picture in the series at 1.5% strain, calculated at 20×100 points.

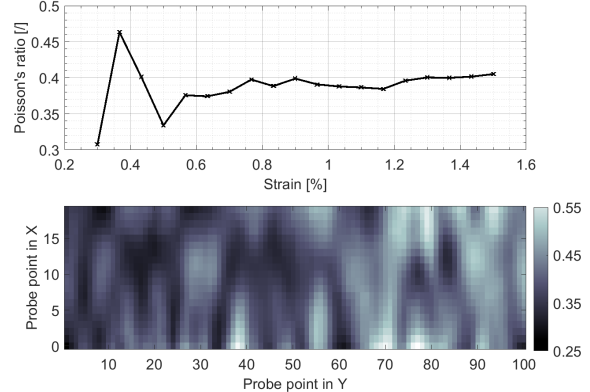


Fig. 8. Top: Evolution of Poisson’s ratio of the Formlabs Tough 2000 sample over strain range. Bottom: Local Poisson ratio of the last picture in the series at 1.5% strain, calculated at 20×100 points.

Charpy Impact Test. The Formlabs Tough 2000 resin showed the highest average impact energy absorption capabilities with 63.4kJ/m², but also a large standard deviation of ±33.1kJ/m² with a minimum test result of 4.85kJ/m² and a maximum 113.7kJ/m². Next follow, with their average values listed in descending order, HP PA12 (19.9kJ/m²), Sinterit PA12 (10.3kJ/m²) and lastly, the Formlabs Clear samples (3.45kJ/m²). The last exhibited meagre impact resistance, and no test sample absorbed more than 10% of the impact energy. All specimens showed complete failure after the test, and no partial failures occurred. The test results are displayed as a box plot in Fig. 9.

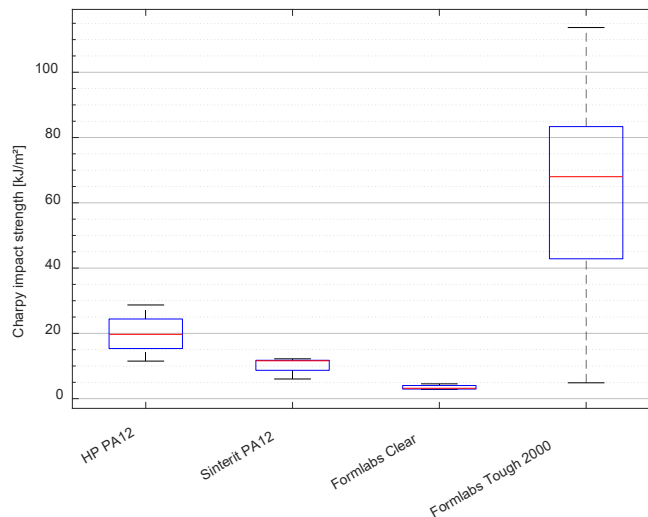


Fig. 9. Charpy impact strength test results.

Fatigue Test. From the S-N plot in Fig. 10, it is visible that the HP PA12 samples exhibit a higher fatigue strength level over the entire testing domain with a shallower slope of the fit line, meaning a lower fatigue strength drop over the cycle range. Approximate fatigue strengths of 26MPa for the HP PA12 samples and 17MPa for the Formlabs Tough 2000 samples at 1×10⁵ cycles can be estimated from the graph. No clear endurance limit can be derived from the data.

Of the HP PA12 samples, one reached 1,9 million cycles, with another overshooting two million cycles, at which point the test was stopped. As for the Formlabs Tough 2000 samples, one broke near the clamping area, and one reached a million cycles, marking the end of the fatigue tests as the results were deemed expressive enough at this point. These four samples were excluded from the fit line calculation but are still included in Fig. 10.

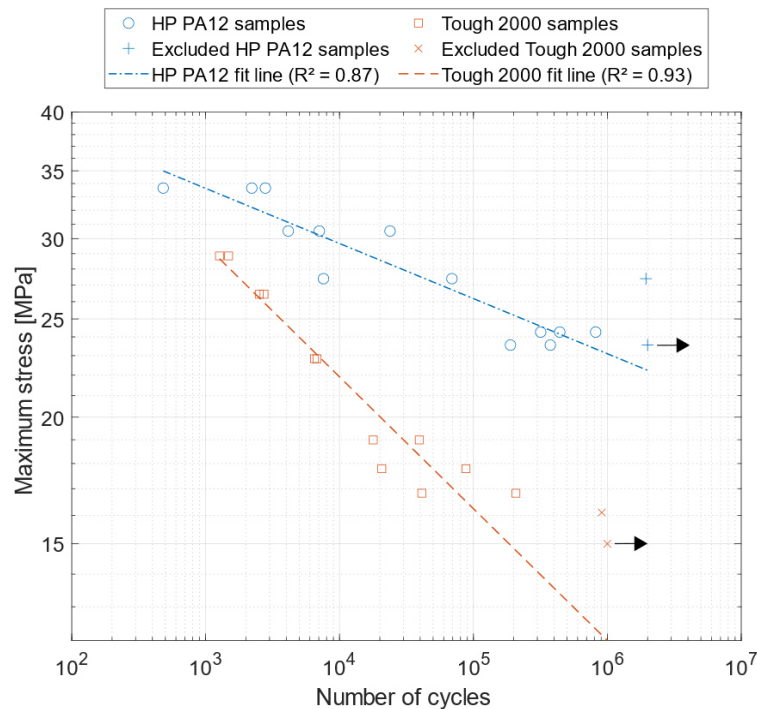


Fig. 10. S-N plot and fit lines of HP PA12 and Formlabs Tough 2000 fatigue samples. Excluded samples were not used in the fit line calculation, and runout samples are marked with an arrow.

Summary & Discussion

The Sinterit samples with an average density of 0.98g/cm³ proved to be 6.5% denser than their nominal value of 0.92g/cm³. Tensile test results of specimens printed in an upright fashion (longitudinal axis oriented along Z) shown in [31] support the findings of this paper, determining an average UTS of 17.1MPa and 6% strain at break and slightly more ductile material behaviour. PA12 samples from the HP MJF machine achieved a density of 0.94g/cm³, which is 6.9% less dense than indicated by the manufacturer. Compared to findings of average ultimate tensile strengths of 49.6MPa at 14.8% ultimate strain in [32], the tensile properties determined in this study are marginally lower. This could possibly be due to the samples' lower density, indicating issues with the powder's moisture content, the manufacturing process etc.

Although the HP PA12 samples reached an average UTS that was fairly close to the manufacturer's indication, the maximum strain reached only 41% of the indicated value for samples oriented along the Z-axis. The Sinterit PA12 samples also fell short of the tensile properties indicated by the manufacturers, reaching only an average UTS of 22.7MPa at 2% strain as compared to 32MPa and 10% strain specified by the data sheet.

The Clear resin tensile test results remained close to the manufacturer's data sheet indications and the findings by Cosmi et al. in [27] but surpassed those determined by Riccio et al. in [33]. The Tough 2000 resin's UTS and strain at break values fell short of the data sheet indications and those reported in the study by Riccio et al. previously mentioned. Its secant modulus was significantly lower than expected, measuring 1160MPa instead of 1900MPa given in the datasheet. Through digital image correlation, Poisson's ratio of the Clear and Tough 2000 resin was estimated to be 0.33 and 0.39, respectively. Additionally, the Clear resin's density was measured to be 1.16g/cm³, and the Tough 2000's density 1.17g/cm³. Both the Poisson's ratio, the densities of the resin specimens and the fatigue behaviour of the Tough 2000 resin appeared to be not available in current papers. Hence the authors they have filled in a knowledge gap about these materials. More precise measurements of the

samples' Poisson's ratio, stresses, strains, and tensile moduli could have been achieved by using an extensometer during tensile testing; however, none was available to the authors at the time of writing.

Except for the Sinterit PA12, the Charpy test results cannot be compared directly to the data sheets as they applied several different testing methods. Sinterit's PA12 material reached an average impact strength of 10.3kJ/m² in this study, a noticeably lower value than the 16kJ/m² indicated by Sinterit. Through the Charpy test, the two toughest materials were shown to be the Tough 2000 resin and HP's PA12. As such, they were subjected to fatigue testing, during which the Tough 2000 resin and HP PA12 exhibited approximate strengths of 17MPa and 26MPa at 1×10⁵ cycles, respectively. Another study treating MJF-fabricated PA12 by Avanzini et al. determined a fatigue strength of 27.7MPa at 1×10⁶ cycles. No study considering the fatigue behaviour of the Tough 2000 resin seems to be available at the time of writing; thus, no comparison can be made.

Acknowledgement

The authors express their gratitude towards Lou Thoussaint for her contributions consisting of manufacturing and testing during her master's projects.

References

- [1] L. Cheng, J. Bai, and A. C. To, "Functionally graded lattice structure topology optimization for the design of additive manufactured components with stress constraints," *Comput Methods Appl Mech Eng*, vol. 344, pp. 334–359, 2019, doi: 10.1016/j.cma.2018.10.010.
- [2] Z. Chen, X. Wu, Y. M. Xie, Z. Wang, and S. Zhou, "Re-entrant auxetic lattices with enhanced stiffness: A numerical study," *Int J Mech Sci*, vol. 178, no. December 2019, p. 105619, 2020, doi: 10.1016/j.ijmecsci.2020.105619.
- [3] W. Chen, X. Zheng, and S. Liu, "Finite-element-mesh based method for modeling and optimization of lattice structures for additive manufacturing," *Materials*, vol. 11, no. 11, Oct. 2018, doi: 10.3390/ma11112073.
- [4] J. C. Najmon, J. Dehart, Z. Wood, and A. Tovar, "Cellular Helmet Liner Design through Bio-inspired Structures and Topology Optimization of Compliant Mechanism Lattices," *SAE Int J Transp Saf*, vol. 6, no. 3, pp. 1–12, 2018, doi: 10.4271/2018-01-1057.
- [5] J. C. Najmon, "Design of Compliant Mechanism Lattice Structures for Impact Energy Absorption," no. December, 2017.
- [6] S. F. Khosroshahi, S. A. Tsampas, and U. Galvanetto, "Feasibility study on the use of a hierarchical lattice architecture for helmet liners," *Mater Today Commun*, vol. 14, pp. 312–323, 2018, doi: 10.1016/j.mtcomm.2018.02.002.
- [7] W. Hou, X. Yang, W. Zhang, and Y. Xia, "Design of energy-dissipating structure with functionally graded auxetic cellular material," *International Journal of Crashworthiness*, vol. 23, no. 4, pp. 366–376, 2018, doi: 10.1080/13588265.2017.1328764.
- [8] Y. Xue, P. Gao, L. Zhou, and F. Han, "An Enhanced Three-Dimensional Auxetic Lattice," 2020.
- [9] F. Wang, "Systematic design of 3D auxetic lattice materials with programmable Poisson's ratio for finite strains," *J Mech Phys Solids*, vol. 114, pp. 303–318, 2018, doi: 10.1016/j.jmps.2018.01.013.
- [10] K. J. Maloney, K. D. Fink, T. A. Schaedler, J. A. Kolodziejska, A. J. Jacobsen, and C. S. Roper, "Multifunctional heat exchangers derived from three-dimensional micro-lattice structures," *Int J Heat Mass Transf*, vol. 55, no. 9–10, pp. 2486–2493, 2012, doi: 10.1016/j.ijheatmasstransfer.2012.01.011.

-
- [11] M. Vlahinos and R. O. Hara, "Unlocking Advanced Heat Exchanger Design and Simulation with nTop Platform and ANSYS CFX," 2020.
- [12] L. Cheng, J. Liu, X. Liang, and A. C. To, "Coupling lattice structure topology optimization with design-dependent feature evolution for additive manufactured heat conduction design," *Comput Methods Appl Mech Eng*, vol. 332, pp. 408–439, 2018, doi: 10.1016/j.cma.2017.12.024.
- [13] H. Niknam and A. H. Akbarzadeh, "Graded lattice structures: Simultaneous enhancement in stiffness and energy absorption," *Mater Des*, vol. 196, Nov. 2020, doi: 10.1016/j.matdes.2020.109129.
- [14] A. Takezawa, X. Zhang, M. Kato, and M. Kitamura, "Method to optimize an additively-manufactured functionally-graded lattice structure for effective liquid cooling," *Addit Manuf*, vol. 28, no. May, pp. 285–298, 2019, doi: 10.1016/j.addma.2019.04.004.
- [15] T. Decker, S. Kedziora, and C. Wolf, "Practical Implementation of Functionally Graded Lattice Structures in a Bicycle Crank Arm," 885th International Conference on Science, Technology, Engineering and Management (ICSTEM), no. November, 2020.
- [16] A. Takezawa, X. Zhang, and M. Kitamura, "Optimization of an additively manufactured functionally graded lattice structure with liquid cooling considering structural performances," *Int J Heat Mass Transf*, vol. 143, p. 118564, 2019, doi: 10.1016/j.ijheatmasstransfer.2019.118564.
- [17] L. Bai et al., "Mechanical properties and energy absorption capabilities of functionally graded lattice structures: Experiments and simulations," *Int J Mech Sci*, vol. 182, Sep. 2020, doi: 10.1016/j.ijmecsci.2020.105735.
- [18] A. Ajdari, H. Nayeb-Hashemi, and A. Vaziri, "Dynamic crushing and energy absorption of regular, irregular and functionally graded cellular structures," *Int J Solids Struct*, vol. 48, no. 3–4, pp. 506–516, Feb. 2011, doi: 10.1016/j.ijsolstr.2010.10.018.
- [19] W. Tao, A. Sutton, K. Kolan, and M. C. Leu, "Design of Lattice Structures with Graded Density Fabricated by Additive Manufacturing Cyber Physical Cloud Manufacturing Systems View project Solvent-based 3D printing of polymer/bioactive glass composites View project 19 PUBLICATIONS 207 CITATIONS SEE PROFILE," 2018, doi: 10.11509/isfa.2018.122.
- [20] W. Hou, X. Yang, W. Zhang, and Y. Xia, "Design of energy-dissipating structure with functionally graded auxetic cellular material," *International Journal of Crashworthiness*, vol. 23, no. 4, pp. 366–376, Jul. 2018, doi: 10.1080/13588265.2017.1328764.
- [21] S. Y. Choy, C. N. Sun, K. F. Leong, and J. Wei, "Compressive properties of functionally graded lattice structures manufactured by selective laser melting," *Mater Des*, vol. 131, pp. 112–120, Oct. 2017, doi: 10.1016/j.matdes.2017.06.006.
- [22] L. Gibson and M. Ashby, "Cellular Solids", doi: <https://doi.org/10.1017/CBO9781139878326>.
- [23] FormLabs, "Standard Materials for High-Resolution Rapid Prototyping," pp. 1–3, 2017.
- [24] Formlabs, "Tough 2000 Resin for Rugged Prototyping," pp. 3–4, 2020.
- [25] Sinterit, "PA12 Smooth," p. 20200713, 2014, [Online]. Available: <https://www.sinterit.com/wp-content/uploads/2014/05/PA12-Specification.pdf>
- [26] R. Quintana, J. W. Choi, K. Puebla, and R. Wicker, "Effects of build orientation on tensile strength for stereolithography- manufactured ASTM D-638 type i specimens," *International Journal of Advanced Manufacturing Technology*, vol. 46, no. 1–4, pp. 201–215, 2010, doi: 10.1007/s00170-009-2066-z.

- [27] F. Cosmi and A. Dal Maso, "A mechanical characterization of SLA 3D-printed specimens for low-budget applications," *Mater Today Proc*, vol. 32, pp. 194–201, 2019, doi: 10.1016/j.matpr.2020.04.602.
- [28] HP Development Company, "HP 3D High Reusability PA 12," pp. 5–6, 2019, [Online]. Available: <http://www8.hp.com/h20195/v2/getpdf.aspx/4AA7-0716ENE.pdf>
- [29] M. Faes, Y. Wang, P. Lava, and D. Moens, "Variability in the mechanical properties of laser sintered PA-12 components," *Proceedings - 26th Annual International Solid Freeform Fabrication Symposium - An Additive Manufacturing Conference, SFF 2015*, no. 2008, pp. 847–856, 2020.
- [30] A. Amado-Becker, J. Ramos-Grez, M. José Yañez, Y. Vargas, and L. Gaete, "Elastic tensor stiffness coefficients for SLS Nylon 12 under different degrees of densification as measured by ultrasonic technique," *Rapid Prototyp J*, vol. 14, no. 5, pp. 260–270, 2008, doi: 10.1108/13552540810907929.
- [31] J. Haworth and P. Vincent, "Mechanical and Structural Evaluation of the PA12 Desktop Selective Laser Sintering Printed Parts Regarding Printing Strategy," *3D Print Addit Manuf*, vol. 8, no. 4, 2021, doi: 10.1089/3dp.2020.0111.
- [32] C. Cai et al., "Comparative study on 3D printing of polyamide 12 by selective laser sintering and multi jet fusion," *Journal of Materials Processing Technology*, vol. 288, 2021. doi: 10.1016/j.jmatprotec.2020.116882.
- [33] C. Riccio et al., "Effects of Curing on Photosensitive Resins in SLA Additive Manufacturing," *Applied Mechanics*, vol. 2, no. 4, pp. 942–955, 2021, doi: 10.3390/applmech2040055.

4.5 Optimization of a Graded Lattice Structure in Compression

In this publication titled *Local Thickness Optimization of Functionally Graded Lattice Structures in Compression* (Decker & Kedziora, 2023a), the method proposed and demonstrated in the previous papers is applied to a cuboid lattice structure in compression. During literature review, it was noted that numerous studies investigated lattices in compression with and without thickness gradients, but very few seemed to explore their optimal material distribution. The studied structures mostly incorporated manually applied thickness gradients, therefore this investigation explores its optimal material distribution. The preceding demonstrations of the method presented in this thesis allowed for the lattice's thickness to be altered independently and on a continuous range. Here, the method is refined by linking the lattice regions' thickness by a mathematical function using its distance from the origin as independent variable. The structures are optimized for maximum specific energy absorption while retaining a mass limit equivalent to the uniform lattice's weight. The optimization routine is then forced to redistribute the mass where beneficial instead of merely increasing the lattice's diameter all throughout to reach the optimization goal. Using a function to link the regions allows for reducing the number of optimization variables from ten to three, greatly reducing the computational efforts. Two lattice types composed of Simple Cubic and Isotruss unit cells made of PA12 produced on a HP MJF printer are explored. Their behaviour while subjected to three different thickness distribution functions is investigated, then one approach per lattice type is produced and physically validated.

The optimization is performed with the Global Response Surface Method (GRSM) algorithm after a DOE run was executed. Contrary to the previous optimization studies, the models at hand are highly nonlinear and could therefore not benefit from a response surface fit approach to reduce the computation time during the optimization step. The simulative assessments predict an increase in specific energy absorption of up to 29% for the optimized Simple Cubic lattice structure, whereas the improvements were only marginal with a 5% increase in case of the Isotruss lattice. Creating the correlation between simulations and physical tests proved to be difficult as thickness deviations influenced the results. Measurements indicated that struts turn out too thin when the manufacturing method's limits are approached. Additionally, the buckling strength of the Simple Cubic lattices was severely overestimated in the FEA models since their idealized representations does not consider material or geometry imperfections. As soon as the root causes of the deviations were found and mitigated, the simulation results aligned well with the tests. Furthermore, weight differences between the FEA models, nTop models and physical samples resulted in specific energy absorption deviations. However, considering the non-normalized energy absorption values demonstrates the modelling approach's ability to recreate the physical behaviour adequately, as do the comparisons of the reaction force curves. Repeating the models under consideration of the additional knowledge was not feasible due to time restrictions. Results of the mesh morphing studies and lattices produced with Formlabs Tough 2000 resin that were omitted from the publication text can be found in the Addendum in section 7.8.

The author contributed to this paper through the development of the concept and methodology to optimize the lattice structures, deciding on the test setup, manufacturing the test samples, performing the physical compression tests as well as the simulations and optimizations. Further, the author performed the data analysis and visualization, wrote the original paper manuscript, and edited it based on reviewer comments.

Article

Local Thickness Optimization of Functionally Graded Lattice Structures in Compression

Thierry Decker *  and Slawomir Kedziora 

Faculty of Science, Technology and Medicine, University of Luxembourg, L-1359 Luxembourg, Luxembourg;
slawomir.kedziora@uni.lu

* Correspondence: thierry.decker@uni.lu

Abstract: This paper presents a new method for optimizing the thickness distribution of a functionally graded lattice structure. It links the thickness of discrete lattice regions via mathematical functions, reducing the required number of optimization variables while being applicable to highly nonlinear models and arbitrary optimization goals. This study demonstrates the method's functionality by altering the local thickness of a lattice structure in compression, optimizing the structure's specific energy absorption at constant weight. The simulation results suggest significant improvement potential for the investigated Simple Cubic lattice, but less so for the Isotruss variant. The energy absorption levels of the physical test results closely agree with the simulations; however, great care must be taken to accurately capture material and geometry deviations stemming from the manufacturing process. The proposed method can be applied to other lattice structures or goals and could be useful in a wide range of applications where the optimization of lightweight and high-performance structures is required.

Keywords: functionally graded lattice structure; finite element analysis; optimization



Citation: Decker, T.; Kedziora, S. Local Thickness Optimization of Functionally Graded Lattice Structures in Compression. *Appl. Sci.* **2023**, *13*, 12969. <https://doi.org/10.3390/app132312969>

Academic Editors: Qi Xia, Hui Liu and Kai Long

Received: 23 October 2023
Revised: 23 November 2023
Accepted: 4 December 2023
Published: 4 December 2023



Copyright: © 2023 by the authors. Licensee MDPI, Basel, Switzerland. This article is an open access article distributed under the terms and conditions of the Creative Commons Attribution (CC BY) license (<https://creativecommons.org/licenses/by/4.0/>).

1. Introduction

1.1. Functionally Graded Lattice Structures

The constant need for greater sustainability in production environments and the minimisation of resource usage has forced researchers and manufacturers to explore new design approaches. One of the resulting concepts is structures containing locally varying properties of their structure, for instance, their material composition [1]. These so-called functionally graded materials (FGMs) are designed such that their thermal, structural, vibrational, or other functions can be controlled or optimized. Common applications of FGMs are found in thermal insulation tasks involving metal–ceramic composite materials [2], for example, to improve the heat insulation of bolted joints [3]. A subcategory of FGMs is functionally graded lattice structures (FGLSs), which are macroscopic cellular structures containing a locally varying porosity gradient as a function of external factors such as stress or temperature. Their concept stems from structures that can commonly be found in nature [4], where the available material is intended to be optimally distributed, minimizing resource usage. The use of and research on FGLSs has been greatly accelerated by additive manufacturing (AM) since it readily allows for the production of such intricate designs.

Cellular structures are characterized by the porous composition of cells enclosed by edges or walls, and their exterior dimensions can cover relatively large spans while being lightweight at the same time. Naturally occurring cellular structures have evolved to fulfil various functions such as filtering, insulation, fluid transportation, load-carrying, weight reduction, and other tasks that are equally relevant for numerous engineering applications. They can be composed of vastly different materials and are found on several length scales, such as corals, honeycombs, sponges, cork, wood, and cancellous bone. In industrial settings, artificial cellular structures find use as filters, thermal or sound insulators, lightweight load-bearing elements, or protective liners for a wide variety of tasks.

Cellular structures are categorized according to their three-dimensional composition, regularity, and unit cell type. Planar cellular structures are generally referred to as honeycombs even if they do not contain the characteristic hexagonal pattern known from beehives. Three-dimensional structures characterized by a stochastic distribution of cell walls and sizes composed of open or closed polyhedra are categorized as foams. On the other hand, non-stochastic (i.e., regular, repeating) three-dimensional structures are classified as lattices. The smallest repeating entity of a lattice is the unit cell, which can be composed of struts or surfaces. Strut-based (also called graph-based) unit cells are categorized into bending-dominated and stretching-dominated types depending on their connectivity state at the corner nodes. Surface-based unit cells are divided into three-dimensional honeycombs and triply periodic minimal surface (TPMS) cells. TPMS lattices possess the useful property of dividing the occupied space into two separate volumes, rendering them especially suited for use as heat exchangers.

Lattice structures behave much like expanded foam materials under compressive loads. Their performance during the compressive phase is strongly influenced by the relative density, $\rho_{rel} = \rho^* / \rho_s$, where ρ^* is the apparent density of the cellular structure as determined by its external volume and total mass, and ρ_s is the density of the base material. A structure's porosity is, therefore, defined as $1 - \rho_{rel}$. Structures with a relative density of less than 30% are considered to be cellular, whereas they are considered to behave more like solids with isolated pores above this threshold [5]. In compression, foams exhibit an initially linear elastic regime wherein the response is governed by cell wall bending or stretching, depending on the cell morphology. The initial part of the stress–strain curve is the linear elastic phase; its derivative is defined as the apparent Young's modulus, E^* . It is followed by a long collapse plateau at nearly constant (in the case of elastic–plastic materials) or slowly rising (in the case of elastomeric materials) stress until full densification is reached. Elastic–brittle materials cause a sharp stress decrease after the linear regime; the plateau is characterized by stress fluctuations caused by the successive brittle failure of the cells. Ductile materials show a smoother transition after the linear elastic regime with few or no fluctuations in the plateau phase. Both brittle and ductile material types may show successive layer collapses during the plateau phase, which is recognizable by its large, low-frequency force fluctuations. The long progression of the plateau phase permits large kinetic energy absorption potential that renders foams and lattice structures well suited for use as protection devices for sensitive electronics, wearable padding for sports purposes, etc. Lastly, densification is reached at the end of the plateau regime when opposing cell walls come into contact. The compressive response is then governed by the properties of the base material.

Lattice structures share the described characteristics with foamed materials; however, the lattice's unit cell category can further influence their compressive response in different manners. Bending-dominated unit cell types (see Figure 1a) collapse early on because of the formation of compliant plastic hinges, causing a relatively smooth transition to the plateau regime (Figure 1b). On the other hand, stretching-dominated types yield later and more abruptly because of rupturing or buckling struts, causing a higher force peak at the end of the linear elastic regime and a sharp drop to the plateau regime stress level. The lattice categories are further subdivided into many different cell types such as the Simple Cubic (SC) cell, Face-Centred Cubic, Body-Centred Cubic, Fluorite, Diamond, Kelvin, Re-entrant, Weaire–Phelan, and combinations or alterations thereof. Although the unit cell type evidently influences the structural response of a lattice, its impact is noticeably smaller compared with the choice of base material, relative density, and unit cell category.

Lattice structures can be readily adapted to improve their performance or to specifically tailor them as needed. Such modifications can include strut thickness optimizations [6], bidirectional cell size grading [7], unit cells designed via topology optimization [8], combinations of differing unit cell sizes in honeycombs [9], unit cell type and orientation changes mimicking crystal grain structures [10], corner node movements allowing lattice struts to follow principal stresses [11], combining unit cell types [12], related methods such as using

topology optimization with certain constraints to achieve fine lattice-like structures [13], and many others.

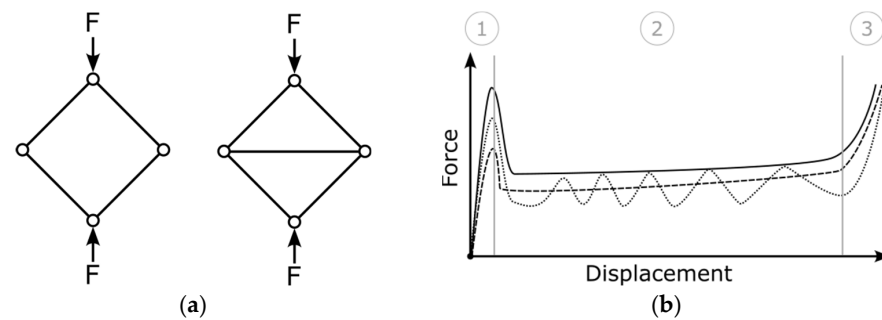


Figure 1. (a) Examples of bending-dominated (left) and stretching-dominated (right) unit cell categories; (b) schematic reaction force development of compressed lattice composed of ductile material with stretching-dominated cells (solid line), bending-dominated cells (dashed line) and a brittle lattice exhibiting sequential layer collapse (dotted line). Three distinct regions are visible—(1) linear elastic part, (2) plateau region, (3) densification.

1.2. Functionally Graded Lattice Structures Incorporating a Thickness Gradient under Compressive Loads

An easily controlled grading variable is the thickness of strut-based lattices while the cell type and size are kept constant. Several publications have considered the thickness-grading styles of lattices in quasi-static or dynamic compressive load cases and noted potential performance improvements compared with uniform lattices of the same relative density. Niknam et al. [14] studied six different lattice types at 50% porosity made of Formlabs Elastic 50 A resin in quasi-static compression, comparing them with four linearly varying thickness distributions along a single axis. The lattices were loaded along or perpendicular to the gradient direction to assess potential differences. They concluded that the uniform lattices were mostly capable of higher stress levels and absorbing more energy than the graded lattices at low compression strains; however, this trend was reversed at higher compressive strain levels. Furthermore, applying a gradient perpendicular to the loading direction appeared to outperform a parallel gradient in most of the model configurations. The performance of lattices under compressive loads is commonly assessed via specific energy absorption (SEA), a measurement dividing the absorbed compressive energy by the structure's mass.

Ajdari et al. [15] investigated a two-dimensional hexagonal aluminium honeycomb at 5% relative density under dynamic compression. At low speeds, the uniform configuration showed the largest energy absorption and the graded variants the lowest. During high-velocity compression, differences in behaviour start to occur at different compression stages. Up to 25% compression, a positive gradient with more mass located near the moving plate shows significantly increased energy absorption compared with the inverted gradient, while the uniform distribution's absorption level is nearly the average of the graded lattices' performance. At approximately 55% compression, all graded lattices have reached comparable energy absorption levels only to diverge again at higher compression levels. Between 60 and 80% compression, lattices with a negative gradient (less mass near the moving plate) show the greatest energy absorption capabilities. The same study also considered a honeycomb Voronoi lattice structure in the same load case, and similar findings were reported.

Maskery et al. [16] studied two cuboid lattice structures at a relative density of 19% made of polyamide 12 produced with a Selective Laser Sintering (SLS) machine. A constant gradient was applied to BCC and BCCz lattices (which are BCC unit cells with additional vertical struts) along the compression direction. In quasi-static compression, the uniform lattice structures exhibit long, flat plastic plateaus, whereas the graded structures show pronounced sequential layer collapses. Both types of graded structures outper-

formed the uniform counterparts vastly with 80% (BCC) and 114% (BCCz) higher specific energy absorption.

In a similar study by Maskery et al. [17], a BCC lattice structure made of Al-Si10-Mg produced via Selective Laser Melting (SLM) with heat treatment was tested under quasi-static compression. A relative density of 22% was set for both the uniform lattice and a linearly changing thickness distribution. The graded lattice showed a slight increase in SEA of approximately 10%. A uniform, non-heat-treated specimen failed because of shear band formation and large-scale diagonal failure in the early compression stages with 10% strain. This was accompanied by the near-total loss of load-bearing capacity until the densification stage began.

Choy et al. [18] studied two lattice structures produced with SLM using grade 23 Ti-6Al-4V in quasi-static compression. The lattices included an identical linear thickness change along the compression direction and were designed with high average relative densities of 29% for the cubic lattice and 48% for the hexagonal honeycomb lattice. The reported specific energy absorption of up to 50% strain was 40% lower for the cubic lattice and 10% higher for the hexagonal lattice. Upon rotating the lattice geometries by 90 degrees, with the thickness gradient applied to the compression direction, the graded cubic and hexagonal lattices showed increased absorption capabilities of 68% and 19% compared with the uniform lattices, respectively.

A study by Tao et al. [19] considered a TPMS lattice made of 304 L stainless steel produced with Selective Laser Melting. Five different continuous, linear thickness changes oriented along the compression direction were examined. The relative density was kept constant at approx. 56% for all specimens. The experimental verification of two thickness gradient choices showed nearly identical load–displacement curves and did not allow for a clear ordering of their specific energy absorption capabilities.

Bai et al. [20] compared a BCC lattice with uniform and nonlinearly changing thickness. Additionally, a variant with non-uniform unit cell height was considered. The specimens had an average relative density of approx. 18%, were manufactured via SLS using PA2200, and were compressed in a quasi-static manner. In a strain range of up to 55%, both the uniform lattice and the one with non-uniform cell height showed an almost linear increase in specific energy absorption, with the latter being slightly higher. The thickness-graded lattice exhibited far lower SEA during most of the compression procedure, but its SEA curve grew approx. cubically and reached a performance level almost equal to the uniform and size-graded variants at their respective final strain values.

1.3. Motivation, Aim, and Scope

Upon reviewing the studies summarized in the previous section, it becomes evident that graded lattices possess greater energy absorption potential than uniform structures with identical weights. The achievable performance improvements reported by the considered studies differ strongly because of the various combinations of grading styles, lattice types, compression speeds, materials, relative densities, and levels of compressive strain. Seemingly no study has investigated a method of finding an ideal thickness gradient through optimization for the considered load case, lattice type, and material choice. Only manually specified gradients that closely adhered to linearly changing thicknesses have been investigated. Therefore, this investigation aims to expand on previous studies and to find an optimal thickness distribution for the chosen lattice structure in a compressive load case, potentially enhancing a multitude of applications.

To render the proposed optimization procedure compatible with current finite element analysis (FEA) solvers, the model must be separated into discrete regions, each possessing an element thickness property that can be altered separately. However, using every single thickness property as a separate optimization variable would result in unmanageable computation times. The lattice's thickness distribution is, therefore, governed by a predefined mathematical function to reduce the number of optimization variables and to enable an efficient optimization process with FEA. The method's utility is not limited to this specific

load case or structure. It may be adapted to arbitrary goals and geometries as long as 1D or 2D elements are used for the lattice's geometrical discretization.

Two graph unit cell types (bending-dominated versus stretching-dominated) are examined in a compressive load case to assess their performance differences and improvement potential. Three thickness-grading styles are proposed, and the best-performing option is physically tested. Surface-based lattices are not investigated in this publication. Only a limited number of lattice and material options can be considered here; the investigation is, therefore, not intended to provide a universally valid gradient recommendation. Rather, the proposed optimization approach should be used to efficiently explore the improvement potential of other lattice configurations, materials, and load cases.

2. Materials and Methods

2.1. Geometry

A cuboid lattice geometry is created in nTop, a design program specifically focused on lattice structures using an implicit body approach [21]. The structures are filled with Simple Cubic and Isotruss unit cells, as depicted in Figure 2. They are considered for this study to represent examples of a bending-dominated type and a stretching-dominated type, respectively. The centres of the cube's edge nodes are spaced 50 mm apart, and it contains five unit cells per axis, as shown in Figure 3. The models possess a uniform cell size of 10 mm per axis and a constant thickness of 1.3 mm. The total extents of the lattices are, therefore, increased to 51.3 mm per axis.

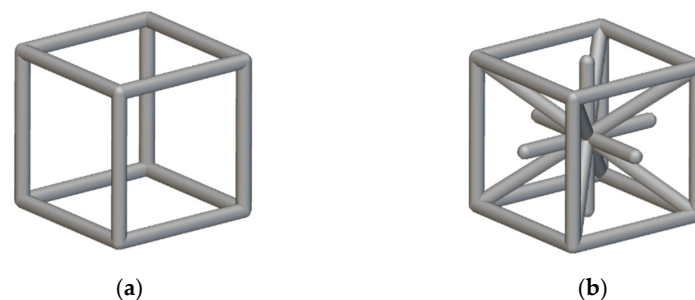


Figure 2. (a) Simple Cubic and (b) Isotruss unit cells.

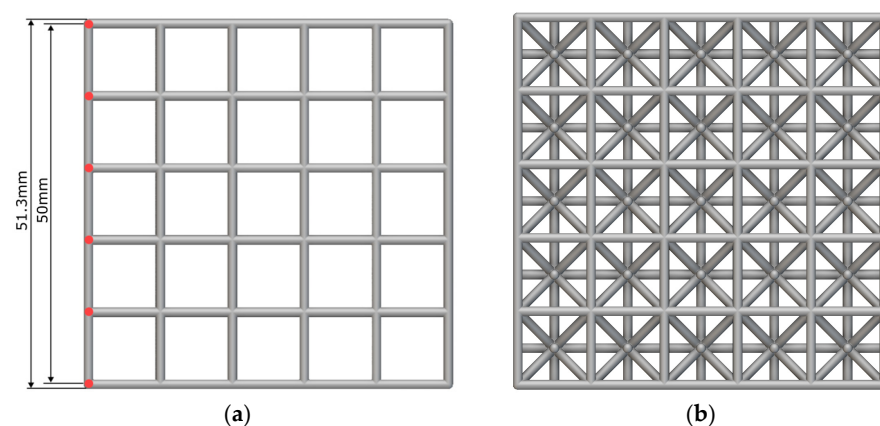


Figure 3. (a) Simple Cubic and (b) Isotruss lattice structures with unit cells of 10 mm edge length. The cubes possess equal external dimensions of 51.3 mm per axis, the centres of their corner nodes are distanced 50 mm apart.

2.2. Material Parameters and Sample Manufacturing

The test geometries were manufactured with High Reusability Polyamide 12 (PA12) created by HP and produced with an HP Multi Jet Fusion (MJF) machine [22] by an external supplier. A standard layer height of 0.080 mm is applied, and samples are oriented such that their build direction is equal to the loading direction, as indicated by the red

arrow in Figure 4. Each sample is built within a protective structure to reduce potential damage occurring during the standard postprocessing step of sandblasting to remove excess powder.

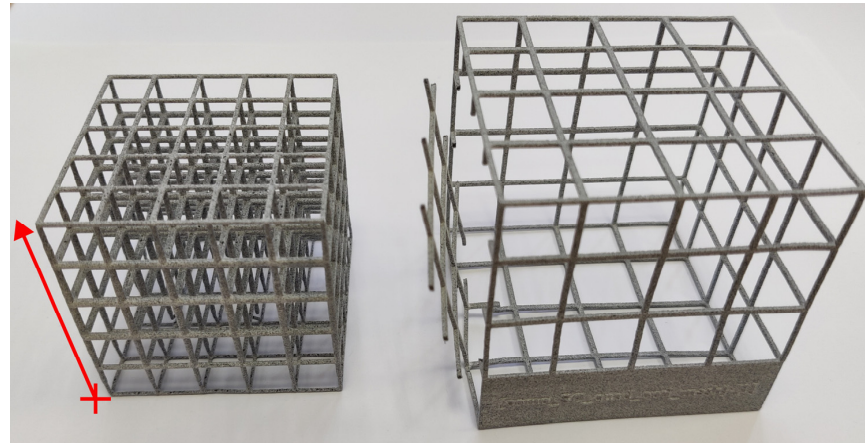


Figure 4. Printed sample next to its protective cage, necessary during postprocessing with sandblasting. The part’s build direction is identical to the load direction and is marked by a red arrow.

Table 1 and Figure 5 summarize the experimentally determined physical properties from tensile testing. A bilinear stress–strain curve was constructed (Figure 5b) based on the averaged results from five test samples (Figure 5a; see [23]). All samples were manufactured with their longitudinal axis oriented in parallel to the build direction to consider the worst-case loading scenario, wherein the load acts perpendicularly to the weakest plane. A Poisson ratio of 0.4 for as-built PA12 from Power Bed Fusion (PBF) machines is used [24]. The friction coefficient of PA12 in short-duration contact with steel is assumed to be 0.33 (c.f. [25]) and 0.4 in self-contact (c.f. [26]).

Table 1. Average material properties of HP PA12.

Physical Properties of HP PA12	
Secant modulus at 0.1% strain	1480 MPa
Poisson’s ratio	0.4 (from [24])
Density	0.94 g/cm ³
Ultimate tensile strength	50.6 MPa
Offset yield strength, $Rp_{0.2\%}$	29.6 MPa
Engineering strain at break	5.1%

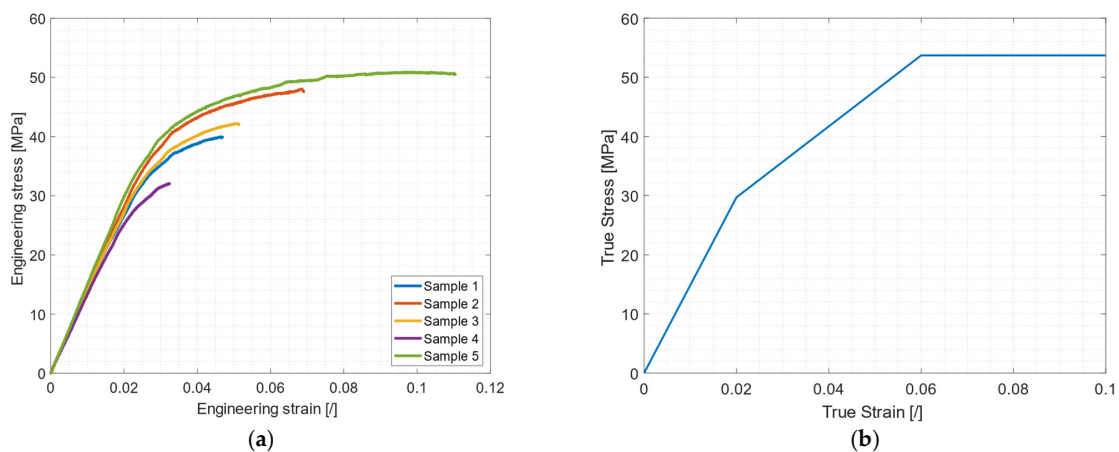


Figure 5. (a) Stress–strain data obtained from tensile testing. (b) Averaged, piece-wise linear true stress–strain data used for FEA modelling.

2.3. Finite Element Model and Optimization Setup

2.3.1. The Finite Element Model Setup

The explicit FEA solver Altair RADIOSS version 2021.2 [27] is used for the simulation series. Altair's FEA preprocessor HyperMesh [28] is used to prepare and set up the models. A stationary rigid steel plate below the lattice cube acts as a foundation with a second rigid plate compressing it at a constant speed of 1000 mm/s from the top, as depicted in Figure 6. The velocity was chosen such that no inertial effects occur in the model, while the computation completes quickly enough for an acceptable total duration when executed several hundred times during the optimization. The moving plate does not have any rotational degrees of freedom and is restricted to move only on the vertical axis. The cube is compressed by 25 mm (or 50%) during a run time of 25 milliseconds. The minimum time step is limited to 0.15 microseconds to keep mass scaling significantly below 1%. Contact between beam elements is realised with a TYPE11 line contact, whereas contact between the rigid plates and the lattice body is set up with a TYPE7 general penalty contact. The latter has a constant gap factor such that the plates always touch the lattice body in an identical fashion independently of the beam element thickness. To avoid any artificial movement restrictions from the cube, no additional boundary conditions are imposed on it. Coulomb friction is applied between all parts with the friction coefficients listed in Section 2.2. The moving plate's reaction force is traced at 20 kHz to accurately assess SEA performance during the optimization runs.

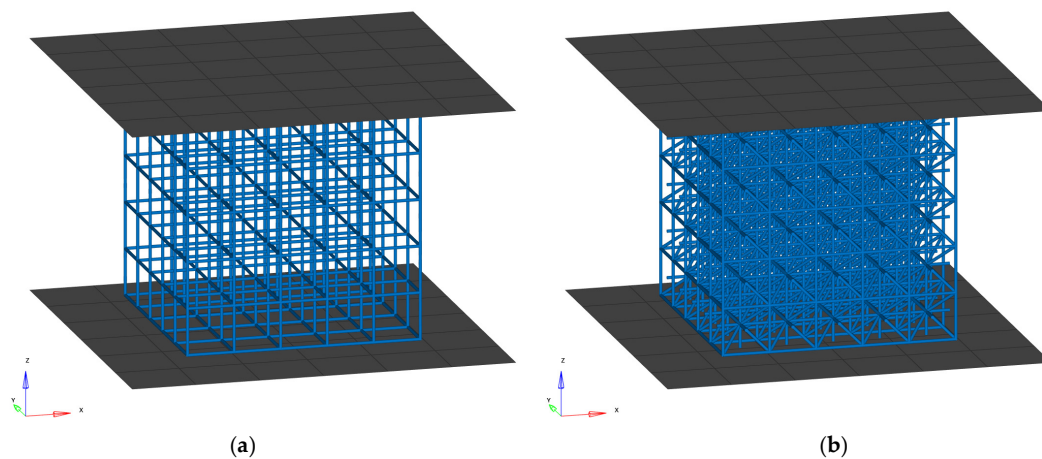


Figure 6. FEA model setup showing the Simple Cubic (a) and Isotruss (b) lattice structures discretized with 1D elements between the two steel plates. The lower plate is stationary and rigidly fixed, while the top plate moves downwards at 1000 mm/s for 25 ms.

The lattice geometry is represented by 1D beam elements since this enables the easy manipulation of their thickness properties, a requirement for the proposed thickness grading method. Each strut of the lattice is split into 10 beam elements (see detail in Figure 7), ensuring that buckling can be captured adequately. Full geometric nonlinearities are considered; integrated beam elements (P18_INT_BEAM) with a circular cross-section and four integration points per section are utilized. An isotropic piecewise linear elastic–plastic material law (LAW36) is applied to model the nonlinear material behaviour. Strain rate effects are not considered since only data at one single strain rate are available to the authors.

By default, the piecewise linear elastic–plastic law extrapolates the stress–strain curve linearly beyond the given strain range, which can result in overly stiff geometry in the post-failure strain region. Therefore, an alternative approach must be found. In Altair RADIOSS, material failure in integrated beam elements can be considered by applying a simple element deletion method when the first principal strain in an element's integration point reaches the material's failure strain. However, this results in severely underpredicted

reaction forces and is, therefore, not used. An alternative to this would be a gradual, linear stress reduction to zero in elements exceeding the failure strain, but RADIOSS' implementation for integrated beam elements is faulty and not in a functioning state. Other failure models for beam elements are not available in RADIOSS. A different approach must be considered, which is why the stress–strain curve was continued at the ultimate tensile stress level. This avoids a further reaction force increase but adds to the overall compressive energy absorption of the geometry during the simulation. This is considered to be the best compromise of the given options.

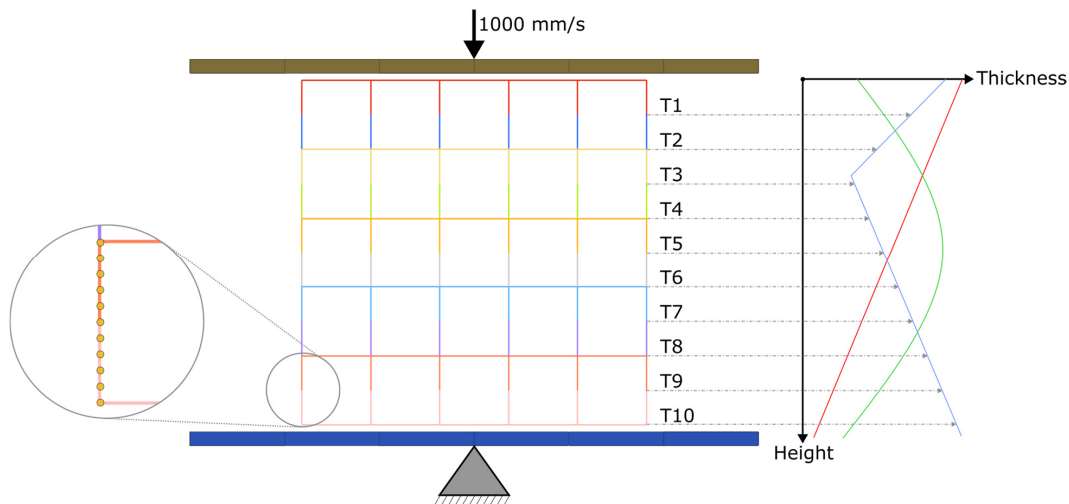


Figure 7. Splitting and linking of the lattice geometry. The graph on the right schematically shows the stepwise thickness distribution linked to mathematical functions that can be defined arbitrarily. The detail on the left side shows the subdivision of the beam into ten beam elements for increased accuracy.

2.3.2. Splitting and Linking of the Lattice

After the FEA model is set up in HyperMesh, the lattice is split into ten separate, equidistant regions along its height, as marked by the colours in Figure 7. The region identifier numbering scheme starts from T1 at the top of the lattice to T10 at the bottom. Each region possesses a single thickness attribute, and every layer of the unit cells is split in half. The RADIOSS solver input file is then exported for the subsequent steps.

Altair HyperStudy v.2021.2, a general optimization suite able to control and assess virtually any executable calculation software and its outputs [29], is used to link the separate lattice regions, control their thickness, and perform the optimizations. The procedure demonstrated here makes use of the fact that the thickness assignment of idealized 1D and 2D elements is achieved by providing a single thickness value in the solver input file. A section describing the beam element properties of a RADIOSS v.2021.2 input file is shown in Figure 8a. It contains information about its cross-section; iteration point distribution; and, among other things, the element group's radius assignment marked by a red rectangle. HyperStudy allows to parameterize it, as shown in Figure 8b, and it can then be altered freely for parameter studies or optimization runs.

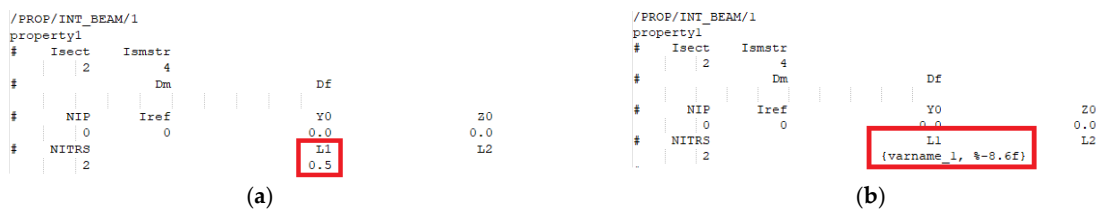


Figure 8. Beam element property definition of a RADIOSS model input file with its thickness property marked in red (a) and the same section after parameterization of the thickness value in HyperStudy (b).

Upon importing the input file into HyperStudy, it is parameterized by defining each thickness property as an optimization variable. However, performing optimization runs with ten separate variables would require significant computational resources. Therefore, the thickness parameters are linked by a mathematical function using the lattice's height as an independent variable. The lattice's origin point is located at the top layer, while the height is assessed at the lower edge of each region (at 5 mm, 10 mm, etc.), as indicated by the arrows in Figure 7. Three different functions are considered:

$$\text{Linear law : } T(h) = a * |h + c| + b \quad (1)$$

$$\text{Quadratic law : } T(h) = a * (h + c)^2 + b \quad (2)$$

$$\text{Power law : } T(h) = a * h^c + b \quad (3)$$

The linear law (Equation (1)) was chosen to add to the investigations reviewed in Section 1.2, which also considered linear thickness progressions and demonstrated significant performance improvements. It is defined such that it can include an inflexion point via the insertion of the absolute value function. The quadratic law (Equation (2)) follows a similar approach but is intended to provide larger thickness differences between regions than the linear law to investigate any potential differences. Both functions include a scaling factor, a ; a constant factor, b ; and a shifting factor, c , allowing the inflexion point to be altered. The limits of the shifting parameter, c , allow the inflexion point to be moved outside of the considered range, which also permits purely increasing or decreasing thickness progression. The power law (Equation (3)) makes identical use of the a and b parameters, but the c parameter acts as an exponent in this case. It is set up symmetrically with respect to the middle plane (i.e., T1 is equal to T10, T2 is equal to T9, etc.) to prevent extreme thickness values at the upper and lower regions. The linear and quadratic laws possess no such inherent symmetry. The power law was added to investigate the performance of a thickness distribution similar to what occurs in pomelo skin, where the cell walls are very thick and close to the outer edges while decreasing to a near-constant level in between [30]. Since pomelo fruits fall from heights of up to 10 m to the ground without fracturing, this indicates that this approach may possess high energy absorption capabilities.

In each approach, the number of optimization variables is decreased from ten to three, reducing the computational effort for finding an optimum distribution drastically. Generally, the laws linking the discrete regions may be arbitrarily chosen, and independent variables other than the height can be considered.

2.3.3. Thickness Optimization Procedure

The goal is to maximize and compare the specific energy absorption capabilities of each approach while restricting the mass of the geometry to a constant value. SEA is defined as the integral of the transient reaction force, F_R , at the moving plate over its travelled distance, s , normalized by the structure's mass, m_0 , as shown in Equation (4).

$$SEA = \frac{1}{m_0} \int_0^s F_R(a, b, c, s) ds \quad (4)$$

The goal is, therefore, the maximization of SEA by altering the parameters a , b , and c as expressed by Equation (5). Their limits, provided in Table 2, are chosen such that a broad design space is covered to permit numerous explorable combinations. More important than these limits are the constraints imposed on each region's minimum and maximum radiuses, which can lie between 0.4 and 1 mm. The lower bound ensures reasonable manufacturability, while the upper bound leaves sufficient space between their outer edges such that the lattice is not entirely compressed at the chosen compression level.

$$\max_{a,b,c}(SEA) \quad (5)$$

Table 2. Optimization variable limits. N.B.: The limits and functions determine the element’s radius, not its diameter.

	a	b	c
Linear law	± 0.02	± 4	± 200
Quadratic law	± 0.001	± 1	± 50
Power law	± 2	± 2	± 2

A mass limit is imposed to prevent the optimization algorithm from simply increasing the thickness endlessly to fulfil the maximization goal and to keep the relative density constant, ensuring comparability between models. It is equal to each reference lattice’s mass with a 1.3 mm uniform beam diameter, which is the thickness of the uniform lattice structures to which the optimized ones are compared. The standard constraint enforcement of HyperStudy is enabled, which considers a constraint violation of 0.5% acceptable, reducing the required optimization iterations. The mass is only parsed once in the initial step of the simulation to avoid any influence of mass scaling that may occur during the simulation.

A Design of Experiment (DOE) study using the Modifiable Extensible Lattice Sequence (MELS; see [31]) approach is run first with 50 iterations to explore the design space and provide initial sampling points for the optimization procedure. It is then relayed into the optimization run, which employs the Global Response Search Method (GRSM; see [32]) algorithm with an upper limit of 500 iterations. The GRSM algorithm is a gradient-based optimization method that uses a response surface fit with global sampling to increase the probability of finding the global optimum. Its fundamental principle is represented schematically in Figure 9. The exact methodology is proprietary and not available to the public; therefore, no further information can be provided here.

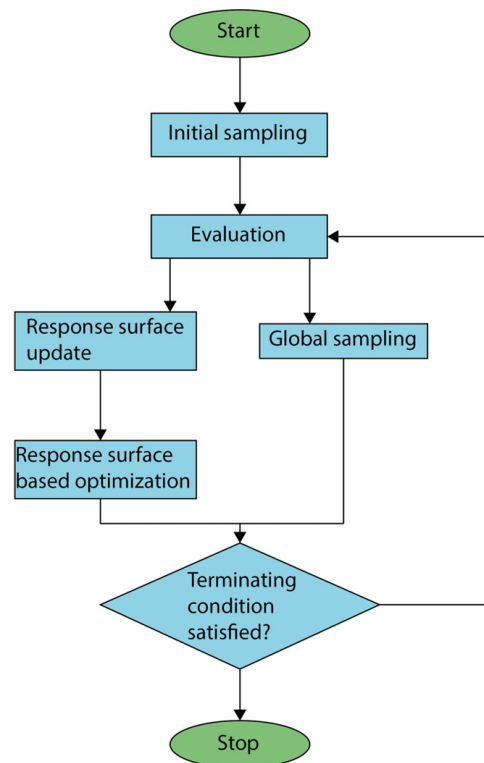


Figure 9. Fundamental principle of the GRSM optimization algorithm, recreated based on [32].

2.4. Physical Testing

The results of the base models and optimized models are verified by compressing the lattice structures on a universal testing machine, a Form + Test UP 5E. Given its movement

speed limits, the compression velocity of 1000 mm/s used in the simulation models cannot be applied in the physical tests and is thus lowered to 1 mm/s.

3. Results

3.1. Physical Test of Uniform Lattice Structures

A comparison of weights reported from the FEA model, the nTopology model, and the physical measurements is reported in Table 3. The Simple Cubic lattice FEA model has a mass of 6.7 g, whereas the Isotruss lattice FEA model has a mass of 22.2 g. It is worth noting that the FEA models do not accurately capture overlapping beams at their connecting nodes; therefore, their weights are slightly higher than those of the actual geometry reported in nTopology or from physical weighing. The reported mass in nTopology amounts to 6.2 g for the Simple Cubic lattice with a relative density of 5% and 19.0 g for the Isotruss lattice with a relative density of 15%.

Table 3. Weights of the investigated geometries as reported with the FEA model, the nTop model, and their physical sample weights.

	Simple Cubic Lattice	Isotruss Lattice
FEA model weight (g)	6.74	22.22
nTop model weight (g)	6.2	19.0
Actual weights (g)	5.9/6.0/5.7	20.0/18.7/20.3
Average of actual weights (g)	5.86	19.67

Figure 10a depicts compression test results for the three Simple Cubic lattice samples versus the FEA model, plotted as the moving plate's reaction force versus its displacement. The experimental reaction force curves clearly show a linear elastic region up to the first layer collapse beginning at 400–450 N, after which, the force fluctuates in a plateau region at a level of approximately 200 N. The plateau region is characterized by two layer collapses at a displacement of 10 mm and 17.5 mm. The FEA model's reaction force greatly surpasses that of the experimental tests up to the initial layer collapse, reaching 1273 N. Beyond its linear elastic region, the plateau phase of the FEA model coincides well with the experimental results both quantitatively and qualitatively, but it does not adequately capture the reaction force peak caused by the layer collapse at the 10 mm mark. The increased buckling strength of the FEA model is explained by its flawless geometry and material composition. It contains no deviations in the geometry and material composition found in physical parts, artificially increasing the buckling strength of the structure. To test this statement, the model was also simulated after introducing random deviations to the elements' nodal positions. Figure 11 compares the base model with two versions with random nodal deviations of up to 0.1 mm and 0.2 mm, respectively. The force peak is markedly reduced and approaches the level seen from the test samples, while the plateau regions remain comparable but slightly elevated. Their energy absorption values amount to approximately 5.9 J for both variants. The potential material property deviations of the FEA model were not explored in this context.

Figure 10b shows the experimental and simulative results of the Isotruss lattice models. The peak reaction forces of the linear elastic region of the experimental curves range from 3420 N to 3950 N, while the FEA model reaches 3215 N. The ensuing plateau region of test sample 1 is marked by two clearly discernible force peaks caused by sequential layer collapse. As for test sample 2, the same region shows a much smaller reaction force fluctuation range, remaining close to 2250 N. Test sample 3 shows total brittle failure immediately after the linear elastic region, at which point, it completely loses its load-bearing capacity until the compression plate contacts the structure again and reaches a reaction force level similar to the other test samples during the plateau phase.

The FEA model peaks at 3220 N at the end of the linear elastic region and, in the plateau region, closely follows the force fluctuations observed for samples 1 and 2. The most noticeable difference between experiment and simulation is the failure mode that occurred,

which is not directly visible by observing the plots. All the samples first experienced a beginning layer collapse in the top and bottom lattice layers, which was also present in the FEA model. While the latter continued exclusively via consecutive layer collapse over the course of the compression, the physical samples failed through shear banding in addition to layer collapse. According to Liu et al. [33], shear band formation is favoured by material concentrations around a lattice’s nodes rather than its struts. Given the geometrical discretization at nodes during meshing (see Figure 12) and deviations stemming from the manufacturing technique, differences from the target thickness that cause this behaviour can occur. Despite this difference in behaviour, the reaction force levels were fairly aligned throughout the whole procedure.

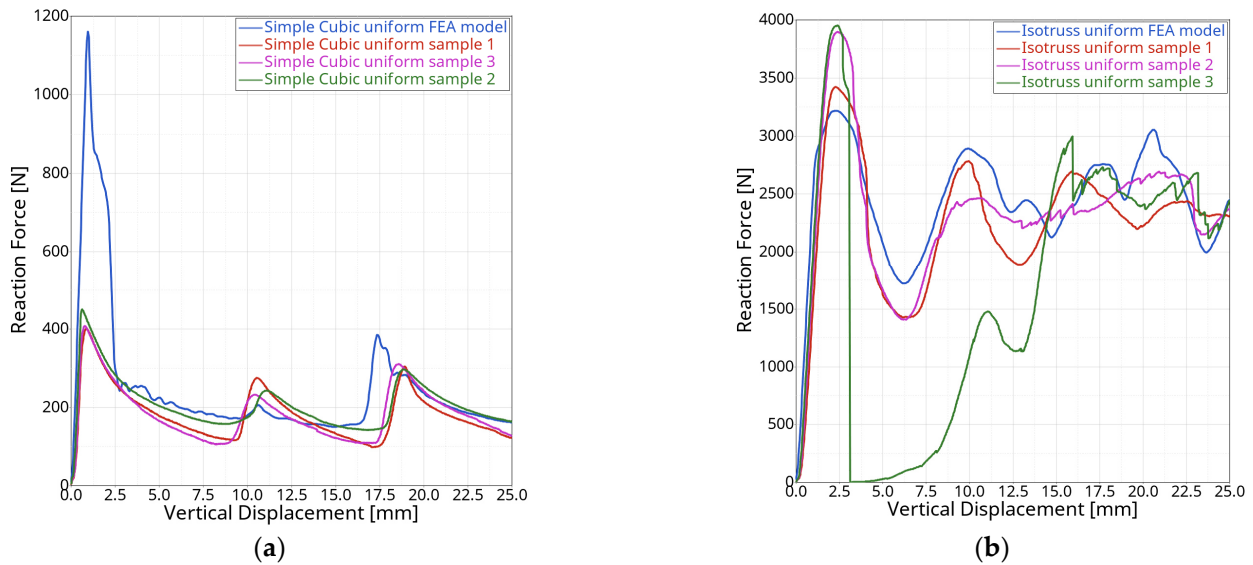


Figure 10. (a) Reaction force versus displacement plots of the Simple Cubic lattice tests and simulations with uniform geometry. (b) Reaction force versus displacement plots of the Isotruss lattice tests and simulations with uniform geometry.

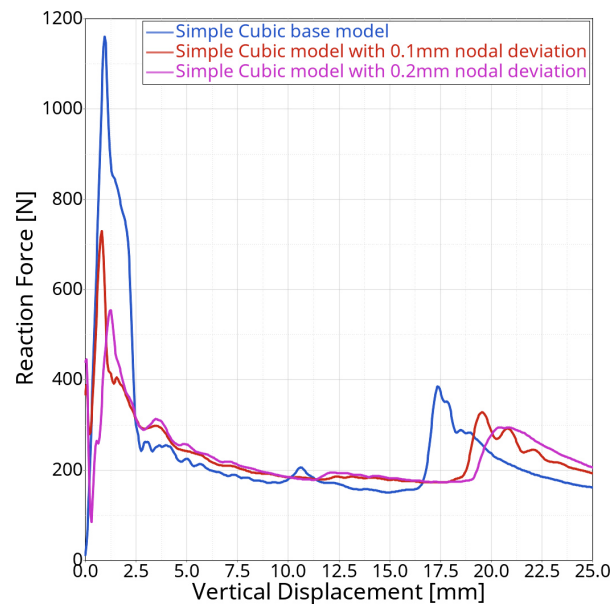


Figure 11. Comparison of the Simple Cubic lattice’s FEA model reaction force with models incorporating random node position deviations of up to 0.1 mm and 0.2 mm.

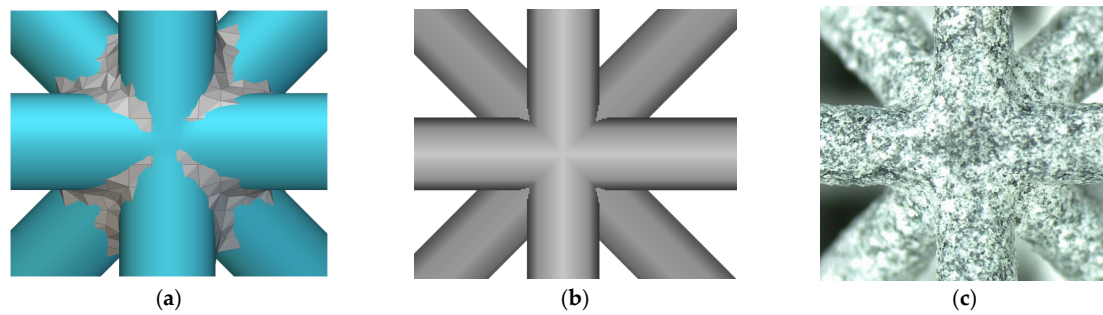


Figure 12. Geometrical deviation from the target caused by the meshing procedure used to export the geometry (a); FE representation of cylindrical beam elements overlapping at nodes (b); and printed lattice geometry (c).

Note that the result curves from the simulations are shown after filtering with an SAE J211/1 filter, but the numerical values were calculated based on nonfiltered results. Reaction force curves from the test samples were not subject to filtering.

The sequences of images in Figures 13 and 14 depict the experimental behaviours of the structures compared with their Finite Element models. After surpassing the linear elastic phase, the uniform Simple Cubic lattice sample exhibits buckling beams in the second and last layers from the bottom. To compensate for the reduced height availability, the entire section is shifted forward. In the FE model, there is a more localized layer shift where only one section of horizontally oriented beams moves sideways because of buckling.

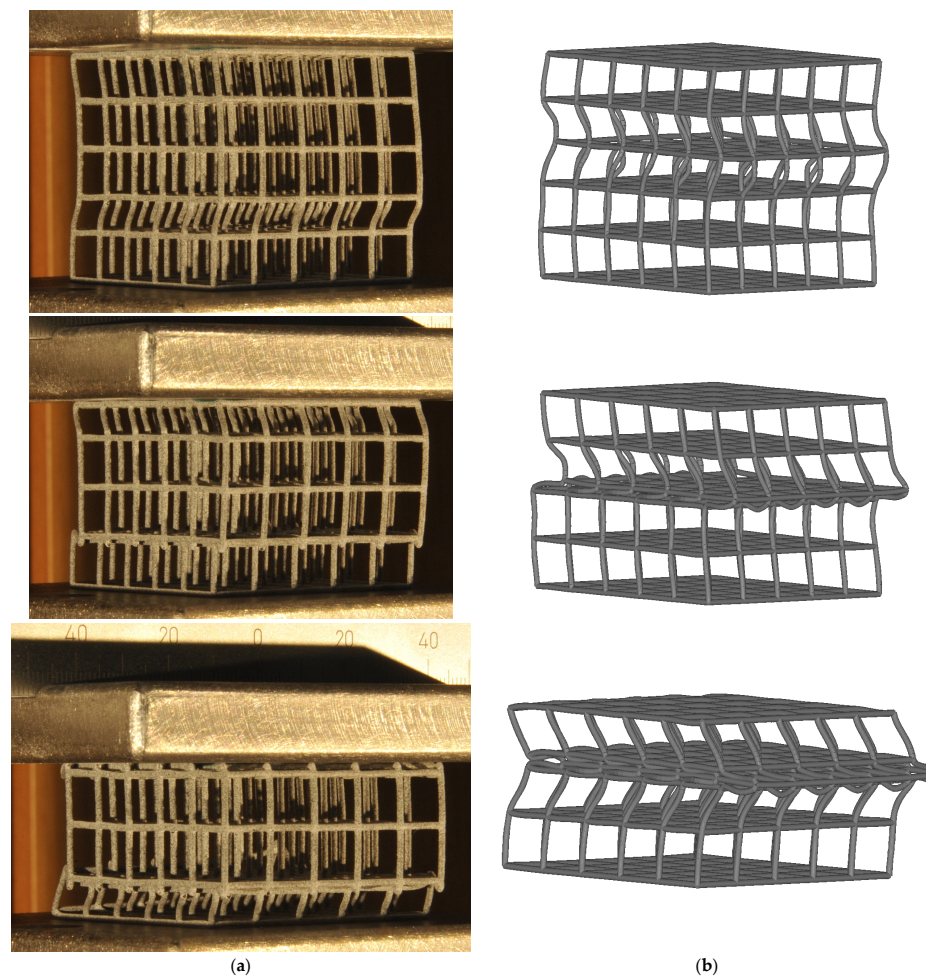


Figure 13. Comparison of structural behaviour between physical testing of the Simple Cubic lattice (sample 1) (a) and its FEA model (b) at identical plate displacements of 2.5 mm, 10 mm, and 20 mm.

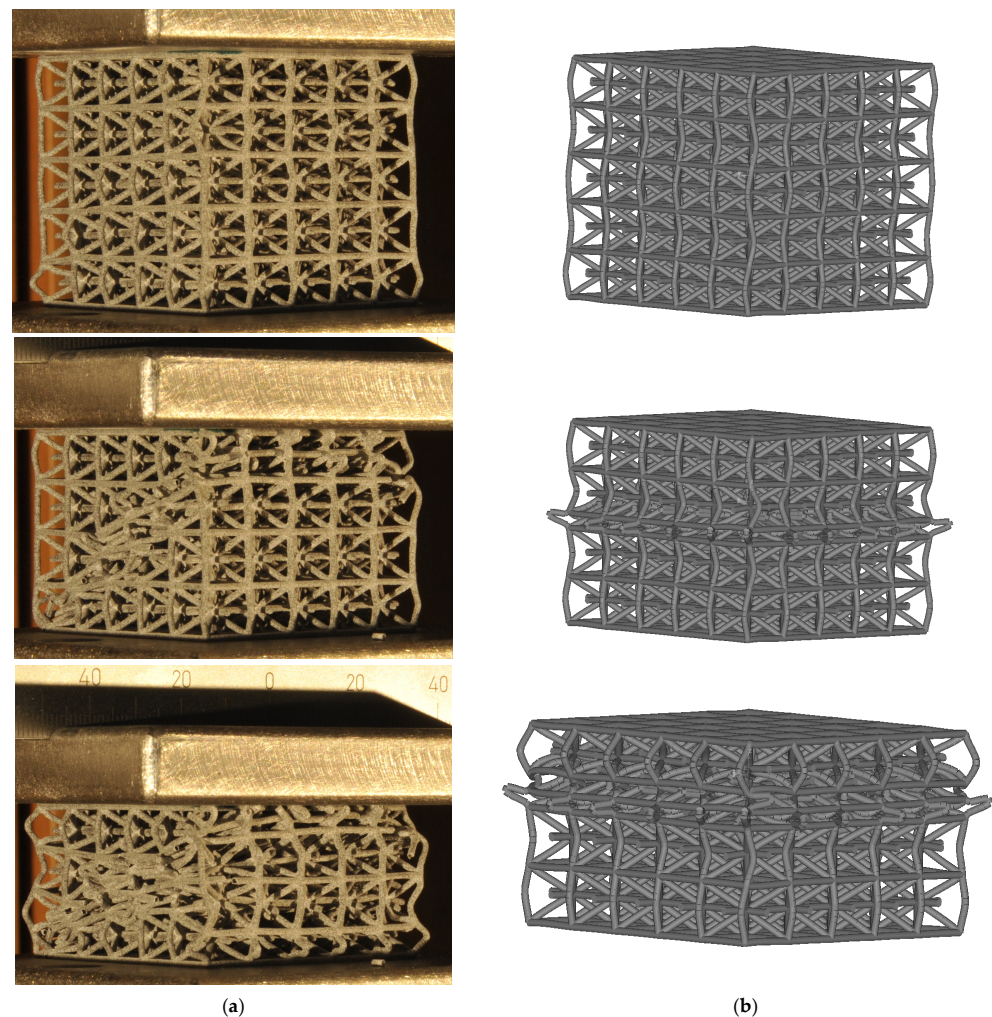


Figure 14. Comparison of structural behaviour between physical testing of the Isotruss lattice (sample 1) (a) and its FEA model (b) at identical plate displacements of 2.5 mm, 10 mm, and 20 mm.

Similar to the physical test sample, the Isotruss FEA model displays the most significant buckling response in the lowest and uppermost cell layers, where the corner beams bend outward more than in other layers. The FEA model then shows a complete layer collapse in the middle section first, while the physical model fails because of shear banding throughout the entire structure.

Table 4 summarizes the total absorbed energy per sample and its specific energy absorption attained during the compression test. The Simple Cubic lattice's SEA value, as determined using the FEA model, lies 14.9% above the average results obtained from the physical tests. This is explained by the significantly higher force peak during the linear elastic region of the compression procedure, as shown in Figure 10a. On the other hand, the SEA performance values of samples 1 and 2 of the Isotruss lattices are 1% and 12% higher than those predicted with the FEA model, whereas sample 3 only reaches 75% because of its complete loss of load-bearing capacity during the test.

The absorbed energy levels are overestimated by the FE models compared with the averaged values of both lattice types. In the case of the SC lattice, this can be explained by the increased buckling strength of the FEA model since the remaining part of the curve coincides very well with the test results. If only samples 1 and 2 of the Isotruss lattice test are considered, and the third sample is discarded as an outlier, their average energy absorption amounts to 57.2 J, which comes within 8% of the value predicted by the FEA model.

Table 4. Total absorbed energy and specific energy absorption (SEA) values of the Simple Cubic and Isotruss lattice structures with uniform beam diameters. Sample 3 of the Isotruss model is considered an outlier and marked by a star (*).

	Simple Cubic Lattice			Isotruss Lattice		
	Absorbed Energy (J)	Weight (g)	SEA (J/kg)	Absorbed Energy (J)	Weight (g)	SEA (J/kg)
Sample 1	4.6	5.9	777	56.2	20.0	2809
Sample 2	5.2	6.0	866	58.2	18.7	3114
Sample 3	4.6	5.7	810	42.3 *	20.3	2084
Avg. samples	4.8	5.9	818	52.2	19.7	2669
Simulated	6.3	6.74	940	61.8	22.22	2780

3.2. FEA Optimization Results

SEA values resulting from the optimization runs are summarized in Table 5; their thickness distributions are displayed in Figure 15. For the Simple Cubic lattice, the thickness value curve of the linear law approach shows an inflexion point between the T3 and T4 regions, situating the thickest part of the lattice in its upper half. The thickness values do not deviate strongly from the initial distribution, varying from 1.4 mm at its thickest part to 1.2 mm at its thinnest. The quadratic law approach shows a much larger spread, with a thickness of 1.05 mm in the first region, 1.6 mm in the middle, and 0.82 mm in the last region. Given its definition, the power law approach shows a symmetric thickness distribution, with the thinnest regions situated in the middle section of the lattice. Here, the outer regions’ diameters increase to 1.32 mm and reduce to 1.26 mm in the middle section. They remain 3.4% below the mass limit, while the other approaches make full use of it. All three approaches attain significant SEA value improvement predictions, with the linear law approach reaching a 29% increase over the uniform lattice. On the other hand, the same thickness optimization approaches yield only marginal changes in the Isotruss lattice structure. The quadratic law approach allows for a 5.1% increase in SEA, while the power law approach yields a slightly negative result.

Table 5. Total absorbed energy and specific energy absorption (SEA) values of the Simple Cubic and Isotruss lattice structures with uniform beam diameter.

Grading Approach	Simple Cubic Lattice			Isotruss Lattice		
	Absorbed Energy (J)	Weight (g)	SEA (J/kg)	Absorbed Energy (J)	Weight (g)	SEA (J/kg)
Baseline value	6.3	6.74 g	940	61.8	22.22 g	2780
Linear law	8.1	6.71 g	1213 (+29.0%)	62.6	22.20 g	2819 (+1.4%)
Quadratic law	8.2	6.74 g	1210 (+28.7%)	65.1	22.27 g	2921 (+5.1%)
Power law	7.2	6.51 g	1105 (+17.5%)	61.7	22.23 g	2775 (−0.2%)

The reaction force evolutions of each lattice type and optimisation strategy plotted versus the displacements of the compression plate are plotted in Figure 16. It appears that the maximal response force levels for the Simple Cubic lattice structure reach values that are comparable to those of the uniform base model. Only the quadratic thickness distribution approach model peaks at a much lower level. The increase in energy absorption is caused by a considerably greater mean reaction force level in the plateau phase for all thickness optimisation techniques. It becomes visible when comparing the plateau regions of the linear and quadratic law approaches that the linear law approach gains the majority of the absorbed energy in the first half, up to a displacement of 12.5 mm, while the quadratic law approach gains it in the second.

All of the Isotruss models’ reaction force curves peak in the linear elastic phase at about 3000 N to 3250 N of force. The force levels of the thickness optimisation methods

then move through a trough that descends to 1500 N–1750 N before fluctuating around 2500 N.

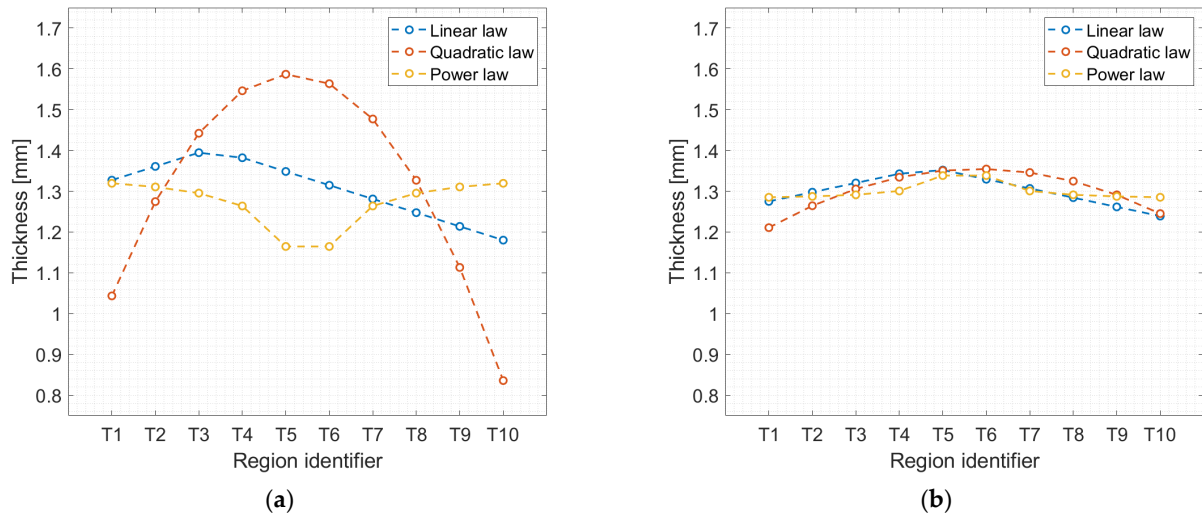


Figure 15. Diameter values of Simple Cubic (a) and Isotruss (b) lattices after optimization (T1: bottom, T10: top).

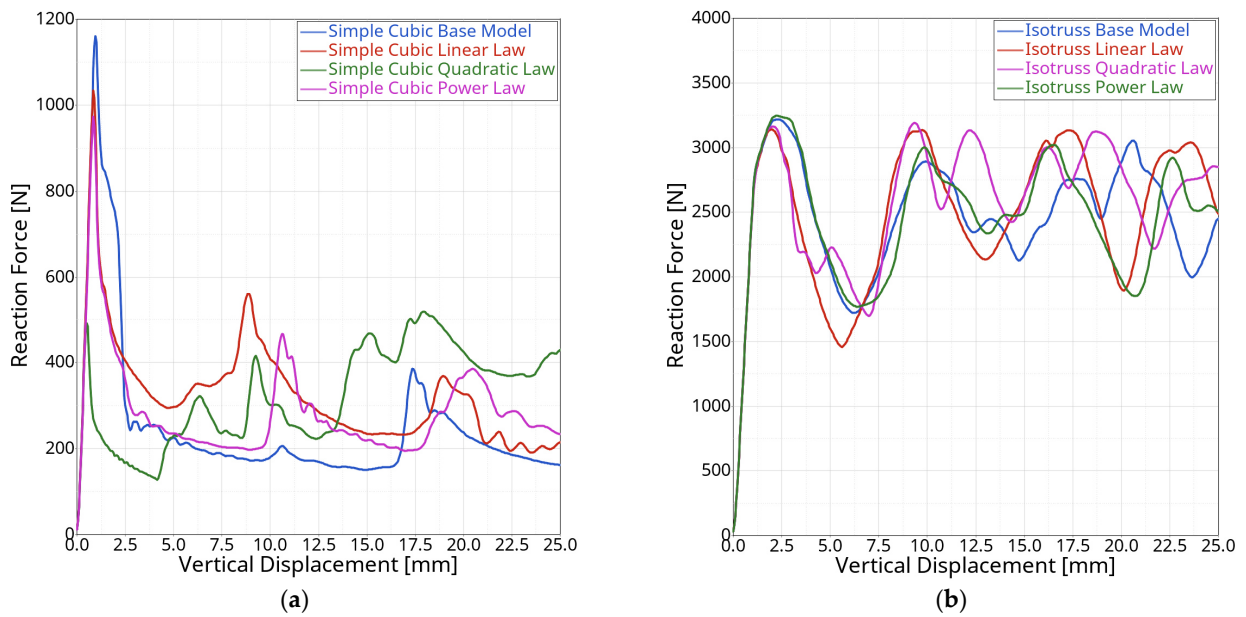


Figure 16. Reaction force versus compression plate displacement of the optimized Simple Cubic lattice geometries (a) and the Isotruss lattice geometries (b) compared with results from the uniform lattice structures.

The linear and quadratic thickness distribution approaches yield nearly identical improvements for the Simple Cubic lattice, whereas the quadratic distribution law performs better than the others in the case of the Isotruss lattice structure. It is chosen for the optimization step of the study.

3.3. Physical Test Results of Optimized Lattices

The reaction force plots of the optimized lattices from the physical tests are shown in Figure 17 with their respective results from the simulations. The Simple Cubic lattice samples again show lower force peaks compared with the simulations, analogously to the samples with uniform thickness discussed previously. The Simple Cubic lattice FEA

model sufficiently predicts when force peaks from sequential layer collapse will occur but produces significantly higher reaction forces. The Isotruss lattice FEA model underestimates the achieved force peaks slightly but remains close to the plateau force seen in the later stages of the compression test.

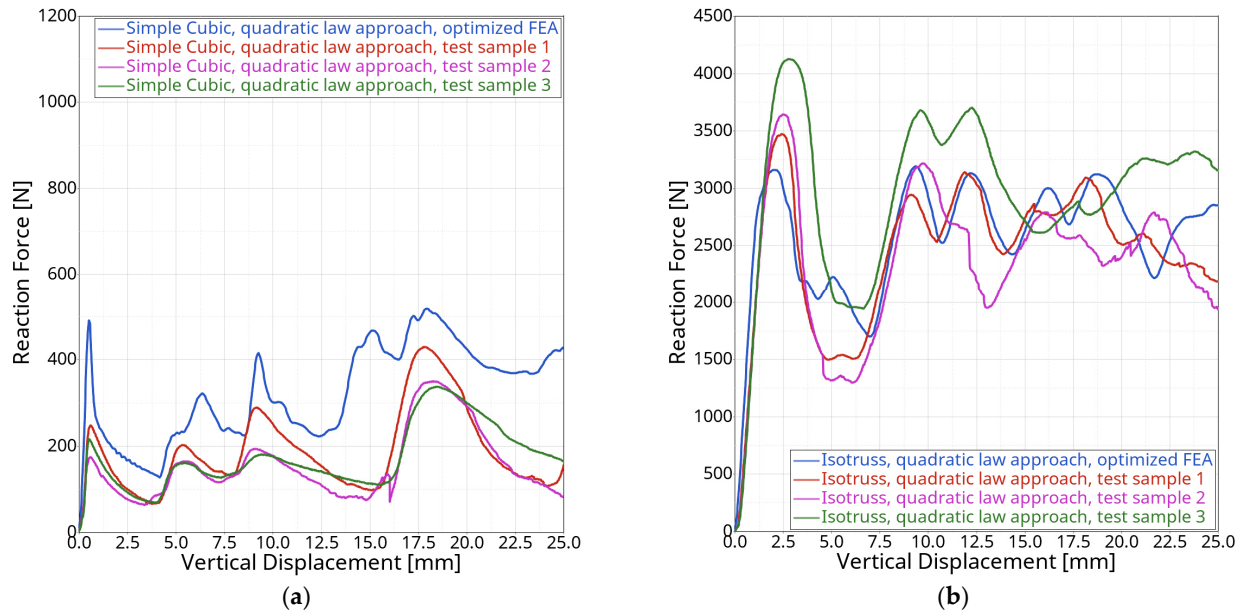


Figure 17. Reaction force versus compression plate displacement of the Simple Cubic lattice geometries (a) and the Isotruss lattice geometries (b) with the quadratic thickness optimization approach.

All of the models’ absorbed energies and SEA values are listed in Table 6. The lattice samples all weigh considerably less than what was assumed in the FEA model, which impacts their SEA performance positively. The absorbed energy of the Simple Cubic lattice simulation is nearly twice as large as that of the test samples, as can be estimated from the corresponding graph in Figure 17a, where the FEA model predicts a large initial force peak and then consistently overestimates the force level greatly. Thickness measurements of the samples revealed that their diameters were 0.1–0.2 mm lower than expected in regions with a required thickness under 1 mm. The simulation was repeated with uniform diameter reductions of 0.1 mm and 0.2 mm. The results are shown in Figure 18, and a much closer fit is apparent. Their absorbed energies were 4.7 J and 3.4 J for 0.1 mm and 0.2 mm thickness reductions. The SEA performance amounted to 796 J/kg with a 0.1 mm reduction and 690 J/kg with a 0.2 mm reduction. The former model reaches energy absorption and SEA levels that are comparable to the samples’ average, indicating that the negative thickness deviation is at the root of the performance difference.

Table 6. Total absorbed energy and specific energy absorption (SEA) values of the Simple Cubic and Isotruss lattice samples after optimization with the quadratic thickness distribution approach.

	Simple Cubic Lattice			Isotruss Lattice		
	Absorbed Energy (J)	Weight (g)	SEA (J/kg)	Absorbed Energy (J)	Weight (g)	SEA (J/kg)
Sample 1	4.7	6.0	784	61.5	18.8	3269
Sample 2	3.9	5.4	719	58.8	18.9	3109
Sample 3	4.4	5.8	752	73.9	20.3	3939
Avg. samples	4.1	5.7	752	64.7	19.3	3439
Simulated	8.2	6.74	1210	65.1	22.27	2921

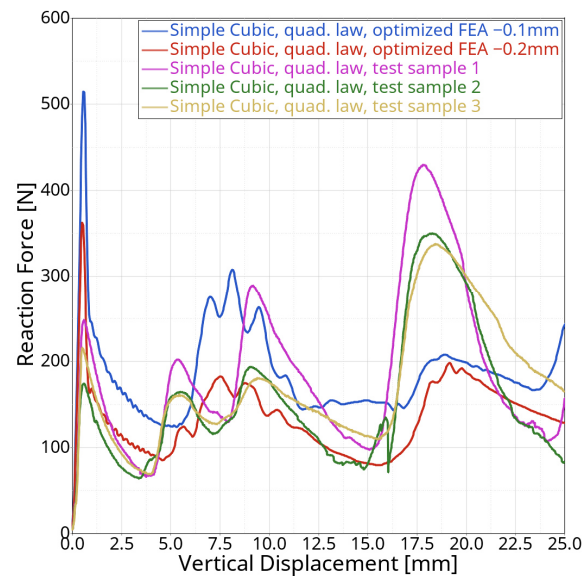


Figure 18. Comparison of optimised Simple Cubic FEA model with quadratic thickness distribution and 0.1 mm constant diameter reduction vs. the test samples.

The Isotruss lattice samples achieve 17.7% higher SEA values than those predicted with their FE models. However, focusing on their non-normalized absorbed energies alone, their differences are significantly smaller and only amount to 1% and 4%. The disparities in SEA levels, therefore, stem from the differing sample weights compared with FE model weights.

3.4. Discussion of the Results

Difficulties arise when correlating FEA models with physical test results, highlighting the challenges that occur when simulating additively manufactured lattice structures. Parts exhibit material and geometry imperfections that are challenging to account for in advance, and their influence can result in vastly different model behaviour. The tensile properties of the tested material samples varied significantly, with ultimate tensile strengths ranging from 32 MPa to 51 MPa and maximum strains ranging from 3.5% to 11%. Using their average properties might not necessarily be transferrable to a different batch of samples from a later date or be transferrable to singular samples. Printing orientation also influences the final part properties, as the undersides of surfaces exhibit higher porosity than those of the top surfaces, and tolerances vary depending on features being oriented horizontally, vertically, or at any angle in between. While samples were all manufactured with identical orientations, angled structures can differ from their horizontally or vertically oriented counterparts in the same sample, influencing its global response in FEA models. Moreover, possible geometrical deviations such as warping, material accumulation at lattice nodes due to discretization from meshing the geometry, and feature size tolerances from sandblasting during postprocessing and when nearing the production method's limits exacerbate accurate modelling even further. The buckling response of the investigated unit cell types reacts very sensitively to any imperfections occurring in test samples, as evidenced by these findings.

Beyond these issues, the assumptions regarding the general setup of the FEA models were confirmed to be adequate and accurate for the models, as evidenced by our results. Models with the necessary changes applied to them closely matched both the reaction force curves of the test samples and the accumulated average energy absorption values. The specific energy absorption reported from the FEA models was slightly underestimated since the reported sample weights were overestimated because of overlapping beam elements at unit cell corner nodes. This can be corrected by using the non-normalized absorbed energy of the lattice instead of SEA while still limiting the structure's maximum weight and calculating the SEA value based on the physical sample weights. The choice of using

SEA as the optimization metric was made to allow the study to also explore lower lattice weights, but the optimizer mostly operated above or very close to the upper limit and did not significantly venture in the opposite direction.

4. Summary and Discussion

A method of optimizing lattice structures was demonstrated and tested for maximum specific energy absorption in compressive load cases. The method links the thicknesses of discrete lattice regions via three different mathematical functions using the physical height as the independent variable. The number of required optimization variables is reduced from one per single lattice region to a total of three, thus reducing the required computation time significantly. The method can be used for highly nonlinear simulations and arbitrary optimization goals. The simulations predict a large improvement potential for the Simple Cubic lattice structure when using the proposed linear and quadratic thickness distribution approaches. The optimization simulations of the Isotruss lattice yielded only minute changes.

Although the improvements anticipated from the initial FEA optimizations were not fully realized during physical testing, the results became remarkably close after addressing the deviations. Thus, the authors are confident that the optimization method and the FEA modelling approach are reliable and can produce the expected results when manufacturing constraints are respected.

Improvements to the study can be achieved by exploring different graph and surface unit cell types, relative densities, and material options, as they can result in vastly different optimization potentials compared with the ones presented. Avoiding graph lattice types prone to buckling could facilitate the correlation of tests and FEA models, as they are highly sensitive to a multitude of factors that are difficult to control. Furthermore, avoiding feature sizes approaching the manufacturing method's limits is advisable to mitigate feature sizes that significantly deviate from the target. Moreover, other optimization goals and lattice topologies, such as surface-based lattices, should be explored using this method.

Author Contributions: Conceptualization, T.D. and S.K.; methodology, T.D.; software, T.D.; validation, T.D.; formal analysis, T.D.; investigation, T.D.; resources, S.K.; data curation, T.D.; writing—original draft preparation, T.D.; writing—review and editing, S.K.; visualization, T.D.; supervision, S.K.; project administration, S.K.; funding acquisition, S.K. All authors have read and agreed to the published version of the manuscript.

Funding: This research received no external funding.

Institutional Review Board Statement: Not applicable.

Informed Consent Statement: Not applicable.

Data Availability Statement: The data are contained within the article.

Conflicts of Interest: The authors declare no conflict of interest.

References

1. Anné, G.; Vleugels, J.; Van Der Biest, O. Functionally graded ceramics. In *Ceramic-Matrix Composites: Microstructure, Properties and Applications*; Elsevier: Amsterdam, The Netherlands, 2006; pp. 575–596. [[CrossRef](#)]
2. Shabana, Y.M.; Noda, N.; Tohgo, K. Elasto-plastic thermal stresses in functionally graded materials considering microstructure effects. In Proceedings of the Seventh Cairo University International MDP Conference, Cairo, Egypt, 15–17 February 2000.
3. Zhou, W.; Ai, S.; Chen, M.; Zhang, R.; He, R.; Pei, Y.; Fang, D. Preparation and thermodynamic analysis of the porous $ZrO_2/(ZrO_2 + Ni)$ functionally graded bolted joint. *Compos. Part B Eng.* **2015**, *82*, 13–22. [[CrossRef](#)]
4. Noronha, J.; Dash, J.; Leary, M.; Watson, M.; Qian, M.; Kyriakou, E.; Brandt, M. Additively Manufactured Functionally Graded Lattices: Design, Mechanical Response, Deformation Behavior, Applications, and Insights. *JOM* **2023**, *75*, 5729–5754. [[CrossRef](#)]
5. Gibson, L.J.; Ashby, M.F. *Cellular Solids: Structure & Properties*; Cambridge University Press: Oxford, UK, 1988. [[CrossRef](#)]
6. Chen, W.; Zheng, X.; Liu, S. Finite-element-mesh based method for modeling and optimization of lattice structures for additive manufacturing. *Materials* **2018**, *11*, 2073. [[CrossRef](#)] [[PubMed](#)]
7. Yang, J.; Chen, X.; Sun, Y.; Zhang, J.; Feng, C.; Wang, Y.; Wang, K.; Bai, L. Compressive properties of bidirectionally graded lattice structures. *Mater. Des.* **2022**, *218*, 110683. [[CrossRef](#)]

8. Song, J.; Wang, Y.; Zhou, W.; Fan, R.; Yu, B.; Lu, Y.; Li, L. Topology optimization-guided lattice composites and their mechanical characterizations. *Compos. Part B Eng.* **2018**, *160*, 402–411. [[CrossRef](#)]
9. Rahman, H.; Yarali, E.; Zolfagharian, A.; Serjouei, A.; Bodaghi, M. Energy absorption and mechanical performance of functionally graded soft–hard lattice structures. *Materials* **2021**, *14*, 1366. [[CrossRef](#)] [[PubMed](#)]
10. Pham, M.-S.; Liu, C.; Todd, I.; Lertthanasarn, J. Damage-tolerant architected materials inspired by crystal microstructure. *Nature* **2019**, *565*, 305–311. [[CrossRef](#)] [[PubMed](#)]
11. Daynes, S.; Feih, S.; Lu, W.F.; Wei, J. Optimisation of functionally graded lattice structures using isostatic lines. *Mater. Des.* **2017**, *127*, 215–223. [[CrossRef](#)]
12. Chen, Z.; Xie, Y.M.; Wu, X.; Wang, Z.; Li, Q.; Zhou, S. On hybrid cellular materials based on triply periodic minimal surfaces with extreme mechanical properties. *Mater. Des.* **2019**, *183*, 108109. [[CrossRef](#)]
13. Wu, J.; Aage, N.; Westermann, R.; Sigmund, O. Infill Optimization for Additive Manufacturing—Approaching Bone-Like Porous Structures. *IEEE Trans. Vis. Comput. Graph.* **2017**, *24*, 1127–1140. [[CrossRef](#)] [[PubMed](#)]
14. Niknam, H.; Akbarzadeh, A. Graded lattice structures: Simultaneous enhancement in stiffness and energy absorption. *Mater. Des.* **2020**, *196*, 109129. [[CrossRef](#)]
15. Ajdari, A.; Nayeb-Hashemi, H.; Vaziri, A. Dynamic crushing and energy absorption of regular, irregular and functionally graded cellular structures. *Int. J. Solids Struct.* **2011**, *48*, 506–516. [[CrossRef](#)]
16. Maskery, I.; Hussey, A.; Panesar, A.; Aremu, A.; Tuck, C.; Ashcroft, I.; Hague, R. An investigation into reinforced and functionally graded lattice structures. *J. Cell. Plast.* **2016**, *53*, 151–165. [[CrossRef](#)]
17. Maskery, I.; Aboulkhair, N.T.; Aremu, A.O.; Tuck, C.J.; Ashcroft, I.A.; Wildman, R.D.; Hague, R.J.M. A mechanical property evaluation of graded density Al-Si10-Mg lattice structures manufactured by selective laser melting. *Mater. Sci. Eng. A* **2016**, *670*, 264–274. [[CrossRef](#)]
18. Choy, S.Y.; Sun, C.-N.; Leong, K.F.; Wei, J. Compressive properties of functionally graded lattice structures manufactured by selective laser melting. *Mater. Des.* **2017**, *131*, 112–120. [[CrossRef](#)]
19. Tao, W.; Liu, Y.; Sutton, A.; Kolan, K.; Leu, M.C. EasyChair Preprint Design of Lattice Structures with Graded Density Fabricated by Additive Manufacturing “Design of lattice structures with graded density fabricated by additive manufacturing”. In Proceedings of the 2018 International Symposium on Flexible Automation, ISFA 2018, Kanazawa, Japan, 15–19 July 2018.
20. Bai, L.; Gong, C.; Chen, X.; Sun, Y.; Xin, L.; Pu, H.; Peng, Y.; Luo, J. Mechanical properties and energy absorption capabilities of functionally graded lattice structures: Experiments and simulations. *Int. J. Mech. Sci.* **2020**, *182*, 105735. [[CrossRef](#)]
21. nTop. Available online: <https://www.ntop.com> (accessed on 31 October 2023).
22. HP MJF. Available online: <https://www.hp.com/us-en/printers/3d-printers/learning-center/3d-printing-process.html#section=hp-multi-jet-fusion> (accessed on 31 October 2023).
23. Decker, T.; Kedziora, S.; Museyibov, E. Comparison of Strength Properties of Common Powder Bed Fusion and Stereolithography Materials. In Proceedings of the 11th International Conference on Nano and Materials Science, Singapore, 13–15 January 2023.
24. Faes, M.; Wang, Y.; Lava, P.; Moens, D. Variability in the mechanical properties of laser sintered PA-12 components. In Proceedings of the 26th Annual International Solid Freeform Fabrication Symposium—An Additive Manufacturing Conference, Austin, TX, USA, 10–12 August 2015; SFF: Singapore, 2015; pp. 847–856.
25. Aldahash, S.A. Friction and wear properties of oriented Polamide 12 objects manufactured by SLS Technology. *J. Engin. Appl. Sci.* **2019**, *15*, 9–25.
26. Roppenecker, D.B.; Grazek, R.; Coy, J.A.; Irlinger, F.; Lueth, T.C. Friction coefficients and surface properties for laser sintered parts. In Proceedings of the ASME International Mechanical Engineering Congress and Exposition, Proceedings (IMECE), San Diego, CA, USA, 15–21 November 2013; Volume 2, pp. 1–10.
27. Altair. Available online: <https://altair.com> (accessed on 31 October 2023).
28. Altair HyperMesh. Available online: <https://altair.com/hypermesh/> (accessed on 31 October 2023).
29. Altair HyperStudy. Available online: <https://altair.com/hyperstudy/> (accessed on 31 October 2023).
30. Fischer, S.F.; Thielen, M.; Loprang, R.R.; Seidel, R.; Fleck, C.; Speck, T.; Bührig-Polaczek, A. Pummelos as concept generators for biomimetically inspired low weight structures with excellent damping properties. *Adv. Eng. Mater.* **2010**, *12*, B658–B663. [[CrossRef](#)]
31. Modifiable Extensible Lattice Sequence (MELS). Available online: https://2021.help.altair.com/2021.2/hwdesktop/hst/topics/design_exploration/method_modified_extensible_lattice_sequence_doe_r.htm (accessed on 31 October 2023).
32. Global Response Search Method (GRSM). Available online: https://2021.help.altair.com/2021.2/hwdesktop/hst/topics/design_exploration/method_global_response_surface_method_r.htm (accessed on 31 October 2023).
33. Liu, X.; Wada, T.; Suzuki, A.; Takata, N.; Kobashi, M.; Kato, M. Understanding and suppressing shear band formation in strut-based lattice structures manufactured by laser powder bed fusion. *Mater. Des.* **2021**, *199*, 109416. [[CrossRef](#)]

Disclaimer/Publisher’s Note: The statements, opinions and data contained in all publications are solely those of the individual author(s) and contributor(s) and not of MDPI and/or the editor(s). MDPI and/or the editor(s) disclaim responsibility for any injury to people or property resulting from any ideas, methods, instructions or products referred to in the content.

4.6 Optimizing the Thickness of a Graded Lattice in a Bicycle Helmet

This study titled *Optimizing the Thickness of Functionally Graded Lattice Structures for High-Performance Energy Absorption: A Case Study based on a Bicycle Helmet* (Decker & Kedziora, 2023b, in review) focuses on implementing a functionally graded lattice in a bicycle helmet. It replaces the commonly used foam liner which absorbs the impact energy during a crash. It assembles the knowledge gained from the previous publications achieved during the research project. The optimization method's versatility is demonstrated by altering the lattice such that the modified Head Injury Criterion HIC(d) is minimized.

Reviewing existing literature shows that only few comparable studies were performed. The relevant ones focus on a small number of lattice types, exclusively perform simulative studies, examine only simplified helmet geometries or sections of it, and do not perform any lattice optimization to improve the helmet's performance. The presented study improves on all of these points while additionally considering the manufacturing of a complete helmet fit for testing.

Fourteen graph lattice types with a uniform thickness of 1.0mm are implemented in a realistic helmet geometry and compared to commercially available foam helmets. The worst-performing lattice type is chosen to be optimized similarly to the previous publication. Its lattice is split adhering to the helmet's shape with a TCL/TK script (found in the Addendum, section 7.3), and its local thickness values are linked via a quadratic function whose parameters are optimized such that the injury risk occurring during a crash is minimized. The resulting helmet is manufactured in one piece using PA12 produced with a HP MJF printer and is physically tested in accordance with EN 1078. To assess its performance, it is compared to an FEA model of the same helmet geometry with an EPS60 foam liner, as well as physical tests of five commercially available mountain bike helmets incorporating foam liners.

The physical tests of the helmets with foam liner yield peak acceleration results ranging from 149G to 205G, and HIC(d) values from 782 to 1244. The FEA model of the foam helmet predicts a peak acceleration of 189G and a HIC(d) level of 1445. The identical helmet geometry incorporating different lattice types yields much lower values. The acceleration reaches between 95G and 154G, while the HIC(d) values range from 493 to 701 with exception of one model. The model with Re-entrant lattice structure is unable to cushion the head adequately upon impact and is entirely compressed, resulting in a peak acceleration of 293G and a HIC(d) value of 1325. It was chosen to traverse the optimization procedure as the other models were already close to the manufacturing process' smallest manufacturable feature size limit. Optimizing the other lattices' thickness would mean reducing the 1mm thin beams further, entailing consistency issues.

The Re-entrant lattice's thickness was therefore increased to 1.5mm as an adequate starting point for the optimizer. Its thickness is linked via a quadratic function to reduce the amount of optimization variables similar to the method employed in the previous publication. It can be altered on continuous thickness range of 1mm to 2.5mm. A DOE study consisting of 50 runs exploring the design space is performed and relayed into the optimization study using the GRSM method with 250 runs. The model's peak acceleration is improved from 166G to 137G, and its HIC(d) value is reduced from 913 to 716 approaching the performance levels of the helmet models with uniform lattice variants using a 1mm diameter.

Article

Optimizing the Thickness of Functionally Graded Lattice Structures for High-Performance Energy Absorption: A Case Study Based on a Bicycle Helmet

Thierry Decker ^{1*}, Slawomir Kedziora ¹¹ Faculty of Science, Technology and Medicine; University of Luxembourg

* Correspondence: thierry.decker@uni.lu

Abstract: This study explores the potential of Functionally Graded Lattice Structures (FGLS) produced with Additive Manufacturing (AM) in impact energy absorption tasks, particularly as protective liners in bicycle helmets. Fifteen conformal, strut-based lattices are implemented in a realistic mountain bike helmet. They are simulated in a standardized impact scenario in accordance with EN 1078. A lattice optimization method locally altering its thickness is applied to improve one model, which undergoes physical testing and is compared to simulation results. The study addresses limitations in prior research, emphasizing manufacturability in an AM context, lattice type exploration, comparability, and numerical modeling choices. The findings provide insights into lattice structures' performance in helmets, emphasizing careful design and optimization for effective impact energy absorption.

Keywords: Functionally Graded Lattice Structures, Finite Element Analysis, Helmet, Optimization, Additive Manufacturing

1. Introduction

Additive Manufacturing (AM) has allowed the effective production of complex geometries such as lattice structures which are increasingly present in various fields [1-3]. They are composed of unit cells, the smallest repeating entity consisting of surfaces or struts. Examples of regular, strut-based lattices are shown in Figure 1. Graph lattice structures are subcategorized into bending-dominated and stretching-dominated types depending on their strut connectivity state. When considering the cells shown in Figure 2 as struts with freely rotating joints under vertical loads, the bending-dominated cell would simply collapse, whereas the stretching-dominated one would be able to resist the loads. Like a truss, its struts would carry a tensile or compressive axial force, while the bending-dominated cell could carry none. Transferring this load scenario to cells with rigid joints, the bending-dominated cell's struts would be deformed through bending while the stretching-dominated one would be deformed by the compressive and tensile forces [4]. It is thus significantly stiffer and stronger than a bending-dominated cell, a behavior which also transfers over to entire lattice structures under compressive loads [5].

Due to their comparable cellular composition, lattice structures behave similarly to foams [6] and can be described by the model established by Gibson and Ashby [7], wherein numerous lattice properties can be directly related to its relative density. It is defined as a structure's apparent density ρ^* divided by the density of its constituent material ρ . It strongly influences a lattice structure's apparent Young's modulus, shear modulus, elastic strength, yield strength, and densification strain at which a lattice is entirely compacted. Other characteristics such as the cell size, type, orientation also influence its response, but do not take on the same importance as the relative density. It is therefore

Citation: To be added by editorial staff during production.

Academic Editor: Firstname Last-name

Received: date

Revised: date

Accepted: date

Published: date



Copyright: © 2024 by the authors. Submitted for possible open access publication under the terms and conditions of the Creative Commons Attribution (CC BY) license (<https://creativecommons.org/licenses/by/4.0/>).

one of the most important characteristics pertaining to a lattice's composition, along with its base material.

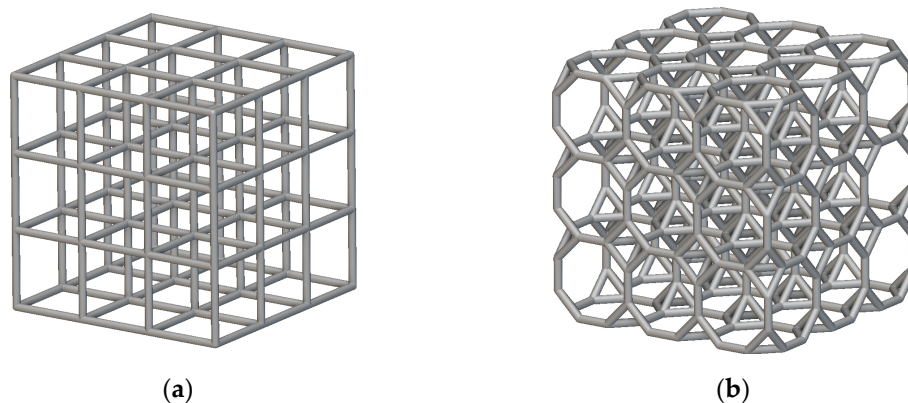


Figure 1: Example of regular lattice structures with Simple Cubic (a) and Truncated Cube (b) unit cells.

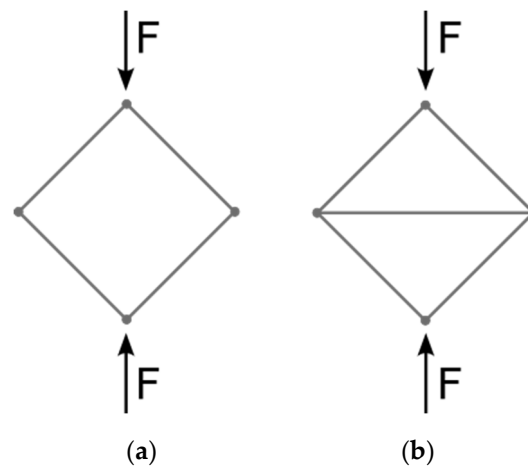


Figure 2: Bending-dominated (a) and stretching-dominated (b) unit cell types (recreated from [4]).

Regular lattice structures possess a uniform composition, i.e. their cell size, type, orientation, and thickness does not change throughout the geometry. Due to their similarities with expanded foam materials, they also excel in compressive energy absorption tasks [8–11] enabling their potential use as protective structures in sports equipment [12] or bumpers in automotive applications [13]. In this use case, ungraded lattice structures demonstrate excellent energy absorption performance at very low weight and material usage. Auxetic unit cell types such as the Re-entrant cell are especially intriguing in this scenario. They possess a negative Poisson ratio and contract upon compression [12–15], however they tend to have a low stiffness [16].

When a lattice structure exhibits local composition changes, it is categorized as a Functionally Graded Lattice Structure (FGLS). Redistributing the structure's material to where it is needed can greatly improve its performance. The property gradient may be defined manually during the design stage such as shown in Figure 3, in which the structure's strut thickness changes linearly with its height. Other composition changes can involve the lattice type, the unit cell size or its orientation [17–19]. Most notably, for lattices in compressive load cases, manual beam or wall thickness alterations are a common grading method due to their easy implementation [20–26].

Advanced approaches permit the creation of gradients based on optimization routines as function of external factors like structural loads, fluid flow, or heat flow, and are

at the center of many research studies. Numerous methods emerged, such as topology optimizations of the unit cell itself [27-30], topology optimization mixed with hierarchical alterations of the lattice [31], optimization of unit cell position and orientation as a function of isostatic stress lines [32], [33] amongst others. Such property changes can yield performance improvements like reducing a part's weight at a given stiffness [34], enhancing thermal conductivity [35-37], or enhancing sound absorption [38].

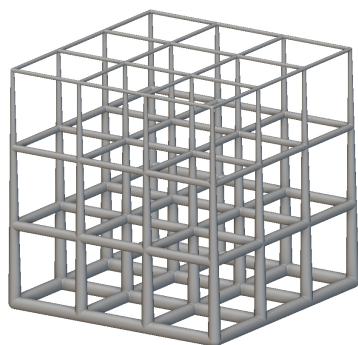


Figure 3: Functionally graded lattice structure with linearly changing strut thickness.

Since lattice structures perform well in impact energy absorption tasks, several research groups investigated the potential use of lattice structures as a replacement for protective foam liners in helmets. Leng et al. summarized current related trends in bicycle helmet development [39], among which are commercially available helmets incorporating honeycomb lattice structures: Bontrager [40] helmets with WaveCel technology [41], Koroyd structures [42] being licensed to several bicycle manufacturers, and HEXR helmets [43] using an additively manufactured hexagonal structure. Bliven et al. tested the WaveCel technology in an oblique impact scenario [44] and compared it with a control helmet model with a standard foam liner, as well as one helmet variant with Multi-directional Impact Protection System (MIPS) technology allowing for relative shearing motion between the helmet's shell and liner, reducing rotational accelerations of the head. The helmet variant with the WaveCel honeycomb structure surpassed the others regarding protection against both translational and rotational acceleration. Soe et al. performed simulative comparisons of a simplified helmet geometry with foam liners versus thermoplastic elastomeric lattice liners of differing relative densities and composed of Simple Cubic unit cells [45]. The investigation concluded that the studied TPE lattice structures all greatly reduced peak linear accelerations and increased the impact time, overall lowering the potential for injury significantly. Khosroshahi et al. performed simulative comparisons between helmet models with an expanded polystyrene (EPS) liner and versions incorporating two lattice types made of polyamide, each with a uniform and graded cell size distribution [46]. Their findings indicate that the lattices with lower relative densities possessed greater specific energy absorption capacity and that they better succeeded in dissipating impact energy. The investigated lattice configurations with size grading performed better than the EPS liner and non-graded lattice variants. It is stated in the publication that the main advantage of lattice structures lies in a greater area contributing to the impact energy absorption as compared to EPS foam. Naderi et al. studied simulative models of a helicopter helmet geometry combining expanded polyurethane foam and an arrowhead auxetic lattice in the same liner [47]. Several foam and lattice material options were investigated, revealing that each combination of the hybrid liner provided greater protection than a unibody foam liner. Nasim et al. explored the performance of three different uniform lattice types which were additively manufactured with polyamide 12 and incorporated into a protective liner for a motorcycle helmet [48]. Simulative and physical

testing showed greatly increased protection by some lattice types compared to EPS liners, while others fell short. They also demonstrated that a lattice's energy absorption capability during a quasi-static compression test is not necessarily an adequate predictor for its performance during an impact test.

As demonstrated by these publications, lattices can indeed provide sufficient protection when used in helmets. The authors of this paper therefore aim to further investigate this topic by expanding on certain aspects. Fourteen strut-based types of lattices that closely conform to a realistic mountain bike helmet geometry are simulated in a standardized impact test scenario and compared to commercially available foam helmets. In addition, a lattice optimization method proposed in a previous study by the authors (see [49]) is applied to improve the performance of one lattice type. It is subjected to physical testing and compared to the simulation results. This study aims to address issues of the aforementioned studies regarding feasibility in an AM context, weight, limited exploration of lattice types, comparability between lattices of differing relative densities, and numerical modelling choices. More specifically, Khosroshahi et al. studied only two lattice types with two configurations in a simulative approach without physical testing. While the study by Soe et al. investigated different lattice densities, only one unit cell type was used. Additionally, the head and helmet geometries were simplified to a sphere impacting a small lattice section, potentially missing effects observed in more realistic geometries. No physical tests of the lattice structures were performed by them, only material testing and simulative studies of the impact scenario. Similarly, Nasim et al. investigated only part of the helmet geometry, albeit with a realistic dummy head model both in simulations and in physical testing. Their choice was due to meshing of the lattice with tetrahedral elements, causing a considerable simulation duration and potential numerical instabilities stemming from severe element distortion. Choosing to create the lattice structure using traditional CAD software drastically limits the potential for easily iterating various lattice designs and types. This is overcome by utilizing nTop [50], a specialized software designed specifically for the creation of lattice structures. Another issue seen in the aforementioned papers is the comparability of the investigated lattices, as they possess differing relative density values which causes vastly different behavior. The authors of this paper therefore intend to mitigate these issues in the presented work.

2. Materials and Methods

2.1. Procedure and Goal

This study is a continuation of previous work by the authors where a generalized workflow for the optimization of FGLS was established (c.f. [49], [51], [52]). These studies focused on two different approaches to demonstrate the method's versatility: two studies investigated the stiffness maximization of a bicycle crank with weight and manufacturability constraints, whereas one study explored the optimal thickness distribution of lattices in compression at identical weights, maximizing their specific energy absorption capability. The current study continues this work by developing and enhancing a bicycle helmet by introducing a FGLS instead of the conventional protective foam liner. The design approaches are assessed through structural simulations and physical testing to evaluate their relative performance. Additionally, to gain insights into the market landscape, tests are conducted on a range of commercially available helmets in accordance with current standards. One helmet design is simulated using a foam liner and fourteen types of lattice structures to compare their relative performance. The design is further improved by optimizing the thickness of the lattice liner at a local level governed by a mathematical equation to reduce computational demands. Further, the simulations are complemented by physical tests.

2.2. Performance metric and test standard

The crash event utilized in this study adheres to the EN 1078 standard for bicycle helmet testing [53]. A drop from a height of 1.5m, equivalent to an impact speed of 5.4m/s onto a flat anvil, is outlined as test scenario. It dictates that the peak acceleration magnitude is not allowed to exceed 250G to meet the standard's requirements, however it does not take into account the acceleration duration or its progression. Therefore, the modified Head Injury Criterion HIC(d) [54] is used here to assess each helmet's performance as it considers characteristics of the complete acceleration history. The standard HIC is defined as:

$$HIC = \max_{(t_1, t_2)} \left\{ (t_2 - t_1) \cdot \left[\frac{1}{t_2 - t_1} \int_{t_1}^{t_2} a(t) dt \right]^{2.5} \right\} \quad (1)$$

where $a(t)$ is the head's acceleration magnitude measured in multiples of Earth's acceleration constant G (9.81m/s^2), while the start and end times t_1 and t_2 are the optimization variables to be modified such that the function reaches its maximum value. The HIC was initially designed for assessing dummy head accelerations attached to dummy bodies in automotive test environments. To account for the behavior of unconnected dummy heads, the modified head injury criterion HIC(d) was introduced to allow for equal comparisons between both [54]. It is defined as:

$$HIC(d) = 0.75446 \cdot HIC + 166.4 \quad (2)$$

The HIC(d) values can be correlated to the Abbreviated Injury Scale (AIS) indicating the probability of suffering six different levels of traumatic injury [55]. For example, an HIC value of 1000 relates to a 50% probability of experiencing a moderate head injury (AIS-3) and 15% for a severe injury (AIS-4).

2.3. Test stand and data acquisition setup

A test stand was designed and built for the purpose of conducting impact tests in accordance with EN 1078. It includes a steel base weighing 500kg as well as a sled guided on linear rails allowing the head to fall freely from varying heights. The helmeted dummy head can be positioned at various angles on the sled. A steel anvil with a diameter of 130mm and interchangeable faces is used to represent the impact surface, however only a flat surface is used in this study. An electromagnet holds the sled in position and releases it upon a button trigger. A TE Connectivity 633 inertial measurement unit [52] with six degrees of freedom is mounted on the head's cone to log the occurring accelerations. The sensor has the capacity to measure translational accelerations up to $\pm 500\text{G}$ and rotational velocities up to $\pm 12,000$ deg/s. Signals are registered at a frequency of 51.2kHz and filtered with an SAE J211/1 filter (CFC 1000).

2.4. Tests of commercially available mountain bike helmets

To provide a performance reference, five commercially available foam helmet models (see Table 1) were tested following EN 1078. The tests were performed externally by SQLab GmbH [56] and provided to the authors for this study.

Table 1: List of commercially available foam helmet models used for comparison.

Manufacturer	Model
6D	ATB 1T
IXS	Trail AS
Smith	ForeFront
Specialized	Ambush
Sweet Protection	Bushwhacker

2.5 Software

The study relies on a multitude of software suites for the lattice design, geometry preparation for simulation purposes, the simulation itself, and preparation of the results for Additive Manufacturing. The lattice design is performed in nTop (version 4.6, [50]), a software specifically designed for the creation of complex lattice structures. It does not rely on the boundary representation method usually employed by Computer Aided Design (CAD) software. It is based on connected surfaces, vertices, vectors, splines etc. to characterize bodies [57]. nTop makes use of Signed Distance Functions, defining geometries by a set of mathematical functions that are easily controllable by parameter variation [58]. This allows for versatile and quick design iterations of highly complex geometries such as these lattices. nTop enables exporting these structures to data formats usable for engineering purposes such as surface meshes (STL, OBJ formats) or meshes for Finite Element Analysis (FEA) solvers containing 1D beam, 2D shell, or 3D solid elements.

The workflow is continued in Altair HyperMesh (version 2021.2, [59]), a general pre-processor for FEA solvers, in which the remaining model is meshed, boundary conditions are applied, and solver settings are defined. It is also used to split the lattice in separate regions for their thickness optimization, as described later. The solver used in this investigation is Altair RADIOSS (version 2021.2, [60]), an explicit FEA solver for calculating highly nonlinear structural models involving contact, large deformations, and material failure. During the optimization studies, RADIOSS is controlled by Altair HyperStudy (version 2021.2, [61]), a general optimization suite able to evaluate a model's output responses and to vary its parameters accordingly. After optimization, a custom MATLAB [62] script extracts the individual lattice regions from the solver input file and translates them into the LTXC data format, which is native to nTop. Here, they are reassembled into a single geometry, and an STL mesh is extracted for Additive Manufacturing.

2.6. Helmet and dummy head geometry

The helmet geometry shown in Figure 4 used in this study was supplied by SQLab GmbH [56]. It exhibits typical features of commercially available bicycle helmets such as a polymer shell and a single foam liner with ventilation holes. The foam liner's thickness varies locally, transitioning from 30mm at the front, to 32mm at the top, 30mm towards the rear, and 20mm on its sides. The design is simplified for the purpose of simulation and does not include common features such as a head harness or pads to enhance comfort.

In accordance with EN 1078 regulations for bicycle helmet testing, the dummy head (c.f. Figure 5) chosen for the study is in compliance with the EN 960 standard [63]. It is composed of AZ91 cast magnesium and weighs 4.7kg (size J, 575mm circumference). It represents approximately the 50th centile head size of a sample of British male adults with a height of 180cm [64]. The head features a magnesium dome which allows for the placement of an acceleration sensor at the center of mass. A modal analysis was conducted to verify that the lowest eigenfrequency of the head assembly is above 2000Hz, and therefore meets the EN 1078 requirement.

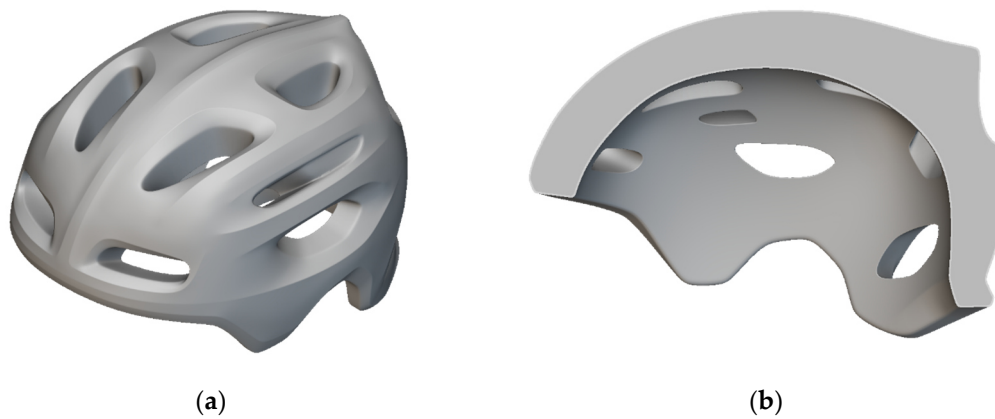


Figure 4: Foam helmet geometry (a) and its section view (b).

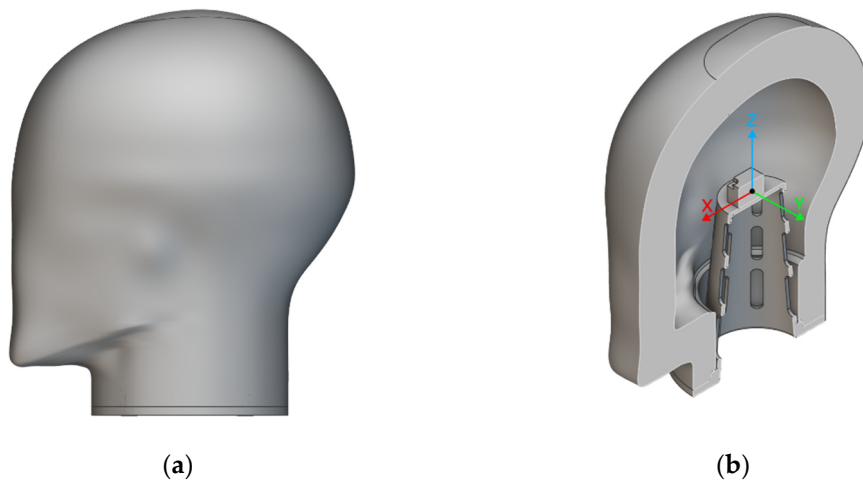


Figure 5: Side view (a) and section view (b) of the cast magnesium dummy head in compliance with EN 960, with its inner cone for sensor mounting and the local coordinate system.

2.7. Lattice design procedure and lattice types

To prepare the helmet geometry for utilization in nTop and to introduce a lattice structure, the first step is to separate the helmet's outer and inner surfaces. Faces on their borders are removed to create an open lattice that facilitates the removal of excess powder after manufacturing. A conformal unit cell map is created by generating quadrilateral elements on the helmet's inner surface which are extended towards the outer surface. The resulting conformal map can be filled with unit cells to create a congruent lattice structure as shown in Figure 6. The lattice's size is controlled by altering the dimensions of the quadrilateral mesh and by the amount of cell layers extruded outwards. A symmetry constraint is applied to ensure an identical lattice composition of the left and right model halves. To fill the ridge near the back of the helmet, the lattice map needs to extend beyond the actual helmet geometry. The lattice is then trimmed to be contained entirely within the helmet's volume. While the lattice structure resulting from this approach closely follows the helmet's shape and possesses an approximately constant number of cell layers in radial direction between both surfaces, it also entails that the unit cell height varies with the helmet's thickness. Finally, for manufacturing purposes, a detailed mesh of the merged shell and lattice components is generated, resulting in a unibody design.

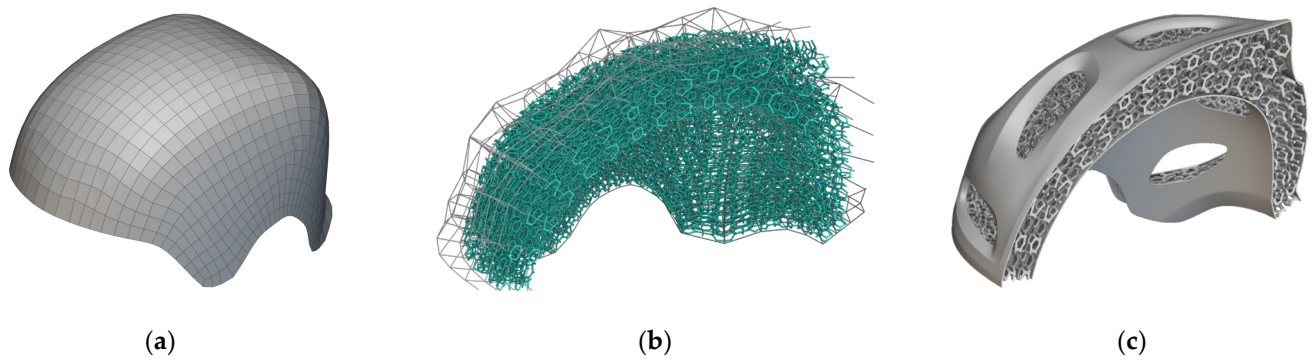


Figure 6: Lattice creation process: (a) Quadrilateral mesh formed on the inner helmet surface from which a cell map is extruded towards the outer surface; (b) Section view of conformal unit cell map extruded from the inner to the outer helmet surface; (c) Section view of the unified shell and lattice helmet geometry.

Twelve suitable regular graph unit cell types available within nTop (shown in Figure 7) are explored, as well as two pseudo-stochastic lattice varieties (Tetrahedral and Dual lattices) to assess each type’s performance. The regular graph unit cells are composed identically in all three planes except for the Re-entrant unit cell, which is therefore investigated in two different orientations. Surface-based lattices such as honeycombs and Triply Periodic Minimal Surfaces (TPMS) are not considered in this study as they do not adequately allow the removal of excess powder after manufacturing without adding numerous evacuation holes to the structure.

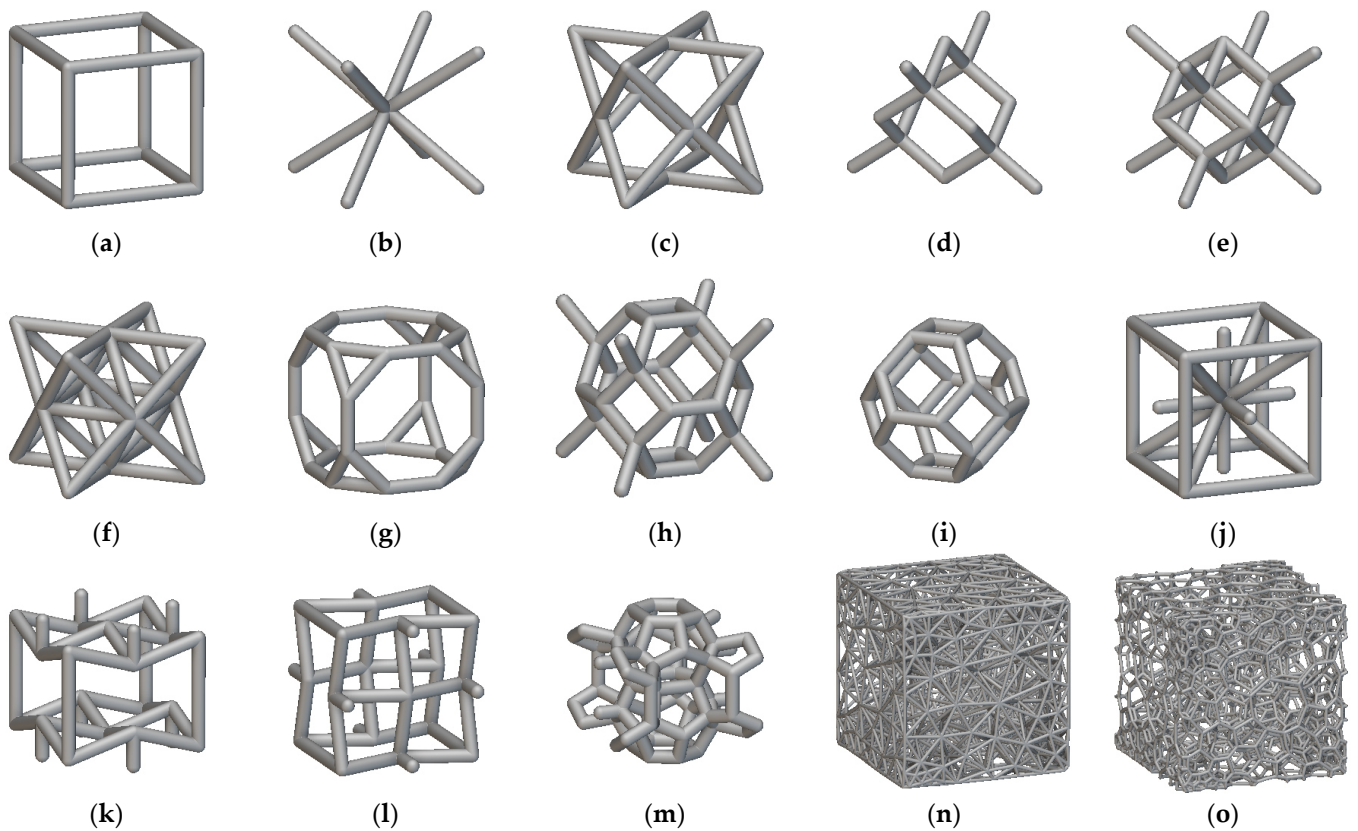


Figure 7: Graph lattice types utilized in this study. (a) Simple Cubic, (b) Body Centered Cubic, (c) Face Centered Cubic, (d) Diamond, (e) Fluorite, (f) Octet, (g) Truncated Cube, (h) Truncated Octahedron, (i) Kelvin cell, (j) Isotruss, (k) Re-entrant in orientation A, (l) Re-entrant in orientation B, (m) Weaire-Phelan, (n) Tetrahedral lattice, (o) Dual lattice.

2.8. Manufacturing

The lattice helmet's structure is entirely made from polyamide 12 (PA12) produced on an HP Multi-Jet Fusion (MJF) machine [65]. It was chosen since powder-bed based AM methods lend themselves well to the production of complex structures such as lattices, and the material possesses adequate physical properties. The unibody design eliminates potential issues stemming from gluing or otherwise attaching separately produced parts. The default layer height of 0.08mm is applied, and the geometry oriented as shown in Figure 8 for production.

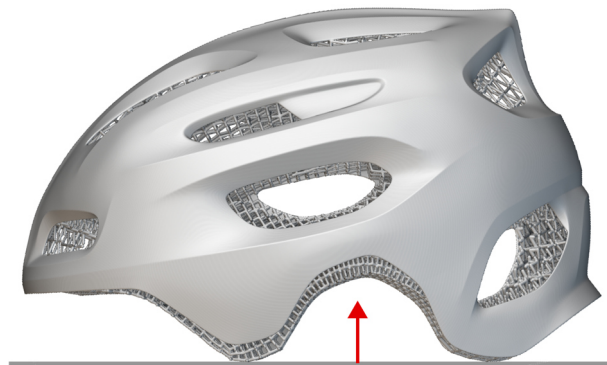


Figure 8: Helmet build orientation during manufacturing.

Measurements taken of several lattice structures produced during the investigation indicated that their diameters deviated from the expected values. A test geometry was therefore manufactured to investigate the occurring differences as a function of the beam diameter and orientation. It consists of a cuboid geometry with an Isotruss lattice and a linearly varying thickness ranging from 0.7mm to 2mm. The geometry and its build direction during manufacturing are shown in Figure 9. It has external dimensions of 80mm × 80mm × 160mm and a 45° twist along its longitudinal axis.

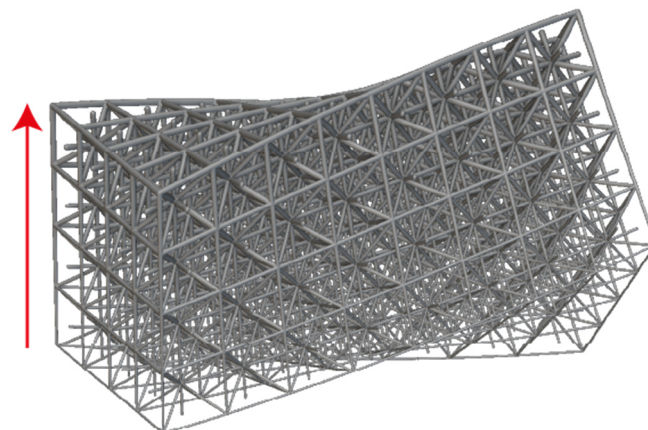


Figure 9: Test lattice for measuring thickness deviations at different orientations and positions, build direction marked with red arrow.

2.9. Materials

Two sets of materials are required for the simulative models, one for the foam helmet model and one for the helmet models including lattices. The foam helmet is assumed to be composed of materials commonly used for mountain bike helmets: a 0.5mm polycarbonate (PC) shell and an expanded polystyrene foam liner with a density of approximately 60kg/m³ (EPS60). Four stress-strain curves of EPS60 at various strain rates were obtained from Ouellet et al. (c.f. [66]). The material data for PC used here was obtained by Cao et al. (c.f. [67]). Its Young's modulus and offset yield strength were estimated from the stress-strain data provided in their publication. The stress-strain curves of EPS60 and PC are depicted in Figure 10 and assembled in Table 2. To secure the helmet to the dummy head, a chin strap intended to resemble woven high-density polyethylene (HDPE) fibers is added to the FEA model. Its material properties are of lesser importance for this study and are estimated from commonly found values. The dummy head is composed of cast Mg AZ91 and the properties available on MatWeb were used [68].

The physical characteristics of the HP PA12 material were determined through experimental assessments in a previous study by the authors (c.f. [69]). Tensile test specimens were subjected to loads perpendicular to their build direction in order to stress the components in their weakest plane, simulating the most critical loading scenario. The resulting properties are given in Table 2 and Figure 10. They are used as reference data for the Johnson-Cook material law parameter approximation as discussed in section 2.11.

Friction assumes a significant role in this study due to the multitude of contact interactions that take place during the impact simulations. They involve lattice beams contacting one another and the helmet's shells, the outer shell colliding with the steel anvil, and the magnesium head impacting the inner shell or the foam liner. The friction coefficients used in this study are listed in Table 3. For values lacking a source indication, estimations were required as the data was not available in existing literature.

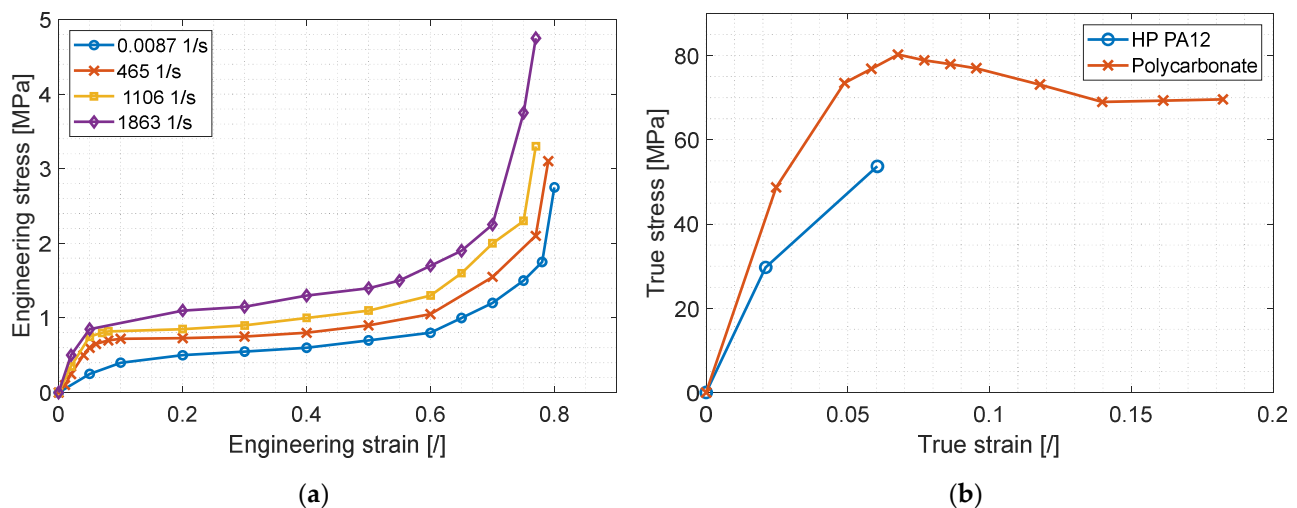


Figure 10: Curves utilized for material modelling: (a) Modified engineering stress-strain data of EPS60 in compression at varying strain rates, data adapted from [66]; (b) True tensile stress-strain plots of Polycarbonate (data from [67]) and Polyamide 12; (data from [69]).

Table 2: Material properties used in the simulations.

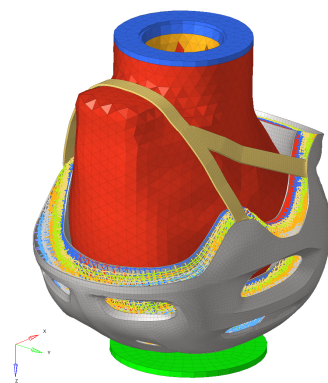
Property	PA12	PC	EPS60	HDPE fibers	Mg AZ91
E [MPa]	1480	1900	6	1000	45000
ρ [g/cm ³]	0.94	1.22	0.061	0.95	1.80
ν [-]	0.4	0.36	0.05	0.46	0.35
σ_y [MPa]	29.6	51	-	-	-
ϵ_{ult} [%]	6	18	-	-	-
σ_{UTS} [MPa]	53.7	80.1	-	-	-

Table 3: Dry friction coefficients of contact pairs.

Material A	Material B	Friction coefficient
PA12	PA12	0.4 [70]
	Mg AZ91	0.2
Mg AZ91	EPS60	0.3
	HDPE fibers	0.2
Steel	PA12	0.33 [71]
	PC	0.2 [72]

2.10. FEA model setup

During the drop test simulation, the steel anvil is modelled by a circular rigid shell surface with a diameter of 130mm as shown in Figure 11. The helmet is positioned within 2mm to the rigid surface such that no initial penetration is present and only a negligible amount of time is spent in free fall. The assembly is assigned an initial velocity of 5.4m/s in accordance with the standard as well as a gravitational acceleration load of 9.81m/s². The dummy head assembly, consisting of the head itself and the sensor cone, is modelled as a rigid part. Tetrahedral elements are used to mesh the head, while the cone is meshed by shell elements. The sensor is modelled by a concentrated mass of 50g at its center of mass and rigidly connected to the cone. And the time history of values, such as the head's acceleration, is probed at this node.

**Figure 11:** FE model of the helmet with lattice liner and anvil.

A general contact interface with penalty formulation (TYPE7 [73]) between the dummy head and the EPS foam component or the PA12 shell is defined, respectively.

The chin strap is modelled by shell elements with reduced integration (QEPH type [74]), a thickness of 2mm, linear elastic material behavior and a single integration point

through its thickness such that it behaves like woven tissue. It is attached to the sides of the outer shell via a tie constraint and interacts with the helmet and dummy head through another TYPE7 general contact interface.

The foam liner of the conventional helmet is modelled via 6mm large second order tetrahedral elements. The small strain formulation is used in conjunction with self-contact of the foam elements to improve the solving stability and to prevent sudden element collapse. The relatively large element size is also intended to prevent element collapse upon encountering large compressive strains. A viscoelastic tabulated foam material model (LAW70 [75]) is used with the four strain-rate dependent stress-strain curves shown in Figure 10. Strain rate smoothing is activated, and stresses are interpolated by the solver between the provided curves. The last curve is copied and reinserted with a strain rate of 10000/s to prevent the solver from extrapolating beyond the available data. In addition, the curves had to be slightly modified such that they no longer cross each other, as this would lead to numerical instabilities.

The 0.5mm thick polycarbonate shell is modelled by a quad-dominant mesh with 5mm edge length and 5 integration points across its thickness. An isotropic tabulated elastic-plastic material law (LAW36 [76]) is used to model the stress-strain curve depicted in Figure 10. The fully integrated four-node element type (QBAT [77]) is employed using the large strain formulation with the possibility of switching to the small strain formulation for improved numerical stability.

As for the lattice helmet model, the anvil, dummy head, sensor, and chin strap are modelled in an identical manner. The inner and outer shells of the lattice helmet are discretized with a fully integrated QBAT quad-dominant shell mesh having an edge length of 3mm, a thickness of 1mm, five integration points across the thickness, with consideration of full geometric nonlinearities, and with the possibility to switch to the small strain formulation if required for stability purposes. The PA12 parts are modelled by the isotropic elastic-plastic Johnson-Cook material model (LAW2 [78]) with consideration of strain rate effects. Material failure of the PA12 parts is modelled via element deletion when the principal stress reaches the maximum allowable plastic strain in any of an element's integration points.

The lattice consists of first order integrated beam elements based on the Timoshenko theory with a circular cross-section (TYPE18 INT_BEAM [79]). They are usable for short beam cases and possess four integration points. A tie contact interface (TYPE2 [80]) connects the shell and beam elements within a search distance of 2mm between nodes. The lattice's struts were subdivided in nTop based on the total length between lattice nodes before being exported. Nodes within a distance of less than 1mm are merged, eliminating the connecting strut. Struts with a length of up to 3mm were not subdivided and are modelled by a single beam element. Struts having a length between 3mm and 6mm were split once, being modelled by two beam elements, and any strut longer than 6mm is modelled by three beam elements. This way, a minimum beam element length of 1mm is ensured and longer struts can capture buckling thanks to the subdivision. Contact interactions between beam elements are enabled via an edge-to-edge contact interface (TYPE11 [81]) which takes individual thickness values of each element into account.

A total run time of 15ms was applied to entirely capture the entire impact event having a duration of approximately 10ms. The minimum time step is defined to be 0.5 μ s for the foam model and 0.25 μ s for the lattice models with a scaling factor of 0.9 to limit mass scaling to a minimum. Time history files are updated at 200kHz for a total of 3000 data points per run.

2.11. Johnson-Cook material parameter optimization

As discussed in section 2.9., the material data of PA12 given in Table 2 was obtained from quasi-static tensile tests. The impact scenario considered in this study is highly dynamic and strain rate effects on the material properties become relevant, hence the data

cannot be used as is. Since no physical properties of PA12 produced with MJF over a wide range of strain rates could be found in literature, an approximation based on the available data is performed. The Johnson-Cook material model is therefore chosen since it considers the strain rate effect on the stress level based on parameters obtained at a reference strain rate, i.e. the tensile test data. It calculates the stress σ as:

$$\sigma = (A + B \cdot \varepsilon_p^n) \cdot (1 + c \cdot \ln \frac{\dot{\varepsilon}}{\varepsilon_0}) \quad (3)$$

with the yield stress A , the plastic hardening parameter B , the true plastic strain ε_p , the hardening exponent n , the strain rate coefficient c , the current strain rate $\dot{\varepsilon}$ and the reference strain rate ε_0 at which the base parameters were determined. RADIOSS offers a simplified input method which is used in this study. Then the parameters A , B and n are calculated based on the yield stress σ_y , the ultimate tensile strength σ_{UTS} and the engineering strain at the ultimate tensile strength ε_{UTS} obtained from tensile tests. The material law's implementation in RADIOSS supports the option of considering the influence of strain rate on the maximum stress σ_{max} , which is also applied here. It is calculated as:

$$\sigma_{max} = \sigma_{max,0} \cdot (1 + c \cdot \ln \frac{\dot{\varepsilon}}{\varepsilon_0}) \quad (4)$$

With the available material data and the Johnson-Cook law, a preliminary investigation is performed to find adequate variable values. A helmet incorporating a Truncated Cube lattice liner with a uniform thickness of 1.5mm was manufactured and physically tested to correlate it with the simulation results using the Johnson-Cook material law. To find approximate material parameter values, an optimization study was set up with HyperStudy to minimize the difference between the acceleration curves obtained from the simulation and the physical test. The optimization variables were chosen to be Young's modulus E , the strain rate parameter c , the maximum plastic strain ε_p^{max} and the maximum stress $\sigma_{max,0}$ defining the plateau of the stress-strain curve at the reference strain rate ε_0 . The latter is $2.8 \cdot 10^{-4}/s$, the standard strain rate of an ISO 527-2 tensile test using a 1BA specimen [82]. Young's modulus was defined as an optimization variable because it is significantly influenced by the strain rate in the case of polymeric materials such as PA12. A Design of Experiment (DOE) run with 50 iterations using the Modifiable Extensible Lattice Sequence method (MELS [83]) was performed first. It is then relayed into an optimization study using the Global Response Search Method algorithm (GRSM [84]), a gradient-based global optimization method, with a maximum of 150 iterations. The optimization study aims to minimize the difference between the acceleration curves of the simulation model and the physical results, yielding approximated material parameters.

2.12. Simulations of helmet models with uniform lattice thickness

Preliminary simulations using the parameters obtained from the material parameter optimization study indicated that a relative density of 7% is a suitable starting point for this impact scenario. With an identical beam thickness, different unit cell types occupy varying volume fractions. The relative density target is therefore met by altering the number of unit cell layers between the two surfaces, along with the number of quadratic elements on the inner surface that are extruded outwards. These settings were chosen such that the unit cells were approximately equally sized in all three dimensions.

A uniform diameter of 1mm is used for all of the lattice types shown in Figure 7, however an exception was made for the tetrahedral lattice. It required a 0.95mm beam diameter to meet the relative density target. This adjustment was necessary because nTop offers limited control over the 3D mesh generation, leaving only the option of modifying

the diameter. The relative density target was satisfied within a $\pm 0.2\%$ deviation for all lattices, which corresponds to an average lattice weight of 132g. The inner and outer shells are assigned a thickness of 1mm and weigh a combined 146g. The average total helmet weight therefore amounts to 278g which is comparable to conventional bicycle foam helmets.

2.10. Lattice splitting and thickness optimization procedure

In conventional FEA programs, each component containing 1D beam or 2D shell elements requires a separate thickness property assignment. Therefore, to assign different thickness values to each of the lattice components, the structure first has to be split into discrete regions. To achieve a separation conforming to the helmet's shape, an ellipsoidal surface function was established that approximates the inner surface of the helmet:

$$\sqrt{\left(\frac{x}{105}\right)^2 + \left(\frac{y}{80}\right)^2 + \left(\frac{z}{105}\right)^2} - 1 = 0 \quad (5)$$

A TCL/TK script [85] was devised and executed in HyperMesh to segregate the beam elements in equidistant steps based on their distance to this surface. It bins the elements into a user-defined number of separate components based on each element's averaged nodal position. Element groups containing only few elements are manually merged with their larger neighbors afterwards. Figure 12 shows the separate, color-coded lattice groups after the separating process into eight bins. Six components are present at the top of the helmet to allow sufficient control over the thickness changes.

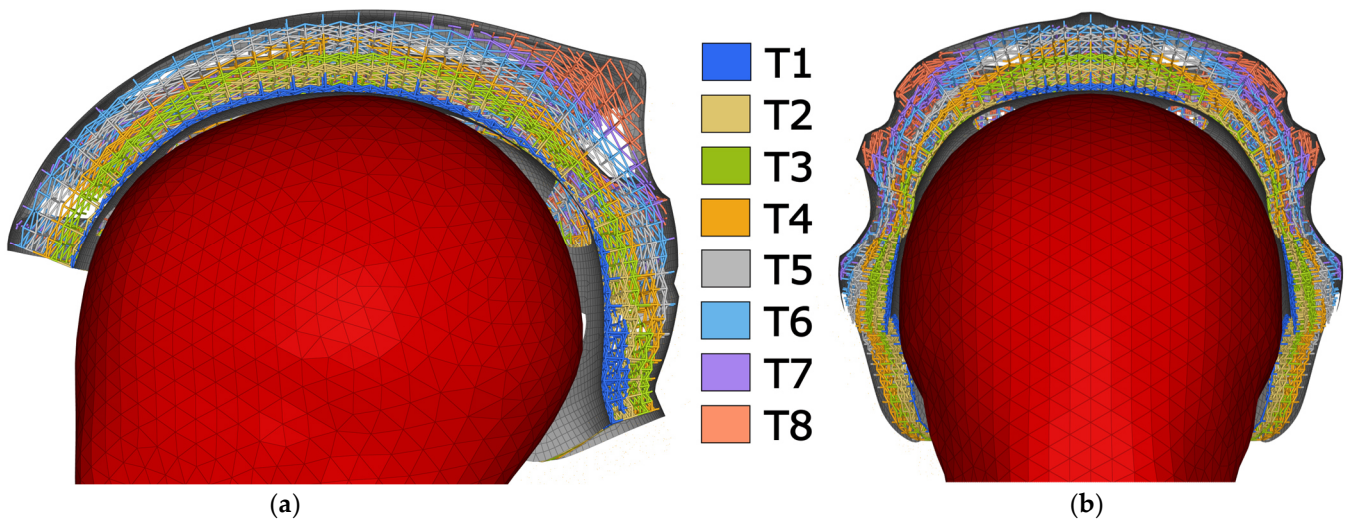


Figure 12: Side section view (a) and front section view (b) of the eight color-coded lattice components, denoted T1-T8 from innermost to outermost region.

The model is then imported into HyperStudy where the thickness value of each lattice component is parameterized. Each component's numerical thickness value T in the solver input file is defined as a variable. Their values are then linked by a quadratic function of the form:

$$T(a, b, c, r) = a \cdot (r + c)^2 + b \quad (6)$$

where r is the radial distance magnitude from the helmet's origin to the innermost edge of each respective layer. The parameters a , b and c are defined as optimization variables, thus omitting the need to optimize every thickness property value separately. This effectively decreases the amount of optimization variables from eight to three and reduces the calculation efforts greatly. The choice of the function is inspired by the pomelo fruit. It can endure falls from heights of 10 meters unharmed thanks to its shell having a similar distribution with greater cell density near its edges and lower density in-between [86]. This approach was also part of a previous investigation of the authors, where the optimal material distribution of a cuboid lattice in compression following various functions was investigated [38]. The function and its independent variable can generally take any arbitrary form.

The variables are subject to a uniform distribution and their ranges listed in Table 4. Additionally, the diameters are only allowed to be changed on a continuous range from 1mm to 2.5mm. A DOE study with 50 runs is performed first to explore the design space using the MELS method to distribute data points across the design space. It is fed into the subsequent optimization run to provide an initial solution surface to the GRSM optimization method, which is permitted a maximum of 250 runs. The HIC(d) value is to be minimized with no other constraints being imposed on the optimizer, apart from the ones mentioned. The worst-performing helmet model is subjected to the optimization procedure, further reasoning for this choice is given in section 3.2.3.

Table 4: Optimization variable bounds and their initial values

Variable	Lower bound	Initial value	Upper bound
a	-1×10^{-3}	data	1×10^{-3}
b	-2	1	2
c	-145	0	0

3. Results

3.1. Results of helmets with foam liner

Among the five assessed models, three (6D, IXS, and Smith) exhibit peak acceleration levels exceeding 200G and HIC(d) values surpassing 1000 as outlined in Figure 13. These helmet models show impact durations ranging from 6ms to 8ms. In contrast, the Sweet Protection model demonstrates a notably lower peak acceleration of 149.3G and an HIC(d) value of 782.4, with a slightly prolonged impact duration of 10ms. The Specialized Ambush helmet model lies in-between, with a peak acceleration of 181.6G and an HIC(d) value of 943.3. As for the simulated helmet geometry, it registers the highest HIC(d) value at 1445.0, accompanied by a peak acceleration of 188.0G. The elevated HIC(d) value stems from consistently high acceleration levels combined with an extended impact duration of around 10ms. Assessing the results from the physical drop tests and the simulated model, it can be concluded that the chosen material assumptions are adequate, and a comparison with models containing a lattice liner can be established. Figure 14 depicts the stress contour plots of the foam liner at the 5ms time mark when the peak acceleration occurs. The foam liner is compressed from its original thickness of 32mm at the uppermost point of the dummy head to 13.6mm during the impact, a compressive strain of 57.5%.

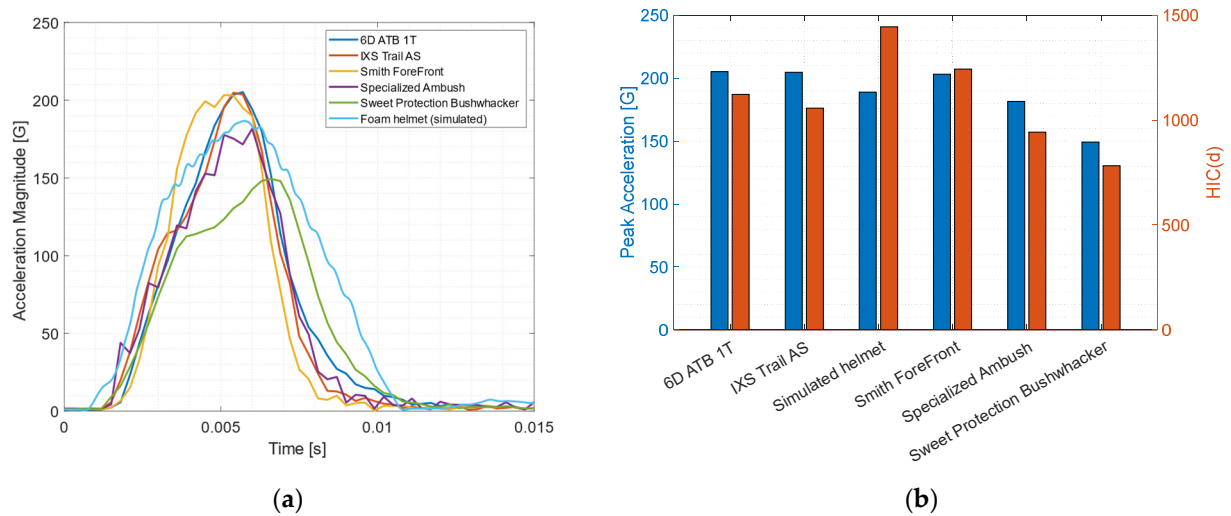


Figure 13: (a) Acceleration magnitude progression of foam helmets during drop test; (b) Peak acceleration and HIC(d) values of the foam helmets during drop test.

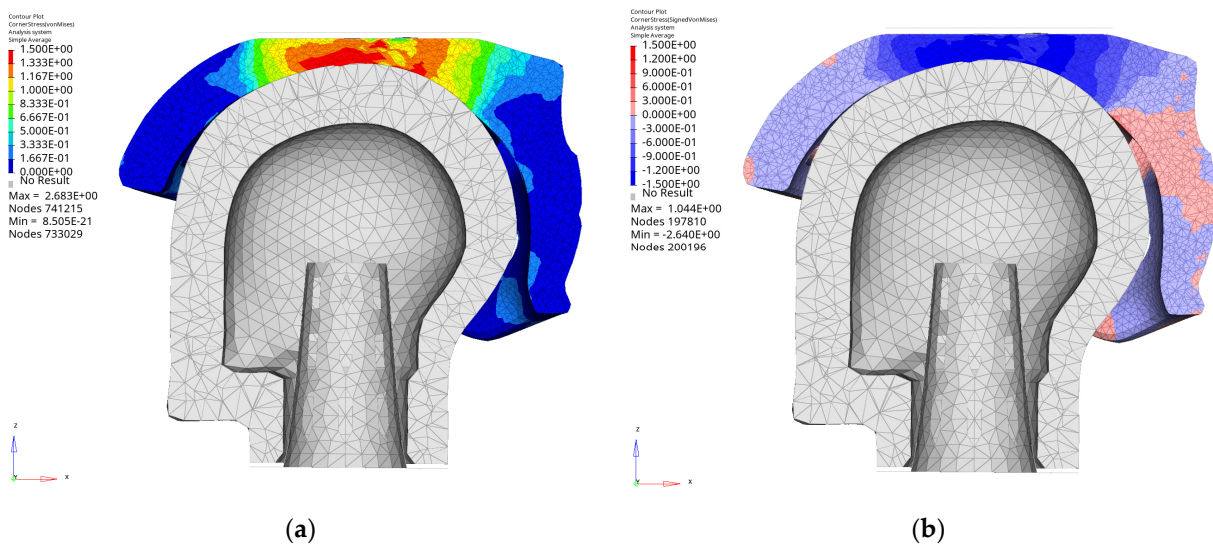


Figure 14: Foam helmet geometry with stress contour plots at the 5ms time mark: von Mises stress (a) and signed von Mises stress (b) showing equivalent tensile and compressive stresses.

3.2. Results of helmets with lattice liner

3.2.1. Results of material parameter approximation

The helmet geometry incorporating a Truncated Cube lattice with a 1.5mm beam diameter was analyzed in the material parameter optimization study. It resulted in Young’s modulus value E of 2003MPa, a maximum plastic strain value ϵ_p^{max} of 7.64%, a strain rate coefficient c of 0.048, and a maximum stress $\sigma_{max,0}$ of 78.6MPa. These properties translate to the more commonly used Johnson-Cook parameters $A = 29.7\text{MPa}$, $B = 35.2\text{MPa}$ and $n = 0.129$. While the strain at break commonly decreases with increased strain rate, the optimization procedure predicts that it is larger than determined by the tensile tests. It is still within a plausible range as the manufacturer’s data sheet states maximum strains of 15-20% [87]. A part’s property deviations may be caused by differing manufacturing or post-processing conditions, as well as loading conditions and manufacturing orientations.

The simulated acceleration curve closely resembles the test results as shown in Figure 15. The curve's slope and peak acceleration levels exhibit strong similarity. The physical test curve has a fluctuating and slowly declining acceleration magnitude after the impact (8ms time mark), which is not visible in the simulation's acceleration curve. It is likely caused by vibrations of the magnesium cone onto which the acceleration sensor is fastened (visible in Figure 5). Since this part is assumed to be a rigid body in the FEA model, the same behavior cannot occur here. Peak strain rates of over 4000/s are observed in the elements of the outer shell, with large-scale levels around 1000/s shortly before and after the peak acceleration time stamp.

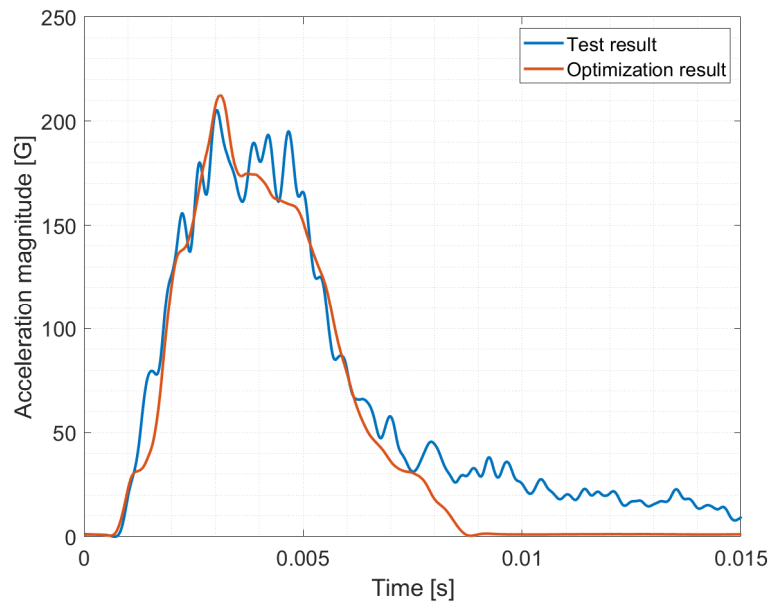


Figure 15: Acceleration magnitude of the lattice helmet model with optimized material curve (orange) versus the physical test (blue).

3.2.2. Results of helmet model simulations with uniform beam diameter

The helmets incorporating a lattice liner with uniform thickness were simulated with the Johnson-Cook material parameters determined from the preceding optimization run. Their peak acceleration magnitudes and HIC(d) results are depicted in Figure 16, along with the foam helmet FEA model results. The findings range from 95G and an HIC(d) level of 493.8 achieved by the Octet lattice model to 293.5G and an HIC(d) level of 1325.3 reached by the Re-entrant model. On average, the peak acceleration reaches 134.5G, and the HIC(d) value is 662.6.

At the chosen configuration and with the assumed material properties, every helmet variant with a lattice liner outperforms the previously tested helmets with a foam liner with the exception of the model with the Re-entrant unit cell in orientation A. It is entirely compressed and fails to sufficiently support the head during impact. Other helmet models were approaching the maximum liner compression capacity and were nearly bottoming out, but achieved very low acceleration and HIC(d) values).

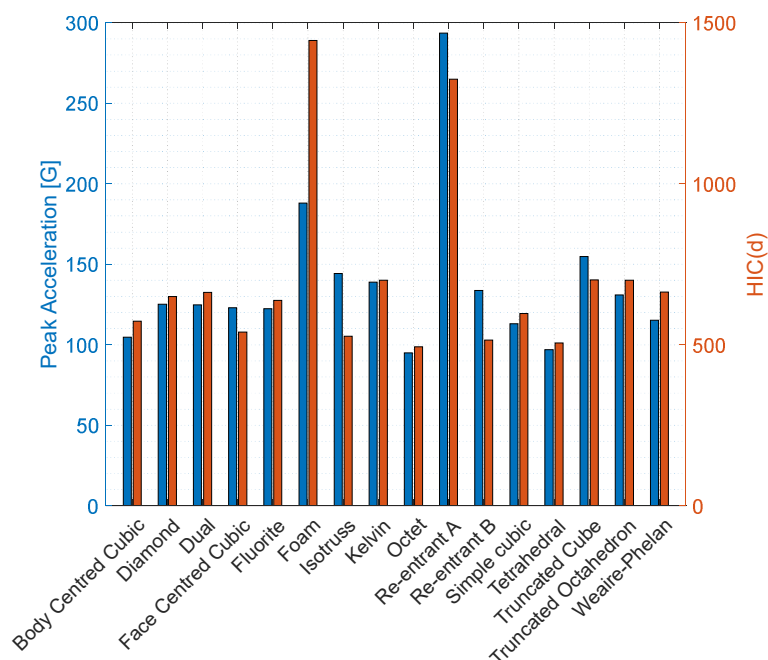


Figure 16: Peak acceleration magnitudes and HIC(d) values of the investigated lattice types.

3.2.3. Results of lattice optimization procedure

The Re-entrant lattice type in orientation A is chosen for the subsequent optimization study as a demonstration for the presented method for two reasons. Firstly, beams with diameters significantly below 1mm are difficult to produce reliably with the chosen manufacturing method. It was noted during preliminary investigations that thin beams showed negative diameter deviations of up to 0.2mm depending on their orientation and their target thickness, which impacts their load bearing capacity significantly. The feature size is at the lower end of the feasibility of this manufacturing process, and the sandblasting step for evacuating loose powder after printing can remove further material, causing reduced structural integrity. Choosing any of the other lattice types for optimization would only result in diameter reductions since their impact absorption capacity was not yet completely exhausted, reducing beam diameters to regions in which producibility becomes an issue. Since the Re-entrant lattice helmet model completely failed in the simulation, its lattice diameter can only be increased by the optimizer for acceptable performance, avoiding geometrical accuracy issues stemming from production and postprocessing. Secondly, choosing a lattice type with good or even the best performance such as the Octet lattice could only yield small or no improvements since it may already operate close to its optimum. Therefore, choosing the worst-performing type is considered to be a better option for demonstrating the method's capabilities. Since a strut diameter of 1mm was insufficient for the Re-entrant lattice, it was increased to 1.5mm to establish a suitable starting point for the optimization.

The reference model attains a maximum acceleration of 165.7G and a HIC(d) value of 913 with a uniform diameter of 1.5mm. After the optimization procedure, the HIC(d) value was improved to 716.0 and the peak acceleration decreased to 136.6G. The acceleration curves of both FEA models with uniform and optimized lattice thicknesses are shown in Figure 17. The optimized model's liner experienced a compression of 66%, reducing the distance between the inner and outer shell from 32mm to 10.8mm. Since its capacity is not entirely exhausted, a larger number of optimization iterations could possibly improve the helmet's performance further. The resulting optimized lattice structure is shown in Figure 18 (a). The optimization variables' final values are $a = 9.63 \times 10^{-4}$, $b = 0.61$ and $c = -128.8$; the resulting thickness distribution is displayed in Figure 18 (b). The

diameter changes from approximately 1.9mm in the innermost lattice group (T1) to 1.2mm in the middle group (T5) and 1.7mm in the outermost group (T8).

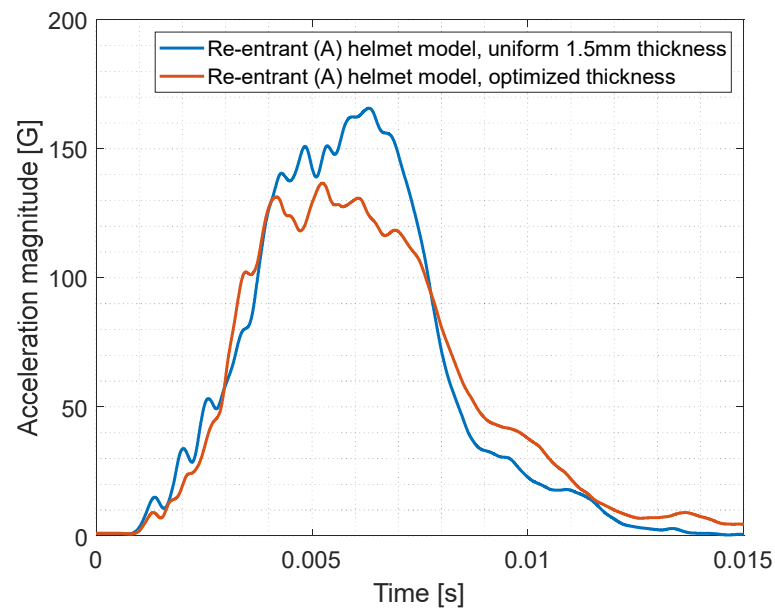


Figure 17: Acceleration curves of unoptimized Re-entrant (orientation A) lattice helmet model with 1.5mm uniform thickness (blue) and model with optimized thickness (red)

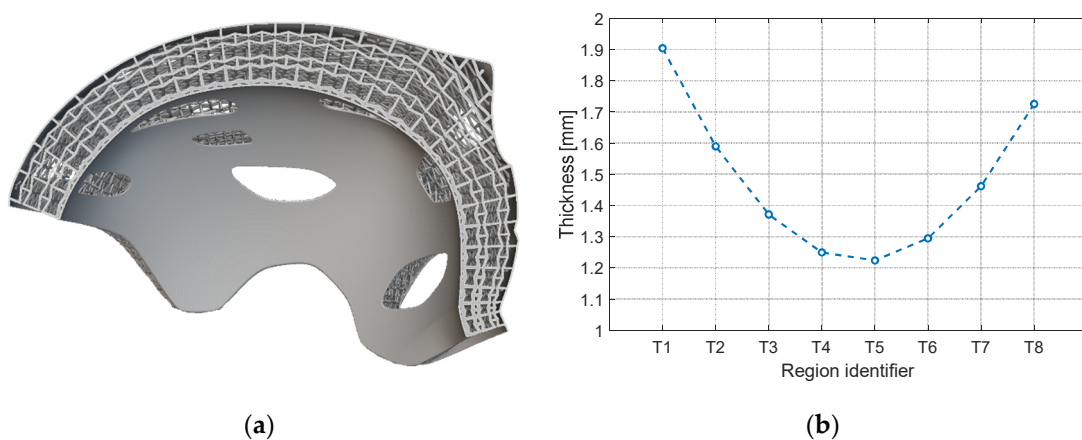


Figure 18: (a) Section cut of the Re-entrant helmet geometry with optimized lattice thickness; (b) Thickness distribution of optimized lattice liner (T1: innermost group, T8: outermost group)

3.2.4. Lattice thickness measurements

The beam diameters of the test structure shown in Figure 9 were assessed with calipers at regular intervals, the measurements are depicted in Figure 19. “Flat” beams are oriented along the piece’s longitudinal axis, while “upright” beams are oriented in parallel to the thickness gradient and build direction. Both the beam orientation and target thickness impact the actual thickness, and the deviations are primarily negative. Based on these findings, the deviations were averaged and an offset of +0.04mm was applied to beam diameters with a nominal value between 1.3-1.6mm, while diameters below 1.3mm had an offset of +0.08mm applied to them before manufacturing the helmet samples.

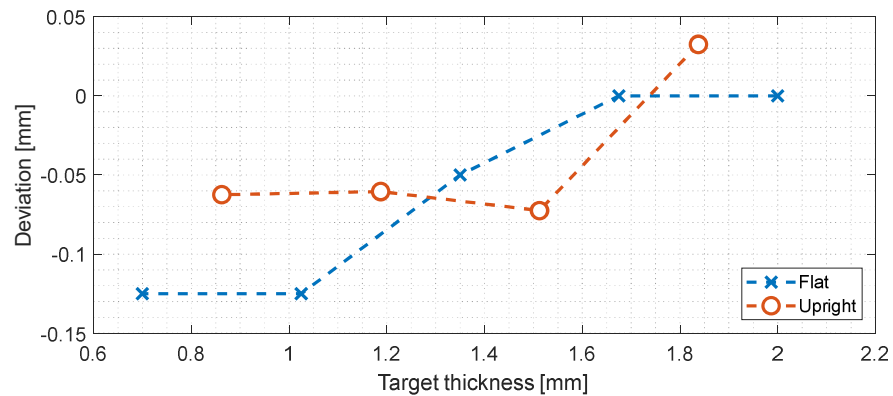


Figure 19: Diameter deviations as measured at different orientations and thicknesses in the test lattice geometry.

3.2.5. Test results of helmet model with optimized lattice structure

Two helmet specimens with the optimized lattice are manufactured and tested. The drop test results displayed in Figure 20 show that the first helmet sample is immediately fully compressed and provides no gradual cushioning, as a large amount of powder was present in the lattice structure. The acceleration magnitude reaches 591G, with the HIC(d) reaching a fatal level of 2933. Afterwards, a second helmet with several orifices with a 10mm diameter (see Figure 22) for better powder removal was manufactured and tested. While its acceleration curve shows a gradual increase, the lattice is completely compacted at the 7ms mark, and the curve subsequently increases to 224G at the 8ms mark. Contrasting it to the curve obtained from the optimized FEA model, it is evident that the test model's lattice has a significantly lower stiffness and is not able to absorb the impact in the expected manner. Its HIC(d) value reaches 778, which is comparable to the best-performing foam helmet model (Sweet Protection Bushwhacker) tested in section 3.1 despite a higher peak acceleration. It performs noticeably better than its counterpart with a foam liner, which achieves an HIC(d) value of 1445.

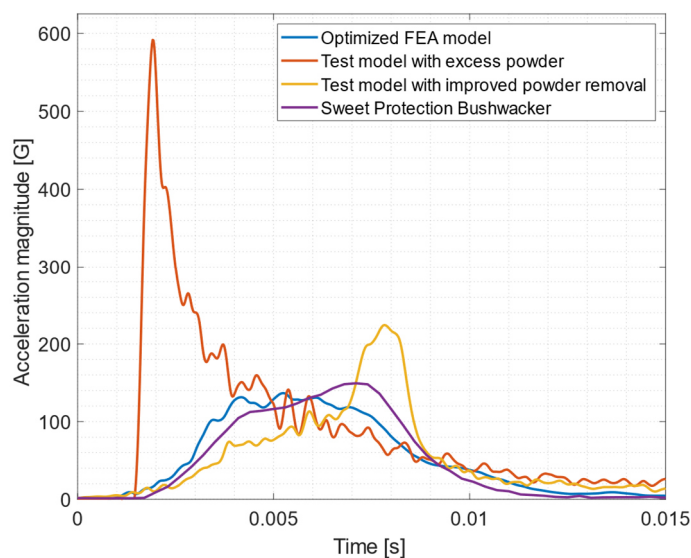


Figure 20: Acceleration curves of the FEA model with optimized Re-entrant lattice (orientation A) the curves of the two physical tests, and the curve of the best-performing foam helmet (Sweet Protection Bushwhacker).

3.2.6. Helmet sample examination after testing

The first helmet sample weighs 661.8g, whereas it was expected to weigh 400g based on the nTop model geometry and the density determined during the material investigation by the authors (c.f. [69]). The second sample weighs 482.3g which is a significant improvement over the previous attempt, but still 20% heavier than anticipated. As can be deduced by the first test sample's weight, a large amount of excess powder was trapped in the lattice despite great efforts to remove it during postprocessing using sandblasting and ultrasound baths. Figure 21 depicts the compacted powder at the impact site after testing, as well as the helmet geometry after it has been cut in half for closer examination. A large amount is adhering to the lattice structure all throughout the helmet. The affected areas are difficult to target during sandblasting from the outside without additional access holes. The powder removal orifices added to the second helmet sample were distributed over the inner helmet surface as shown in Figure 22 and yielded better results.



Figure 21: First helmet model after testing: (a) Helmet test sample containing excess powder directly after impact test; (b) Helmet test sample containing excess powder cut open for examination after impact test.

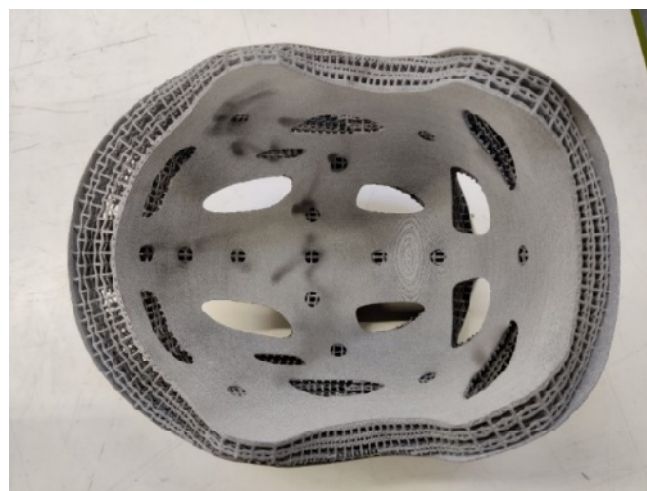


Figure 22: Second helmet test sample with added powder removal orifices.

The large amount of remaining powder in the first helmet sample prevented taking accurate thickness measurements, and additional sand blasting would have inadvertently reduced the lattice's thickness further and influenced the results. Therefore, the resulting lattice thickness was measured using the second helmet sample after testing. With application of the corrective measure, the beams assessed along the helmet ridge (see Figure 23) were found to be 0.05mm thinner on average. The differences were more pronounced at the helmet's front area with deviations of up to -0.11mm. Near the impact site, their diameters were closer to the target values. Measurements across the helmet ridge (see Figure 24) were found to have greater deviations of up to -0.17mm at the left and right measurement points. Yet, the average difference amounted to only +0.01mm since more than half of the measurements showed positive deviations.

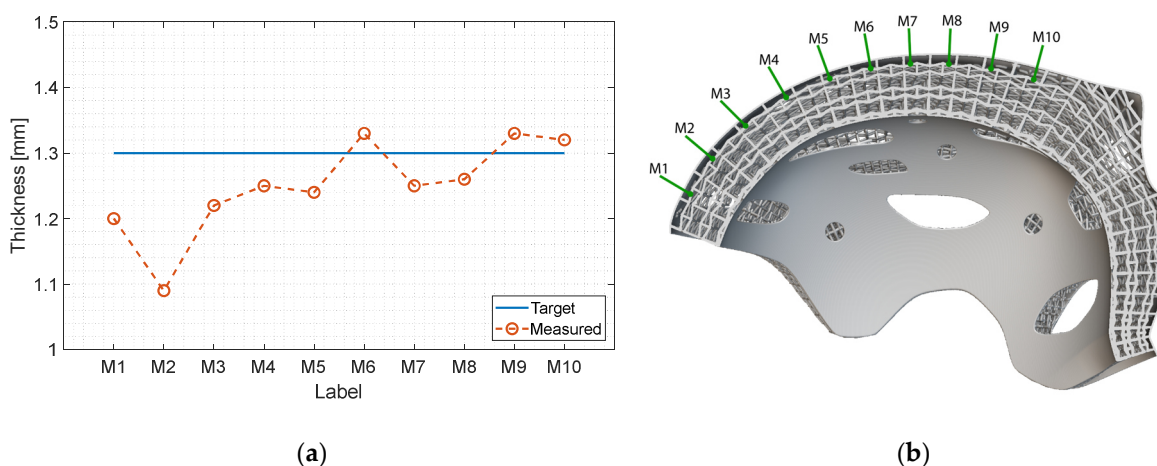


Figure 23: Thickness measurements along helmet ridge (a) and their measurement points (b).

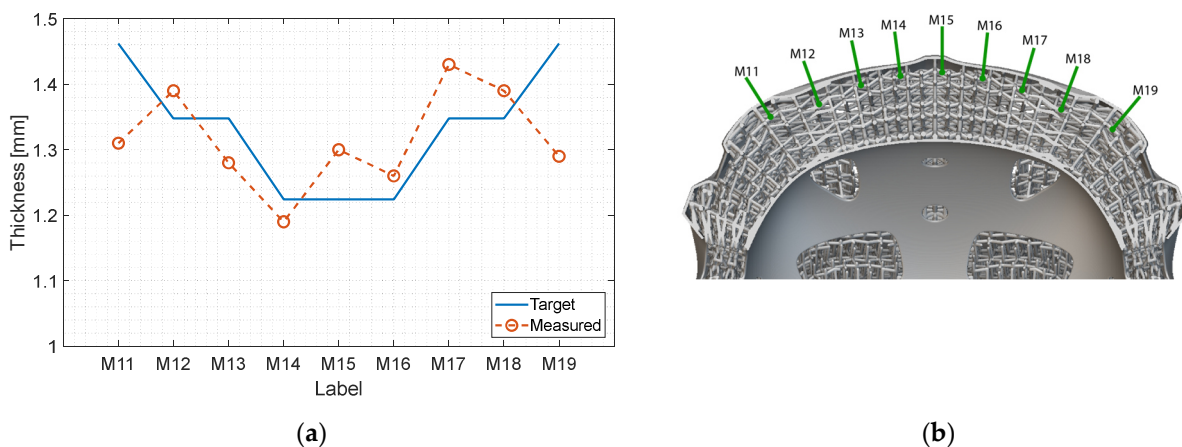


Figure 24: Thickness measurements perpendicular to helmet ridge (a) and their measurement points (b).

4. Summary and Discussion

The research presented here demonstrates the implementation of a conformal lattice structure into a realistic bicycle helmet design, adhering to engineering requirements such as adequate simulative modelling and manufacturing constraints. Fourteen suitable lattice types are investigated, evaluating their performance using appropriate FEA modelling methods. This work represents an advancement over previous studies which

commonly focus on a small number of lattice types and the use of simplified helmet geometries. The lattices were analyzed at consistent relative densities, enabling better comparability of the different lattice type's effectiveness. They are assessed together with the same helmet geometry possessing a foam lattice liner via simulation in addition to five commercially available helmets for a direct comparison. Further, the study demonstrates the use of an optimization approach able to alter the thickness of discrete lattice regions. The use of a unibody helmet design simplifies the production process by reducing time, steps, and materials. The workflow aligns with real-world engineering constraints such as lattice design, its optimization, appropriate FEA model representation, reassembly of the final geometry for manufacturing, and production limitations. However, the numerous software packages and file conversions required for this workflow highlight the lack of a unifying tool combining or at least reducing the engineering steps.

The FEA results suggest that the majority of the simulated lattice types may offer better protection compared to foam alternatives based on the assumed material parameters. The lattice helmets demonstrate average peak acceleration values of 134.5G and HIC(d) levels of 662.6. The best model achieves a peak acceleration of only 95G and an HIC(d) level of 493.8. In contrast, the foam models exhibit an average peak acceleration of 188.9G and an HIC(d) value of 1099.2, while the most effective model achieves a peak acceleration of 149.3G and an HIC(d) value of 782.4. The worst-performing lattice variant was chosen to be optimized. Its peak acceleration of 165.7G and HIC(d) value of 913.0 with the uniform, 1.5mm thick lattice were reduced to 136.6G and a HIC(d) level of 716.0.

Manufacturing and material modelling issues encountered during the physical assessments rendered the correlation of simulation results with the tests challenging. The measurements taken from the helmets and the test lattice revealed that the manufactured diameters are inconsistent, depend on the beam thickness and printing orientation, and tend to be smaller than targeted. Since the production was outsourced to a supplier, the authors had no direct control over manufacturing parameters, post-processing, or the possibility to adequately investigate the process outcomes with faster testing cycles. Additionally, the sand-blasting step required to remove excess powder after manufacturing is prone to produce deviations of the final geometry since it is a manual and difficult-to-control procedure. Even small diameter deviations evidently may have a large influence on the results since a strut's load-bearing capacity and stiffness directly depend on it. Further, the base material exhibited strong deviations from the tensile strength and strain at break indicated by the manufacturer, as well as a significant spread among samples as seen during tensile testing. The thusly obtained parameters or those determined from correlating the Johnson-Cook parameters with the single drop test may therefore not necessarily be transferrable to samples from different production batches or machines. The issues may be exacerbated at the high strain rates seen during this load case. Additionally, although the Johnson-Cook material parameters determined from the calibration study seem plausible, they may not accurately represent the material's actual behavior. Tensile testing at higher strain rates would have been preferable, permitting more precise material parameter determination. Unfortunately, these tests could not be performed within the scope of this study due to time and budget limitations.

The success of the test runs also depends on the successful removal of excess powder in the lattice structure. It adheres to the beams and decreases the available travel at which the lattice is fully compacted. Throughout the course of the investigation, two additional test series with helmets incorporating a tetrahedral lattice and truncated octahedron lattice were carried out, but not included here. Despite not having additional powder evacuation orifices in the inner shell, they did not exhibit the same tendency to retain such a large amount of loose powder as these lattice types were much less intricate. Additional iterations of the design intended to adapt it to production constraints would likely aid in mitigating these issues, but budget and time limits prevented the authors from further pursuing this avenue.

Improvements to the study could be made in several manners, for example by choosing a different FEA solver with more failure models as well as material models compatible with beam elements. RADIOSS' implementation of simple element deletion does not discern between compressive and tensile stresses and cannot account for partial strut failure. Additionally, the investigated helmet model does not include any padding or head harness which could further lower peak acceleration values. To avoid the accumulation of excess powder in certain areas, the helmet geometry could be produced without the inner shell such that the lattice is more easily reachable and cleanable. Opting for a multi-part approach instead of a unibody design would also offer more flexibility in terms of material choice and production methods. Manufacturing the lattice in parts and attaching it to the shell could enable more efficient cleaning of the lattice if produced with Powder Bed Fusion methods. Alternatively, manufacturing the sections with resin-based stereolithography (SLA) printers would circumvent the issues regarding powder removal entirely. They could potentially mitigate the thickness deviation issues as SLA printers provide very high manufacturing resolutions, provided that warping during printing and curing can be controlled.

Additional insights could be gained by exploring more ductile materials such as polypropylene or thermoplastic elastomers since they are also manufacturable by MJF and provide potentially fitting or superior material properties. Using multiple lattice types in different regions such as the sides or rear of the helmet could improve local protection, as could opting for a multilayer approach with differing lattice types in the radial direction. Automating and controlling the entire design and optimization chain in HyperStudy by linking it with nTop command line interface and running a script controlling the FEA model setup in HyperMesh would enable a powerful procedure capable of autonomously exploring a much larger design space and fine-grained local control over the lattice, however significant computational power would be required.

Author Contributions: Conceptualization, T.D. and S.K.; methodology, T.D.; software, T.D.; validation, T.D.; formal analysis, T.D.; investigation, T.D.; resources, S.K.; data curation, T.D.; writing—original draft preparation, T.D.; writing—review and editing, T.D.; visualization, T.D.; supervision, S.K.; project administration, S.K.; funding acquisition, S.K. All authors have read and agreed to the published version of the manuscript.

Funding: This research received no external funding.

Institutional Review Board Statement: Not applicable.

Informed Consent Statement: Not applicable.

Data Availability Statement: The data is contained within the article.

Acknowledgments: The authors thank SQLab GmbH for providing the helmet's CAD file as well as for the drop test data of the commercially available mountain bike helmets.

Conflicts of Interest: The authors declare no conflict of interest.

References

- [1] E. Uribe-Lam, C. D. Treviño-Quintanilla, E. Cuan-Urquizo, and O. Olvera-Silva, "Use of additive manufacturing for the fabrication of cellular and lattice materials: a review," *Materials and Manufacturing Processes*, vol. 36, no. 3, pp. 257–280, Feb. 2021, doi: 10.1080/10426914.2020.1819544.
- [2] A. Seharing, A. H. Azman, and S. Abdullah, "A review on integration of lightweight gradient lattice structures in additive manufacturing parts," *Advances in Mechanical Engineering*, vol. 12, no. 6, pp. 1–21, Jun. 2020, doi: 10.1177/1687814020916951.
- [3] S. Aghajani, C. Wu, Q. Li, and J. Fang, "Additively manufactured composite lattices: A state-of-the-art review on fabrications, architectures, constituent materials, mechanical properties, and future directions," *Thin-Walled Structures*, p. 111539, Dec. 2023, doi: 10.1016/j.tws.2023.111539.

- [4] V. S. Deshpande, M. F. Ashby, and N. A. Fleck, "Foam topology: Bending versus stretching dominated architectures," *Acta Mater*, vol. 49, no. 6, pp. 1035–1040, 2001, doi: 10.1016/S1359-6454(00)00379-7.
- [5] F. Tamburrino, S. Graziosi, and M. Bordegoni, "The design process of additively manufactured mesoscale lattice structures: A review," *J Comput Inf Sci Eng*, vol. 18, no. 4, pp. 1–16, 2018, doi: 10.1115/1.4040131.
- [6] M. F. Ashby, "The properties of foams and lattices," *Philosophical Transactions of the Royal Society A: Mathematical, Physical and Engineering Sciences*, vol. 364, no. 1838, pp. 15–30, Jan. 2006, doi: 10.1098/rsta.2005.1678.
- [7] L. J. Gibson and M. F. Ashby, *Cellular Solids*. Cambridge University Press, 1997. doi: 10.1017/CBO9781139878326.
- [8] T. Tancogne-Dejean, A. B. Spierings, and D. Mohr, "Additively-manufactured metallic micro-lattice materials for high specific energy absorption under static and dynamic loading," *Acta Mater*, vol. 116, pp. 14–28, 2016, doi: 10.1016/j.actamat.2016.05.054.
- [9] R. Gümruk, R. A. W. Mines, and S. Karadeniz, "Static mechanical behaviours of stainless steel micro-lattice structures under different loading conditions," *Materials Science and Engineering A*, vol. 586, pp. 392–406, Dec. 2013, doi: 10.1016/j.msea.2013.07.070.
- [10] R. Mahshid, H. N. Hansen, and K. L. Højbjerg, "Strength analysis and modeling of cellular lattice structures manufactured using selective laser melting for tooling applications," *Mater Des*, vol. 104, pp. 276–283, 2016, doi: 10.1016/j.matdes.2016.05.020.
- [11] M. della Ripa, D. S. Paolino, A. Amorese, and A. Tridello, "Numerical modelling of the mechanical response of lattice structures produced through AM," *Procedia Structural Integrity*, vol. 33, no. C, pp. 714–723, 2021, doi: 10.1016/j.prostr.2021.10.079.
- [12] M. Sanami, N. Ravirala, K. Alderson, and A. Alderson, "Auxetic Materials for Sports Applications."
- [13] W. Hou, X. Yang, W. Zhang, and Y. Xia, "Design of energy-dissipating structure with functionally graded auxetic cellular material," *International Journal of Crashworthiness*, vol. 23, no. 4, pp. 366–376, Jul. 2018, doi: 10.1080/13588265.2017.1328764.
- [14] Y. Xue, P. Gao, L. Zhou, and F. Han, "An Enhanced Three-Dimensional Auxetic Lattice," 2020.
- [15] Z. Chen, X. Wu, Y. M. Xie, Z. Wang, and S. Zhou, "Re-entrant auxetic lattices with enhanced stiffness: A numerical study," *Int J Mech Sci*, vol. 178, no. December 2019, p. 105619, 2020, doi: 10.1016/j.ijmecsci.2020.105619.
- [16] X. Cheng *et al.*, "Design and mechanical characteristics of auxetic metamaterial with tunable stiffness," *Int J Mech Sci*, vol. 223, p. 107286, Jun. 2022, doi: 10.1016/j.ijmecsci.2022.107286.
- [17] M. S. Pham, C. Liu, I. Todd, and J. Lertthanasarn, "Damage-tolerant architected materials inspired by crystal microstructure," *Nature*, vol. 565, no. 7739, pp. 305–311, Jan. 2019, doi: 10.1038/s41586-018-0850-3.
- [18] O. Al-Ketan, D.-W. Lee, R. Rowshan, and R. K. Abu Al-Rub, "Functionally graded and multi-morphology sheet TPMS lattices: Design, manufacturing, and mechanical properties," *J Mech Behav Biomed Mater*, vol. 102, p. 103520, Feb. 2020, doi: 10.1016/j.jmbbm.2019.103520.
- [19] I. Maskery, A. O. Aremu, L. Parry, R. D. Wildman, C. J. Tuck, and I. A. Ashcroft, "Effective design and simulation of surface-based lattice structures featuring volume fraction and cell type grading," *Mater Des*, vol. 155, pp. 220–232, Oct. 2018, doi: 10.1016/j.matdes.2018.05.058.
- [20] L. Bai *et al.*, "Mechanical properties and energy absorption capabilities of functionally graded lattice structures: Experiments and simulations," *Int J Mech Sci*, vol. 182, Sep. 2020, doi: 10.1016/j.ijmecsci.2020.105735.
- [21] H. Niknam and A. H. Akbarzadeh, "Graded lattice structures: Simultaneous enhancement in stiffness and energy absorption," *Mater Des*, vol. 196, Nov. 2020, doi: 10.1016/j.matdes.2020.109129.
- [22] I. Maskery *et al.*, "An investigation into reinforced and functionally graded lattice structures," *Journal of Cellular Plastics*, vol. 53, no. 2, pp. 151–165, 2017, doi: 10.1177/0021955X16639035.

- [23] S. Y. Choy, C. N. Sun, K. F. Leong, and J. Wei, "Compressive properties of functionally graded lattice structures manufactured by selective laser melting," *Mater Des*, vol. 131, pp. 112–120, Oct. 2017, doi: 10.1016/j.matdes.2017.06.006.
- [24] A. Ajdari, H. Nayeb-Hashemi, and A. Vaziri, "Dynamic crushing and energy absorption of regular, irregular and functionally graded cellular structures," *Int J Solids Struct*, vol. 48, no. 3–4, pp. 506–516, Feb. 2011, doi: 10.1016/j.ijsolstr.2010.10.018.
- [25] W. Tao, A. Sutton, K. Kolan, and M. C. Leu, "Design of Lattice Structures with Graded Density Fabricated by Additive Manufacturing Cyber Physical Cloud Manufacturing Systems View project Solvent-based 3D printing of polymer/bioactive glass composites View project 19 PUBLICATIONS 207 CITATIONS SEE PR," 2018, doi: 10.11509/isfa.2018.122.
- [26] J. Yang *et al.*, "Compressive properties of bidirectionally graded lattice structures," *Mater Des*, vol. 218, p. 110683, 2022, doi: 10.1016/j.matdes.2022.110683.
- [27] Y. Xu, T. Li, X. Cao, Y. Tan, and P. Luo, "Compressive Properties of 316L Stainless Steel Topology-Optimized Lattice Structures Fabricated by Selective Laser Melting," *Adv Eng Mater*, vol. 23, no. 3, 2021, doi: 10.1002/adem.202000957.
- [28] Z. Xiao, Y. Yang, R. Xiao, Y. Bai, C. Song, and D. Wang, "Evaluation of topology-optimized lattice structures manufactured via selective laser melting," *Mater Des*, vol. 143, pp. 27–37, 2018, doi: 10.1016/j.matdes.2018.01.023.
- [29] J. Song *et al.*, "Topology optimization-guided lattice composites and their mechanical characterizations," *Compos B Eng*, vol. 160, pp. 402–411, Mar. 2019, doi: 10.1016/j.compositesb.2018.12.027.
- [30] Y. Du, H. Li, Z. Luo, and Q. Tian, "Topological design optimization of lattice structures to maximize shear stiffness," *Advances in Engineering Software*, vol. 112, pp. 211–221, 2017, doi: 10.1016/j.advengsoft.2017.04.011.
- [31] Y. Han and W. F. Lu, "A novel design method for nonuniform lattice structures based on topology optimization," *Journal of Mechanical Design, Transactions of the ASME*, vol. 140, no. 9, pp. 1–10, Sep. 2018, doi: 10.1115/1.4040546.
- [32] S. Daynes, S. Feih, W. F. Lu, and J. Wei, "Optimisation of functionally graded lattice structures using isostatic lines," *Mater Des*, vol. 127, no. February, pp. 215–223, Aug. 2017, doi: 10.1016/j.matdes.2017.04.082.
- [33] J. Wu, W. Wang, and X. Gao, "Design and Optimization of Conforming Lattice Structures," 2019.
- [34] X. Wang, L. Zhu, L. Sun, and N. Li, "A study of functionally graded lattice structural design and optimisation," in *Proceedings - 2020 6th International Conference on Mechanical Engineering and Automation Science, ICMEAS 2020*, Institute of Electrical and Electronics Engineers Inc., Oct. 2020, pp. 50–55. doi: 10.1109/ICMEAS51739.2020.00017.
- [35] A. Takezawa, X. Zhang, M. Kato, and M. Kitamura, "Method to optimize an additively-manufactured functionally-graded lattice structure for effective liquid cooling," *Addit Manuf*, vol. 28, no. May, pp. 285–298, 2019, doi: 10.1016/j.addma.2019.04.004.
- [36] K. J. Maloney, K. D. Fink, T. A. Schaedler, J. A. Kolodziejska, A. J. Jacobsen, and C. S. Roper, "Multifunctional heat exchangers derived from three-dimensional micro-lattice structures," *Int J Heat Mass Transf*, vol. 55, no. 9–10, pp. 2486–2493, 2012, doi: 10.1016/j.ijheatmasstransfer.2012.01.011.
- [37] L. Cheng, J. Liu, X. Liang, and A. C. To, "Coupling lattice structure topology optimization with design-dependent feature evolution for additive manufactured heat conduction design," *Comput Methods Appl Mech Eng*, vol. 332, pp. 408–439, 2018, doi: 10.1016/j.cma.2017.12.024.
- [38] M. D. Guild, M. Rothko, C. F. Sieck, C. Rohde, and G. Orris, "3D printed sound absorbers using functionally-graded sonic crystals," *J Acoust Soc Am*, vol. 143, no. 3, pp. 1714–1714, 2018, doi: 10.1121/1.5035582.

- [39] B. Leng, D. Ruan, and K. M. Tse, "Recent bicycle helmet designs and directions for future research: A comprehensive review from material and structural mechanics aspects," *Int J Impact Eng*, vol. 168, no. June, p. 104317, 2022, doi: 10.1016/j.ijimpeng.2022.104317.
- [40] "Bontrager." Accessed: Nov. 27, 2023. [Online]. Available: https://www.trekbikes.com/international/en_IN_TL/bontrager?clear=true
- [41] "WaveCel Helmets | Trek Bikes." Accessed: Nov. 19, 2021. [Online]. Available: https://www.trekbikes.com/us/en_US/wavecel/
- [42] "Koroyd." Accessed: Nov. 24, 2023. [Online]. Available: <https://koroyd.com/>
- [43] "Hexr." Accessed: Nov. 27, 2023. [Online]. Available: <https://hexr.com>
- [44] E. Bliven *et al.*, "Evaluation of a novel bicycle helmet concept in oblique impact testing," *Accident Analysis and Prevention*, vol. 124, pp. 58–65, 2019. doi: 10.1016/j.aap.2018.12.017.
- [45] S. P. Soe, P. Martin, M. Jones, M. Robinson, and P. Theobald, "Feasibility of optimising bicycle helmet design safety through the use of additive manufactured TPE cellular structures," *International Journal of Advanced Manufacturing Technology*, vol. 79, no. 9–12, pp. 1975–1982, Aug. 2015, doi: 10.1007/s00170-015-6972-y.
- [46] S. F. Khosroshahi, H. Duckworth, U. Galvanetto, and M. Ghajari, "The effects of topology and relative density of lattice liners on traumatic brain injury mitigation," *J Biomech*, vol. 97, p. 109376, Dec. 2019, doi: 10.1016/j.jbiomech.2019.109376.
- [47] A. A. Naderi, K. Imani, and H. Ahmadi, "Crashworthiness Study of an Innovative Helmet Liner Composed of an Auxetic Lattice Structure and PU Foam," *Mechanics of Advanced Composite Structures*, vol. 9, no. 1, pp. 25–35, 2022, doi: 10.22075/mac.2021.23224.1338.
- [48] M. Nasim, M. J. Hasan, and U. Galvanetto, "Impact behavior of energy absorbing helmet liners with PA12 lattice structures: A computational study," *Int J Mech Sci*, vol. 233, no. April, p. 107673, 2022, doi: 10.1016/j.ijmecsci.2022.107673.
- [49] T. Decker and S. Kedziora, "Local Thickness Optimization of Functionally Graded Lattice Structures in Compression," *Applied Sciences*, vol. 13, no. 23, p. 12969, Dec. 2023, doi: 10.3390/app132312969.
- [50] "nTop." [Online]. Available: <https://www.ntop.com>
- [51] T. Decker, S. Kedziora, and C. Wolf, "Practical Implementation of Functionally Graded Lattice Structures in a Bicycle Crank Arm," *885th International Conference on Science, Technology, Engineering and Management (ICSTEM)*, no. November, pp. 58–64, 2020.
- [52] S. Kedziora, T. Decker, and E. Museyibov, "Application of Functionally Graded Shell Lattice as Infill in Additive Manufacturing," *Materials*, vol. 16, no. 12, p. 4401, Jun. 2023, doi: 10.3390/ma16124401.
- [53] European Committee for Standardization. Technical Committee CEN/TC 158 "Head Protection.," British Standards Institution, and British Standard Institution. BS EN 1078:2012+A1 2012., *EN 1078:2012 - Helmets for pedal cyclists and for users of skateboards and roller skates.*
- [54] U.S. Department of Transportation - National Highway Traffic Safety Administration, "Occupant Protection in Interior Impact - Upper Interior Impact Protection." Accessed: Jan. 16, 2024. [Online]. Available: https://www.nhtsa.gov/sites/nhtsa.gov/files/documents/tp-201u-02_tag.pdf
- [55] L. Chybowski and W. Przetakiewicz, "Estimation of the Probability of Head Injury at a Given Abbreviated Injury Scale Level by Means of a Function of Head Injury Criterion," *System Safety: Human - Technical Facility - Environment*, vol. 2, no. 1, pp. 91–99, 2020, doi: 10.2478/czoto-2020-0012.
- [56] "SQLab GmbH." Accessed: Nov. 24, 2023. [Online]. Available: <https://www.sq-lab.com/en/>
- [57] Ian. Stroud, *Boundary representation modelling techniques*. Springer, 2006.

- [58] G. Allen, "nTopology Modeling Technology," 2019.
- [59] "Altair HyperMesh." [Online]. Available: <https://altair.com/hypermesh/>
- [60] "Altair RADIOSS." Accessed: Nov. 24, 2023. [Online]. Available: <https://altair.com/radioss>
- [61] "Altair HyperStudy." [Online]. Available: <https://altair.com/hyperstudy/>
- [62] "Mathworks MATLAB." Accessed: Nov. 24, 2023. [Online]. Available: <https://www.mathworks.com/products/matlab.html>
- [63] European Committee for Standardization, *EN 960:2006 - Headforms for use in the testing of protective helmets*.
- [64] K. M. D. Bushby, T. Cole, J. N. S. Matthews, and J. A. Goodship, "Centiles for adult head circumference," *Arch Dis Child*, vol. 67, no. 10, pp. 1286–1287, 1992, doi: 10.1136/adc.67.10.1286.
- [65] "HP Multi Jet Fusion 3D Printing Technology," <https://www.hp.com/us-en/printers/3d-printers/learning-center/3d-printing-process.html#section=hp-multi-jet-fusion>. Accessed: Oct. 31, 2023. [Online]. Available: <https://www.hp.com/us-en/printers/3d-printers/learning-center/3d-printing-process.html#section=hp-multi-jet-fusion>
- [66] S. Ouellet, D. Cronin, and M. Worswick, "Compressive response of polymeric foams under quasi-static, medium and high strain rate conditions," *Polym Test*, vol. 25, no. 6, pp. 731–743, 2006, doi: 10.1016/j.polymertesting.2006.05.005.
- [67] K. Cao, X. Ma, B. Zhang, Y. Wang, and Y. Wang, "Tensile behavior of polycarbonate over a wide range of strain rates," *Materials Science and Engineering A*, vol. 527, no. 16–17, pp. 4056–4061, Jun. 2010, doi: 10.1016/j.msea.2010.03.088.
- [68] "Mg AZ91." Accessed: Jan. 16, 2024. [Online]. Available: <https://www.matweb.com/search/datasheet.aspx?MatGUID=07baafb9c364fb18fd413bceced867f>
- [69] T. Decker, S. Kedziora, and E. Museyibov, "Comparison of Strength Properties of Common Powder Bed Fusion and Stereolithography Materials," *Key Eng Mater*, vol. 969, pp. 11–20, Dec. 2023, doi: 10.4028/p-Sgu1sR.
- [70] D. B. Roppenecker, R. Grazek, J. A. Coy, F. Irlinger, and T. C. Lueth, "Friction coefficients and surface properties for laser sintered parts," *ASME International Mechanical Engineering Congress and Exposition, Proceedings (IMECE)*, vol. 2 A, pp. 1–10, 2013, doi: 10.1115/IMECE2013-64549.
- [71] S. A. Aldahash, "Friction and wear properties of oriented Polamide 12 objects manufactured by SLS Technology," vol. 15, no. 2, pp. 9–25, 2019.
- [72] J. H. Lee, G. H. Xu, and H. Liang, "Experimental and numerical analysis of friction and wear behavior of polycarbonate," *Wear*, vol. 250–251, no. PART 2, pp. 1541–1556, 2001, doi: 10.1016/s0043-1648(01)00788-8.
- [73] "Altair RADIOSS TYPE7 General Contact Interface." Accessed: Dec. 01, 2023. [Online]. Available: https://2021.help.altair.com/2021/hwsolvers/rad/topics/solvers/rad/default_inter_type7_starter_r.htm?zoom_highlight=type7
- [74] "Altair RADIOSS Shell Elements Overview." Accessed: Dec. 01, 2023. [Online]. Available: https://2021.help.altair.com/2021/hwsolvers/rad/topics/solvers/rad/theory_elements_shell_elem_overview_r.htm
- [75] "Altair RADIOSS LAW70 Tabulated Viscoelastic Foam Material Law." Accessed: Dec. 01, 2023. [Online]. Available: https://2021.help.altair.com/2021/hwsolvers/rad/topics/solvers/rad/mat_law70_foam_tab_starter_r.htm
- [76] "Altair RADIOSS LAW36 Elastic Plastic Piecewise Linear Material." Accessed: Dec. 01, 2023. [Online]. Available: https://2021.help.altair.com/2021/hwsolvers/rad/topics/solvers/rad/explicit_structural_fea_elasto_plastic_c.htm#elastic_plastic_piecewise_linear_material_r

- [77] "Altair RADIOSS QBAT Element Type." Accessed: Dec. 01, 2023. [Online]. Available: https://2021.help.altair.com/2021/hwsolvers/rad/topics/solvers/rad/theory_element_fully_integrated_shell_element_qbat_r.htm
- [78] "Altair RADIOSS LAW2 Johnson-Cook Elastic-Plastic Material Model." Accessed: Dec. 01, 2023. [Online]. Available: https://2021.help.altair.com/2021/hwsolvers/rad/topics/solvers/rad/mat_law2_plas_johns_starter_r.htm
- [79] "Altair RADIOSS TYPE18 Integrated Beam Element." Accessed: Dec. 01, 2023. [Online]. Available: https://2021.help.altair.com/2021/hwsolvers/rad/topics/solvers/rad/prop_type18_int_beam_starter_r.htm?zoom_highlightsub=type18
- [80] "Altair RADIOSS TYPE2 Tied Contact Interface." Accessed: Dec. 01, 2023. [Online]. Available: https://2021.help.altair.com/2021/hwsolvers/rad/topics/solvers/rad/tied_contact_intro_r.htm
- [81] "Altair RADIOSS TYPE11 Edge-to-Edge Contact Interface." Accessed: Dec. 01, 2023. [Online]. Available: https://2021.help.altair.com/2021/hwsolvers/rad/topics/solvers/rad/default_inter_type11_starter_r.htm?zoom_highlight=type11
- [82] "ISO 527-2:2012 Plastics Determination of tensile properties Part 2: Test conditions for moulding and extrusion plastics." Accessed: Nov. 24, 2023. [Online]. Available: <https://www.iso.org/standard/56046.html>
- [83] "Modifiable Extensible Lattice Sequence (MELS)." [Online]. Available: https://2021.help.altair.com/2021.2/hwdesktop/hst/topics/design_exploration/method_modified_extensible_lattice_sequence_doe_r.htm
- [84] "Global Response Search Method (GRSM)." [Online]. Available: https://2021.help.altair.com/2021.2/hwdesktop/hst/topics/design_exploration/method_global_response_surface_method_r.htm
- [85] "TCL/TK Homepage." Accessed: Nov. 27, 2023. [Online]. Available: <https://www.tcl.tk>
- [86] S. F. Fischer *et al.*, "Pummelos as concept generators for biomimetically inspired low weight structures with excellent damping properties," in *Advanced Engineering Materials*, Dec. 2010. doi: 10.1002/adem.201080065.
- [87] HP Development Company, "HP 3D High Reusability PA 12," pp. 5–6, 2019, [Online]. Available: <http://www8.hp.com/h20195/v2/getpdf.aspx/4AA7-0716ENE.pdf>

Disclaimer/Publisher's Note: The statements, opinions and data contained in all publications are solely those of the individual author(s) and contributor(s) and not of MDPI and/or the editor(s). MDPI and/or the editor(s) disclaim responsibility for any injury to people or property resulting from any ideas, methods, instructions or products referred to in the content.

The model's physical drop tests results did not match the simulative assessments due to material modelling and manufacturing issues. Since no suitable material data covering high strain rates was available in literature and the necessary test equipment to obtain them was not accessible to the authors, a simulative material correlation was performed based on a drop test. Even though the resulting material parameters seem plausible, their validity is uncertain. In addition, the lattice geometry exhibited significant thickness deviations that vary depending on their printing orientation and target thickness. Even though a corrective thickness offset based on measurements was applied, the lattice incorporated in the helmet samples were still too thin. Comparing the acceleration curves of the simulation and test, it can be concluded that the lattice's stiffness is overestimated by the FEA model. The test sample's acceleration curve possesses a shallower slope followed by a sudden increase caused by complete compression of the lattice. Its acceleration peak of 224G is within the standard's upper limit of 250G, and the HIC(d) level of 778 matches the best-performing foam helmet.

The demonstrated lattice helmet is able to outperform four out of five tested helmets incorporating a conventional foam liner. Repeating the simulations and optimization with accurate material properties as well as better knowledge and control over the manufacturing method would most likely allow for further improvements. Despite the aforementioned limitations, this paper demonstrates that the implementation of a lattice structure in a realistic appliance is feasible, and that the optimization method leads to substantial improvements. Additional pictures of the tested helmet designs are shown in the Addendum in section 7.10.

The author contributed to this paper by continuing to evolve the concept and methodology, designing the lattice structures used in the helmet, performing the simulations of the foam helmet model as well as the lattice helmets and their optimizations, and physically testing the resulting samples. Further, the author performed the data analysis and visualization, wrote the original draft of the manuscript, and performed edits based on reviewer comments.

5 Discussion

This chapter provides answers to the research questions and critically discusses the results as well as the procedure presented in the thesis.

5.1 Responses to Research Questions

- *RQ1: How to design and optimize FGLS for mechanical parts with consideration of engineering requirements?*

At the start of the doctoral project, nTop was the only viable option for designing complex lattice structures in a streamlined manner, offering sufficient manipulation and export options for engineering purposes. Normal CAD programs are not suitable for this task due to their limitation stemming from the boundary representation of geometries. While custom scripts or workflows in specialized software like Rhinoceros3D with the Grasshopper plugin can be used, the time and complexity drawbacks may significantly impact their usability in an industry setting. Engineering software manufacturers have recognized the demand for adequate software solutions. Consequently, big players such as Autodesk introduced the option to design basic graded lattices in Fusion 360 and will allow importing implicit bodies from nTop for production preprocessing in 2024. Likewise, Altair has introduced implicit body modelling in Inspire 2023.0 allowing the design, simulation, and optimization of lattice structures. More versatility and further software solutions are expected to follow in the future to satisfy the industry's needs.

File formats are still an issue and will likely be for the foreseeable future. STL is the de facto standard for geometries in the 3D printing domain, however efforts are made for slicers to accept nTop-native files, STEP files or other mesh formats such as 3MF, but their adoption is not wide-spread yet. In the meantime, conversion scripts or workarounds involving several different file formats or software suites may be required.

As for analysis and optimization, it was found that FE solvers offering a wide range of options and a sophisticated preprocessor like HyperMesh are required. Basic FEA solvers like the ones included in CAD software are insufficient, and advanced ones like Altair OptiStruct and RADIOSS, Ansys Mechanical and LS-Dyna, or Abaqus are required. Their optimization can be performed by parameterizable input files in general optimizers like HyperStudy or Ansys Design Explorer.

The lattice optimization method proposed and demonstrated in this thesis (Decker et al., 2020; Decker & Kedziora, 2023b, 2023a; Kedziora et al., 2023) splits the lattice structure into discrete regions either via manual operations or a scripted routine for more advanced contours. It is making use of the fact that each lattice region's thickness can easily be modified by changing a parameter of the 1D or 2D finite element representation. The best choice of a specific type of optimization solver, such as the Adaptive Response Surface Method, Global Response Search Method, Genetic Algorithm, Sequential Quadratic Programming etc. strongly depends on the system behaviour and must be considered individually for each model. In the presented studies, the Global Response Search Method proved to be a reliable choice. Using template models in nTop, HyperMesh, HyperStudy, and scripts for file conversion permits quick design iterations where only few manual operations are required.

The production of lattice structures proved to be more challenging than their design and optimization despite the limitations of current software solutions. Additive Manufacturing is a comparatively new process with some subcategories being in need of maturity. In principle, all three of the dominant AM methods can produce lattice structures to varying degrees of size and accuracy. The properties and suitability of each one need to be assessed individually as they have differing strengths and weaknesses. Both metal and polymer PBF methods provide a good balance of large build volumes, geometrical freedom, high accuracy, and vast material selections. Polymer FDM boasts great ease of use, whereas metal FDM should be avoided entirely as evidenced by the difficulties surrounding the production of the crank arm. SLA provides very high levels of detail and smooth surface finishes. Metal PBF methods attain consistent material properties, whereas all three main AM methods for polymers show significant deviations that have to be accounted for in both the design and simulation of lattice structures. In addition, geometrical deviations as well as thermal warping quickly become relevant. Lattice structures are commonly composed of thin and tall features that are approaching the machine's lower feasibility limits due to the nozzle or laser size. Great care must therefore be taken to avoid these issues wherever possible.

- *RQ2: How well do FGLS perform in realistic mechanical appliances?*

The literature review conducted at the beginning of the study suggests that the performance of mechanical parts may be increased significantly by the addition of FGLS given the right conditions. The projects presented here show that not every part may be well-suited to incorporate a lattice, considering the achieved improvements and manufacturing constraints. In retrospect, choosing the bicycle crank arm was suboptimal due to its geometry and the encountered manufacturing issues. The steel's modulus, the crank's shape and its solid skin already lend it significant rigidity. Hence, incorporating a lattice geometry provided no benefit compared to the hollow geometry in terms of the stiffness-to-weight ratios determined in (Decker et al., 2020; Kedziora et al., 2023). Nonetheless, the models surpassed the stiffness-to-weight ratio of the commercially available aluminium crank to which it was compared by 65% with graph lattices and 110% with a Gyroid lattice, respectively. In addition, the studies were able to adequately demonstrate the feasibility of incorporating FGLS in a realistic geometry, as well as showing the design and optimization method's functionality.

The helmet geometry considered in (Decker & Kedziora, 2023b) is a better demonstration of a suitable lattice implementation. Since the lattice occupies a large volume, its influence on the results is much more pronounced than that of the helmet's shell. The tested model containing an optimized lattice structure performs better than four out of five conventional foam helmets and is on par with the best-performing model. In addition, it greatly improves upon the performance of the same helmet design incorporating a conventional foam liner. However, limitations regarding production and material data prevented correlating the simulations and test results. Therefore, it is assumed that the helmet's performance can be further improved once these issues are mitigated.

- *RQ3: How can FGLS be modelled and simulated adequately?*

Since the thesis studies lattice structures in the context of AM, each method's limits and properties must be examined before the lattices can be reliably modelled numerically. The material investigations (Decker et al., 2023; Kedziora et al., 2022) conducted during this endeavour revealed that certain AM methods produce parts with a high degree of anisotropy and large material property spreads. The values determined from testing greatly deviated from the manufacturer's data sheets, therefore independent testing is essential. Additionally, lattice structures tend to possess thin features that may border on the feasibility limits of some AM methods as determined during the presented studies (Decker & Kedziora, 2023b, 2023a). These deviations have to be accounted for either by avoiding the use of thin features by altering the lattice properties, or by adding thickness corrections to the manufactured parts based on testing. However, applying reliable corrections is not trivial since the deviations depend on the part's manufacturing orientation.

Regarding Finite Element Analysis of structural applications, the most appropriate method to model lattices is to use 1D beam and 2D shell elements whenever feasible and to avoid 3D solid elements. First and foremost, the proposed optimization method is only compatible with 1D and 2D elements. Second, they greatly reduce a model's complexity and improve the solver performance. Lattice structures tend to be very intricate, requiring great care during 3D solid element meshing to ensure acceptable element quality. Beam and shell elements significantly simplify the discretization step, but evidently require more attention in other domains. Element penetrations and intersections at contact or tie interfaces must be mitigated to prevent solver issues. If nonlinear phenomena such as yielding or buckling in graph unit cells need to be modelled, they must be discretized by a sufficient number of elements via beam subdivisions to be adequately captured. 3D solid elements can be considered for validation studies of models with simplified geometries, but it may not always be reasonable or even possible regarding preprocessing and solving efforts. For other applications such as Computational Fluid Dynamics studies, the use of 3D solid elements may be the only option.

Capable preprocessors such as Altair HyperMesh along with adequate solvers offering advanced material models, contact interfaces etc. are recommended to set up and run FE lattice models. Using fully integrated first order elements or second order elements with full or reduced integration is encouraged, but the exact element type evidently depends on the load case and solver type at hand.

- *RQ4: How can the computational effort of lattice optimization studies be reduced?*

Reducing the computational cost can be approached from several angles. Common techniques applied in the domain of structural FE modelling make use of symmetry or submodelling such that only part of the model needs to be considered in an analysis. Other avenues include the simplification of geometrical features such as the removal holes and fillets, the use of first order elements instead of second order elements, using reduced integration elements, or simply to decrease the amount of used elements. Slowly moving processes models may be considered quasi-static to avoid using a dynamic implicit solver, reducing solving time. Models requiring the use of a dynamic explicit solver can benefit from larger element sizes and mass scaling to improve the solving time. Most of these options entail a decrease in fidelity, and their suitability must be assessed for each individual case.

Another avenue is to alter the optimization routine's settings. In the presented projects, each optimization study was preceded by a DOE run to provide adequate starting points for the optimization algorithm. For models with only a moderately nonlinear response, the system behaviour can be approximated by a response surface fit based on the DOE data. It may subsequently be used for the optimization step instead of executing numerous runs of a full simulation to save a significant amount of time. In addition, instead of changing the optimization variables' values on a continuous range, they may be bound to discrete ranges with a finite number of steps between their limits. Further, as demonstrated by the thesis' proposed optimization method, the optimization variables can be linked by a mathematical function. Thus, the number of variables is greatly reduced, and the optimization solver requires vastly fewer runs. However, the solver's chance of finding a global optimum is reduced this way and only a local optimum might be found.

- *RQ5: Which unit cell types are suitable for the considered tasks?*

The selection of suitable unit cell types depends on numerous aspects and has to be assessed individually for each application. It is influenced by the choice of manufacturing method, the targeted part behaviour, its relative density, base material etc. as shown in *Figure 5.1*. Certain criteria may be the dominant factors during the design phase and directly impact the choice of other lattice properties.

As stated in (Gibson & Ashby, 1997), the unit cell types are not of primary importance for a lattice structure, but their relative density is the main influence. The lattice type is a secondary variable to be altered after having specified the performance criteria. Surface and beam lattices have differing, but overlapping application areas. When using common AM methods, surface lattices tend to require a higher relative density compared to graph lattices to ensure their manufacturability. The minimum manufacturable wall thickness partially dictates the lowest relative density level, but this can be counteracted within limits via the unit cell size. Thus, graph unit cell types are preferred for applications with low relative density, while both are suitable for medium to high relative density applications. Choosing higher relative densities is beneficial for the rigidity and strength load-bearing structures, while compressive energy absorption applications benefit from lower relative densities to prevent excessive stiffness.

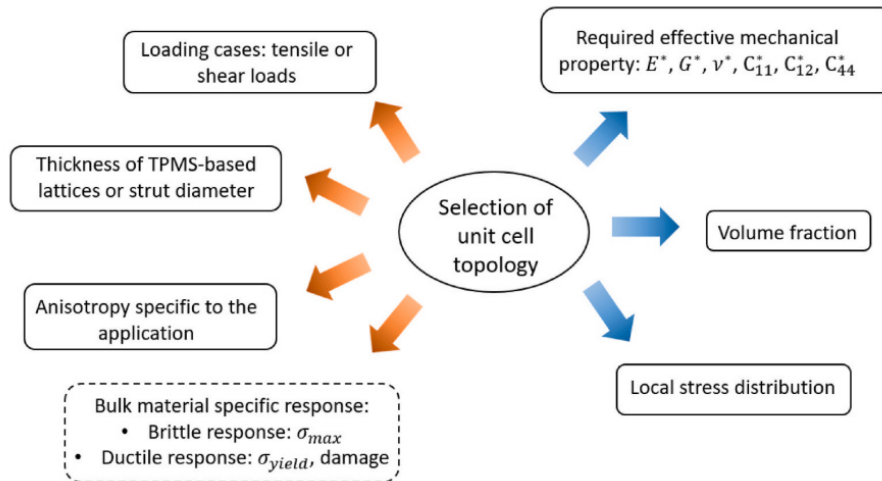


Figure 5.1: Influences of application constraints on choice of unit cell type (Chatzigeorgiou et al., 2022)

In structural applications, the composition of TPMS unit cells is beneficial for a part's longevity. Their smooth surfaces are free of stress concentrations and thus improve the fatigue life as demonstrated by the results obtained in the studies on the crank arms (Decker et al., 2020; Kedziora et al., 2023). Additionally, the considered TPMS lattice provided a much greater stiffness-to-weight ratio at identical part weight compared to the graph lattices. While no further surface-based lattice types were assessed in this project, several graph unit cell types were considered. Comparing them at equal unit cell size and strut thickness (i.e. not at equal relative density), their lowest and highest stiffness-to-mass ratios differ by 33%. Manufacturability was the decisive factor in choosing an adequate lattice type for production of the prototype. Producing a graph-based lattice crank prototype with SLM would have been a valid choice, but local manufacturing with metal FDM was preferred. Therefore, a surface-based unit cell type was the only viable option since manufacturing graph-based unit cells of this size would not have been feasible with the Markforged Metal X system.

As for the study revolving around the helmet (Decker & Kedziora, 2023b), graph-based unit cell types were chosen for two reasons. They permit the production of lattices with very low relative density, whereas TPMS or other surface-based lattice types entail higher densities at comparable cell size. As a lattice's impact absorption properties greatly depend on its relative density, graph-based unit cells were the preferred choice to achieve an adequate balance of strut thickness and unit cell size. In addition, it was determined early in the project that a PBF method for polymer materials is the only adequate method capable of producing the entire helmet. Employing surface-based unit cells would have rendered removal of excess powder after printing practically impossible. Hence, graph-based unit cells were clearly better-suited for this project. At identical relative density, the modified Head Injury Criterion performance difference between the best-performing and worst-performing lattice types amounts to 43%. One outlier model fails to sufficiently absorb the impact energy which results in a 168% higher HIC(d) level compared to the best lattice type. Two of the considered graph lattice types were stochastic, i.e. randomly oriented and foam-like. Their performance was among the three best contenders in the considered impact scenario, and only one regular lattice type outperformed them. It is assumed that their uniform and quasi-isotropic properties played a considerable role in their relative

performance positioning. Further, the considered regular lattice types exhibit a noticeable degree of orthotropy which could be detrimental here. In principle, stochastic lattices are well-suited for localized size adaptations. It would be feasible to control its local density via the cell size and thickness parameters by linking its command line interface with Altair HyperStudy. The FE model setup could be automated with HyperMesh, and optimization studies could be run completely independent of manual intervention. Conversely, regular lattice unit cells usually are confined to rectangular or hexagonal shapes. Adapting them to regions with significant size changes is more challenging, as the unit cells must be stretched or truncated to follow the geometry.

The graph-based lattice's subcategorization into bending-dominated, stretching-dominated and overconstrained types becomes relevant in large strain compression cases such as the one investigated in (Decker & Kedziora, 2023a). Here, the uniform, bending-dominated lattice achieved only a third of the specific energy absorption (SEA) compared to the stretching-dominated lattice. On the other hand, the bending-dominated type achieved a much greater SEA improvement after the optimization. An increase of up to 29% was reached compared to a maximum increase of 5% with the stretching-dominated lattice. While the limited scope of the study does not permit a general statement, it indicates at differences in performance and their potential improvement between them.

5.2 Limitations

The limitations regarding the design, modelling, optimization and production of FGLS that were encountered during the course of the thesis are assembled and discussed critically in this section.

The optimization procedure is proven to be appropriate for engineering workflows and effective in fulfilling its task as demonstrated by the presented publications and projects. Establishing and refining it was relatively straight-forward thanks to the versatile lattice design software nTop and established FEA suites enabling complex model setup and solving. Conversely, the greatest hindrances tied to the workflow stemmed from material inconsistencies, manufacturing deviations and software limitations. Overall, processes involved significant manual input as soon as models had to be transferred from one step to the next, and a streamlined suite capable of handling everything is not yet available.

As shown in the publication presented in section 4.2, metal FDM manufacturing possesses considerable limitations stemming from its extrusion-based process. It can be clearly seen that the test samples did not reach the values claimed by the respective manufacturer's data sheets. Parts have high surface roughness values, high porosity with sharp voids, weak layer bonding, large deviations, and overall subpar material properties that severely limit their use. In addition, the process can only be reliably applied to small parts with comparatively low complexity which do not exceed 60mm per axis, with 100mm per axis being the upper recommended limit by the manufacturers. Even when the size restrictions were respected, parts frequently fractured during sintering or delaminated while printing. Numerous attempts of printing large parts such as the crank arm geometry resulted in failure. Opting for a Powder Bed Fusion method would have been the preferable choice for producing the crank arm in retrospect. However, metal FDM was chosen in the initial project stage since it enables the on-site, low-cost production of the Gyroid lattice in the crank arm without the need for numerous powder release channels as required by PBF methods, which would compromise the geometry's stiffness. The graph lattice investigated in the first publication would have been manufacturable by SLM with only

few powder evacuation holes, alas printing the intricate geometry was not feasible with the Markforged system.

During the course of the projects involving polymer lattices, limitations of the chosen manufacturing methods became evident here as well. The publication involving their material investigation (see section 4.4) partly showed important result spreads occurring in samples of both resin-based and powder-based manufacturing methods, rendering reliable material behaviour predictions difficult. Since polymer part properties are strongly influenced by numerous external factors before, during and after production, singular parts from different production batches subjected to slightly different conditions may not be well-represented by the properties established from the tests. This was especially noticeable during the optimization of lattice cubes in compression described in section 4.5, when lattices produced with Formlabs Tough 2000 were to be correlated with the simulations based on material properties established from tests. No match could be established between the approaches, and it is assumed that the differing time spans between production and testing are at the root of the issue. Since the material is sensitive to ultraviolet light, it is continuously cured after printing when left exposed to ambient conditions, which causes material property changes over time. It was not possible to match the physical test results with the simulations using material properties obtained from tensile testing since their properties did not match. The lattice models using the Tough 2000 material were therefore discarded.

In addition to the material deviations, manufacturing issues of both PBF and SLA methods exacerbated the correlations further. Although the geometries possessed feature sizes above the manufacturers' stated minimum feature sizes, thickness deviations and considerable warping occurred below certain beam diameters. Some could be mitigated by the use of more support structures in case of SLA printing or, in case of PBF, part cages protecting the geometry from excessive abrasion during post-processing with sandblasting. The improvements were limited or cancelled by the increased risk of breaking a thin beam during support structure removal. Certain lattice types implemented in the helmet geometry rendered excess powder removal increasingly difficult, up to the point that some models possessed a 60% higher weight than expected. Additional drainage holes had to be included for improved accessibility. Since powder handling was estimated to be an issue at the beginning of the project, test prints of a scaled-down version of the helmet geometry with a lattice liner were executed with Formlabs Form 2 SLA printers to circumvent it entirely. However, the geometry required the extensive use of support structures and still did not finish printing successfully. The outer shells, being large and thin, were prone to sagging and detaching. The support structures needed to reach far into the lattice structure to support the shells, which made their removal impossible without destroying the lattice. The lattice itself was not dense enough to fully support the shells during the print. Using PBF methods for producing the helmet geometry was therefore seen as the only choice for the full-scale geometry.

Software limitations were encountered at different design steps. Although nTop permits exporting 1D lattice geometries in various FE input file formats, it only does so for lattices with uniform thickness. A custom MATLAB script had to be devised to convert the nTop-native LTCX file format (based on XML), binning the beams into the desired number of separate groups, and writing them to OptiStruct's input file format. It was initially intended to extend the script to also support converting tapered beam elements, but the script was not used extensively during the course of the thesis, and the

extension was not pursued. A TCL/TK script was developed to split a beam or shell lattice geometry in HyperMesh following an arbitrarily shaped 3D function, enabling a more refined splitting approach for the helmet geometry. Since the split lattice geometry also had to be transferred to nTop again after the optimization procedure in order to apply the resulting thickness distribution and to reassemble the entire geometry for printing, another MATLAB script was developed which translates the corresponding RADIOSS input file to separate LTCX files, each containing the corresponding graph lattice. It was primarily intended for transferring the resulting lattice after a mesh morphing optimization, however it proved to be useful for the lattices obtained from thickness optimizations as well. Additionally, software restrictions limiting the capability of the Metal X system halted the project's progress for a significant time. Its closed source approach requires the use of their proprietary Eiger.io slicer software, which offered very limited print setting options at the time of the initial investigations. It supported a maximum geometry file size of 20MB which is extremely limiting considering that the crank mesh surpassed 600MB with only acceptable fidelity. Additionally, the slicer automatically and aggressively placed support structures beneath overhangs with no possibility for manual editing, rendering a successful print practically impossible. Several routes attempting to bypass this restriction were tried without success, such as using the Markforged material on an open-source Prusa i3 MK3 FDM printer. Another potential, yet unsuccessful avenue was to replace the entire support structure by ceramic release material and preventing its extrusion such that only the main structure is printed. The alternative choice was made to also explore the BASF Ultrafuse material's properties since it can be manufactured with any slicer and FDM printer, hence why it was included in the material investigation shown in section 4.2. Printing tests of a lattice structure and multiple crank prototypes produced with both materials are shown in the Addendum in section 7.5. Small sections of the crank were successfully produced with BASF Ultrafuse 316L on a Prusa i3 MK3 FDM printer but attempts of printing the entire geometry failed often. Material accumulated around the nozzle during the extrusion, causing surface defects and clumps in the lattice structure. This was mitigated by installing a wire brush at the printer's side over which the nozzle was swiped after each layer finished. However, layer delamination occurred during printing or sintering due to inhomogeneous heat distribution causing internal stresses. Some of the attempts are found in the Addendum in section 7.7.

Another software-related limitation concerned the chosen FEA solver, which became visible during the mesh morphing simulations of the PA12 Isotruss lattice mentioned in section 4.5. The results exhibited inconsistent and unrealistic buckling behaviour. While the exact cause remains unidentified, only switching to RADIOSS version 2022.3 from 2021.2, combined with a reduced compression speed, led to buckling behaviour that matched the observations during tests. Decreasing the speed in the older solver version did not produce a similar change. None of the other models exhibited a comparable dependence on movement speed and aligned well with the physical test results. Consequently, the mesh morphing studies were abandoned.

Despite the complications encountered during these projects, manufacturers are aware of the limitations and the development of lattice design software is steadily advancing. The features of nTop are continuously expanded, allowing more geometry import and export options. For example, a cooperation with EOS enabled the direct import of nTop implicit geometry files in EOS' slicer, entirely removing the need to convert the implicit body into a mesh or CAD file (Hong, n.d.). Similarly, an announced cooperation with Autodesk aims to enable the same functionality with Fusion 360 in 2024 (Ozel, 2023).

6 Summary & Outlook

This chapter summarizes the project results and proposes directions for potential future work.

6.1 Summary

The thesis provides an overview of current applications and limitations of functionally graded lattice structures (FGLS) as they are studied in scientific publications and applied in industrial contexts. FGLS have gained significant attention due to their wide range of applications and improvement potential compared to traditional appliances. However, their novelty comes with challenges, particularly in terms of design, optimization, and production methods as highlighted here.

Numerous existing studies rely on customized scripts for lattice design and optimization, but these approaches may not be suitable for engineering workflows. They require geometries compatible with Computer-Aided Design (CAD), Finite Element Analysis (FEA) software, and manufacturing needs. Therefore, this thesis focuses on developing and demonstrating a workflow tailored for engineering purposes. Two appliances are fitted with lattice structures in order to test the practicality and limits of the process. The development of a versatile lattice optimization method capable of addressing diverse objectives is subsequently presented. The approach enables the use of nonlinear FE analyses, ensuring a robust simulative evaluation of lattice structures. The thesis also provides investigations on material properties, exploring suitable additive manufacturing techniques and material options.

A steel bicycle crank arm geometry incorporating a lattice structure was designed as an initial trial of the developed optimization method. The first investigation focused on testing the performance of several different graph lattice types in the crank arm, two of which were chosen for the thickness optimization process (Decker et al., 2020). The load scenario follows the ISO 4210 standard. After manual splitting of the lattice into discrete regions with symmetry constraints, their thickness was altered such that the crank's displacement was minimized while considering a mass limit in conjunction with a stress limit based on estimations extracted from the material's data sheets. The study was limited to simulative modelling, as the manufacturing system (Markforged Metal X) was not yet operational. The primary investigation is carried out with a simplified, second order beam element representation of the graph lattice to simplify the analysis procedures. It is followed up with a validation simulation of the optimized lattice structure consisting entirely of second order tetrahedral elements, which confirms the results gained from the approach using 1D elements. While the optimization study does not achieve a significant stiffness increase of the crank arm, the lattice's material is redistributed to its outer sections, improving its stress distribution.

The subsequent two studies investigated the properties of materials produced with manufacturing methods that are potentially suitable for lattice structures. The first material study concentrates on examining the properties of Markforged 17-4 PH and BASF 316L produced with metal FDM. They are compared with two 316L SLM steel variants from EOS and Renishaw (Kedziora et al., 2022). The materials' roughness, hardness, tensile properties, fatigue strength and Charpy impact strength was reported along with microscopy imagery of selected test samples. All the samples are tested in their worst-case loading scenario, where their potential anisotropy resulting from the production method is most relevant. The findings show that metal FDM samples are significantly weaker and show vastly increased deviations compared to their counterparts produced with SLM or Metal Injection Moulding

in every test. The strength decrease is especially noticeable during the fatigue and Charpy impact tests. The microscopy imagery of the metal FDM samples show incomplete layer bonding and voids, which negatively impact the material's strength strongly. Conversely, the SLM test samples show full density, near-zero porosity, and consistent test results. The study is the first to present such an extensive investigation of Markforged and BASF steel produced with metal FDM, highlighting the issues stemming from the production method.

The second material property investigation concentrates on common additive manufacturing methods for polymers (Decker et al., 2023). The goal is to establish knowledge about the materials' behaviour for subsequent studies. Formlabs standard resin and Tough 2000 engineering grade resin material produced with SLA as well as two polyamide 12 variants produced with SLS (Sinterit) and MJF (HP) are examined and compared. Similar to the previous material investigation, the samples are all produced and loaded in their weakest orientation to emulate the worst-case scenario. The study is composed of tensile testing, fatigue testing of Formlabs Tough 2000 and HP PA12 materials, and Charpy impact testing. From these samples, the materials' secant modulus and density are derived. Additionally, Poisson's ratio of the resin test samples is determined via Digital Image Correlation (DIC). The study is the first to report the density, fatigue behaviour, and Poisson's ratio of Formlabs resin materials, filling current research gaps.

Based on the knowledge gained from the material investigations, the steel crank arm model was reanalysed with a more refined approach (Kedziora et al., 2023). It now incorporates a Gyroid lattice structure modelled with 2D shell elements, and a scripted lattice splitting method is used for creating conformal regions following the expected stress distribution. The design process respected the material's limitations and production restrictions more closely, considering its actual fatigue strength and minimum producible feature size determined from testing. More refined design approaches are employed such as Design Exploration and Multi-Objective Optimization methods. With the optimized Gyroid lattice, the crank geometry achieved the highest stiffness-to-weight ratio of the investigated crank geometries. With a much smoother stress distribution in the lattice, it also respected the maximum allowable stress constraint. A prototype was produced successfully as a proof of concept.

The thesis' publications are continued by studying the application of the optimization method to two cubic lattice structures subjected to large compression. (Decker & Kedziora, 2023a). A Simple Cubic lattice as well as an Isotruss lattice produced with PA12 using MJF were examined. They are optimized for maximum specific energy absorption, and a mass limit equal to the uniform lattice's mass was imposed. Their thickness distributions are constrained to follow three different mathematical functions to explore their performance: a linear, quadratic, and power law distribution, respectively. Linking the lattice's thickness in such a manner reduces the computational effort greatly as only the function's variables need to be altered instead of each of the separate lattice regions' thickness value. Previous investigations reported in literature primarily focused on examining fixed, manually defined thickness changes of lattice structures in compressive load cases, often following linear patterns due to their simplicity of implementation. The current study therefore expands on these publications by exploring their optimal thickness distribution following different approaches. The results are validated by physical testing, correlating the simulative behaviour with its physical counterparts. The findings show that the improvement potential of energy absorption at identical weight can be significant, but it is not identical for different lattice types. The Simple Cubic lattice is found to achieve approximately

29% higher specific energy absorption after its optimization with the linear and quadratic thickness distribution approach, however the highest increase seen with the Isotruss lattice amounts to 5% after optimization when the quadratic thickness distribution is applied. The study also points out issues that arise when simulating and correlating lattice models exhibiting. In addition, geometrical deviations of thin features occurring at the manufacturing method's limits were noted.

The knowledge gained throughout the course of the projects was applied to a final project: a realistic bicycle helmet geometry including a conformal, optimized lattice structure. Few related scientific publications studying helmets incorporating lattice liners exist, providing investigations with limited scope. They examined a low amount of lattice types and commonly use simplified helmet geometries or only sections of it. Moreover, they do not consider optimizations of the utilized lattice structures. The presented study expands upon these publications by investigating a larger number of graph lattice types implemented in a complete and realistic helmet, and by optimizing one of them. The helmet was designed to be manufactured in a single part on a HP MJF printer using PA12. It was tested following the EN 1078 standard on a test stand designed and built for this purpose during this project. The lattice was split such that the discrete regions closely follow the helmet's shape. The regions' thickness values were linked via a quadratic function, reducing the amount of optimization variables. Its performance was evaluated based on the wearer's injury risk during a standardized impact test, and the resulting helmet geometry was physically tested. First, fourteen graph lattice types with uniform thickness are implemented in the helmet geometry and evaluated via FE modelling. The worst-performing lattice type was subjected to the optimization routine to improve its performance, a choice made to avoid the manufacturing method's feature size limitations. It was physically tested to compare the findings with the simulation models. While an improvement over conventional helmets was not yet achieved due to material modelling shortcomings, the lattice helmet's performance matched the best-performing foam helmet model and passed the standard's requirements. Refined material testing would enable pursuing further improvements of the investigated lattice structure.

6.2 Outlook

This research serves as a starting point for additional evaluations and applications of the optimization methodology. The presented projects can be further refined, primarily by additional physical testing and by exploring other manufacturing options. Printing the crank arm with a PBF method would raise the level of attainable part quality and material properties compared to the Metal X system. The simulations and tests of the helmet model should be repeated after obtaining accurate material data covering the tensile behaviour at high strain rates. Moreover, changing the applied manufacturing method to a locally available alternative would greatly facilitate the material and part investigations. The influence of printing parameters on part accuracy and accurately producible lattice sizes could then be studied adequately.

The thesis' scope can be extended by including an automated optimization approach making use of nTop's command line interface, allowing for more extended control over the latticing strategy. It would enable control over advanced features such as refined cell size control in local regions of stochastic lattices. Investigations involving different physical aspects, such as the optimization of heat transport and fluid dynamics of a heat sink, would constitute suitable studies for additional demonstration purposes.

7 Addendum

7.1 MATLAB Conversion Code from LTCX to OptiStruct Input File

```

clear all
clc
tic

%ONLY LINEAR ELEMENTS
%DO NOT REMOVE SPACES IN PRINTED OUTPUT
%WRITE ORDER DOES NOT MATTER
%IMPORT IN HM: CREATE COMPS BY HM COMMENTS

property_name="prop";
beam_section_name="beamsec";
component_name="comp";
file_to_read='testlattice.ltcx';

converted_file=append(extractBefore(file_to_read,')','_from_matlab.fem');
struct_raw_data=xml2struct(file_to_read);
number_of_node_lines=numel(struct_raw_data(2).Children(2).Children);
number_of_nodes=(number_of_node_lines-1)/2;
G0=number_of_nodes+1;
fprintf('Number of nodes = %d\n',number_of_nodes);
beam_line_number=numel(struct_raw_data(2).Children(4).Children);
number_of_beams=(beam_line_number-1)/2;
fprintf('Number of beams = %d\n',number_of_beams);

%HANDLE NODE DATA
node_input_values=zeros(number_of_nodes,5);
for i=2:2:number_of_node_lines
    struct_input_nodes=struct2cell(struct_raw_data(2).Children(2).Children(i).Attributes);
    sq=squeeze(struct_input_nodes);
    temp_values=sq(2,:);
    node_input_values(i/2,:)=str2double(temp_values);
end

%SPLIT STUFF
node_radius=node_input_values(:,2);
node_coords=node_input_values; node_coords(:,2)=[]; %split into radius vector and node ids+coordinates
node_coords(:,1)=node_coords(:,1)+1;

%HANDLE RADIUS DATA
keep=1;
radii_available=unique(node_radius);
radii_chosen=radii_available(1:keep:end); %ELIMINATE THICKNESS VALUES AS NEEDED, ADD SORTING OF MISSING
THICKNESSES
% radii_chosen=round(radii_chosen,2);
number_of_chosen_radii=length(radii_chosen);
fprintf('Number of chosen radii = %d\n',number_of_chosen_radii);
fprintf('Radii chosen = %f\n',radii_chosen);
fprintf('Radii available = %f\n',radii_available);

%HANDLE BEAM ELEMENTS
beam_input_values=zeros(number_of_beams,3);
for j=2:2:beam_line_number
    struct_input_beams=struct2cell(struct_raw_data(2).Children(4).Children(j).Attributes);
    sq=squeeze(struct_input_beams);
    temp_values=sq(2,:);
    beam_input_values(j/2,:)=str2double(temp_values);
end
beam_input_values=beam_input_values+1;

%CREATE INPUT FILE
fileID=fopen(converted_file,'w');
fprintf(fileID,'$$CONVERTED FROM NTOP BEAM FILE TO OPTISTRUCT INPUT FILE\n\n');
fprintf(fileID,'BEGIN BULK\n');

%WRITE BEAM SECTION COLLECTOR

```

7. Addendum

```
fprintf(fileID, '\n$HMNAME BEAMSECTCOLS      1"%s_col"\n', beam_section_name);

%WRITE BEAMSECTIONS
for k=1:number_of_chosen_radii
    fprintf(fileID, '$HMNAME BEAMSECTS\n');
    fprintf(fileID, '$   %s      1"%s%d"\n', pad(num2str(k),8,'left'), beam_section_name, k);
    fprintf(fileID, '$       2   7   1   0   1.0   1.0   0.0   0.0   0.0\n');
    fprintf(fileID, '$       0.0   1\n');
    fprintf(fileID, '$HMNAME BEAMSECTS BEAMSECTIONSTANDARD   11   1   0Rod\n');
    fprintf(fileID, '$HMNAME BEAMSECTS BEAMSECTIONSTANDARD PARAMETERS ');
    fprintf(fileID, '%s%s   10.0   \n', pad(num2str(radii_chosen(k)),8,'left'), pad(num2str(radii_chosen(1)),8,'left'));
    fprintf(fileID, '$HMNAME BEAMSECTS END\n');
end

%CREATE COMPONENTS
for p=1:number_of_chosen_radii
    fprintf(fileID, '$HMNAME COMP                                %s"%s%d"   %s   "%s%d"   3
\n', pad(num2str(p),8,'left'), component_name, p, pad(num2str(p),8,'left'), beam_section_name, p);
    fprintf(fileID, '$HWCOLOR COMP                                %s%s\n', pad(num2str(p),8,'left'), pad(num2str(p),8,'left'));
end

%WRITE PROPERTIES
%PBEAM PID MID A(A) I1(A) I2(A) I12(A) J(A) NSM(A)
% C1(A) C2(A) D1(A) D2(A) E1(A) E2(A) F1(A) F2(A)
fprintf(fileID, '\n\n$$ PBEAM DATA\n\n$');
for o=1:number_of_chosen_radii
    A(o)=pi*radii_chosen(o)^2; J(o)=0.5*pi*radii_chosen(o)^4;
    I1(o)=0.25*pi*radii_chosen(o)^4; I2=I1;
    o_string=pad(num2str(o),8,'left');
    fprintf(fileID, '$HMNAME PROP                                %s"%s%d" 3\n', o_string, property_name, o);
    fprintf(fileID, '$HWCOLOR PROP                                %s%s\n', o_string, o_string);
    fprintf(fileID, '$HMBEAMSEC PBEAMASSOC %s%s\n', o_string, o_string);
    fprintf(fileID, 'PBEAM,%d,1,%f,%f,%f,0.0,%f,\n', o, A(o), I1(o), I2(o), J(o));
    fprintf(fileID, '+,\n+,\n+,,,,,0.0,0.0,0.0,0.0,\n\n$');
end

%CREATE MATERIAL
% MAT1 MID E G NU RHO A TREF GE
% ST SC SS
fprintf(fileID, '$$ MAT1 DATA\n');
fprintf(fileID, '$HMNAME MAT 1, "material1", 1\n$HWCOLOR MAT 1, 1,\n');
fprintf(fileID, 'MAT1, 1, 210000., 0.3, 7.85E-9\n\n');

%WRITE GRID DATA
% GRID ID CP X1 X2 X3 CD PS
fprintf(fileID, '$$\n$$ GRID DATA\n\n$');
fprintf(fileID, 'GRID,%d,%,%,%,%,\n', node_coords);
fprintf(fileID, 'GRID, %d,.,0.1,0.1,0.1,\n', G0);
fprintf(fileID, '\n\n$');

%ASSIGN COLLECTOR IDS FOR BEAM ELEMENTS
for k=1:number_of_beams
    temp_node_id_A(k,1)=beam_input_values(k,2); %get NID1 for element end A
    temp_node_id_B(k,1)=beam_input_values(k,3); %get NID2 for element end B
    radius_A(k,1)=node_radius(temp_node_id_A(k));
    radius_B(k,1)=node_radius(temp_node_id_B(k));
    [min_value_A, min_index_A]=min(abs(radii_available-radius_A(k)));
    [min_value_B, min_index_B]=min(abs(radii_available-radius_B(k)));
    col_id_A(k,1)=min_index_A;
    col_id_B(k,1)=min_index_B;
end

beams=[beam_input_values(:,1), col_id_A, beam_input_values(:,2), beam_input_values(:,3), ones([number_of_beams,1])*G0];

%WRITE CBEAM ELEMENTS
% CBEAM EID PID GA GB X1/G0 X2 X3 OFFT
% PA PB W1A W2A W3A W1B W2B W3B
fprintf(fileID, '$$\n$$ CBEAM ELEMENTS\n\n$');
```

7. Addendum

```
fprintf(fileID,'CBEAM,%d,%d,%d,%d,%d,,,\n',beams');
fprintf(fileID,'\n');

%HMMOVE
for component_id=1:number_of_chosen_radii

    for y=1:number_of_beams
        if beams(y,2)==component_id
            element_ids_in_component(y,component_id)=beams(y,1);
        end
    end
    interm=nonzeros(element_ids_in_component(:,component_id));
    number_of_els_in_comp(component_id)=length(interm);
    fprintf('Number of elements in component %d = %d\n',component_id,number_of_els_in_comp(component_id));
    fprintf(fileID,'\n$HMMOVE %s\n',pad(num2str(component_id),8,'left'));
    fprintf(fileID,$ %s%s%s%s%s%s%s%s\n',pad(string(interm),8,'left'));
end

%CHECK
fprintf('Total number of moved elements = %d\nDifference to total number of elements =
%d\n',sum(number_of_els_in_comp),number_of_beams-sum(number_of_els_in_comp));

%END
fprintf(fileID,'\n\nENDDATA');
fclose('all');
toc
```

7.2 MATLAB Conversion Code from RADIOSS Input File to LTCX

```

%%%%%%%%% Convert .RAD to .LTCX %%%%%%%%%%
%%%%%%%%% Author: Thierry Decker %%%%%%%%%%
%%%%%%%%% %%%%%%%%%%

%%
clc
clear all

inFile = 'bcc_helmet_0000.rad';
fid = fopen(inFile);
time=[];
inNode = false;
inBeam = false;
line = "";
comp=[];
linecounter = 0;

%%%%%%%%%
%% File reading section following below provided by user bog in ComputerBase forum
%% https://www.computerbase.de/forum/threads/matlab-gemischte-textdatei-lesen-und-umformatieren.2039920/
%%%%%%%%%

tic
%Finding /BEAMS and /NODES
while ischar(line)
    line = fgetl(fid);
    linecounter = linecounter+1;
    if length(line) <= 1 || line(1) == '#' % skipping comments, empty lines
        continue;

    elseif line(1) == '/' % handle node/beam starts
        inNode = startsWith(line, '/NODE');
        inBeam = startsWith(line, '/BEAM/');

        if inBeam
            comptemp = str2double(line(7:end));
        end

        continue;

    end

    if inNode || inBeam % node/beam active? extract numbers
        if inNode
            val = [str2double(strtrim(line(1:10)))];
            for i = 11:20:length(line)
                substr = line(i : i + 20 - 1);
                val = [val, str2double(strtrim(substr))];
            end

            if exist('nodesTable', 'var') == 0
                nodesTable = val;
            else
                nodesTable = [nodesTable; val];
            end
        elseif inBeam
            comp = [comp; comptemp];
            val = [];
            for i = 1:10:length(line)
                substr = line(i : i + 10 - 1);
                val = [val, str2double(strtrim(substr))];
            end
            if exist('beamsTable', 'var') == 0
                beamsTable = val;
            else
                beamsTable = [beamsTable; val];
            end
        end
    end
end
end
end
end

```

7. Addendum

```
fclose(fid);
time=[time,toc];

%% Sort beams per comp, get unique nodes
tic
beamsTable(:,4) = comp;
uniqueComps = unique(comp);
uniqueNodes = unique(beamsTable(:,2:3));
nodesToWrite = zeros(length(uniqueNodes),4);

for j = 1:length(uniqueNodes)
    index = find(nodesTable(:,1) == uniqueNodes(j));
    nodesToWrite(j,:) = nodesTable(index,:);
end
beamsTable = sortrows(beamsTable,[4,1]);
time=[time,toc];

%% Reassembling per comp
for m = 1:length(uniqueComps)
    beamsInComp = zeros(length(beamsTable),3);

    tic
    for n = 1:length(beamsTable)
        if beamsTable(n,4) == uniqueComps(m)
            beamsInComp(n,:) = beamsTable(n,1:3);
        end
    end

    nodesInComp = nonzeros(unique(beamsInComp(:,2:3)));
    beamsInComp = beamsInComp(any(beamsInComp,2),:);
    fprintf('Nodes in comp %d: %d\nBeams in comp %d: %d\n', uniqueComps(m), length(nodesInComp), uniqueComps(m),
length(beamsInComp))
    time=[time,toc];

    %%add node coordinates to nodesInComp(2:4)
    tic
    for k = 1:length(nodesInComp)
        index = find(nodesTable(:,1) == nodesInComp(k));
        nodesInComp(k,2:4) = nodesTable(index,2:4);
    end
    time=[time,toc];

    %%Renumbering nodes starting from 1 per comp
    tic
    nodesRenumbered = [(0:length(nodesInComp)-1)', nodesInComp(:,2:4)];
    beamsRenumbered = (0:length(beamsInComp)-1)';

    node1 = zeros(length(beamsRenumbered),1);
    node2 = node1;

    for o = 1:length(beamsRenumbered)
        node1(o) = find(nodesInComp(:,1) == beamsInComp(o,2));
        node2(o) = find(nodesInComp(:,1) == beamsInComp(o,3));
    end

    beamsRenumbered = [beamsRenumbered, node1-1, node2-1];
    time=[time,toc];

    %% Writing
    tic
    fileName = strcat('comp',num2str(uniqueComps(m)),'.Itcx');
    fileID = fopen(fileName,'w');
    fprintf(fileID,'<?xml version="1.0" encoding="UTF-8"?>\n<!--comment-->\n<graph id="0" name="" units="mm" type="rmd">\n
<nodegroup>\n');
    fprintf(fileID,'    <node id="%d" x="%6.14f" y="%6.14f" z="%6.14f"/>\n',nodesRenumbered);
    fprintf(fileID,' </nodegroup>\n <beamgroup>\n');
    fprintf(fileID,'    <beam id="%d" n1="%d" n2="%d"/>\n',beamsRenumbered);
    fprintf(fileID,' </beamgroup>\n</graph>');
    fclose(fileID);
    time=[time,toc];
end
%%
disp(sum(time))
```

7.3 Beam Lattice Splitting Script in TCL/TK

```
#####
# File   : Variable distribution of diameters of beam elements
# Date   : April 30, 2022
# Created by: Slawomir Kedziora
# mail   :slawomir.kedziora@uni.lu
#####
# File   : Variable distribution of diameters of beam elements
# Date   : April 26, 2022
# Created by: Slawomir Kedziora
# mail   : slawomir.kedziora@uni.lu
# Purpose : Variable diameters distribution for beam elements with a given
#         : number of diameters. The procedure works for Radioss solver.
#####
if { [ namespace exists ::BeamByEquation ] } {
    namespace delete ::BeamByEquation
}
namespace eval ::BeamByEquation {
    # Global variables
    # A number of bins of beam elements.
    variable g_steps 12
    # An equation of beam diameters, it must be abs(). It is valid only in a global coordinate system.
    variable g_equation 0.005*(z*z+y*y+x*x+0.0001)*0.5
    # A name of lattice components
    variable g_compName "lattice"
    # A name of lattice properties
    variable g_propName "prop_lattice"
    # A name of material assigned for the lattice components.
    variable g_matName "PA_tab"
}
#
#####
# Procedure(Main)
#####
proc ::BeamByEquation::Main { } {
    # Purpose: To define a variable diameter of beam elements based
    # on a defined equation in a global coordinate system of a model.
    # The beam elements are grouped in (g_step) components with the name of "lattice_*". Each of the components has
    # defined properties "prop_lattice_*)" and material "PA_tab)".
    # Args: None
    # Returns: None
    # Notes:
    #
    variable g_equation
    set equation $g_equation
    variable g_steps
    set n_steps $g_steps
    variable g_compName
    set compName $g_compName
    variable g_propName
    set propName $g_propName
    variable g_matName
    set matName $g_matName
    #
    # Selection of beam elements of the lattice; they must be a type - bar2 and
    # must be in the component "lattice".
    #
    *createmark elems 1 "by config" bar2
    *createmark elems 2 "by collector" $compName
    *markintersection elems 1 elems 2
    *createmark nodes 1
    set elements [hm_getmark elems 1]
    *clearmark elems 1
    *clearmark elems 2
    #
    set propDiams {}
    #
    foreach elem $elements {
        set location {}
        set node1 [ hm_getentityvalue elements $elem node1.id 0]
        set node2 [ hm_getentityvalue elements $elem node2.id 0]
        # Calculation of a center of gravity of the each selected element.
        set x1 [hm_getentityvalue nodes $node1 "x" 0]
        set y1 [hm_getentityvalue nodes $node1 "y" 0]
    }
}

```

7. Addendum

```
set z1 [hm_getentityvalue nodes $node1 "z" 0]
set x2 [hm_getentityvalue nodes $node2 "x" 0]
set y2 [hm_getentityvalue nodes $node2 "y" 0]
set z2 [hm_getentityvalue nodes $node2 "z" 0]
set x0 [ expr {($x1+$x2)/2.0} ]
set y0 [ expr {($y1+$y2)/2.0} ]
set z0 [ expr {($z1+$z2)/2.0} ]
lappend location $x0
lappend location $y0
lappend location $z0
# Calculation of a diameter for each element using the given equation.
set diam [ expr { 2.0*[ variable_radii $g_equation $location ] } ]
set location {}
lappend propDiams $diam
}
#
# Sorting the elements in bins( containers).
#
set results [ bins $propDiams $n_steps ]
#
# Results organization
set propIndexs [ lindex $results 0 ]
set meanDiams [ lindex $results 1 ]
#
# Preparation of a list with new beam element properties.
# An array to contains results - the array of lists; the index of the array is a bin number,
# and the array element is list of the elements with the defined diameter.
# The elements are save in elemBins(i), where i is the bin number counting from 0 <= i < n_steps.
#
set elemBins() {}
#
for { set i 0 } { $i < $n_steps } { incr i } {
    set id_prop [lsearch -all $propIndexs $i]
    foreach id_prop $id_prop {
        lappend elemBins($i) [ list [lindex $elements $id_prop ] ]
    }
}
#
# Creating properties of and components for the defined beam bins (containers).
#
set matsId [hm_getvalue mats name=$matName dataname=id ]
#
for { set i 0 } { $i < $n_steps } { incr i } {
    set newIdProp [ expr { [ hm_latestentityid props ] + 1 } ]
    set newIdComp [ expr { [ hm_latestentityid comps ] + 1 } ]
    set newIdMat [ expr { [ hm_latestentityid mats ] + 1 } ]
    #
    set newNameProp [hm_getincrementalname props $propName -1 0 "_"]
    set newNameComp [hm_getincrementalname comp $compName -1 0 "_"]
    #
    # Create a new properties and assign a new radius.
    *createentity props cardimage=P18_INT_BEAM includeid=0 name=$newNameProp
    *setvalue props id=$newIdProp STATUS=1 5158=2
    *setvalue props id=$newIdProp STATUS=1 5152=4
    *setvalue props id=$newIdProp STATUS=1 7250=3
    # Radius
    set radius [ expr {0.5*[ lindex $meanDiams [lsearch $propIndexs $i] ] } ]
    *setvalue props id=$newIdProp STATUS=1 4506=$radius
    *setvalue props id=$newIdProp STATUS=0 4507=0.0
    #
    *createentity comps cardimage=Part includeid=0 name=$newNameComp
    *setvalue comps id=$newIdComp STATUS=2 4358=0
    *setvalue comps id=$newIdComp propertyid={ props $newIdProp }
    *setvalue comps id=$newIdComp materialid={ mats $matsId }
    #
    #
    # Move appropriate elements to new components according to the defined bins.
    if [info exist elemBins($i)] {
        eval *createmark elems 1 [join [ list $elemBins($i) ] " "]
        set NumOfElems [llength [hm_getmark elems 1]]
        puts $NumOfElems
        *movemark elems 1 $newNameComp
        *clearmark elems 1
    }
}
}
```

7. Addendum

```
#
unset elemBins
unset g_steps
unset g_equation
unset g_compName
unset g_propName
unset g_matName
}
#####
# End (Main)
#####
#
proc ::BeamByEquation::variable_radii {equation location} {
# Purpose: To calculate a diameter based on the equation given at a location x,y,z (location)
# Args: Two lists equation string and list of x y z coordinates of the location.
# Returns: list of calculated values of the beam radius for the given location x y z.
# Notes: None
#
set sequ [string map {x $x y $y z $z} $equation]
set x [lindex $location 0]
set y [lindex $location 1]
set z [lindex $location 2]
set result [expr double($sequ)]
return $result
}
#
proc ::BeamByEquation::bins {items nSteps} {
# Purpose: Creates nSteps bins of for items (list of diameters) with a constant value per the bin.
# Args: A list of items to group with based on a constant value, nSteps - a number of the bins.
# Returns: Two lists: the urpose: Creates a nSteps bins of for items (list of diameters) with a constant value per the bin.
# Args: A list of items to group with based on a constant value, nSteps - a number of the bins.
# Returns: Two lists: the first one contains the bin index (starting with 0) and
# the second one is the list with a new constant diameter value per the bin.
# Notes: The final constant value of the items per the bin is calculated as an average
# of the bin boundary values.
# Output: Two lists:
# 0 - the list of the indexes of the bins (from 0 to the defined number of the bins).
# 1 - the list of values of the defined diameters.
#
set max_items [tcl::mathfunc::max {*}$items]
set min_items [tcl::mathfunc::min {*}$items]
set delta_items [expr {($max_items-$min_items)/double($nSteps)}]
set index {}
set values {}
set results {}
set value 0.0
#
foreach item $items {
for {set j 0} {$j < $nSteps} {incr j} {
if { $item >= [expr { ($min_items + $delta_items*($j)) } ] } {
if { $item <= [expr { $min_items + $delta_items*($j + 1) } ] } {
set value [expr {(2.0*$min_items + $delta_items*(2.0*$j + 1.0))/2.0} ]
lappend index $j
lappend values $value
break
}
}
}
set value 0.0
}
}
set results [list $index $values]
return $results
}
#####
# Execute procedure
#####
::BeamByEquation::Main
#####
```

7.4 Shell Lattice Splitting Script in TCL/TK

```
#####
# File   : Variable thickness of shell elements
# Date   : April 11, 2020
# Created by: Slawomir Kedziora
# mail    : slawomir.kedziora@uni.lu
# Purpose : Variable thickness for shell elements with a selected
#         : number of thickness.
#####

#catch { namespace delete thickByEquation }
namespace eval ::thickByEquation {
    # Global variables
    variable g_steps 8;
    # Limit of thickness value of shell elements
    variable g_equation 0.685-(x*1.0e-3)+(y*y*3.0e-3)-(x*y*y*3.331e-5)+(x*x*y*y*1.172e-7)
    # Equation defined in local or global coordinate system, it must be abs().
    variable g_localSystem 1;
    # Coordinate system default global one - 0
}
#####
# Procedure(main)
#####
proc ::thickByEquation::main { } {
    # Purpose: To define a variable thickness of shell elements
    # based on an defined equation.

    # Args: Defined above
    # Returns: None
    # Notes:

    #speed boost start
    hm_commandfilestate 0
    hm_blockerrormessages 1
    hm_blockmessages 1
    *entityhighlighting 0
    hwbrowsermanager view flush false
    variable g_equation
    set equation $g_equation
    variable g_steps
    set n_steps $g_steps
    variable g_localSystem
    set localSystem $g_localSystem
    set template_dir [hm_info -appinfo SPECIFIEDPATH TEMPLATES_DIR];

    *collectorcreateonly loadcols "temp_pressures" "" 57
    *createmark elems 1 "by config" tria3 quad4 tria6 quad8
    *createmark elems 2 "displayed"
    *markintersection elems 1 elems 2
    *createmark nodes 1
    *pressuresonentity_function elements 1 1 0 0 0 1 30 1 0 0 0 "$equation" $localSystem
    *createmark loads 1 "by colector" "temp_pressures"
    set all_loads [hm_getmark loads 1]

    set list_magnitude { }
    foreach load $all_loads {
        set magnitude [hm_getentityvalue loads $load "magnitude" 0]
        lappend list_magnitude $magnitude
    }
    set maxMagnitude [ findmax $list_magnitude ]
    set minMagnitude [ findmin $list_magnitude ]
    #
    set deltaMagnitude [expr { ($maxMagnitude-$minMagnitude)/double($n_steps) } ]
    # for each load that is created create a property with its magnitude and assign it to the elements
    foreach load $all_loads {
        set element_id [hm_getentityvalue loads $load "element.id" 0];
        set magnitude [hm_getentityvalue loads $load "magnitude" 0];
    }
}
#####
```

7. Addendum

```
for { set istep 1 } { $istep <= $n_steps } { incr istep } {
    if { $magnitudo >= [ expr { ($minMagnitudo+$deltaMagnitudo*($istep-1)) } ] } {
        if { $magnitudo <= [ expr { ($minMagnitudo+$deltaMagnitudo*$istep) } ] } {
            set magnitudo [ expr { (2.0*$minMagnitudo+$deltaMagnitudo*(2.0*$istep-1.0))/2.0 } ]
        }
    }
}

break
}

set magnitudo [ expr abs([ format "%.2f" $magnitudo ]) ];

if { [ catch { *collectorcreateonly properties "pshell_$magnitudo" "" 5 } ] } {
    *createmark elements 1 $element_id
    *propertyupdate elements 1 "pshell_$magnitudo"

    } else {
    *createmark properties 1 "pshell_$magnitudo"
    *dictionaryload properties 1 "$template_dir/feoutput/nastran/general" "PSHELL"
    *initializeattributes properties "pshell_$magnitudo"
    *createmark properties 1 "pshell_$magnitudo"
    set prop_id [hm_getmark props 1];
    *attributeupdatedouble properties $prop_id 95 1 1 0 $magnitudo
    *createmark elements 1 $element_id
    *propertyupdate elements 1 "pshell_$magnitudo"
    }
}

#speed boost end
*entityhighlighting 1
hm_commandfilestate 1
hm_blockerrormessages 0
hm_blockmessages 0
hwbrowsermanager view flush true

#cleanup pressures and property colors
*createmark props 1 "all"
*autocolorwithmark properties 1
*createmark loadcols 1 "temp_pressures"
*deletemark loadcols 1
}

proc ::thickByEquation::findmax { items } {
    # Purpose: To find a maximal element of the list (items)
    # Args: list items
    # Returns: It gives the maximal element of the list
    # Notes: None
    set max -1e8
    foreach i $items {
        if { $i > $max } {
            set max $i
        }
    }
    return $max
}

proc ::thickByEquation::findmin { items } {
    # Purpose: To find a minimal element of the list (items)
    # Args: list items
    # Returns: It gives the minimal element of the list
    # Notes: None
    set min 1e8
    foreach i $items {
        if { $i < $min } {
            set min $i
        }
    }
    return $min
}
```

7. Addendum

```
#####  
# Execute procedure  
#####  
::thickByEquation::main  
#####
```

7.5 Supplemental Content of Investigation on Graph Lattice in Crank Geometry

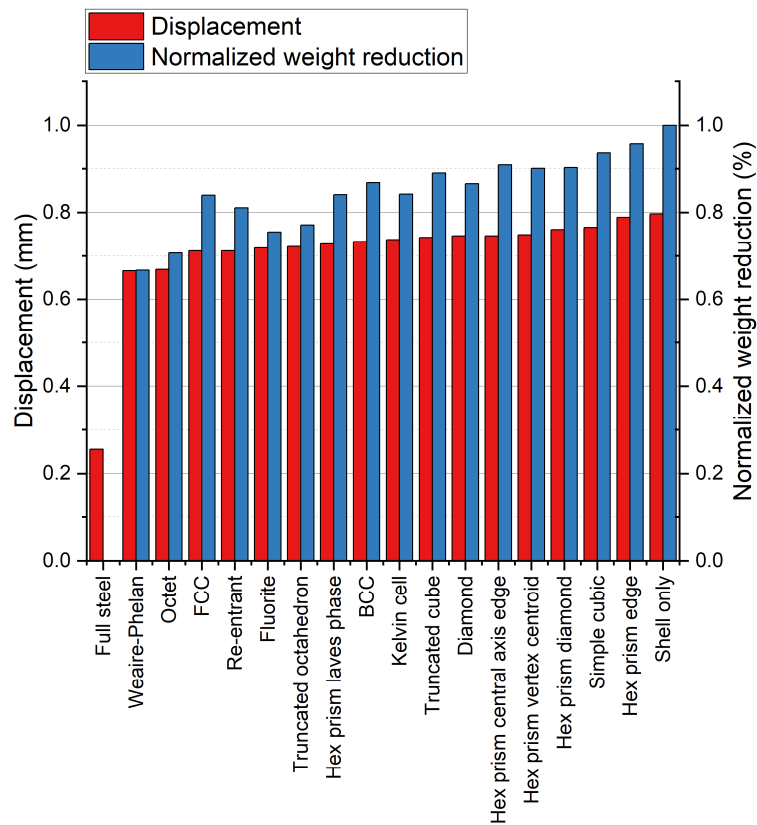


Figure 7.1: Overview of all tested unit cell types used in the preliminary crank tests

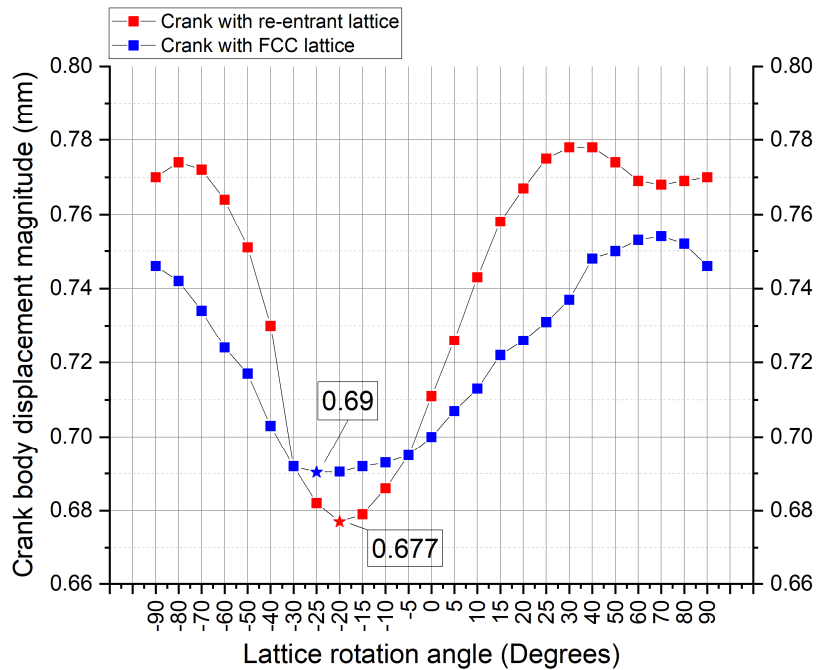


Figure 7.2: Influence of lattice rotation on crank displacement for both chosen types

7. Addendum

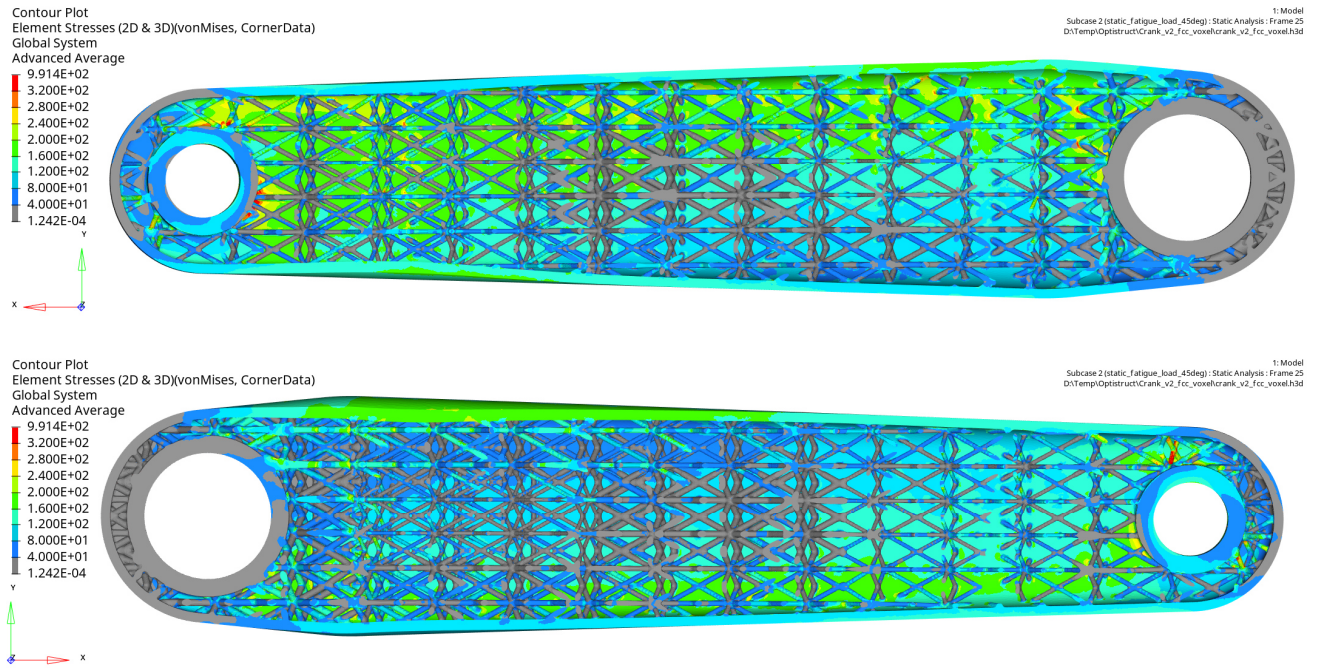


Figure 7.3: Cross-section of von Mises stresses in validation model of crank with optimized FCC lattice

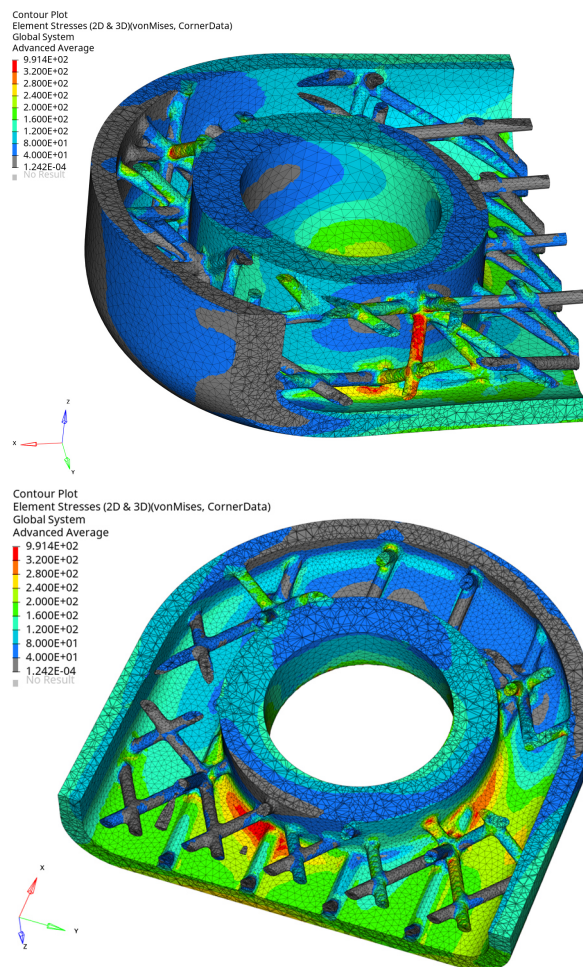


Figure 7.4: Details of von Mises stress concentrations in validation model of crank with optimized FCC lattice

7. Addendum

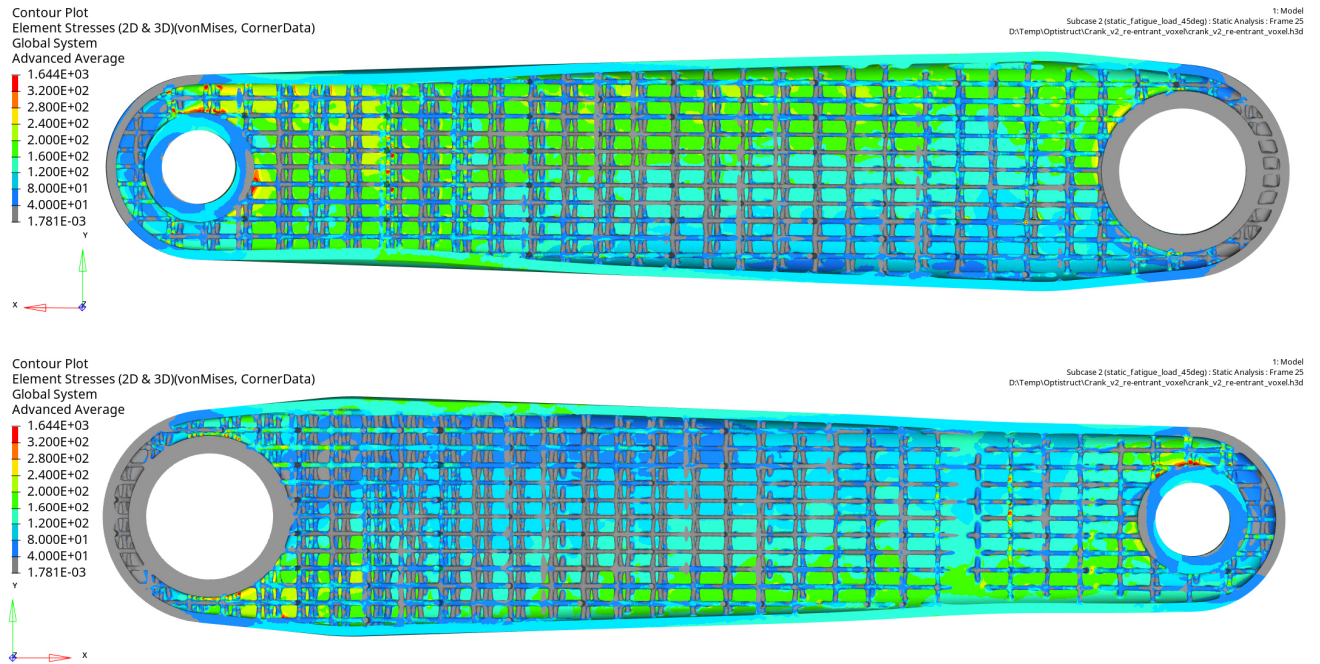


Figure 7.5: Cross-section of von Mises stresses in validation model of crank with optimized Re-entrant lattice

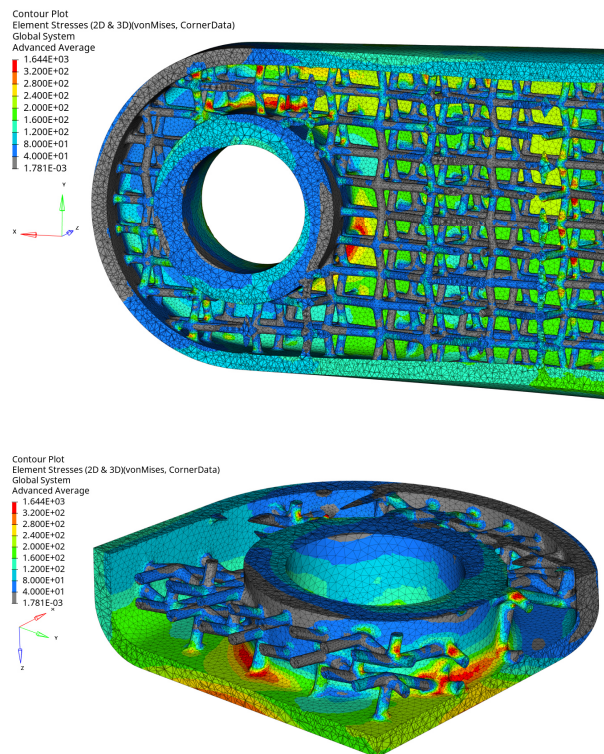


Figure 7.6: Details of von Mises stress concentrations in validation model of crank with optimized Re-entrant lattice

7.6 Markforged Metal X System

Markforged aims to provide a metal additive manufacturing ecosystem that's easier in handling and significantly cheaper than many of the powder bed fusion (PBF) based systems on the market. Where industrial selective laser melting (SLM) machines usually start at 500.000\$ and need a substantial amount of specific knowledge, time and security measures for powder handling and manufacturing, the Metal X system attempts to reduce this complexity as much as possible. The metal material is contained within a polymer binding material provided in the form of filament spools, similarly to polymer FDM printing methods. An additional filament spool containing a ceramic release material is required for printing. The ceramic acts as a separation layer between support structures and the actual parts. Prints are prepared for printing via Eiger.io, their proprietary pre-processor software, where most of the settings like upscaling to account for shrinkage, printing speed and temperatures etc. are fixed. It's a choice Markforged made to reduce any user input needed to improve success rates and quick turnover in an industrial setting. Filament rolls are exclusively offered by Markforged with options like 17-4 precipitation hardened stainless steel, Inconel 625, H13, A2 and D2 tool steel, and copper. After a successful print, the so-called "green" part passes through a debinding step by immersing it in refrigerated Opteon SF79, an industrial liquid solvent, for a minimum of 12 hours to remove most of the wax holding the metal particles. Subsequently, the part is in the "brown" state and ready to be sintered. The support structures and base raft can be removed relatively easily after sintering due to the ceramic release layer separating them from the part. A few taps with a hammer are needed to detach them. Finally, the part can be postprocessed like any other metal part. The system installed at the University of Luxembourg is depicted in Figure 7.7



Figure 7.7: Markforged Metal X system installed at the University of Luxembourg with its sintering oven (left), washing station for chemical binder removal (middle) and the printer (right). Picture kindly provided by Rabie Hayder.

As previously mentioned, several avenues were tested to circumvent the system's limitations. One such method was to circumvent the mandatory support placement restraint. Custom ceramic layers were added to the part, entirely replacing the original support structure. Subsequently, a few modifications need to be made to the printer. The ceramic release filament is to be removed while leaving a piece of it inside of the print head such that it activates the light barrier above the extruder, but is not gripped by the extruder gears. Lastly, the material jam detection feature has to be deactivated in the printer settings. With all of this done, the Metal X printer still travels along the original support structure being under the assumption that it's extruding ceramic material.

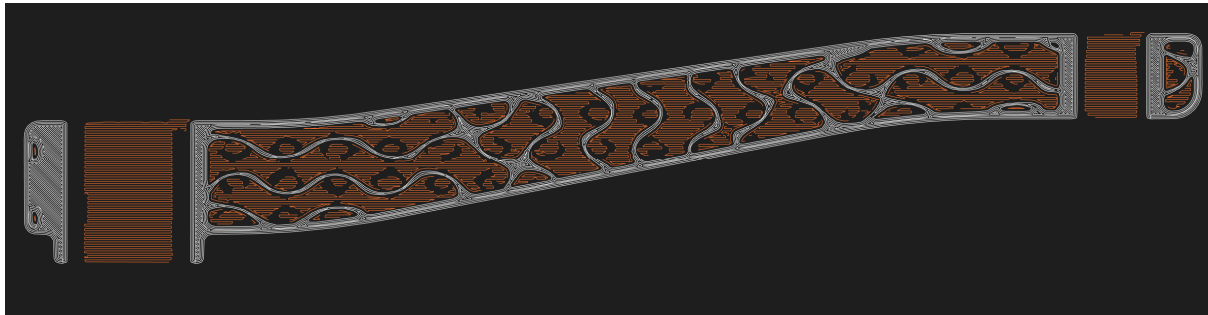


Figure 7.8: Example of custom inserted ceramic release layer (orange), replacing the support structure in the crank model with gyroid lattice (white)

Figure 7.9 shows a test piece intended to be printed on the Metal X machine using 17-4 PH SS filament and the previously explained method. This piece would pose a challenge even for a standard plastic FDM printer. Although the external dimensions only measure 50mm x 50mm x 20mm, Eiger.io estimated approximately four days of total printing time for this piece. An important portion of this time is spent in travel movements for the ceramic release layers, which occupy almost all of the non-metal volume inside the part's bounding box. As shown in Figure 7.10, the Metal X printer did not complete the print. The TPMS-filled quadrants could be considered partially successful, however the strut-filled quadrants failed clearly. Significant stringing and under-extrusion is present in all four of the quadrants, with the tetrahedral lattice showing the worst outcome. Since the majority of the printing time is passed "printing" the ceramic release layers (i.e. the print head is only travelling, but not extruding), the print head handling the metal filament needs to stay heated at 220°C all the time and material starts oozing out of the nozzle, leaving drops and strings of material on the part. Since Eiger.io did not allow for setting changes to vary any relevant parameters at the time of testing, improvements were only possible once the restrictions were lifted.

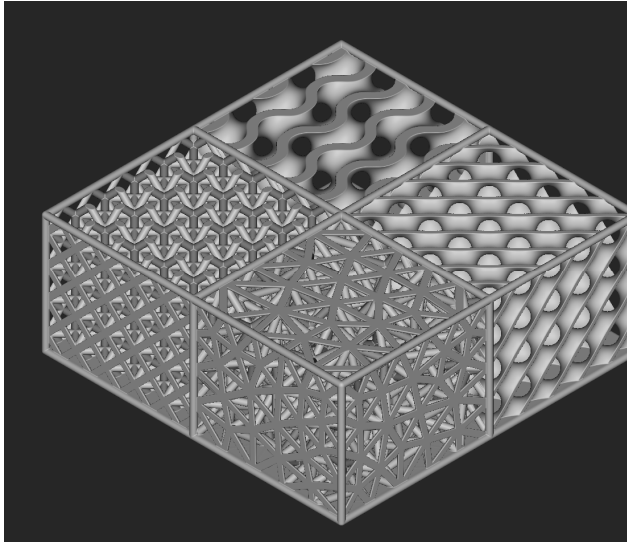


Figure 7.9: Test piece for support bypassing with Face-Centred Cubic lattice (left quadrant, 1mm thickness), Tetrahedral lattice (lower quadrant, 1mm thickness), Diamond TPMS (right quadrant, 1mm thickness) and Gyroid TPMS (upper quadrant, 2mm thickness)



Figure 7.10: Aborted print of test piece due to significant stringing and under-extrusion in the beam lattice structures

Until the limitations were bypassed, other routes such as printing the Markforged filament on an open-source FDM printer were explored. Only few special conditions need to be respected to recreate the necessary conditions for the material. Since the metal-containing filament material by Markforged is very brittle at room temperature, it easily breaks during print head travel movements when cold. The filament roll is therefore located in the upper part of the Metal X's build chamber to minimise its bending radius while the print head is travelling, and it needs to be preheated to 60°C for 30 minutes before printing. The ceramic release material filament is much more flexible and does not need a preheating phase. A build plate temperature of 60°C and nozzle temperature of 220°C are required for printing 17-4 PH SS – conditions most printers can provide. Since the University of Luxembourg possesses multiple Prusa i3 MK3s printers as well as a heated chamber for one of them, testing it seemed straightforward. Unfortunately, the conditions were not ideal, as the height of the heated chamber was insufficient to place the filament spool at a sufficient height above the printer. Additionally, the chamber's heating element was faulty at the time of testing and could not reach a sufficient temperature level to replicate adequate conditions. Nonetheless, the process generally worked and is considered feasible. A hardened steel nozzle with 0.4mm orifice diameter, low printing speed of 15-20 mm/s and no part cooling were chosen to stay close to the original settings used on the Metal X printer. Figure 7.11 shows the first few layers of a calibration test cube with 24mm edge length (upscaled from 20mm edge length to account for shrinkage during sintering). It was interrupted due to constant filament breakage at the spool and material leaking out of the nozzle thread due to a faulty nozzle installation.

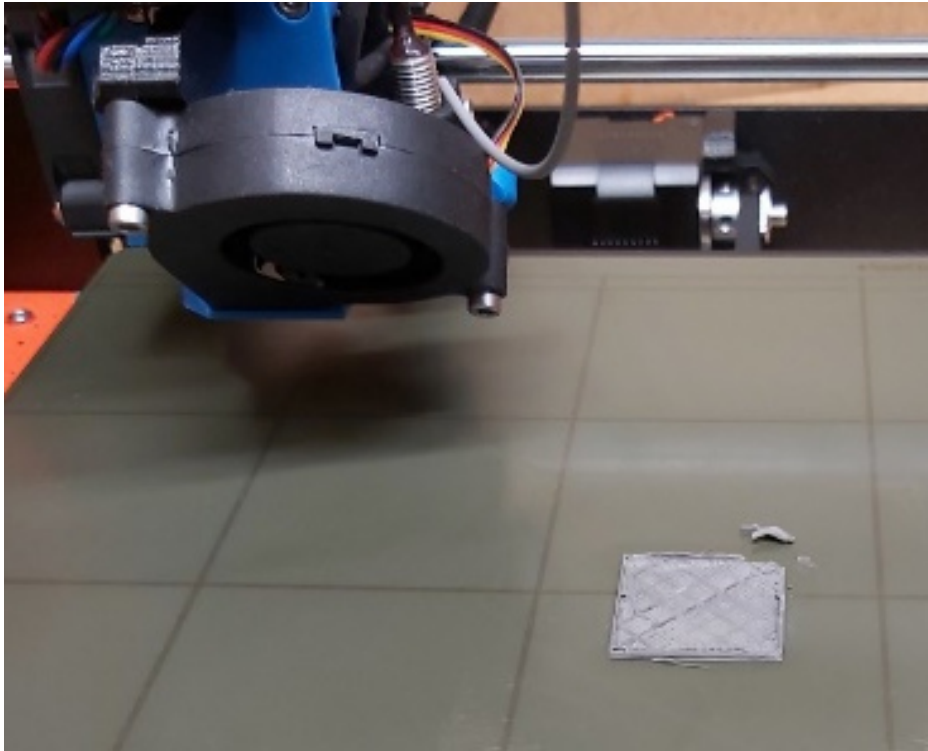


Figure 7.11: First few layers of Markforged 17-4 PH SS metal filament on a Prusa i3 Mk3s printer

7.7 Printing Tests of Crank with Lattice Geometry

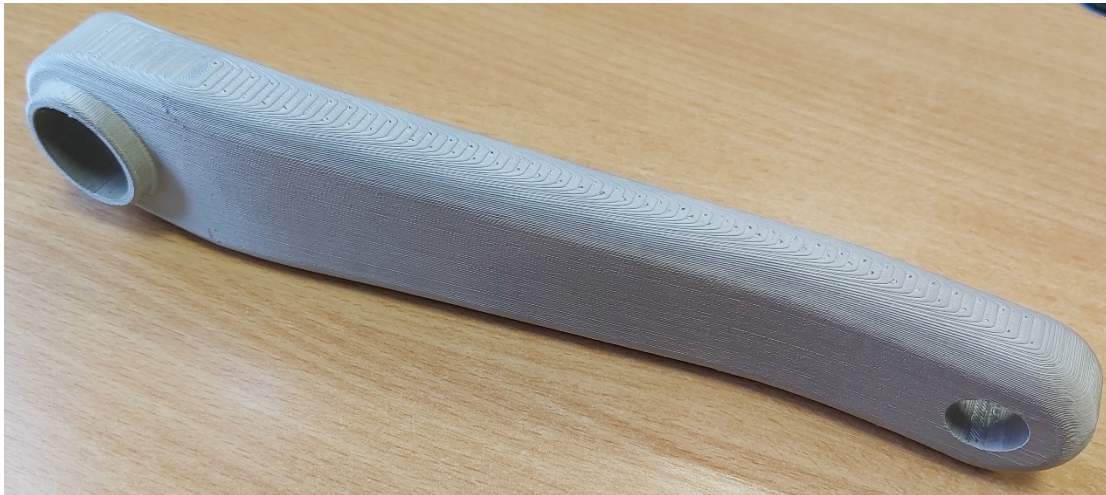


Figure 7.12: Prototype manufactured with the Markforged Metal X system, 17-4 PH SS and regular, triangular infill.

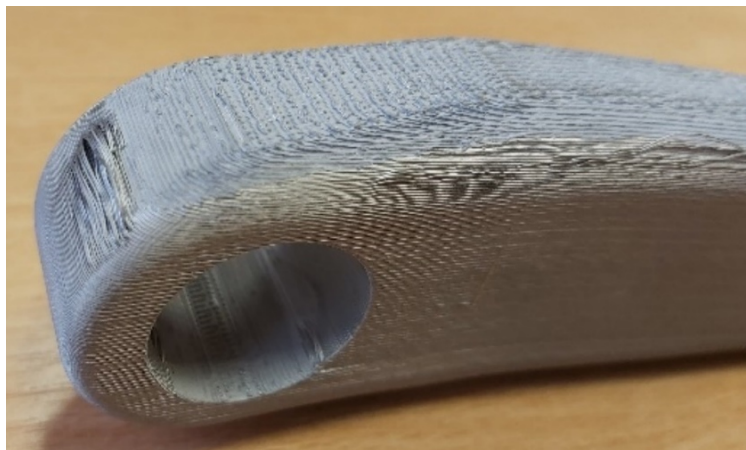


Figure 7.13: Drooping extrusion lines on the underside of the crank manufactured on the Metal X system

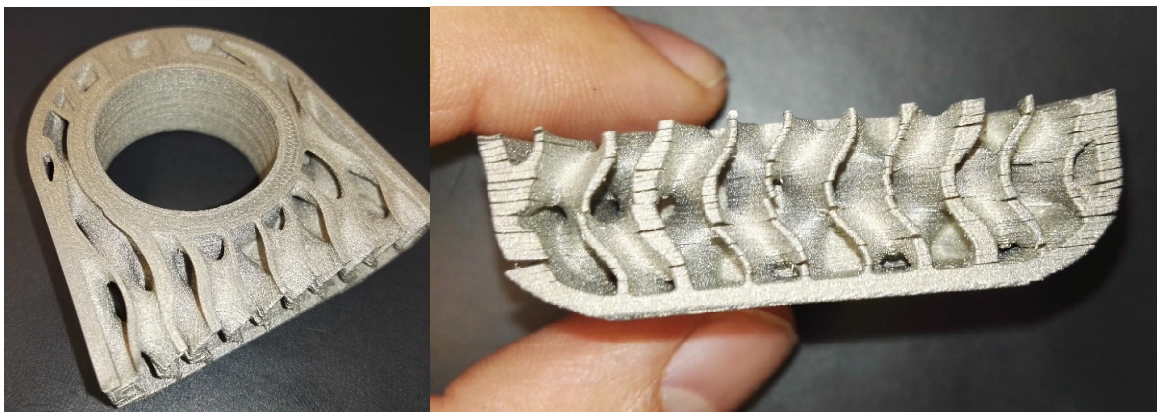


Figure 7.14: Section of crank model with functionally graded TPMS lattice printed with BASF Ultrafuse 316L (Part and image courtesy of Hochschule Trier)



Figure 7.15: Test print of BASF Ultrafuse 17-4 PH SS with cracks occurring during printing



Figure 7.16: Crack happening during printing (left), fracture during removal of support structure (right)

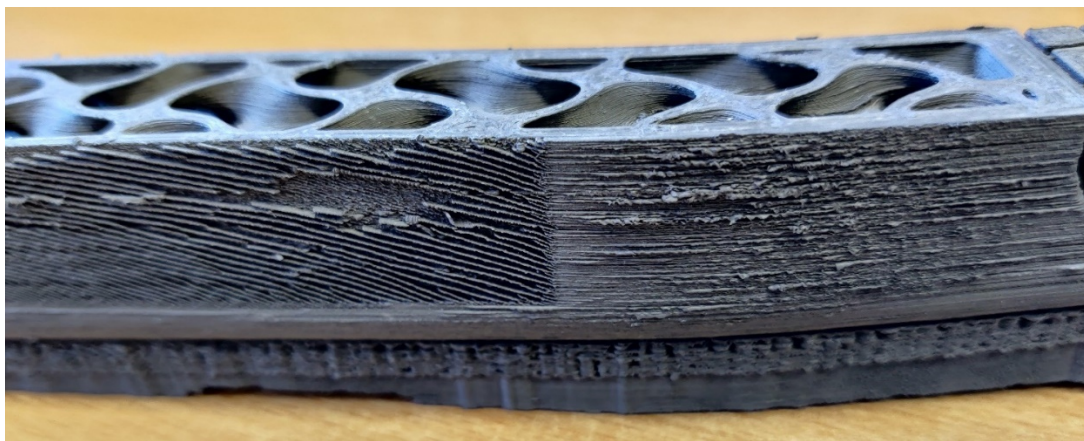


Figure 7.17: Degraded outer wall, probably due to retraction or Z-seam settings



Figure 7.18: Sintered BASF Ultrafuse 17-4 print with cracks caused by layer delamination during sintering



Figure 7.19: Successful print with Markforged 17-4 PH SS

7.8 Omitted Results of Thickness Optimization in Cuboid Lattice Structure

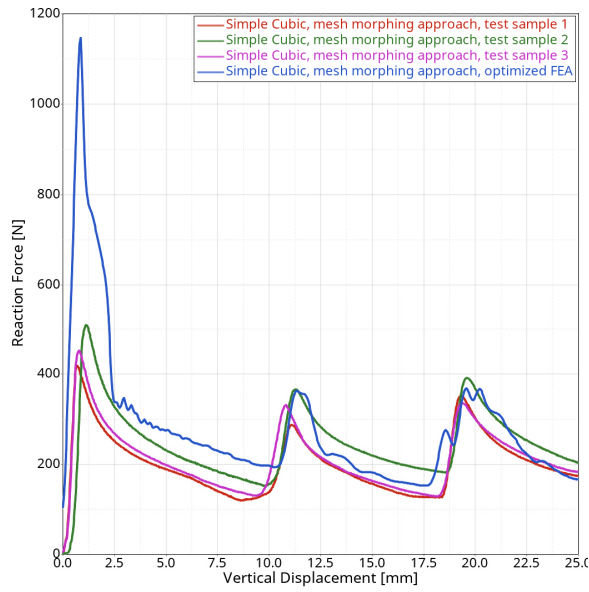


Figure 7.20: Simple Cubic lattice made of PA12 with mesh morphing optimization, tests versus simulation

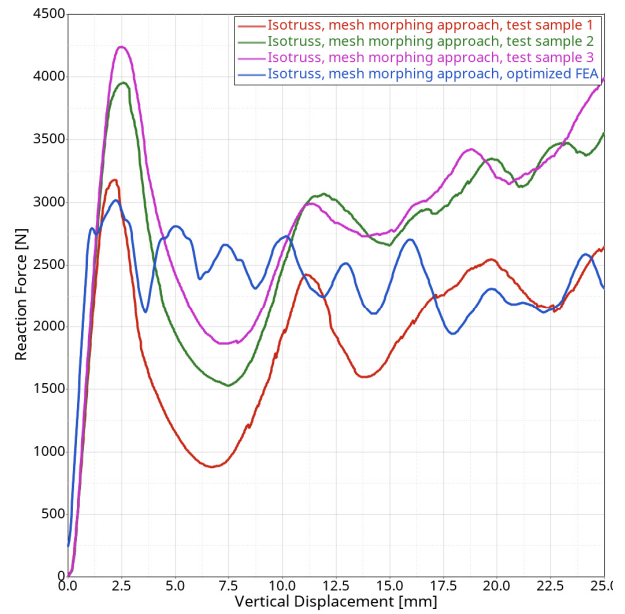


Figure 7.21: Isotruss lattice made of PA12 with mesh morphing optimization, tests versus simulation

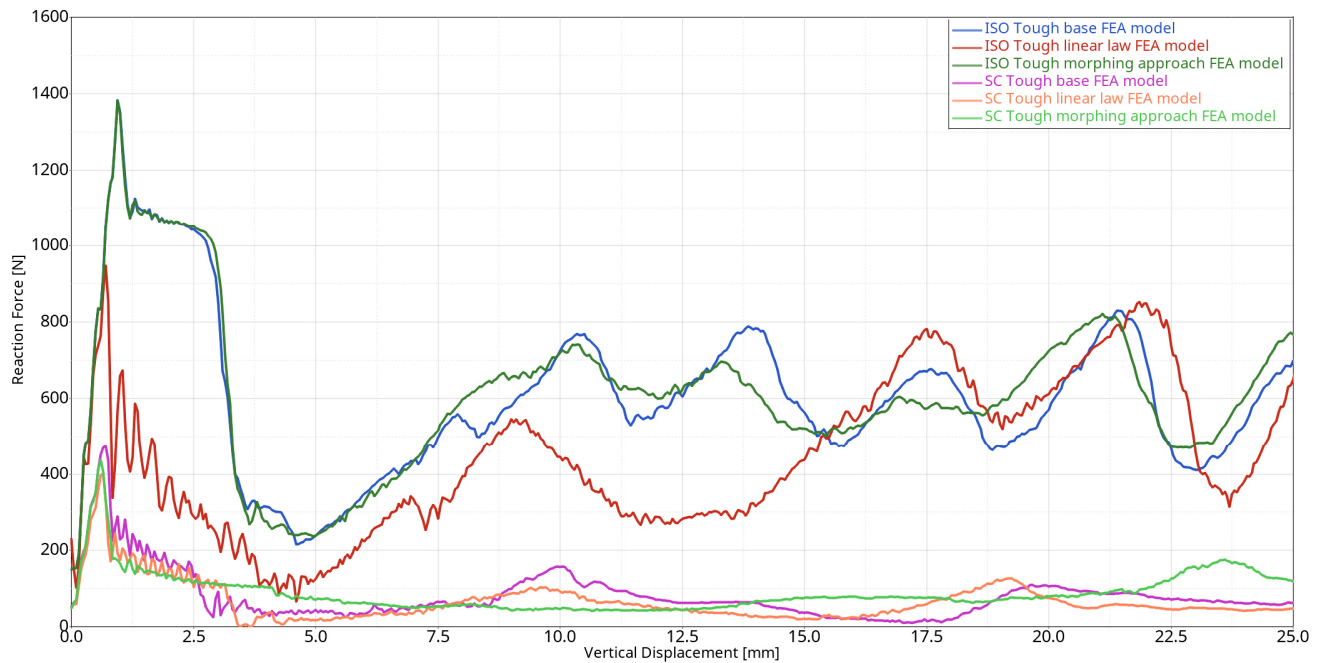


Figure 7.22: Simulations of Simple Cubic and Isotruss lattices made with Tough 2000 resin, FEA model optimization results

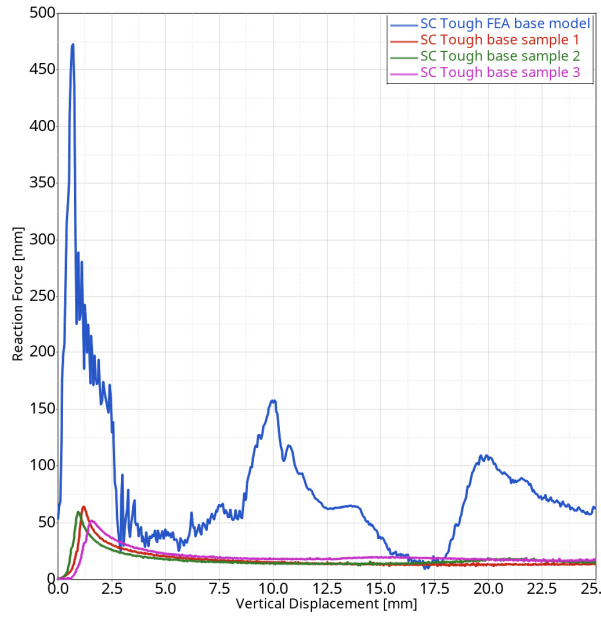


Figure 7.23: Simple Cubic lattice made with Tough 2000 resin, base model, tests versus simulations

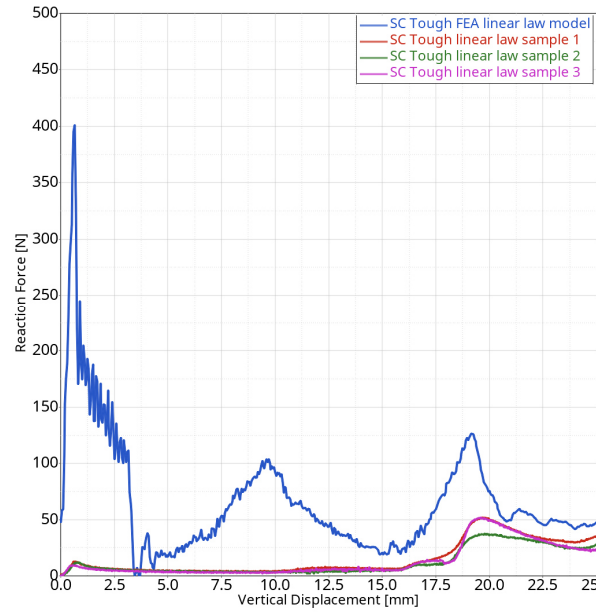


Figure 7.24: Simple Cubic lattice made with Tough 2000 resin, model with linear law thickness optimization, tests versus simulations

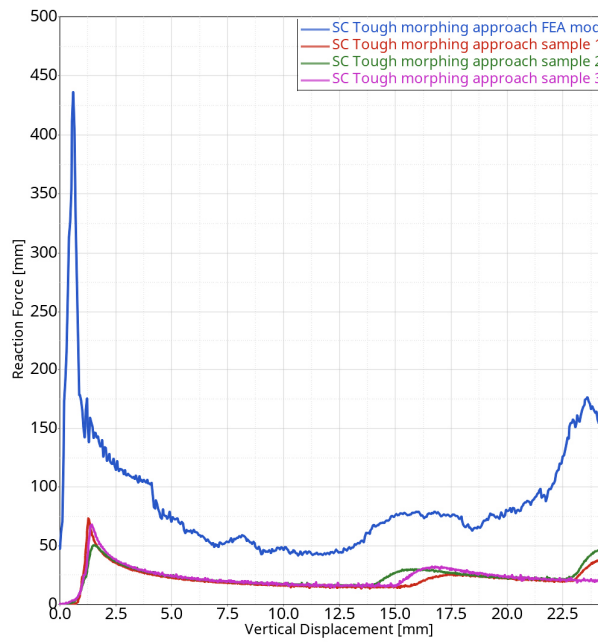


Figure 7.25: Simple Cubic lattice made with Tough 2000 resin, model with mesh morphing optimization, tests versus simulations

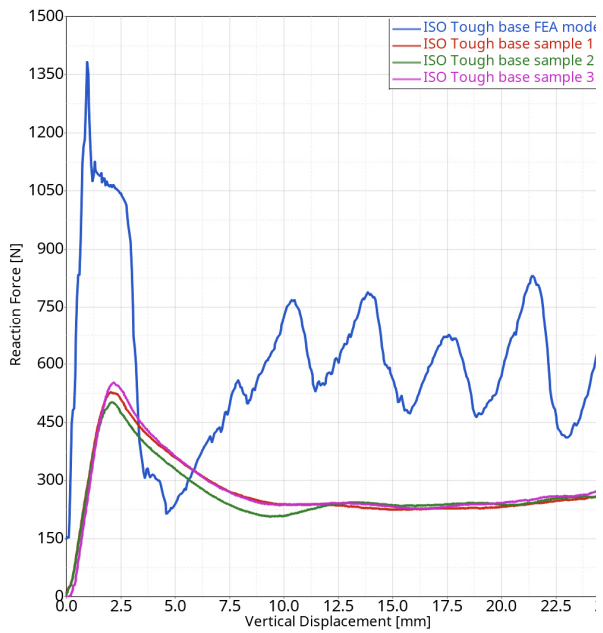


Figure 7.26: Simple Cubic lattice made with Tough 2000 resin, base model, tests versus simulations

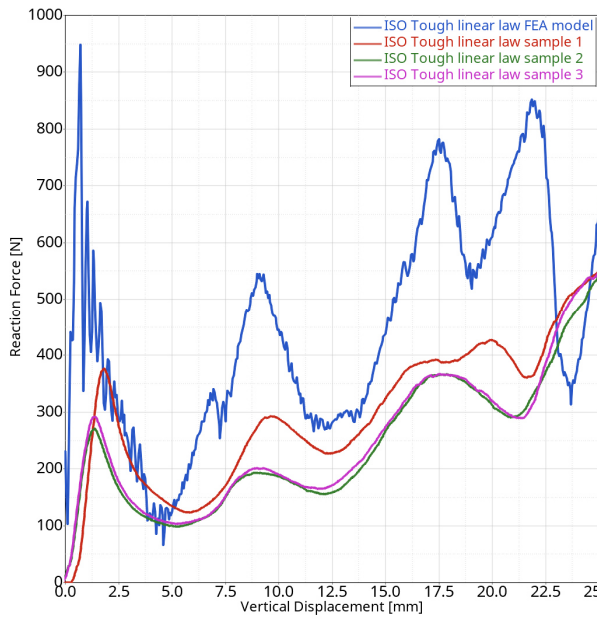


Figure 7.27: Isotruss lattice made with Tough 2000 resin, model with linear law thickness optimization, tests versus simulations

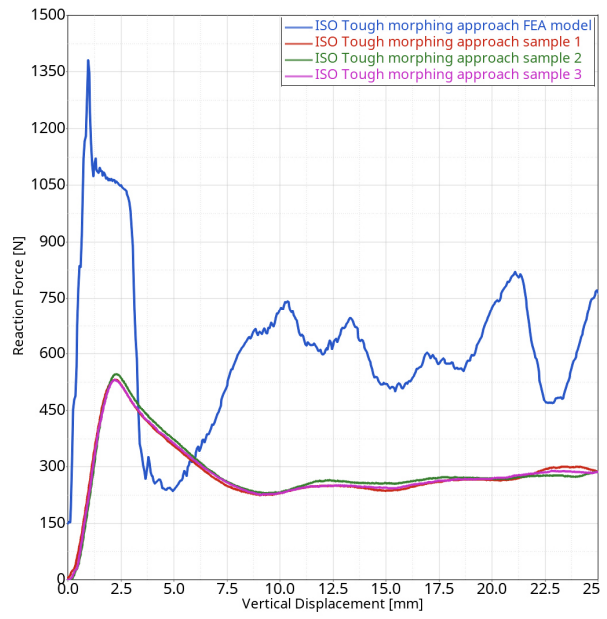


Figure 7.28: Isotruss lattice made with Tough 2000 resin, model with mesh morphing optimization, tests versus simulations

7.9 Test Stand for Helmet Drop Tests



Figure 7.29: Helmet drop test stand



Figure 7.30: Cast AZ91 magnesium dummy head following EN 960

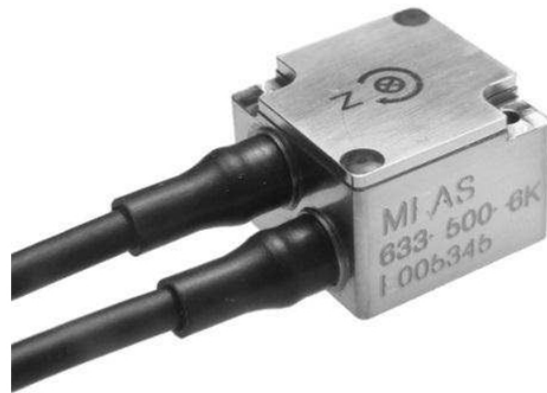


Figure 7.31: TE Connectivity 633 acceleration and gyro sensor with six degrees of freedom with upper limits of $\pm 2000G$ translational acceleration and $\pm 12.000^\circ/s$ rotational velocity capacity



Figure 7.32: Mikrotron Cube 7 high speed camera used for visual correlation with simulations



Figure 7.33: HBM U10 12.5kN load cell placed below the anvil's impact surface to log its reaction force

7.10 Helmet Geometry with Lattice Structure

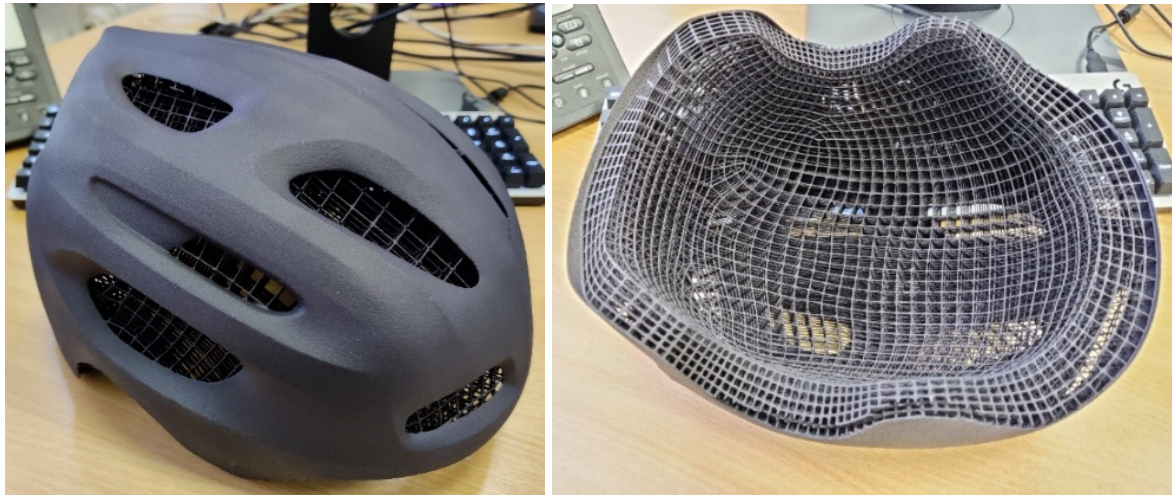


Figure 7.34: First prototype of lattice liner helmet printed with SLS in PA12 by GCL Technologies to check its manufacturability



Figure 7.35: Helmet with Truncated Cube lattice at 1.5mm thickness used for material optimization study



Figure 7.36: Helmet with tetrahedral lattice with insufficient strut thickness



Figure 7.37: Powder accumulation at impact site of optimized Reentrant lattice helmet



Figure 7.38: Re-entrant lattice helmet cut open after test to check the excess powder distribution



Figure 7.39: Re-entrant lattice helmet model with additional powder drainage holes

Bibliography

- 3d Printer Patents* | *UpCounsel* 2021. (n.d.). Retrieved November 2, 2021, from <https://www.upcounsel.com/3d-printer-patents>
- Abueidda, D. W., Elhebeary, M., Shiang, C. S. (Andrew), Pang, S., Abu Al-Rub, R. K., & Jasiuk, I. M. (2019). Mechanical properties of 3D printed polymeric Gyroid cellular structures: Experimental and finite element study. In *Materials and Design* (Vol. 165). <https://doi.org/10.1016/j.matdes.2019.107597>
- Aghajani, S., Wu, C., Li, Q., & Fang, J. (2023). Additively manufactured composite lattices: A state-of-the-art review on fabrications, architectures, constituent materials, mechanical properties, and future directions. *Thin-Walled Structures*, 111539. <https://doi.org/10.1016/j.tws.2023.111539>
- Ahn, S. H., Baek, C., Lee, S., & Ahn, I. S. (2003). Anisotropic tensile failure model of rapid prototyping parts - Fused Deposition Modeling (FDM). *International Journal of Modern Physics B*, 17(8-9 I), 1510–1516. <https://doi.org/10.1142/s0217979203019241>
- Ajdari, A., Nayeb-Hashemi, H., & Vaziri, A. (2011). Dynamic crushing and energy absorption of regular, irregular and functionally graded cellular structures. *International Journal of Solids and Structures*, 48(3–4), 506–516. <https://doi.org/10.1016/j.ijsolstr.2010.10.018>
- Al-Ketan, O., Lee, D.-W., Rowshan, R., & Abu Al-Rub, R. K. (2020). Functionally graded and multi-morphology sheet TPMS lattices: Design, manufacturing, and mechanical properties. *Journal of the Mechanical Behavior of Biomedical Materials*, 102, 103520. <https://doi.org/10.1016/j.jmbbm.2019.103520>
- Allen, G. (2019). *nTopology Modeling Technology*.
- Al-Saedi, D. S. J., Masood, S. H., Faizan-Ur-Rab, M., Alomarah, A., & Ponnusamy, P. (2018). Mechanical properties and energy absorption capability of functionally graded F2BCC lattice fabricated by SLM. *Materials and Design*, 144, 32–44. <https://doi.org/10.1016/j.matdes.2018.01.059>
- Altair Inspire*. (n.d.). Retrieved October 31, 2023, from <https://altair.com/inspire/>
- Altair OptiStruct*. (n.d.). Retrieved October 31, 2023, from <https://altair.com/optistruct/>
- Altair Sulis*. (n.d.). Retrieved October 31, 2023, from <https://altair.com/sulis>
- Altair University Fall Webinar Series 2020*. (n.d.). Retrieved October 26, 2021, from <https://web.altair.com/altair-university-2020-training-series-optistruct-sao>
- Altenbach, H., & Öchsner, A. (2010). *Cellular and Porous Materials in Structures and Processes* (H. Altenbach & A. Öchsner, Eds.; Vol. 521). Springer Vienna. <https://doi.org/10.1007/978-3-7091-0297-8>

- Alvarez C., K. L., Lagos C., R. F., & Aizpun, M. (2016). Investigating the influence of infill percentage on the mechanical properties of fused deposition modelled ABS parts. *Ingenieria e Investigacion*, 36(3), 110–116. <https://doi.org/10.15446/ing.investig.v36n3.56610>
- Ansys Mechanical*. (n.d.). Retrieved October 31, 2023, from <https://www.ansys.com/products/structures/ansys-mechanical>
- Ansys Spaceclaim*. (n.d.). Retrieved October 31, 2023, from <https://www.ansys.com/products/3d-design/ansys-spaceclaim>
- Arulrajah, A., Disfani, M. M., Maghoolpilehrood, F., Horpibulsuk, S., Udonchai, A., Imteaz, M., & Du, Y.-J. (2015). Engineering and environmental properties of foamed recycled glass as a lightweight engineering material. *Journal of Cleaner Production*, 94, 369–375. <https://doi.org/10.1016/j.jclepro.2015.01.080>
- Ashby, M. F. (1983). The mechanical properties of cellular solids. *Metallurgical Transactions A*, 14(9), 1755–1769. <https://doi.org/10.1007/BF02645546>
- Aurenhammer, F., Klein, R., & Lee, D.-T. (2013). *Voronoi Diagrams and Delaunay Triangulations*. WORLD SCIENTIFIC. <https://doi.org/10.1142/8685>
- Autodesk Fusion 360*. (n.d.). Retrieved December 22, 2023, from <https://www.autodesk.com/products/fusion-360/overview>
- Autodesk Netfabb*. (n.d.). Retrieved October 31, 2023, from <https://www.autodesk.com/products/netfabb/overview?term=1-YEAR&tab=subscription>
- Autodesk Within Medical*. (n.d.). Retrieved October 31, 2023, from <https://www.autodesk.com/products/within-medical/overview>
- Badini, S., Regondi, S., Lammi, C., Bollati, C., Donvito, G., & Pugliese, R. (2023). Computational Mechanics of Form-Fitting 3D-Printed Lattice-Based Wrist-Hand Orthosis for Motor Neuron Disease. *Biomedicines*, 11(7), 1787. <https://doi.org/10.3390/biomedicines11071787>
- Baena-Moreno, F. M., González-Castaño, M., Navarro de Miguel, J. C., Miah, K. U. M., Ossenbrink, R., Odriozola, J. A., & Arellano-García, H. (2021). Stepping toward Efficient Microreactors for CO₂ Methanation: 3D-Printed Gyroid Geometry. *ACS Sustainable Chemistry & Engineering*, 9(24), 8198–8206. <https://doi.org/10.1021/acssuschemeng.1c01980>
- Bai, L., Gong, C., Chen, X., Sun, Y., Xin, L., Pu, H., Peng, Y., & Luo, J. (2020). Mechanical properties and energy absorption capabilities of functionally graded lattice structures: Experiments and simulations. *International Journal of Mechanical Sciences*, 182. <https://doi.org/10.1016/j.ijmecsci.2020.105735>

- Barma, P., Rhodes, M. B., & Salovey, R. (1978). Mechanical properties of particulate-filled polyurethane foams. *Journal of Applied Physics*, 49(10), 4985–4991. <https://doi.org/10.1063/1.324444>
- BASF Ultrafuse Metal Filaments*. (n.d.). Retrieved December 18, 2023, from <https://forward-am.com/material-portfolio/ultrafuse-filaments-for-fused-filaments-fabrication-fff/metal-filaments/>
- Bhatia, A., & Sehgal, A. K. (2023). Additive manufacturing materials, methods and applications: A review. *Materials Today: Proceedings*, 81, 1060–1067. <https://doi.org/10.1016/j.matpr.2021.04.379>
- Birchall, J. D., & Thomas, N. L. (1983). On the architecture and function of cuttlefish bone. In *JOURNAL OF MATERIALS SCIENCE* (Vol. 18).
- Cao, L., Fu, Q., Si, Y., Ding, B., & Yu, J. (2018). Porous materials for sound absorption. *Composites Communications*, 10, 25–35. <https://doi.org/10.1016/j.coco.2018.05.001>
- Carbon 3D Print Lattice Innovation — The adidas Story*. (n.d.). Retrieved November 12, 2021, from <https://www.carbon3d.com/resources/whitepaper/the-adidas-story/>
- Chan, R., & Nakamura, M. (1969). Mechanical Properties of Plastic Foams. *Journal of Cellular Plastics*, 5(2), 112–118. <https://doi.org/10.1177/0021955X6900500207>
- Chatzigeorgiou, C., Piotrowski, B., Chemisky, Y., Laheurte, P., & Meraghni, F. (2022). Numerical investigation of the effective mechanical properties and local stress distributions of TPMS-based and strut-based lattices for biomedical applications. *Journal of the Mechanical Behavior of Biomedical Materials*, 126, 105025. <https://doi.org/10.1016/j.jmbbm.2021.105025>
- Chen, W., Zheng, X., & Liu, S. (2018). Finite-element-mesh based method for modeling and optimization of lattice structures for additive manufacturing. *Materials*, 11(11). <https://doi.org/10.3390/ma11112073>
- Chen, X., Hu, M., Sun, Y., Yang, J., Bai, L., & Xiong, Y. (2022). Wide-range tuning of the mechanical properties of TPMS lattice structures through frequency variation. *Materials & Design*, 224, 111370. <https://doi.org/10.1016/j.matdes.2022.111370>
- Chen, Z., Wu, X., Xie, Y. M., Wang, Z., & Zhou, S. (2020). Re-entrant auxetic lattices with enhanced stiffness: A numerical study. *International Journal of Mechanical Sciences*, 178(December 2019), 105619. <https://doi.org/10.1016/j.ijmecsci.2020.105619>
- Cheng, L., Liu, J., & To, A. C. (2018). Concurrent lattice infill with feature evolution optimization for additive manufactured heat conduction design. *Structural and Multidisciplinary Optimization*, 58(2), 511–535. <https://doi.org/10.1007/s00158-018-1905-7>

- Choy, S. Y., Sun, C. N., Leong, K. F., & Wei, J. (2017). Compressive properties of functionally graded lattice structures manufactured by selective laser melting. *Materials and Design*, *131*, 112–120. <https://doi.org/10.1016/j.matdes.2017.06.006>
- Christensen, R. M. (1986). Mechanics of low density materials. *Journal of the Mechanics and Physics of Solids*, *34*(6), 563–578. [https://doi.org/10.1016/0022-5096\(86\)90037-2](https://doi.org/10.1016/0022-5096(86)90037-2)
- Cobra Aero, NTopology, & Renishaw. (2020). *Drone-engine Cylinder Redesigned for Additive Manufacturing*. https://ntopology.com/wp-content/uploads/2020/01/CobraAero_CaseStudy.pdf
- Corbel, S., Dufaud, O., & Roques-Carmes, T. (2011). Materials for Stereolithography. In *Stereolithography* (pp. 141–159). Springer US. https://doi.org/10.1007/978-0-387-92904-0_6
- Davoudinejad, A., Perez, L. C. D., Quagliotti, D., Pedersen, D. B., García, J. A. A., Yagüe-Fabra, J. A., & Tosello, G. (2018). Geometrical and feature of size design effect on direct stereolithography micro additively manufactured components. *Procedia Structural Integrity*, *13*, 1250–1255. <https://doi.org/10.1016/j.prostr.2018.12.256>
- Daynes, S., Feih, S., Lu, W. F., & Wei, J. (2017). Optimisation of functionally graded lattice structures using isostatic lines. *Materials and Design*, *127*(February), 215–223. <https://doi.org/10.1016/j.matdes.2017.04.082>
- Decker, T., & Kedziora, S. (2023a). Local Thickness Optimization of Functionally Graded Lattice Structures in Compression. *Applied Sciences*, *13*(23), 12969. <https://doi.org/10.3390/app132312969>
- Decker, T., & Kedziora, S. (2023b). Optimizing the Thickness of Functionally Graded Lattice Structures for High-Performance Energy Absorption : A Case Study Based on a Bicycle Helmet. *[Submitted for Publication]*, 1–24.
- Decker, T., Kedziora, S., & Museyibov, E. (2023). Comparison of Strength Properties of Common Powder Bed Fusion and Stereolithography Materials. *Key Engineering Materials*, *969*, 11–20. <https://doi.org/10.4028/p-Sgu1sR>
- Decker, T., Kedziora, S., & Wolf, C. (2020). Practical Implementation of Functionally Graded Lattice Structures in a Bicycle Crank Arm. *885th International Conference on Science, Technology, Engineering and Management (ICSTEM), November*, 58–64.
- Demharter, A. (1998). Polyurethane rigid foam, a proven thermal insulating material for applications between +130°C and –196°C. *Cryogenics*, *38*(1), 113–117. [https://doi.org/10.1016/S0011-2275\(97\)00120-3](https://doi.org/10.1016/S0011-2275(97)00120-3)

- Deshpande, V. S., Ashby, M. F., & Fleck, N. A. (2001). Foam topology: Bending versus stretching dominated architectures. *Acta Materialia*, 49(6), 1035–1040. [https://doi.org/10.1016/S1359-6454\(00\)00379-7](https://doi.org/10.1016/S1359-6454(00)00379-7)
- Desktop Metal Homepage*. (n.d.). Retrieved December 18, 2023, from <https://www.desktopmetal.com>
- Diegel, O., Nordin, A., & Motte, D. (2019). *A Practical Guide to Design for Additive Manufacturing*. Springer Singapore. <https://doi.org/10.1007/978-981-13-8281-9>
- Dong, G., Tang, Y., Li, D., & Zhao, Y. F. (2020). Design and optimization of solid lattice hybrid structures fabricated by additive manufacturing. *Additive Manufacturing*, 33, 101116. <https://doi.org/10.1016/j.addma.2020.101116>
- Ellis, A. L., & Lazidis, A. (2018). Foams for Food Applications. In *Polymers for Food Applications* (pp. 271–327). Springer International Publishing. https://doi.org/10.1007/978-3-319-94625-2_11
- Feng, J., Fu, J., Yao, X., & He, Y. (2022). Triply periodic minimal surface (TPMS) porous structures: from multi-scale design, precise additive manufacturing to multidisciplinary applications. *International Journal of Extreme Manufacturing*, 4(2), 022001. <https://doi.org/10.1088/2631-7990/ac5be6>
- Feng, Y., Guo, X., Huang, K., Elsayed, H., Franchin, G., Gong, H., & Colombo, P. (2021). Enhanced electromagnetic microwave absorption of SiOC ceramics targeting the integration of structure and function. *Journal of the European Ceramic Society*, 41(13), 6393–6405. <https://doi.org/10.1016/j.jeurceramsoc.2021.06.007>
- Fernandes, R. R., & Tamijani, A. Y. (2021). Design optimization of lattice structures with stress constraints. *Materials & Design*, 210, 110026. <https://doi.org/10.1016/j.matdes.2021.110026>
- Formnext - Hub for Additive Manufacturing*. (n.d.). Retrieved December 22, 2023, from <https://formnext.mesago.com/frankfurt/en.html>
- Frido Verweij. (2023, October 31). *Voronoi Tessellation*.
- Gan, Z., Turner, M. D., & Gu, M. (2016). Biomimetic gyroid nanostructures exceeding their natural origins. *Science Advances*, 2(5). <https://doi.org/10.1126/sciadv.1600084>
- Gent, A. N., & Thomas, A. G. (1959). The deformation of foamed elastic materials. *Journal of Applied Polymer Science*, 1(1), 107–113. <https://doi.org/10.1002/app.1959.070010117>
- Gent, A. N., & Thomas, A. G. (1963). Mechanics of Foamed Elastic Materials. *Rubber Chemistry and Technology*, 36(3), 597–610. <https://doi.org/10.5254/1.3539591>

- Gibson, L. J. (1985). The mechanical behaviour of cancellous bone. *Journal of Biomechanics*, *18*(5), 317–328. [https://doi.org/10.1016/0021-9290\(85\)90287-8](https://doi.org/10.1016/0021-9290(85)90287-8)
- Gibson, L. J., & Ashby, M. F. (1997). *Cellular Solids*. Cambridge University Press. <https://doi.org/10.1017/CBO9781139878326>
- Gibson, L. J., Ashby, M. F., Schajer, G. S., & Robertson, C. I. (1982). The mechanics of two-dimensional cellular materials. *Proceedings of the Royal Society of London. A. Mathematical and Physical Sciences*, *382*(1782), 25–42. <https://doi.org/10.1098/rspa.1982.0087>
- Gong, H., Snelling, D., Kardel, K., & Carrano, A. (2019). Comparison of Stainless Steel 316L Parts Made by FDM- and SLM-Based Additive Manufacturing Processes. *Jom*, *71*(3), 880–885. <https://doi.org/10.1007/s11837-018-3207-3>
- Gorguluarslan, R. M., Gungor, O. U., Yildiz, S., & Erem, E. (2021). Energy absorption behavior of stiffness optimized graded lattice structures fabricated by material extrusion. *Meccanica*, *56*(11), 2825–2841. <https://doi.org/10.1007/s11012-021-01404-5>
- Grasshopper*. (n.d.). Retrieved October 31, 2023, from <https://www.grasshopper3d.com>
- Green, D. J., & Hoagland, R. G. (1985). Mechanical Behavior of Lightweight Ceramics Based on Sintered Hollow Spheres. *Journal of the American Ceramic Society*, *68*(7), 395–398. <https://doi.org/10.1111/j.1151-2916.1985.tb10151.x>
- Habib, F. N., Iovenitti, P., Masood, S. H., & Nikzad, M. (2018). Fabrication of polymeric lattice structures for optimum energy absorption using Multi Jet Fusion technology. *Materials and Design*, *155*, 86–98. <https://doi.org/10.1016/j.matdes.2018.05.059>
- Hadas, E., Shpigel, M., & Ilan, M. (2009). Particulate organic matter as a food source for a coral reef sponge. *Journal of Experimental Biology*, *212*(22), 3643–3650. <https://doi.org/10.1242/jeb.027953>
- Han, L., & Che, S. (2018). An Overview of Materials with Triply Periodic Minimal Surfaces and Related Geometry: From Biological Structures to Self-Assembled Systems. *Advanced Materials*, *30*(17). <https://doi.org/10.1002/adma.201705708>
- Han, Y., & Lu, W. F. (2018). A novel design method for nonuniform lattice structures based on topology optimization. *Journal of Mechanical Design, Transactions of the ASME*, *140*(9). <https://doi.org/10.1115/1.4040546>
- Helou, M., & Kara, S. (2018). Design, analysis and manufacturing of lattice structures: An overview. *International Journal of Computer Integrated Manufacturing*, *31*(3), 243–261. <https://doi.org/10.1080/0951192X.2017.1407456>
- Hilyard, N. C., & Cunningham, A. (1994). Low density cellular plastics. In N. C. Hilyard & A. Cunningham (Eds.), *Low density cellular plastics*. Springer Netherlands. <https://doi.org/10.1007/978-94-011-1256-7>

- Hong, D. (n.d.). *From implicit to print without making a mesh*.
<https://www.ntop.com/resources/product-updates/from-implicit-to-print/>
- Hössinger-Kalteis, A., Reiter, M., Jerabek, M., & Major, Z. (2021). Overview and comparison of modelling methods for foams. In *Journal of Cellular Plastics* (Vol. 57, Issue 6, pp. 951–1001). SAGE Publications Ltd.
<https://doi.org/10.1177/0021955X20966329>
- Hou, W., Yang, X., Zhang, W., & Xia, Y. (2018). Design of energy-dissipating structure with functionally graded auxetic cellular material. *International Journal of Crashworthiness*, 23(4), 366–376.
<https://doi.org/10.1080/13588265.2017.1328764>
- How nTopology was used to design, analyze and print a fuel-cooled oil cooler*. (n.d.). 12.02.2020. <https://ntopology.com/blog/2020/02/12/how-ntop-platform-was-used-to-design-analyze-and-print-a-fuel-cooled-oil-cooler/>
- Jalali, S. K., Beigrezaee, M. J., Misseroni, D., & Pugno, N. M. (2024). A modified Gibson-Ashby model for functionally graded lattice structures. *Mechanics of Materials*, 188, 104822. <https://doi.org/10.1016/j.mechmat.2023.104822>
- Johnathan, H. (2020). *Control the collapse: Architected materials for impact absorption | nTopology*. <https://ntopology.com/blog/2020/04/15/control-the-collapse-architected-materials-for-impact-absorption/>
- Kang, D., Park, S., Son, Y., Yeon, S., Kim, S. H., & Kim, I. (2019). Multi-lattice inner structures for high-strength and light-weight in metal selective laser melting process. *Materials and Design*, 175. <https://doi.org/10.1016/j.matdes.2019.107786>
- Kazemi, H., Vaziri, A., & Norato, J. A. (2020). Multi-material topology optimization of lattice structures using geometry projection. *Computer Methods in Applied Mechanics and Engineering*, 363, 112895.
<https://doi.org/10.1016/j.cma.2020.112895>
- Kedziora, S., Decker, T., & Museyibov, E. (2023). Application of Functionally Graded Shell Lattice as Infill in Additive Manufacturing. *Materials*, 16(12), 4401.
<https://doi.org/10.3390/ma16124401>
- Kedziora, S., Decker, T., Museyibov, E., Morbach, J., Hohmann, S., Huwer, A., & Wahl, M. (2022). Strength Properties of 316L and 17-4 PH Stainless Steel Produced with Additive Manufacturing. *Materials*, 15(18). <https://doi.org/10.3390/ma15186278>
- Khosroshahi, S. F., Duckworth, H., Galvanetto, U., & Ghajari, M. (2019). The effects of topology and relative density of lattice liners on traumatic brain injury mitigation. *Journal of Biomechanics*, 97, 109376.
<https://doi.org/10.1016/j.jbiomech.2019.109376>

- Khosroshahi, S. F., Tsampas, S. A., & Galvanetto, U. (2018). Feasibility study on the use of a hierarchical lattice architecture for helmet liners. *Materials Today Communications*, *14*, 312–323. <https://doi.org/10.1016/j.mtcomm.2018.02.002>
- Kim, E., Shin, Y.-J., & Ahn, S.-H. (2016). The effects of moisture and temperature on the mechanical properties of additive manufacturing components: fused deposition modeling. *Rapid Prototyping Journal*, *22*(6), 887–894. <https://doi.org/10.1108/RPJ-08-2015-0095>
- Ko, W. L. (1965). Deformations of Foamed Elastomers. *Journal of Cellular Plastics*, *1*(1), 45–50. <https://doi.org/10.1177/0021955X6500100107>
- Körner, C. (2016). Additive manufacturing of metallic components by selective electron beam melting — a review. *International Materials Reviews*, *61*(5), 361–377. <https://doi.org/10.1080/09506608.2016.1176289>
- Kraynik, A. M., & Warren, W. E. (1994). The elastic behavior of low-density cellular plastics. In *Low density cellular plastics* (pp. 187–225). Springer Netherlands. https://doi.org/10.1007/978-94-011-1256-7_7
- Kumar, S. (2003). Selective laser sintering: A qualitative and objective approach. *JOM*, *55*(10), 43–47. <https://doi.org/10.1007/s11837-003-0175-y>
- Kurauchi, T., Sato, N., Kamigaito, O., & Komatsu, N. (1984). Mechanism of high energy absorption by foamed materials-foamed rigid polyurethane and foamed glass. *Journal of Materials Science*, *19*(3), 871–880. <https://doi.org/10.1007/BF00540457>
- Langlois, V., Trinh, V. H., Lusso, C., Perrot, C., Chateau, X., Khidas, Y., & Pitois, O. (2018). Permeability of solid foam: Effect of pore connections. *Physical Review E*, *97*(5), 053111. <https://doi.org/10.1103/PhysRevE.97.053111>
- Le Barbenchon, L., Girardot, J., Kopp, J. B., & Viot, P. (2019). Multi-scale foam : 3D structure/compressive behaviour relationship of agglomerated cork. *Materialia*, *5*. <https://doi.org/10.1016/j.mtla.2019.100219>
- Lederman, J. M. (1971). The Prediction of the Tensile Properties of Flexible Foams. In *JOURNAL OF APPLIED POLYMER SCIENCE* (Vol. 15).
- Lehder, E. F., Ashcroft, I. A., Wildman, R. D., Ruiz-Cantu, L. A., & Maskery, I. (2021). A multiscale optimisation method for bone growth scaffolds based on triply periodic minimal surfaces. *Biomechanics and Modeling in Mechanobiology*, *20*(6), 2085–2096. <https://doi.org/10.1007/s10237-021-01496-8>
- Li, D., Liao, W., Dai, N., & Xie, Y. M. (2020). Anisotropic design and optimization of conformal gradient lattice structures. *CAD Computer Aided Design*, *119*, 102787. <https://doi.org/10.1016/j.cad.2019.102787>
- Ling, C., Cernicchi, A., Gilchrist, M. D., & Cardiff, P. (2019). Mechanical behaviour of additively-manufactured polymeric octet-truss lattice structures under quasi-static

- and dynamic compressive loading. *Materials and Design*, 162, 106–118. <https://doi.org/10.1016/j.matdes.2018.11.035>
- Liu, X., Wada, T., Suzuki, A., Takata, N., Kobashi, M., & Kato, M. (2021). Understanding and suppressing shear band formation in strut-based lattice structures manufactured by laser powder bed fusion. *Materials and Design*, 199, 109416. <https://doi.org/10.1016/j.matdes.2020.109416>
- Maconachie, T., Leary, M., Lozanovski, B., Zhang, X., Qian, M., Faruque, O., & Brandt, M. (2019). SLM lattice structures: Properties, performance, applications and challenges. *Materials & Design*, 183, 108137. <https://doi.org/10.1016/j.matdes.2019.108137>
- Mahmoud, D., & Elbestawi, M. (2017). Lattice Structures and Functionally Graded Materials Applications in Additive Manufacturing of Orthopedic Implants: A Review. *Journal of Manufacturing and Materials Processing*, 1(2), 13. <https://doi.org/10.3390/jmmp1020013>
- Maiti, S. K., Gibson, L. J., & Ashby, M. F. (1984). Deformation and energy absorption diagrams for cellular solids. *Acta Metallurgica*, 32(11), 1963–1975. [https://doi.org/10.1016/0001-6160\(84\)90177-9](https://doi.org/10.1016/0001-6160(84)90177-9)
- Markforged Homepage*. (n.d.). Retrieved December 18, 2023, from <https://markforged.com>
- Maskery, I., Aboulkhair, N. T., Aremu, A. O., Tuck, C. J., & Ashcroft, I. A. (2017). Compressive failure modes and energy absorption in additively manufactured double gyroid lattices. *Additive Manufacturing*, 16, 24–29. <https://doi.org/10.1016/j.addma.2017.04.003>
- Maskery, I., Aremu, A. O., Parry, L., Wildman, R. D., Tuck, C. J., & Ashcroft, I. A. (2018). Effective design and simulation of surface-based lattice structures featuring volume fraction and cell type grading. *Materials and Design*, 155, 220–232. <https://doi.org/10.1016/j.matdes.2018.05.058>
- Maskery, I., Hussey, A., Panesar, A., Aremu, A., Tuck, C., Ashcroft, I., & Hague, R. (2017). An investigation into reinforced and functionally graded lattice structures. *Journal of Cellular Plastics*, 53(2), 151–165. <https://doi.org/10.1177/0021955X16639035>
- Massivit*. (n.d.). N/a. Retrieved November 10, 2023, from <https://www.massivit3d.com>
- Materialise 3-matic*. (n.d.). Retrieved October 31, 2023, from <https://www.materialise.com/en/industrial/software/3-matic>
- Medical Additive Complex Structures - Titanium Complex Medical Structure Manufacturer*. (n.d.). <https://tangiblesolutions3d.com/capabilities/engineering-support/complex-structures/>

- Menges, G., & Knipschild, F. (1975). Estimation of mechanical properties for rigid polyurethane foams. *Polymer Engineering & Science*, 15(8), 623–627. <https://doi.org/10.1002/pen.760150810>
- Meshmixer*. (n.d.). <https://Meshmixer.Com>. Retrieved October 31, 2023, from <https://meshmixer.com>
- Mohamed, O. A., Masood, S. H., & Bhowmik, J. L. (2015). Optimization of fused deposition modeling process parameters: a review of current research and future prospects. *Advances in Manufacturing*, 3(1), 42–53. <https://doi.org/10.1007/s40436-014-0097-7>
- Molz, F. J., & Ikenberry, E. (1974). Water Transport Through Plant Cells and Cell Walls: Theoretical Development. *Soil Science Society of America Journal*, 38(5), 699–704. <https://doi.org/10.2136/sssaj1974.03615995003800050009x>
- Morgan, J. S., Wood, J. L., & Bradt, R. C. (1981). Cell size effects on the strength of foamed glass. *Materials Science and Engineering*, 47(1), 37–42. [https://doi.org/10.1016/0025-5416\(81\)90038-0](https://doi.org/10.1016/0025-5416(81)90038-0)
- Mullen, J. S., & Fischer, P. F. (1999). Filtering techniques for complex geometry fluid flows. *Communications in Numerical Methods in Engineering*, 15(1), 9–18. [https://doi.org/10.1002/\(SICI\)1099-0887\(199901\)15:1<9::AID-CNM219>3.0.CO;2-Y](https://doi.org/10.1002/(SICI)1099-0887(199901)15:1<9::AID-CNM219>3.0.CO;2-Y)
- Nasim, M., Hasan, M. J., & Galvanetto, U. (2022). Impact behavior of energy absorbing helmet liners with PA12 lattice structures: A computational study. *International Journal of Mechanical Sciences*, 233(April), 107673. <https://doi.org/10.1016/j.ijmecsci.2022.107673>
- Nazir, A., Abate, K. M., Kumar, A., & Jeng, J. Y. (2019). A state-of-the-art review on types, design, optimization, and additive manufacturing of cellular structures. *International Journal of Advanced Manufacturing Technology*, 104(9–12), 3489–3510. <https://doi.org/10.1007/s00170-019-04085-3>
- Niknam, H., & Akbarzadeh, A. H. (2020). Graded lattice structures: Simultaneous enhancement in stiffness and energy absorption. *Materials and Design*, 196. <https://doi.org/10.1016/j.matdes.2020.109129>
- Nisja, G. A., Cao, A., & Gao, C. (2021). Short review of nonplanar fused deposition modeling printing. *Material Design & Processing Communications*, 3(4). <https://doi.org/10.1002/mdp2.221>
- Noronha, J., Dash, J., Leary, M., Watson, M., Qian, M., Kyriakou, E., & Brandt, M. (2023). Additively Manufactured Functionally Graded Lattices: Design, Mechanical Response, Deformation Behavior, Applications, and Insights. *JOM*. <https://doi.org/10.1007/s11837-023-06190-x>
- nTop*. (n.d.). <https://www.ntop.com>

- nTop Cross section of a drone engine cylinder designed in nTop Platform by Cobra Aero - MANUFACTUR3D.* (n.d.). Retrieved December 17, 2020, from <https://manufactur3dmag.com/generative-design-tools-that-put-you-in-control-part-ii/ntop-cross-section-of-a-drone-engine-cylinder-designed-in-ntop-platform-by-cobra-aero/>
- O'Connor, H. J., Dickson, A. N., & Dowling, D. P. (2018). Evaluation of the mechanical performance of polymer parts fabricated using a production scale multi jet fusion printing process. *Additive Manufacturing*, 22, 381–387. <https://doi.org/10.1016/j.addma.2018.05.035>
- Ozel, S. (2023). *nTop and Autodesk Fusion Join Forces: Direct Implicit Model Import Will Be Showcased at Formnext 2023.* https://www.autodesk.com/products/fusion-360/blog/ntop-and-autodesk-fusion-join-forces-direct-implicit-model-import-will-be-showcased-at-formnext-2023/?dysig_tid=f0a60cc5a76b40c7a85f22c9e5e7552c&utm_source=LinkedIn&utm_medium=social&utm_campaign=Bonfirefresh
- Pan, C., Han, Y., & Lu, J. (2020). Design and Optimization of Lattice Structures: A Review. *Applied Sciences*, 10(18), 6374. <https://doi.org/10.3390/app10186374>
- Pandzic, A., Hodzic, D., & Milovanovic, A. (2019). Effect of infill type and density on tensile properties of pla material for fdm process. *Annals of DAAAM and Proceedings of the International DAAAM Symposium*, 30(1), 545–554. <https://doi.org/10.2507/30th.daaam.proceedings.074>
- Pellegrino, S., & Calladine, C. R. (1986). Matrix analysis of statically and kinematically indeterminate frameworks. *International Journal of Solids and Structures*, 22(4), 409–428. [https://doi.org/10.1016/0020-7683\(86\)90014-4](https://doi.org/10.1016/0020-7683(86)90014-4)
- Pham, M. S., Liu, C., Todd, I., & Lertthanasarn, J. (2019a). Damage-tolerant architected materials inspired by crystal microstructure. *Nature*, 565(7739), 305–311. <https://doi.org/10.1038/s41586-018-0850-3>
- Pham, M. S., Liu, C., Todd, I., & Lertthanasarn, J. (2019b). Damage-tolerant architected materials inspired by crystal microstructure. *Nature*, 565(7739), 305–311. <https://doi.org/10.1038/s41586-018-0850-3>
- Plocher, J., & Panesar, A. (2019). Review on design and structural optimisation in additive manufacturing: Towards next-generation lightweight structures. *Materials & Design*, 183, 108164. <https://doi.org/10.1016/j.matdes.2019.108164>
- Pollen AM.* (n.d.). Retrieved November 10, 2023, from <https://pollen.am>
- PTC Creo.* (n.d.). Retrieved October 31, 2023, from <https://www.ptc.com/en/products/creo/>

- Pugh, R. J., Hamlett, C. A. E., & Fairhurst, D. J. (2023). A short overview of bubbles in foods and chocolate. *Advances in Colloid and Interface Science*, 314, 102835. <https://doi.org/10.1016/j.cis.2023.102835>
- Puzatova, A., Shakor, P., Laghi, V., & Dmitrieva, M. (2022). Large-Scale 3D Printing for Construction Application by Means of Robotic Arm and Gantry 3D Printer: A Review. *Buildings*, 12(11), 2023. <https://doi.org/10.3390/buildings12112023>
- Qiu, N., Wan, Y., Shen, Y., & Fang, J. (2023). Experimental and numerical studies on mechanical properties of TPMS structures. *International Journal of Mechanical Sciences*, 108657. <https://doi.org/10.1016/j.ijmecsci.2023.108657>
- Qureshi, Z. A., Elnajjar, E., Al-Ketan, O., Al-Rub, R. A., & Al-Omari, S. B. (2021). Heat transfer performance of a finned metal foam-phase change material (FMF-PCM) system incorporating triply periodic minimal surfaces (TPMS). *International Journal of Heat and Mass Transfer*, 170, 121001. <https://doi.org/10.1016/j.ijheatmasstransfer.2021.121001>
- Radiolaria - Geology is the Way*. (n.d.). Retrieved December 27, 2023, from <https://geologyistheway.com/it/sedimentary/radiolaria/>
- Rahman, H., Yarali, E., Zolfagharian, A., Serjouei, A., & Bodaghi, M. (2021). Energy absorption and mechanical performance of functionally graded soft–hard lattice structures. *Materials*, 14(6). <https://doi.org/10.3390/ma14061366>
- Raps, D., Hossieny, N., Park, C. B., & Altstädt, V. (2015). Past and present developments in polymer bead foams and bead foaming technology. *Polymer*, 56, 5–19. <https://doi.org/10.1016/j.polymer.2014.10.078>
- Redwood, B., Schöffner, F., & Garret, B. (2018). *The 3D Printing Handbook*. 347.
- Rhino3D*. (n.d.). Retrieved October 31, 2023, from <https://www.rhino3d.com>
- Röver, T., Kuehne, M., Bishop, F., Clague, L., Bossen, B., & Emmelmann, C. (2023). Design and numerical assessment of an additively manufactured Schwarz diamond triply periodic minimal surface fluid-fluid heat exchanger. *Journal of Laser Applications*, 35(4). <https://doi.org/10.2351/7.0001184>
- Rusch, K. C. (1970). Load-compression behavior of brittle foams. *Journal of Applied Polymer Science*, 14(5), 1263–1276. <https://doi.org/10.1002/app.1970.070140514>
- Sajjad, U., Rehman, T., Ali, M., Park, C. W., & Yan, W.-M. (2022). Manufacturing and potential applications of lattice structures in thermal systems: A comprehensive review of recent advances. *International Journal of Heat and Mass Transfer*, 198, 123352. <https://doi.org/10.1016/j.ijheatmasstransfer.2022.123352>
- Sanami, M., Ravirala, N., Alderson, K., & Alderson, A. (n.d.). *Auxetic Materials for Sports Applications*.

- Seharing, A., Azman, A. H., & Abdullah, S. (2020). A review on integration of lightweight gradient lattice structures in additive manufacturing parts. *Advances in Mechanical Engineering*, *12*(6), 1–21. <https://doi.org/10.1177/1687814020916951>
- Shanmugasundaram, S. A., Razmi, J., Mian, M. J., & Ladani, L. (2020). Mechanical anisotropy and surface roughness in additively manufactured parts fabricated by stereolithography (SLA) using statistical analysis. *Materials*, *13*(11). <https://doi.org/10.3390/ma13112496>
- Sherwood, J. A., & Frost, C. C. (1992). Constitutive modeling and simulation of energy absorbing polyurethane foam under impact loading. *Polymer Engineering & Science*, *32*(16), 1138–1146. <https://doi.org/10.1002/pen.760321611>
- Simpleware CAD*. (n.d.). Retrieved October 31, 2023, from <https://www.synopsys.com/simpleware/software/cad-module.html>
- Simsek, U., Ozdemir, M., & Sendur, P. (2021). An efficient design methodology for graded surface-based lattice structures using free-size optimization and enhanced mapping method. *Materials & Design*, *210*, 110039. <https://doi.org/10.1016/j.matdes.2021.110039>
- Singh, R., Gupta, A., Tripathi, O., Srivastava, S., Singh, B., Awasthi, A., Rajput, S. K., Sonia, P., Singhal, P., & Saxena, K. K. (2020). Powder bed fusion process in additive manufacturing: An overview. *Materials Today: Proceedings*, *26*, 3058–3070. <https://doi.org/10.1016/j.matpr.2020.02.635>
- Song, B., Zhang, L., & Shi, Y. (2023). Microlattice metamaterials. In *Metamaterial Design and Additive Manufacturing* (pp. 223–266). Elsevier. <https://doi.org/10.1016/B978-0-443-18900-5.00006-X>
- Suh, K. W. (2000). Foamed Plastics. In *Kirk-Othmer Encyclopedia of Chemical Technology*. Wiley. <https://doi.org/10.1002/0471238961.06150113192108.a01>
- Suh, K. W., Park, C. P., Maurer, M. J., Tusim, M. H., Genova, R. De, Broos, R., & Sophiaea, D. P. (2000). Lightweight Cellular Plastics. *Advanced Materials*, *12*(23), 1779–1789. [https://doi.org/10.1002/1521-4095\(200012\)12:23<1779::AID-ADMA1779>3.0.CO;2-3](https://doi.org/10.1002/1521-4095(200012)12:23<1779::AID-ADMA1779>3.0.CO;2-3)
- Surjadi, J. U., Gao, L., Du, H., Li, X., Xiong, X., Fang, N. X., & Lu, Y. (2019). Mechanical Metamaterials and Their Engineering Applications. *Advanced Engineering Materials*, *21*(3), 1–37. <https://doi.org/10.1002/adem.201800864>
- S-Works Romin EVO with Mirror*. (n.d.). <https://www.specialized.com/us/en/s-works-romin-evo-with-mirror/p/205228?color=330429-205228>
- Takezawa, A., Zhang, X., & Kitamura, M. (2019). Optimization of an additively manufactured functionally graded lattice structure with liquid cooling considering structural performances. *International Journal of Heat and Mass Transfer*, *143*, 118564. <https://doi.org/10.1016/j.ijheatmasstransfer.2019.118564>

- Tamburrino, F., Graziosi, S., & Bordegoni, M. (2018). The design process of additively manufactured mesoscale lattice structures: A review. *Journal of Computing and Information Science in Engineering*, 18(4), 1–16. <https://doi.org/10.1115/1.4040131>
- Tancogne-Dejean, T., Spierings, A. B., & Mohr, D. (2016). Additively-manufactured metallic micro-lattice materials for high specific energy absorption under static and dynamic loading. *Acta Materialia*, 116, 14–28. <https://doi.org/10.1016/j.actamat.2016.05.054>
- Tao, W., & Leu, M. C. (2016). Design of lattice structure for additive manufacturing. *International Symposium on Flexible Automation, ISFA 2016*, 325–332. <https://doi.org/10.1109/ISFA.2016.7790182>
- Tao, W., Sutton, A., Kolan, K., & Leu, M. C. (2018). *Design of Lattice Structures with Graded Density Fabricated by Additive Manufacturing Cyber Physical Cloud Manufacturing Systems View project Solvent-based 3D printing of polymer/bioactive glass composites View project 19 PUBLICATIONS 207 CITATIONS SEE PR*. <https://doi.org/10.11509/isfa.2018.122>
- The Virtual Foundry Filamet*. (n.d.). Retrieved December 18, 2023, from <https://thevirtualfoundry.com>
- Tony Abbey. (2018, March 15). *Topology Optimization (Part 1) - FETraining Resource Site*.
- Ulm, F.-J. (2001). Construction: Cellular Materials. In *Encyclopedia of Materials: Science and Technology* (pp. 1570–1574). Elsevier. <https://doi.org/10.1016/B0-08-043152-6/00280-1>
- Uribe-Lam, E., Treviño-Quintanilla, C. D., Cuan-Urquizo, E., & Olvera-Silva, O. (2021). Use of additive manufacturing for the fabrication of cellular and lattice materials: a review. *Materials and Manufacturing Processes*, 36(3), 257–280. <https://doi.org/10.1080/10426914.2020.1819544>
- Voo, L., Armand, M., & Kleinberger, M. (2004). Stress fracture risk analysis of the human femur based on computational biomechanics. *Johns Hopkins APL Technical Digest (Applied Physics Laboratory)*, 25(3), 223–230.
- Walter, T. R., Richards, A. W., & Subhash, G. (2009). A Unified Phenomenological Model for Tensile and Compressive Response of Polymeric Foams. *Journal of Engineering Materials and Technology*, 131(1). <https://doi.org/10.1115/1.3026556>
- Wang, W., Feng, D., Yang, L., Li, S., & Wang, C. C. L. (2023). Topology optimization of self-supporting lattice structure. *Additive Manufacturing*, 67, 103507. <https://doi.org/10.1016/j.addma.2023.103507>
- Wang, Y.-T., & Hsu, C.-K. (2023). Novel parameter optimization lattice design for improving osseointegration in hypo-loading regions – A case study of maxillary

- tumor reconstruction implant. *Materials & Design*, 233, 112274. <https://doi.org/10.1016/j.matdes.2023.112274>
- Warren, W. E., & Kraynik, A. M. (1988). The Linear Elastic Properties of Open-Cell Foams. *Journal of Applied Mechanics*, 55(2), 341–346. <https://doi.org/10.1115/1.3173680>
- Warren, W. E., & Kraynik, A. M. (1991). The Nonlinear Elastic Behavior of Open-Cell Foams. *Journal of Applied Mechanics*, 58(2), 376–381. <https://doi.org/10.1115/1.2897196>
- Wilde, P. (2012). Foam formation in dough and bread quality. In *Breadmaking* (pp. 370–399). Elsevier. <https://doi.org/10.1533/9780857095695.2.370>
- Wu, J., Aage, N., Westermann, R., & Sigmund, O. (2018). Infill Optimization for Additive Manufacturing—Approaching Bone-Like Porous Structures. *IEEE Transactions on Visualization and Computer Graphics*, 24(2), 1127–1140. <https://doi.org/10.1109/TVCG.2017.2655523>
- Wu, J., Wang, W., & Gao, X. (2019). *Design and Optimization of Conforming Lattice Structures*.
- Xiao, L., & Song, W. (2018). Additively-manufactured functionally graded Ti-6Al-4V lattice structures with high strength under static and dynamic loading: Experiments. *International Journal of Impact Engineering*, 111, 255–272. <https://doi.org/10.1016/j.ijimpeng.2017.09.018>
- Yan, C., Hao, L., Yang, L., Hussein, A. Y., Young, P. G., Li, Z., & Li, Y. (2021). Metal alloys uniform TPMS structures. In *Triply Periodic Minimal Surface Lattices Additively Manufactured by Selective Laser Melting* (pp. 39–130). Elsevier. <https://doi.org/10.1016/B978-0-12-824438-8.00003-0>
- Yang, J., Chen, X., Sun, Y., Zhang, J., Feng, C., Wang, Y., Wang, K., & Bai, L. (2022). Compressive properties of bidirectionally graded lattice structures. *Materials and Design*, 218, 110683. <https://doi.org/10.1016/j.matdes.2022.110683>
- Yang, L., Harrysson, O., West, H., & Cormier, D. (2013). Modeling of uniaxial compression in a 3D periodic re-entrant lattice structure. *Journal of Materials Science*, 48(4), 1413–1422. <https://doi.org/10.1007/s10853-012-6892-2>
- Yang, W., An, J., Chua, C. K., & Zhou, K. (2020). Acoustic absorptions of multifunctional polymeric cellular structures based on triply periodic minimal surfaces fabricated by stereolithography. *Virtual and Physical Prototyping*, 15(2), 242–249. <https://doi.org/10.1080/17452759.2020.1740747>
- Yap, C. Y., Chua, C. K., Dong, Z. L., Liu, Z. H., Zhang, D. Q., Loh, L. E., & Sing, S. L. (2015). Review of selective laser melting: Materials and applications. *Applied Physics Reviews*, 2(4). <https://doi.org/10.1063/1.4935926>

- Zhang, C., Liu, J., Yuan, Z., Xu, S., Zou, B., Li, L., & Ma, Y. (2021). A novel lattice structure topology optimization method with extreme anisotropic lattice properties. *Journal of Computational Design and Engineering*, 8(5), 1367–1390. <https://doi.org/10.1093/jcde/qwab051>
- Zhang, J., Li, H., Zhou, Y., Chen, S., & Rong, Q. (2023). An Analysis of Trabecular Bone Structure Based on Principal Stress Trajectory. *Bioengineering*, 10(10), 1224. <https://doi.org/10.3390/bioengineering10101224>
- Zhu, L., Li, L., Li, Z., Shi, J., Tang, W., Yang, J., & Jiang, Q. (2019). Design and biomechanical characteristics of porous meniscal implant structures using triply periodic minimal surfaces. *Journal of Translational Medicine*, 17(1), 89. <https://doi.org/10.1186/s12967-019-1834-2>
- Zhu, L., Li, N., & Childs, P. R. N. (2018). Light-weighting in aerospace component and system design. *Propulsion and Power Research*, 7(2), 103–119. <https://doi.org/10.1016/j.jprr.2018.04.001>
- Ziaee, M., & Crane, N. B. (2019). Binder jetting: A review of process, materials, and methods. *Additive Manufacturing*, 28, 781–801. <https://doi.org/10.1016/j.addma.2019.05.031>